UNIVERSITY OF ROCHESTER
LABORATORY FOR LASER ENERGETICS

Volume 132
July–September 2012
DOE/NA/28302-1091

LLE Review

Quarterly Report

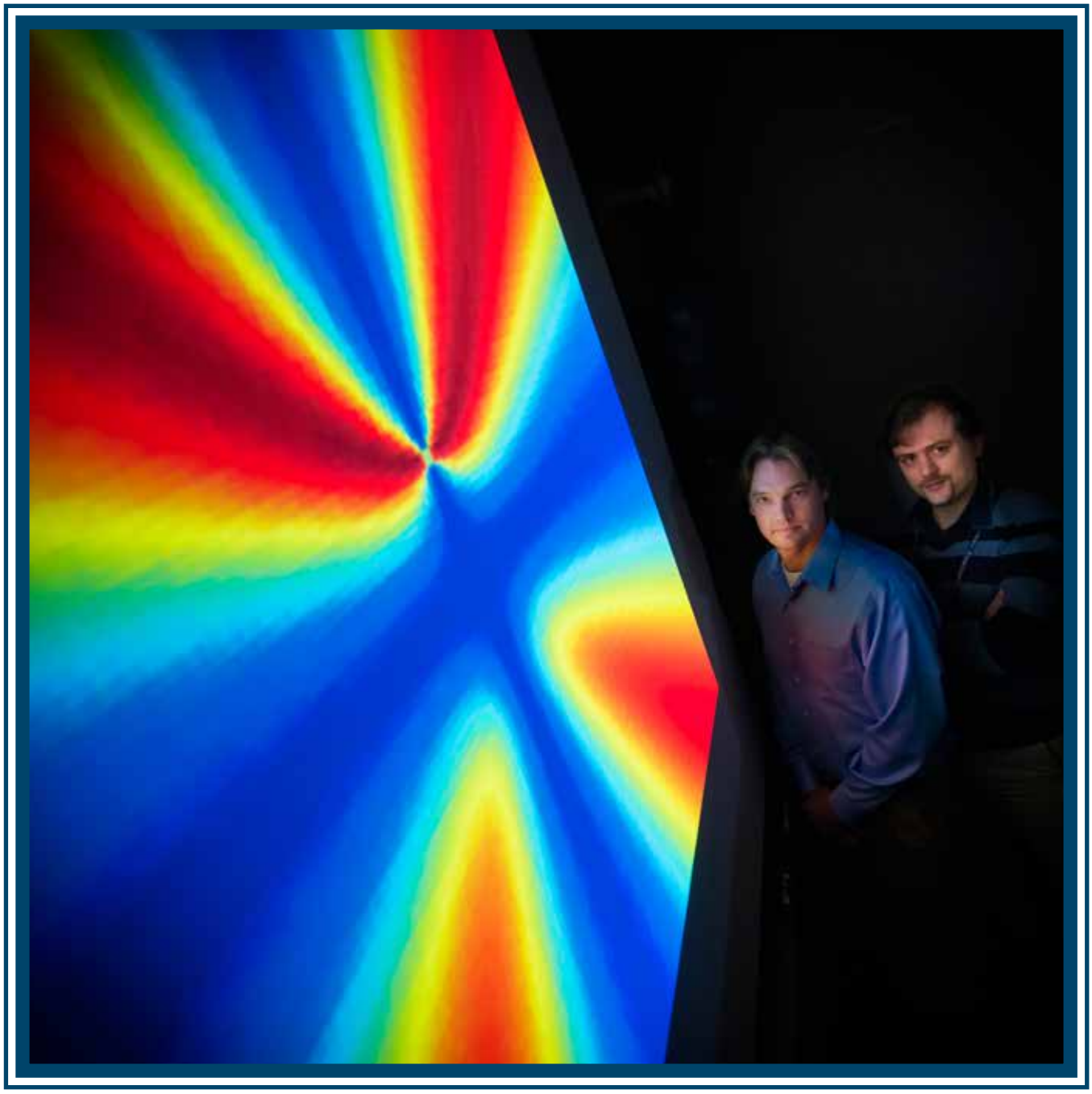

About the Cover:

The cover photo highlights LLE's scientist Dr. Dustin Froula (right) with his postdoc Dr. Tomline Michel (left) who have led laser–plasma interaction (LPI) experiments on the OMEGA Laser System. Direct-drive ignition is susceptible to LPI's that depend on multiple laser beams. Cross-beam energy transfer (CBET) and two-plasmon decay (TPD) are two such instabilities that are driven by the overlapping multiple laser beams. The CBET instability can reduce the hydrodynamic efficiency, while TPD may reduce the compression efficiency. To gain a thorough understanding of these instabilities in ignition-relevant plasma conditions, a series of LPI experiments has been performed on the OMEGA Laser System. The TPD results indicate that, in general, the hot-electron production depends on the configuration of the laser beams and the sum of the intensities of the beams that share the same angle with the common electron plasma wave. This is explained by recent multibeam TPD growth rate calculations that indicate the maximum gain for TPD exists, in general, outside of the plane defined by the laser beams (figure below). These studies have led to a deeper understanding of the instabilities and to potential mitigation strategies for both CBET and TPD.

Common-wave two-plasmon decay

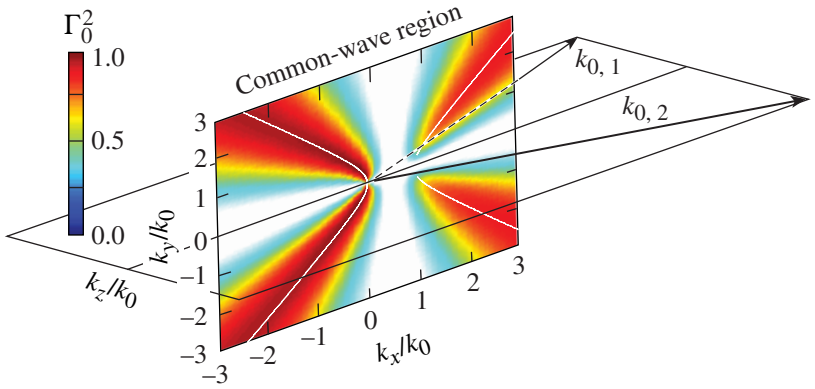

TPD growth rates for two laser beams polarized along the common-wave plane (y axis).

The work described in this volume includes current research at the Laboratory for Laser Energetics, which is supported by New York State Energy Research and Development Authority, the University of Rochester, the U.S. Department of Energy Office of Inertial Confinement Fusion under Cooperative Agreement No. DE-FC52-08NA28302, and other agencies.

Printed in the United States of America
Available from
National Technical Information Services
U.S. Department of Commerce
5285 Port Royal Road
Springfield, VA 22161
www.ntis.gov

For questions or comments, contact
Suxing Hu, Editor
Laboratory for Laser Energetics
250 East River Road
Rochester, NY 14623-1299
(585) 273-3794
www.lle.rochester.edu

UNIVERSITY OF ROCHESTER
LABORATORY FOR LASER ENERGETICS

Volume 132
July–September 2012
DOE/NA/28302-1091

LLE Review

Quarterly Report

UR LLE

Contents

In Brief

This volume of the LLE Review, covering July–September 2012, features "Laser–Plasma Interactions in Direct-Drive–Ignition Plasmas," by D. H. Froula, D. T. Michel, I. V. Igumenshchev, S. X. Hu, B. Yaakobi, J. F. Myatt, D. H. Edgell, R. K. Follett, V. Yu. Glebov, V. N. Goncharov, T. J. Kessler, A. V. Maximov, P. B. Radha, T. C. Sangster, W. Seka, R. W. Short, A. A. Solodov, C. Sorce, and C. Stoeckl. In this article (p. 181), the authors review the current understanding of multibeam laser–plasma instabilities including cross-beam energy transfer (CBET) and two-plasmon decay (TPD) for direct-drive ignition. CBET is driven by multiple laser beams and can significantly reduce the hydrodynamic efficiency in direct-drive experiments on OMEGA. Reducing the radii of the laser beams significantly increases the hydrodynamic efficiency at the cost of an increase in low-mode nonuniformities. The combination of zooming and dynamic bandwidth reduction will provide a 30% effective increase in the drive energy on OMEGA direct-drive implosions. TPD instability can also be driven by multiple laser beams. Both planar and spherical experiments were performed to study the hot electrons generated by TPD at the Omega Laser Facility. The fraction of laser energy converted to hot electrons scales with the hot-electron temperature for all geometries and over a wide range of intensities. At ignition-relevant intensities, the fraction of laser energy converted to hot electrons is measured to decrease by an order of magnitude when the ablator material is changed from carbon-hydrogen to aluminum. The TPD results are compared with a multibeam linear theory and a nonlinear Zakharov model.

Additional highlights of research presented in this issue include the following articles:

- D. R. Harding and W. T. Shmayda report on investigations of stress-radiation–induced swelling in plastic capsules (p. 191). The process of filling targets with DT for cryogenic experiments on the OMEGA laser induces small-scale features on the inner surface of the plastic capsules. Each feature was a cluster of low-level domes (<0.1-μm high) with individual lateral dimensions smaller than 5 μm that collectively covered lateral dimensions of up to 300 μm^2. These features were observed only when a high-radiation dose was combined with high stress in the plastic wall, as occurs when the capsules are permeation filled and transferred at cryogenic temperatures. No porosity or void structure was observed in or below these domes. It is speculated that the domes' swelling is caused by a radiation-induced bond scission and chemical restructuring that reduces the plastic density in localized regions.

- J. Serafini and Y. Wang (LLE and Departments of Physics and Astronomy, University of Rochester); R. Bellman and C. K. Williams (Corning Incorporated); and R. Sobolewski (LLE and Departments of Electric and Computer Engineering and Physics, University of Rochester) present studies on time-resolved carrier dynamics in Si-on-glass absorbers for photovoltaic cells (p. 198). A femtosecond pump–probe spectroscopy method was used to characterize amorphous and microcrystalline silicon films grown on glass substrates as absorbers for photovoltaic applications and collected corresponding transmissivity change ($\Delta T/T$) waveforms. Depending on their growth process, optically excited, ~300-nm-thick Si absorbers exhibited a bi-exponential carrier relaxation with characteristic times varying from picoseconds to nanoseconds. Experimental data were interpreted using a three-rate–equations model, and the relaxation was identified as electron–phonon cooling, followed by carrier trapping and/or Shockley–Read–Hall recombination. An excellent fit between the model and the $\Delta T/T$ transients was obtained, indicating a correlation between the hydrogen content in the film and the trap concentration.

- N. Sinenian, J. A. Frenje, F. H. Séguin, C. K. Li, and R. D. Petrasso (MIT); W. Theobald and C. Stoeckl (LLE); and R. B. Stephens (GA) present measurements of energetic protons in cone-in-shell fast-ignitor experiments at the Omega Laser Facility (p. 204). In these experiments, charged-particle spectrometers were used to measure a significant population (>10^{13}) of energetic protons (7.5 MeV maximum), indicating the presence of strong electric fields. These energetic protons, observed in directions both transverse and forward relative to the direction of the short-pulse laser beam, have been used to study aspects of coupling efficiency of the fast-ignitor. Forward-going protons were less energetic and showed no dependence on laser intensity or whether the cone tip was intact when the short-pulse laser was fired. Maximum proton energies transverse to the cone-in-shell target scale with incident on-target laser intensity (2 to 6 $\times$ 10^{18} W/cm^2), as described by the ponderomotive scaling ($\sim I^{1/2}$). It is shown that these protons are accelerated from the entire cone surface, possibly due to return currents, rather than from the cone tip alone. The proton-inferred lower bound on the hot-electron temperature was hotter than the ponderomotive scaling by a factor of 2 to 3.
- R. D. Petrasso (Plasma Science and Fusion Center, MIT) reports on the Fourth Omega Laser Facility Users' Group Workshop on p. 213.
- This volume concludes with a summary of LLE's Summer High School Research Program (p. 219), the FY12 Laser Facility Report (p. 221), and the National Laser Users' Facility and External Users' Programs (p. 224).

Suxing Hu
Editor

Laser–Plasma Interactions in Direct-Drive–Ignition Plasmas

Introduction

Two approaches to inertial confinement fusion (ICF)[1] employ megajoule-class laser beams[2,3] to compress a fusion capsule to thermal nuclear burn. For the indirect-drive approach,[4] the laser beams are tightly focused through the laser entrance hole into a radiation cavity (hohlraum) resulting in relatively high single-beam laser intensities ($I_s \sim 10^{15}$ W/cm^2). The beams then propagate through a series of plasmas before converting their energy into soft x-ray radiation at the high-Z hohlraum wall.[5–8] The soft x-ray radiation emitted by the hohlraum illuminates a fusion capsule and the ablated material drives a spherical implosion.[4,9] As the high-intensity laser beams propagate to the hohlraum wall, they encounter millimeter-scale-length plasmas that make them particularly susceptible to laser–plasma instabilities[10] that reduce the x-ray drive. This is in contrast to the direct-drive approach,[11] where laser beams directly illuminate the fusion capsule and it is the overlapped laser beam intensity ($I_{ovr} \sim 10^{15}$ W/cm^2) that launches a series of shocks to compress the nuclear fuel to fusion conditions.[12] As laser beams propagate up the density gradient to the critical surface (Fig. 132.1), they are susceptible to several laser–plasma instabilities that can divert their energy, thereby reducing the hydrodynamic efficiency [$\epsilon = (1/2\, mv^2)/E_{laser}$, where m is the mass of the imploding shell, v is the implosion velocity, and E_{laser} is the total laser energy] or the symmetry of the drive. Direct drive is most susceptible to laser–plasma instabilities that depend on multiple laser beams, as the peak single-beam intensities are relatively low ($I_s \approx 8/NI_{ovr}$, where N is the total number of laser beams illuminating the capsule) and the coronal electron temperatures are high ($T_e \simeq 3.5$ keV). Cross-beam energy transfer (CBET)[13] and two-plasmon decay (TPD)[14] are two such instabilities that are driven by the intensities of multiple laser beams.

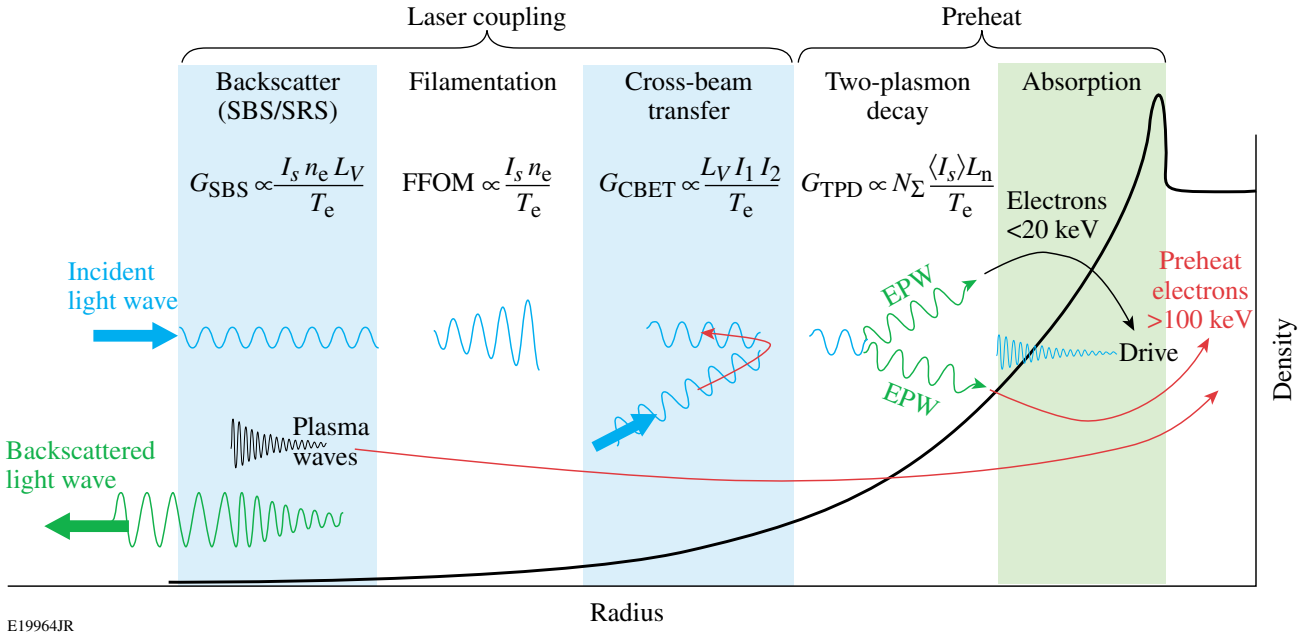

Figure 132.1
Schematic of the direct-drive density profile and potential laser–plasma interactions encountered by incident direct-drive beams. As a result of the relatively low single-beam intensities (I_s), direct-drive experiments are most susceptible to the laser-beam instabilities that are driven by multiple laser beams (e.g., CBET, TPD).

CBET is a mechanism that reduces the hydrodynamic efficiency in high-energy-density laser experiments.[15–19] For direct-drive fusion experiments [Fig. 132.2(a)], CBET was identified by linking discrepancies in the scattered-light spectrum to a lack of energy penetrating to the critical surface.[20] CBET results from large-amplitude ion-acoustic waves [Fig. 132.2(b)] driven by the laser light (k_2) that propagates past the target, seeding stimulated Brillouin scattering[21] along the light from the opposing laser beams (k_1). The enhanced ion-acoustic waves scatter light primarily from the central rays of the incident laser beams to the lower-energy outgoing rays. CBET is driven by the product of the intensity of the crossing beams near the Mach-1 surface.

Experiments focusing on TPD at direct-drive–ignition conditions[22] have shown that the efficiency of hot-electron generation scales with the overlapped laser-beam intensity, and experiments have demonstrated that multiple laser beams can share a common TPD electron plasmon wave.[23,24] The resonant common electron plasma waves are restricted to a region bisecting the laser beams [Fig. 132.2(c)], and the measured efficiency of the hot-electron generation scales rapidly with the maximum convective multibeam (intensity) gain[24,25]

$$G_{\mathrm{MB}} = 2.1\times 10^{-16} N_{\Sigma} f_g \frac{\langle I_{s,\mathrm{q}}\rangle [\mathrm{W/cm}^2] L_{\mathrm{n,q}}[\mu\mathrm{m}]}{T_{\mathrm{e,q}}[\mathrm{keV}]}, \qquad (1)$$

where N_{Σ} is the number of laser beams that share a common angle with the primary electron plasma wave, $\langle I_{s,\mathrm{q}}\rangle$ is the average single-beam intensity, $L_{\mathrm{n,q}}$ is the density scale length, $T_{\mathrm{e,q}}$ is the electron temperature, and q denotes the fact that these parameters are taken at the quarter-critical surface of the laser beams. The factor f_g is determined by the geometry and polarization of the laser beams.[24,25] The geometric factor and the number of symmetric beams are constant for a given configuration, resulting in a common-wave gain proportional to the overlapped laser-beam intensity.

The linear gain calculations provide general guidance for the TPD threshold but the instability is inherently nonlinear. To study the nonlinear behavior of TPD, simulations based on a nonlinear Zakharov model[26] were performed. *ZAK*[27] is a plasma-fluid model that incorporates saturation nonlinearities including density-profile modification,[28] Langmuir wave cavitation,[29] and the generation of ion-acoustic turbulence.[27,30] *ZAK* simulations can describe the growth and nonlinear saturation of the instability but do not include kinetic effects responsible for hot-electron generation. The generalization of the *ZAK* model, *QZAK*,[31–33] accounts for kinetic effects self-consistently in the quasi-linear approximation. The addition of kinetic effects reduces the amplitude of the electron plasma waves for a given $I_{\mathrm{q}} L_{\mathrm{n,q}} / T_{\mathrm{e,q}}$. These models provide a physics-based capability for calculating TPD at ignition conditions and a method for studying different mitigation techniques in this highly nonlinear process.

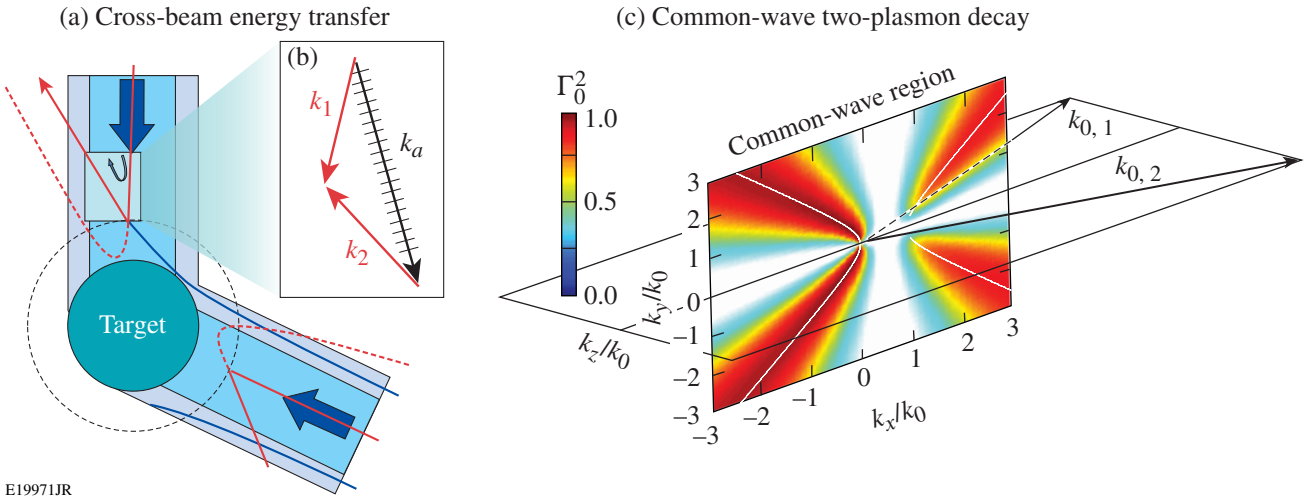

Figure 132.2
(a) Light rays propagating past the target (blue) interact with light rays in the central region of another beam (red). The interacting light rays seed an ion-acoustic wave near the Mach-1 surface (dashed circle). The ion-acoustic wave scatters light before it can penetrate deep into the target (dashed red curves). (b) A wave-vector diagram showing a typical matching condition for CBET. (c) The common-wave TPD growth rate $\left(\Gamma_0^2\right)$ for two OMEGA EP beams that are polarized in the vertical direction (k_y) is plotted in the resonant common-wave region; the common-wave region bisects the laser beams.

Underdense Hydrodynamics

To understand and mitigate the effect of laser–plasma instabilities, it is necessary to characterize the plasma conditions. The laser-intensity threshold for the onset of these instabilities must be taken into account in the design of fusion experiments; small variations in the plasma conditions can greatly impact target performance. Numerous laser–plasma instability studies over the past 20 years have emulated plasma conditions that will be achieved in fusion targets at the National Ignition Facility (NIF).[34–37] Generally, these studies have shown the strong sensitivity of laser–plasma interactions to the exact plasma conditions, highlighting the importance of correctly modeling the underdense plasma. Ultraviolet Thomson scattering provides access to the high densities prevalent in ICF coronal plasmas and is now routinely used as a diagnostic to characterize the electron and ion temperatures.[38–40]

The Thomson-scattering diagnostic on OMEGA employs a 20-J, $\lambda_{4\omega} = 0.26$-μm probe beam.[41] The Thomson-scattered light is collected from a $60 \times 75 \times 75$-mm volume defined by the 60-μm best-focus diameter of the probe beam, the 150-μm-wide spectrometer slit, and the 150-μm-wide streak camera slit.[40,42] The Thomson-scattering diagnostic probes ion-acoustic waves with a wave number $k_a = 2k_{4\omega} \sin(\theta/2)$, where $k_{4\omega} = 2\pi/\lambda_{4\omega}$ and $\theta = 63°$ is the scattering angle.

1. Hydrodynamic Modeling

The direct-drive–implosion experiments are designed using the 1-D hydrodynamics code *LILAC*,[43] which implements a nonlocal heat transport model[44] and a CBET model.[18,19] The CBET model is incorporated into the laser-absorption package, allowing for a self-consistent calculation of laser deposition with CBET. The model considers pairwise interactions of pump light rays with probe light rays and all possible crossings of these rays within the corona plasma. A spatial gain is estimated in the strong damping limit to calculate the energy transfer.

To reproduce the measured laser coupling and the measured hydrodynamic efficiency, both the nonlocal transport and CBET models must be used. The laser coupling is characterized by time-dependent absorption fraction, inferred from scattered-light measurements and the scattered-frequency spectrum.[20] When a flux-limited transport model is used, critical features in the scattering spectrum are not reproduced indicating that the time-dependent coronal conditions have not been simulated correctly. Simulations performed using the nonlocal transport model, but without CBET, drove the implosion too efficiently; the simulated bang time was ~200 ps earlier than measured, which is consistent with the lower shell-trajectory measurements inferred from x-ray self-emission images of the imploding targets.[45]

2. Spherical Geometry

Figure 132.3(a) shows the Thomson-scattering spectra obtained from two shots where 860-μm-diam capsules with 27-μm-thick carbon–hydrogen (CH) walls filled with 10 atm of D_2 gas were driven by a laser pulse consisting of three picket pulses followed by a main drive pulse at $I_{ovr} = 3 \times 10^{14}$ W/cm^2 (Ref. 12). Nearly 0.7 ns after the initial picket illuminated the target, the plasma has expanded to the Thomson-scattering volume located 400 μm from the initial target surface. Two characteristic ion-acoustic features were observed and, to obtain the plasma conditions, the spectra were fit [Fig. 132.3(b)] every 50 ps using a standard theoretical form factor.[46] The light scattered from the ion-acoustic waves was further blue shifted as a result of the outward plasma-flow velocity [Fig. 132.3(d)]; the ion-acoustic wave vectors (k_a) are aligned in the radial direction. The relative amplitude of the ion-acoustic features provides a measure of the drift between the ions and electrons near the phase velocity of the ion-acoustic waves [Fig. 132.3(d)].[46] This drift velocity was caused by the plasma maintaining quasi-neutrality as "fast" heat carrying electrons move outward.

The spectral feature nearest the wavelength of the probe [top feature in Fig. 132.3(a) and expanded in Fig. 132.4(a)] results from light in the wings of the probe beam that is reflected from the plasma; this turning point, located near the 3ω critical surface (the turning point has moved below the 4ω critical density as a result of the glancing incidence of the probe beam), is a result of the 60° angle between the probe beam and the target normal. Figure 132.4(b) shows the calculated spectrum obtained by propagating 4ω light through the simulated plasma conditions. The wavelength shift provides a measure of the changing path length along the probe beam caused by the rapidly changing density[47] and the Doppler shift induced by the moving turning point. The intensity modulation is a result of absorption; between the pickets, the plasma rapidly cools and the probe light is absorbed. These measurements provide a powerful set of criteria to assess the hydrodynamic models used to design direct-drive–fusion experiments and to study laser–plasma instabilities.

3. Planar Geometry

To validate the plasma conditions calculated in planar geometry and used to interpret the two-plasmon–decay results, Thomson-scattering measurements were obtained on OMEGA[48] using the same target platform, pulse shape, and

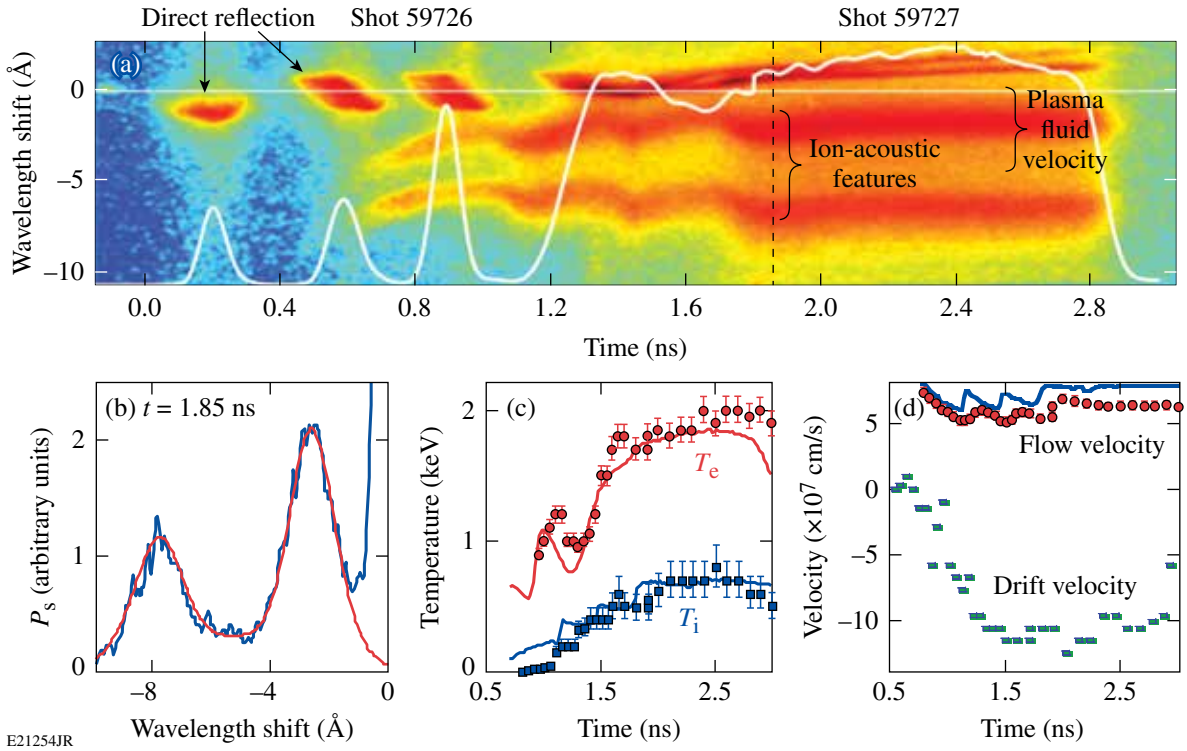

Figure 132.3
(a) The time-resolved Thomson-scattering spectrum obtained from the direct-drive coronal plasma. The pulse shape of the 3ω drive beams is shown (white curve). The Thomson-scattering probe beam was on over nearly the entire record (–0.1 ns to 2.8 ns). (b) The spectrum at 1.85 ns was fit to obtain the electron temperature, flow velocity, and drift velocity. The measured (c) electron temperature and (d) flow and drift velocities are plotted as a function of time. The solid curves are from 1-D hydrodynamic simulations that included nonlocal heat transfer and CBET models.

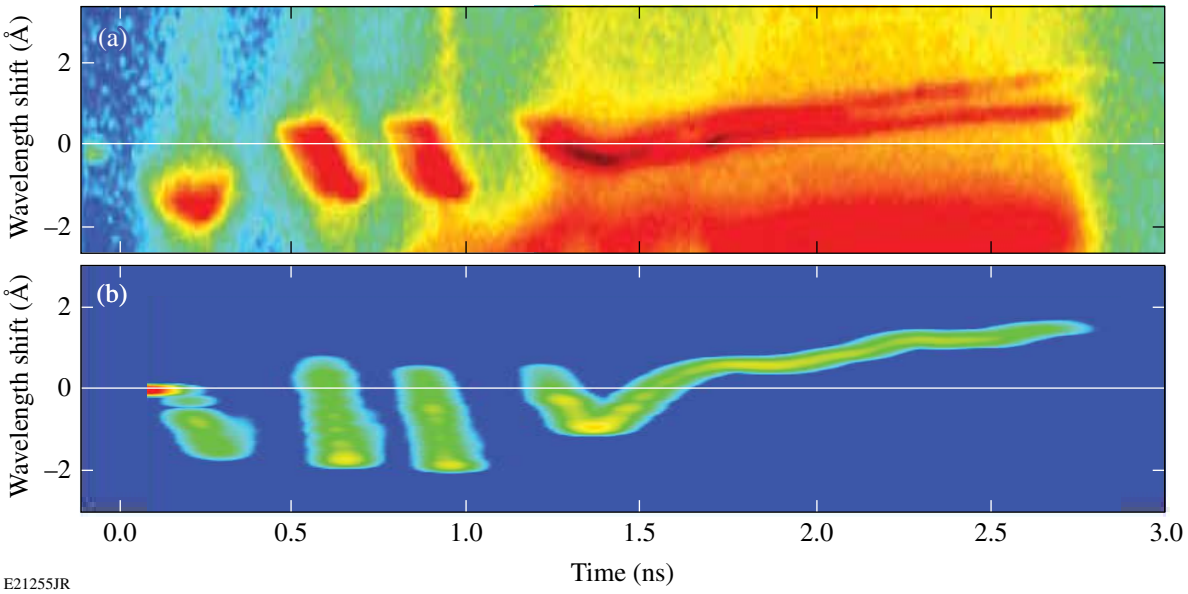

Figure 132.4
(a) The scale from Fig. 132.3(a) was expanded to highlight the spectrum obtained from light reflecting from the target surface. (b) The reflected light was modeled using the simulated plasma conditions.

similar laser beam diameters (490-μm FWHM) as used on the OMEGA EP[49] planar experiments discussed in **Two-Plasmon Decay** (p. 186). The planar targets consist of a 30-μm-thick CH layer deposited on 30-μm-thick molybdenum (Mo). Figure 132.5 shows the electron and ion temperatures as functions of time at the 3ω quarter-critical surface. The wavelength separation is a function of the ion-acoustic sound speed that leads to the direct measure of the electron temperature shown in Fig. 132.3(c). The multiple ion-acoustic modes present in the CH plasma provide an accurate measure of the ion temperature.[50] There is excellent agreement with the 2-D hydrodynamic simulations using the code *DRACO*.[51] Furthermore, the rarefaction wave launched from the CH–Mo interface is observed in the Thomson-scattering spectrum 1.11 ns after the laser beams turn on, which is in agreement with the hydrodynamic simulations. This agreement demonstrates the accuracy of the thermal-conduction model and is a strong indication that the calculated density and temperature profiles are accurate.

Cross-Beam Energy Transfer

1. CBET Experiments

To reduce CBET and increase the implosion velocity in direct-drive experiments, the energy in the rays that bypass the target was reduced by decreasing the radii of the laser beams (R_b) relative to the target radius ($R_t = 430$ μm). Figure 132.6(a) shows that, when the radii of the laser beams are reduced from $R_b/R_t = 1.1$ to 0.75, the measured absorption is increased from 68% to 87% (Ref. 52). This results in an increase in the implosion velocity from 160 to 195 km/s [Fig. 132.6(b)]. Simulations that include both nonlocal heat transport[44] and CBET models[19] developed in the 1-D hydrodynamic code *LILAC* (see **Hydrodynamic Modeling**, p. 183) are in excellent agreement with the measurements shown in Fig. 132.6.

When the CBET model is not included in the simulations, both the absorption and hydrodynamic efficiency increase by ~15% as the tighter focused laser spots direct more energy on target [Fig. 132.6(b)]. This is in contrast to the measured ~35% increase in the hydrodynamic efficiency; a factor of 2 larger than the measured 15% increase in absorption. This enhanced hydrodynamic efficiency is a direct result of reducing CBET, which increases the energy in the central portion of the laser beams, leading to more energy deposited near the critical surface.

Although the hydrodynamic efficiency is significantly increased, reducing the radii of the laser beams with respect to the target radius introduces a nonuniform illumination on the initial target surface [Fig. 132.6(c)], which can lead to low-mode nonuniformities and reduced implosion performance. Figure 132.6(c) shows that the root-mean-square (rms) deviation from the average shell radius (nonuniformities), measured near the ablation front [Fig. 132.6(d)],[45] increased from less than 5 μm to greater than 25 μm as the laser radii were reduced from $R_b/R_t = 1.1$ to 0.5 (Ref. 52).

2. Mitigation of Cross-Beam Energy Transfer

To mitigate CBET and maintain sufficient illumination uniformity in direct-drive implosions, a two-state zooming has been proposed.[53] During the critical time for seeding nonuniformities (laser imprint), before a significant conduction zone is produced, the radii of the laser beams are equal to the target

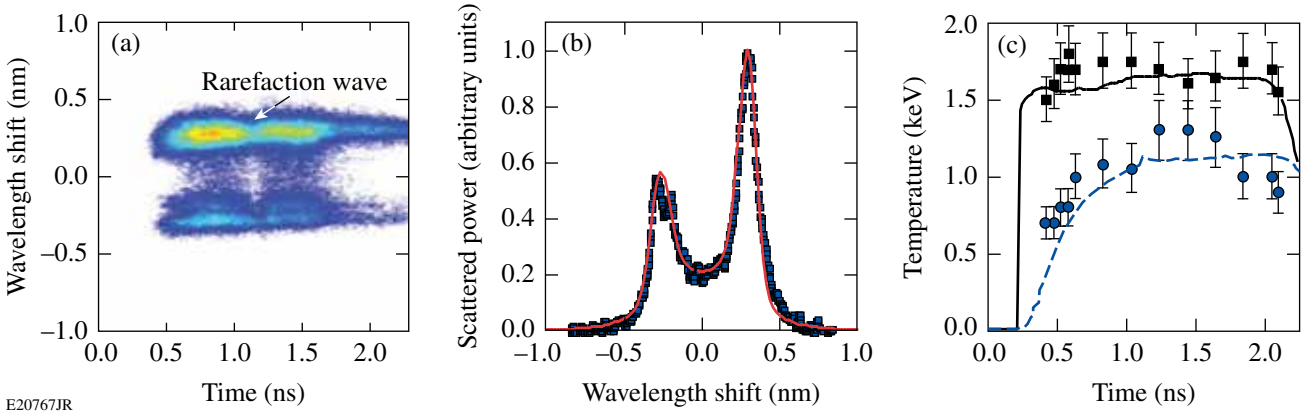

Figure 132.5
(a) The Thomson-scattering spectrum obtained from scattering at the 3ω quarter-critical surface in planar geometry for a drive intensity of $I_{ovr} = 3 \times 10^{14}$ W/cm^2. (b) The spectrum at 0.8 ns is fit to obtain a $T_e = 1.6$ keV and $T_i = 1.0$ keV. (c) The electron (squares) and ion (circles) temperatures are plotted as a function of time and compared with 2-D hydrodynamic modeling.

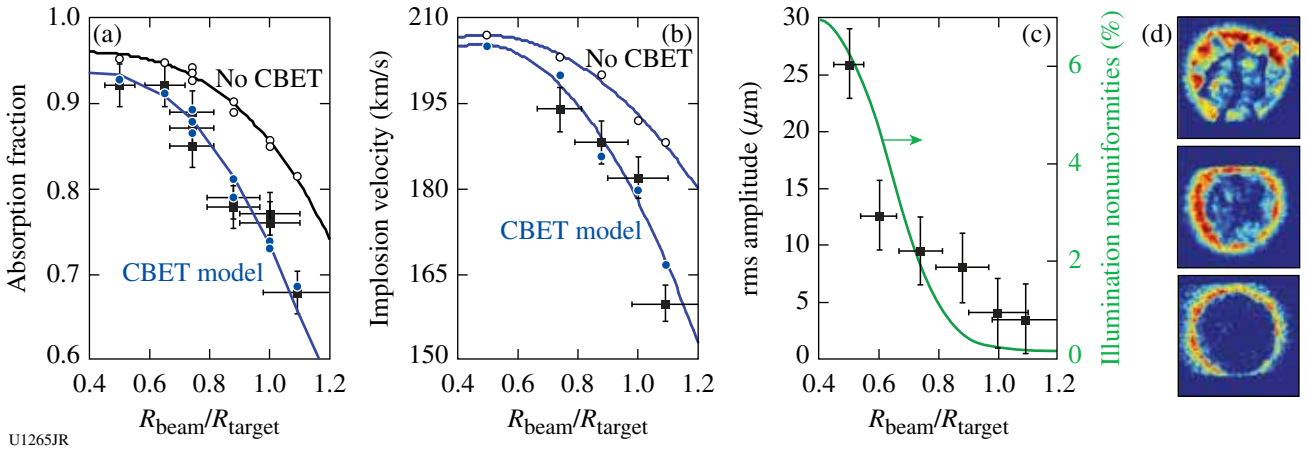

Figure 132.6

(a) The absorbed light, (b) implosion velocity, and (c) rms deviation from the average shell radius (left axis), along with the calculated illumination nonuniformities (right axis) are plotted as functions of the ratio between the laser-beam and target radius. The simulation results that include the CBET model (solid circles) are in excellent agreement with the measurements. Simulations performed without the CBET model (open circles) significantly overestimate the absorbed light and the implosion velocity. (d) X-ray self-emission images are used to determine the nonuniformities at a constant capsule radius of 175 μm; the soft x rays emitted from the ablation surface (outer edge of the imploding shell) were measured for three focus conditions: R_b/R_t = 0.5, 0.75, and 1.0 (from top to bottom).

radius $\left(R_b/R_t = 1.0\right)$, minimizing the laser imprint. Once the plasma has sufficiently expanded, the radii of the laser beams are reduced $\left(R_b/R_t = 0.7\right)$, minimizing CBET. The increase in transverse thermal conduction smooths the low-mode intensity nonuniformities, producing a uniform drive. Initial 2-D hydrodynamic simulations of OMEGA direct-drive experimental conditions indicate that transitioning to smaller laser spots after the picket pulses does not increase the low-mode nonuniformities.[54] The combination of zooming and dynamic bandwidth reduction (removing smoothing by spectral dispersion during the drive[55]) could provide a 30% effective increase in the drive energy for OMEGA direct-drive implosions.

Potential schemes to achieve zooming of the focal spot on target involve modifications to the spatial coherence of the laser that causes broadening in the far field of the laser beams. One method suitable for most high-power laser systems employs a radially varying zoom phase plate (ZPP) and a two-state dynamic near-field profile. The ZPP's central area would produce a large focal spot, while the outer area would produce a smaller focal spot. During the picket pulses, a small-diameter near-field beam propagates through the center region of the ZPP forming a large diameter on-target spot. During the drive pulse, an annulus-shaped near-field profile propagates through the outer region of the ZPP producing a smaller-diameter on-target spot.[56,57]

Two-Plasmon Decay

The large-diameter targets (~3 mm) and moderate overlapped laser intensities ($I_{ovr} \sim 7 \times 10^{14}$ W/cm^2, $I_{s,q} \lesssim 10^{14}$ W/cm^2) proposed for direct-drive–ignition experiments will produce high-temperature ($T_{e,q} \sim 3.5$ keV), long-scale-length ($L_{n,q} \sim 500\ \mu$m) underdense plasmas.[58] Multibeam linear gain calculations [Eq. (1)] and recent results[25] from OMEGA suggest that TPD will be near threshold where details in the exact hydrodynamic conditions and beam pointings may play a significant role in the number of hot electrons produced by TPD. A fraction of the hot electrons produced by two-plasmon decay will be absorbed into the unablated fuel ("preheat"), and may increase the implosion adiabat and reduce the compression efficiency. Typical direct-drive–ignition designs can withstand of the order of 0.1% of the laser energy converted to preheat.[59]

Figure 132.7 shows the results from a series of experiments in planar and spherical geometries that were designed to account for all of the hot electrons generated by TPD.[60] The coupling of these hot electrons to a fusion target (preheat) will be reduced by the electron divergence, the distance between where the electrons are created and where they are absorbed, the energy distribution of the electrons (T_{hot}), and other loss mechanisms. The experiments on OMEGA EP employed a single cone of four beams (23° from the target normal) with ~860-μm FWHM laser spots; the planar experiments on

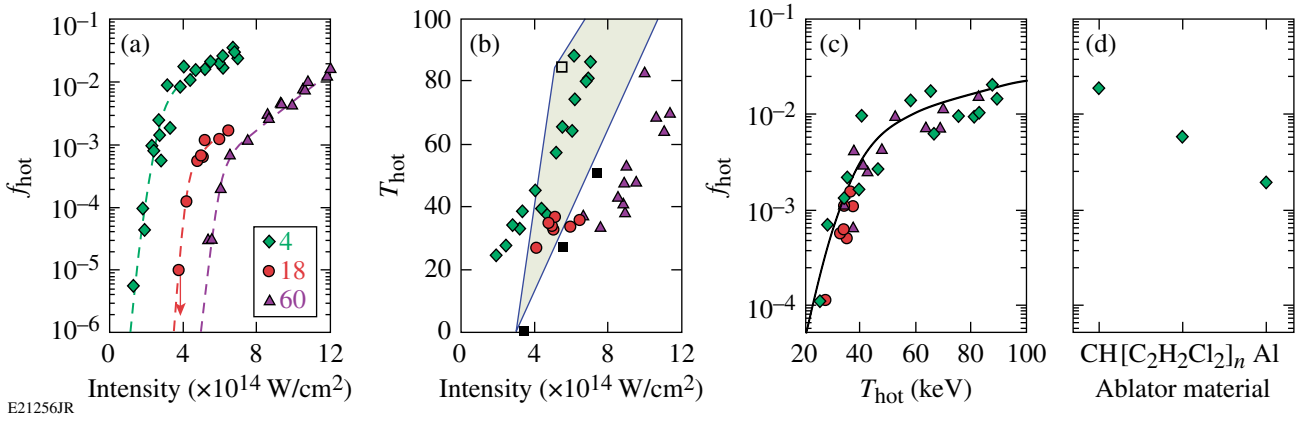

Figure 132.7
(a) The fraction of laser energy converted to hot electrons (f_{hot}) and (b) the hot-electron temperature (T_{hot}) are shown for three beam geometries: four-beam planar (diamonds), 18-beam planar (circles), and 60-beam spherical (triangles) as a function of the vacuum overlapped intensities (I_{ovr}). The hot-electron temperatures calculated by *ZAK* (open squares) and *QZAK* (solid squares) are included for reference. (c) The hot-electron fraction is plotted as a function of the hot-electron temperature for the three target geometries. (d) The f_{hot} measured on the four-beam planar configuration is plotted for a series of ablator materials for a vacuum overlapped intensity of 7×10^{14} W/cm^2.

OMEGA consisted of 18 beams with 710-μm FWHM laser spots in three cones (six at 23°, six at 48°, and six at 60° from the target normal); the spherical experiments used 60 beams and the target diameter was matched to the diameter of the laser spots, where 95% of the laser power illuminates the initial target surface ($R_t = 865$ μm). Each target geometry has its own intensity threshold as a result of the differences in the number of beams that contribute to the common electron plasma wave, scale lengths, electron temperatures, and the geometric factor as indicated in Eq. (1) (see Table 132.I). The hot-electron intensity thresholds shown in Fig. 132.7(a) suggest that the multibeam TPD gain [Eq. (1)] must be greater than $G_{MB} \approx 2$ for a measurable fraction of hot electrons ($f_{hot} \approx 10^{-5}$ is near the detection threshold).

1. Total Hot-Electron Fraction

To study TPD at ignition-relevant plasma conditions, the four ultraviolet (3ω, $\lambda = 0.35$ μm) beams available from OMEGA EP produced the required intensities ($I_{ovr} = 7 \times 10^{14}$ W/cm^2) over a large-diameter laser spot to create 400-μm plasma density scale lengths and $T_e = 2.5$-keV electron temperatures at $n_{cr}/4$. The long-scale-length CH plasma was produced by illuminating a 30-μm-thick CH layer deposited on 30 μm of Mo. The total energy in hot electrons was determined by measuring the K_α yield and the hot-electron temperature.[60]

Figure 132.7(a) shows that the fraction of laser energy converted into hot electrons scales exponentially over nearly three orders of magnitude when the vacuum overlapped intensity is increased from 1.3 to 3×10^{14} W/cm^2 and continues to grow at a slower rate as the intensity is extended to 7×10^{14} W/cm^2 (Ref. 61). The large fraction of laser energy converted into hot electrons along with its observed saturation is a direct consequence of the simultaneous high intensities and long-scale lengths ($L_{n,q} = 400$ μm) in these experiments. Previous TPD studies have shown saturation of the hot-electron generation at 0.1% of the incident laser energy when plotted against the vacuum laser intensity. This apparent saturation and low level of electron generation results from the hydrodynamics; the small laser spots used to produce the highest intensities limited the

Table 132.I: Estimates of the factors used to calculate the common-wave gain at the threshold intensity for each configuration shown.

Configuration	f_g	$N_\Sigma \langle I_{s,q} \rangle$	$L_{n,q}/T_{e,q}$	I_{ovr}^{th}	G_{MB}^{th}
4 beam	0.5	~1/2 I_{ovr}	~170 μm/keV	~2	1.7
18 beam	0.5	~1/4 I_{ovr}	~135 μm/keV	~4	1.4
60 beam	0.5	~1/2 I_{ovr}	~60 μm/keV	~5	1.5

scale length to $L_{n,q} < 200\ \mu$m (Ref. 23). The highest intensity corresponds to a TPD gain larger than those estimated for direct-drive–ignition experiments and the fraction of these electrons that are deposited as preheat in the fuel will be significantly reduced as a result of their divergence and energies.

2. Hot-Electron Temperature (T_{hot})

Figure 132.7(b) shows that, for a given target geometry, the hot-electron temperature scales with the vacuum intensity. The four-beam planar experimental results are compared with the code *ZAK*.[27] While this plasma-fluid model describes the growth and nonlinear saturation of the instability, it does not include kinetic effects responsible for hot-electron generation. An estimate for the hot-electron temperature was instead obtained from the nonlinearly saturated state via the integration of test-electron trajectories in the electrostatic fields associated with the Langmuir turbulence (see Ref. 27 for more details). The solid triangles in Fig. 132.7 show the results of the *QZAK* model where kinetic effects are taken into account self-consistently in the quasi-linear approximation.[62] The addition of kinetic effects lowers the amplitude of the electron plasma waves, reducing the hot-electron temperature for a given $I_q L_{n,q}/T_{e,q}$. The difference between the two model predictions highlights the difficulty in making predictive calculations of a highly turbulent and complex physical system.

Figure 132.7(c) shows the measured correlation, for all three target geometries, between the hot-electron temperature and the fraction of laser energy converted to hot electrons. The fact that each target geometry has its own intensity threshold, even though the hot-electron generation plotted as a function of hot-electron temperature shares a common curve, suggests that the differences in thresholds [Fig. 132.7(b)] result from the laser beam coupling to the TPD instability.[25]

Mitigation of Two-Plasmon Decay

Figure 132.7(d) shows the fraction of hot electrons generated by TPD for various ablator materials measured on OMEGA EP at a vacuum overlapped intensity of 7×10^{14} W/cm^2. Although some of the reduction in the fraction of hot electrons is a result of the changing hydrodynamics (i.e., increased T_e, reduced L_n), recent particle-in-cell simulations indicate a sensitivity of TPD to the electron–ion collisions,[63] and it is plausible that reducing the ion-acoustic wave damping will lead to a reduced TPD saturation level. Previous implosion experiments using silicon dioxide (SiO_2) ablators have observed a significant reduction in the fraction of laser energy converted to hot electrons,[64] and more-recent hydrodynamic studies of direct-drive–implosion designs add Si/Ge doping to the CH ablator to reduce the Rayleigh–Taylor growth.[65,66]

Summary

A series of laser–plasma interaction experiments performed at the Omega Laser Facility have investigated CBET and TPD at direct-drive–ignition conditions. Direct-drive ignition is most susceptible to these multibeam instabilities because the single-beam intensities are low and the electron temperatures in the underdense plasma are high. These studies have led to mitigation strategies for both CBET and TPD; reducing the radii of the laser beams with respect to the target during the main drive minimizes CBET, and varying the ablator material suggests that the hot electrons produced by TPD can be significantly reduced.

ACKNOWLEDGMENT

We acknowledge the OMEGA EP and OMEGA operations teams whose efforts made these results possible. This work was supported by the U.S. Department of Energy Office of Inertial Confinement Fusion under Cooperative Agreement No. DE-FC52-08NA28302, the University of Rochester, and the New York State Energy Research and Development Authority. The support of DOE does not constitute an endorsement by DOE of the views expressed in this article.

REFERENCES

1. J. Nuckolls *et al.*, Nature **239**, 139 (1972).
2. E. I. Moses and C. R. Wuest, Fusion Sci. Technol. **47**, 314 (2005).
3. C. Cavailler, Plasma Phys. Control. Fusion **47**, B389 (2005).
4. J. D. Lindl *et al.*, Phys. Plasmas **11**, 339 (2004).
5. D. H. Froula, L. Divol, R. A. London, R. L. Berger, T. Döppner, N. B. Meezan, J. Ralph, J. S. Ross, L. J. Suter, and S. H. Glenzer, Phys. Plasmas **17**, 056302 (2010).
6. S. H. Glenzer *et al.*, Science **327**, 1228 (2010).
7. W. L. Kruer, *The Physics of Laser–Plasma Interactions*, Frontiers in Physics, Vol. 73, edited by D. Pines (Addison-Wesley, Redwood City, CA, 1988).
8. C. Labaune *et al.*, Plasma Phys. Control. Fusion **46**, B301 (2004).
9. S. H. Glenzer *et al.*, Plasma Phys. Control. Fusion **54**, 045013 (2012).
10. D. H. Froula, L. Divol, N. B. Meezan, S. Dixit, J. D. Moody, P. Neumayer, B. B. Pollock, J. S. Ross, and S. H. Glenzer, Phys. Rev. Lett. **98**, 085001 (2007); D. H. Froula, L. Divol, R. A. London, P. Michel, R. L. Berger, N. B. Meezan, P. Neumayer, J. S. Ross, R. Wallace, and S. H. Glenzer, Phys. Rev. Lett. **100**, 015002 (2008); D. H. Froula, Phys. Rev. Lett. **103**, 045006 (2009).

11. R. L. McCrory, D. D. Meyerhofer, R. Betti, R. S. Craxton, J. A. Delettrez, D. H. Edgell, V. Yu Glebov, V. N. Goncharov, D. R. Harding, D. W. Jacobs-Perkins, J. P. Knauer, F. J. Marshall, P. W. McKenty, P. B. Radha, S. P. Regan, T. C. Sangster, W. Seka, R. W. Short, S. Skupsky, V. A. Smalyuk, J. M. Soures, C. Stoeckl, B. Yaakobi, D. Shvarts, J. A. Frenje, C. K. Li, R. D. Petrasso, and F. H. Séguin, Phys. Plasmas **15**, 055503 (2008).

12. V. N. Goncharov, T. C. Sangster, T. R. Boehly, S. X. Hu, I. V. Igumenshchev, F. J. Marshall, R. L. McCrory, D. D. Meyerhofer, P. B. Radha, W. Seka, S. Skupsky, C. Stoeckl, D. T. Casey, J. A. Frenje, and R. D. Petrasso, Phys. Rev. Lett. **104**, 165001 (2010).

13. C. J. Randall, J. R. Albritton, and J. J. Thomson, Phys. Fluids **24**, 1474 (1981).

14. A. Simon, R. W. Short, E. A. Williams, and T. Dewandre, Phys. Fluids **26**, 3107 (1983).

15. R. K. Kirkwood *et al.*, Phys. Rev. Lett. **76**, 2065 (1996).

16. J. Myatt, A. V. Maximov, W. Seka, R. S. Craxton, and R. W. Short, Phys. Plasmas **11**, 3394 (2004).

17. P. Michel *et al.*, Phys. Rev. Lett. **102**, 025004 (2009).

18. I. V. Igumenshchev, D. H. Edgell, V. N. Goncharov, J. A. Delettrez, A. V. Maximov, J. F. Myatt, W. Seka, A. Shvydky, S. Skupsky, and C. Stoeckl, Phys. Plasmas **17**, 122708 (2010).

19. I. V. Igumenshchev, W. Seka, D. H. Edgell, D. T. Michel, D. H. Froula, V. N. Goncharov, R. S. Craxton, L. Divol, R. Epstein, R. Follett, J. H. Kelly, T. Z. Kosc, A. V. Maximov, R. L. McCrory, D. D. Meyerhofer, P. Michel, J. F. Myatt, T. C. Sangster, A. Shvydky, S. Skupsky, and C. Stoeckl, Phys. Plasmas **19**, 056314 (2012).

20. W. Seka, D. H. Edgell, J. P. Knauer, J. F. Myatt, A. V. Maximov, R. W. Short, T. C. Sangster, C. Stoeckl, R. E. Bahr, R. S. Craxton, J. A. Delettrez, V. N. Goncharov, I. V. Igumenshchev, and D. Shvarts, Phys. Plasmas **15**, 056312 (2008).

21. W. Seka, H. A. Baldis, J. Fuchs, S. P. Regan, D. D. Meyerhofer, C. Stoeckl, B. Yaakobi, R. S. Craxton, and R. W. Short, Phys. Rev. Lett. **89**, 175002 (2002).

22. W. Seka, D. H. Edgell, J. F. Myatt, A. V. Maximov, R. W. Short, V. N. Goncharov, and H. A. Baldis, Phys. Plasmas **16**, 052701 (2009).

23. C. Stoeckl, R. E. Bahr, B. Yaakobi, W. Seka, S. P. Regan, R. S. Craxton, J. A. Delettrez, R. W. Short, J. Myatt, A. V. Maximov, and H. Baldis, Phys. Rev. Lett. **90**, 235002 (2003).

24. D. T. Michel, A. V. Maximov, B. Yaakobi, S. X. Hu, J. F. Myatt, A. A. Solodov, R. W. Short, and D. H. Froula, "Experimental Demonstration of the Two-Plasmon-Decay Common-Wave Process," to be published in Physical Review Letters.

25. D. T. Michel, J. F. Myatt, A. V. Maximov, R. W. Short, J. A. Delettrez, S. X. Hu, I. V. Igumenshchev, W. Seka, A. A. Solodov, C. Stoeckl, B. Yaakobi, J. Zhang, and D. H. Froula, "Measured Multibeam Hot-Electron Intensity Threshold Quantified by a Two-Plasmon–Decay Resonant Common-Wave Gain in Various Experimental Configurations," submitted to Physics of Plasmas.

26. D. F. DuBois, D. A. Russell, and H. A. Rose, Phys. Rev. Lett. **74**, 3983 (1995).

27. J. F. Myatt, J. Zhang, J. A. Delettrez, A. V. Maximov, R. W. Short, W. Seka, D. H. Edgell, D. F. DuBois, D. A. Russell, and H. X. Vu, Phys. Plasmas **19**, 022707 (2012).

28. A. B. Langdon, B. F. Lasinski, and W. L. Kruer, Phys. Rev. Lett. **43**, 133 (1979).

29. G. D. Doolen, D. F. DuBois, and H. A. Rose, Phys. Rev. Lett. **54**, 804 (1985).

30. R. Yan, A. V. Maximov, C. Ren, and F. S. Tsung, Phys. Rev. Lett. **103**, 175002 (2009).

31. H. X. Vu, D. F. Dubois, D. A. Russell, and J. F. Myatt, "Hot-Electron Generation by Cavitating Langmuir Turbulence in the Nonlinear Stage of the Two-Plasmon–Decay Instability," submitted to Physics of Plasmas.

32. H. X. Vu, D. F. Dubois, D. A. Russell, and J. F. Myatt, "Hot-Electron Production and Suprathermal Heat Flux Scaling with Laser Intensity from the Two-Plasmon–Decay Instability," submitted to Physics of Plasmas.

33. J. F. Myatt, H. X. Vu, D. F. DuBois, D. A. Russell, J. Zhang, R. W. Short, A. V. Maximov, W. Seka, and D. H. Edgell, "Mitigation of Two-Plasmon Decay in Direct-Drive Inertial Confinement Fusion Through the Manipulation of Ion-Acoustic and Langmuir Wave Damping," to be submitted to Physics of Plasmas.

34. B. J. MacGowan *et al.*, Phys. Plasmas **3**, 2029 (1996).

35. J. C. Fernández *et al.*, Phys. Plasmas **7**, 3743 (2000).

36. E. Lefebvre *et al.*, Phys. Plasmas **5**, 2701 (1998).

37. D. H. Froula, L. Divol, N. B. Meezan, S. Dixit, P. Neumayer, J. D. Moody, B. B. Pollock, J. S. Ross, L. Suter, and S. H. Glenzer, Phys. Plasmas **14**, 055705 (2007).

38. S. H. Glenzer *et al.*, Rev. Sci. Instrum. **70**, 1089 (1999).

39. J. S. Ross, D. H. Froula, A. J. Mackinnon, C. Sorce, N. Meezan, S. H. Glenzer, W. Armstrong, R. Bahr, R. Huff, and K. Thorp, Rev. Sci. Instrum. **77**, 10E520 (2006).

40. D. H. Froula, J. S. Ross, L. Divol, and S. H. Glenzer, Rev. Sci. Instrum. **77**, 10E522 (2006).

41. A. J. Mackinnon, S. Shiromizu, G. Antonini, J. Auerbach, K. Haney, D. H. Froula, J. Moody, G. Gregori, C. Constantin, C. Sorce, L. Divol, R. L. Griffith, S. Glenzer, J. Satariano, P. K. Whitman, S. N. Locke, E. L. Miller, R. Huff, K. Thorp, W. Armstrong, W. Bahr, W. Seka, G. Pien, J. Mathers, S. Morse, S. Loucks, and S. Stagnitto, Rev. Sci. Instrum. **75**, 3906 (2004).

42. J. Katz, R. Boni, C. Sorce, R. Follett, M. J. Shoup III, and D. H. Froula, Rev. Sci. Instrum. **83**, 10E349 (2012).

43. J. Delettrez, Can. J. Phys. **64**, 932 (1986).

44. V. N. Goncharov, T. C. Sangster, P. B. Radha, R. Betti, T. R. Boehly, T. J. B. Collins, R. S. Craxton, J. A. Delettrez, R. Epstein, V. Yu. Glebov, S. X. Hu, I. V. Igumenshchev, J. P. Knauer, S. J. Loucks, J. A. Marozas, F. J. Marshall, R. L. McCrory, P. W. McKenty, D. D. Meyerhofer, S. P. Regan, W. Seka, S. Skupsky, V. A. Smalyuk, J. M. Soures, C. Stoeckl, D. Shvarts, J. A. Frenje, R. D. Petrasso, C. K. Li, F. Séguin, W. Manheimer, and D. G. Colombant, Phys. Plasmas **15**, 056310 (2008).

45. D. T. Michel, C. Sorce, R. Epstein, N. Whiting, I. V. Igumenshchev, R. Jungquist, and D. H. Froula, Rev. Sci. Instrum. **83**, 10E530 (2012).

46. D. H. Froula, S. H. Glenzer, N. C. Luhmann, and J. Sheffield, *Plasma Scattering of Electromagnetic Radiation: Theory and Measurement Techniques*, 2nd ed. (Academic Press, Burlington, MA, 2011).

47. T. Dewandre, J. R. Albritton, and E. A. Williams, Phys. Fluids **24**, 528 (1981).

48. T. R. Boehly, D. L. Brown, R. S. Craxton, R. L. Keck, J. P. Knauer, J. H. Kelly, T. J. Kessler, S. A. Kumpan, S. J. Loucks, S. A. Letzring, F. J. Marshall, R. L. McCrory, S. F. B. Morse, W. Seka, J. M. Soures, and C. P. Verdon, Opt. Commun. **133**, 495 (1997).

49. J. H. Kelly, L. J. Waxer, V. Bagnoud, I. A. Begishev, J. Bromage, B. E. Kruschwitz, T. J. Kessler, S. J. Loucks, D. N. Maywar, R. L. McCrory, D. D. Meyerhofer, S. F. B. Morse, J. B. Oliver, A. L. Rigatti, A. W. Schmid, C. Stoeckl, S. Dalton, L. Folnsbee, M. J. Guardalben, R. Jungquist, J. Puth, M. J. Shoup III, D. Weiner, and J. D. Zuegel, J. Phys. IV France **133**, 75 (2006).

50. D. H. Froula, J. S. Ross, L. Divol, N. Meezan, A. J. MacKinnon, R. Wallace, and S. H. Glenzer, Phys. Plasmas **13**, 052704 (2006).

51. P. B. Radha, T. J. B. Collins, J. A. Delettrez, Y. Elbaz, R. Epstein, V. Yu. Glebov, V. N. Goncharov, R. L. Keck, J. P. Knauer, J. A. Marozas, F. J. Marshall, R. L. McCrory, P. W. McKenty, D. D. Meyerhofer, S. P. Regan, T. C. Sangster, W. Seka, D. Shvarts, S. Skupsky, Y. Srebro, and C. Stoeckl, Phys. Plasmas **12**, 056307 (2005).

52. D. H. Froula, I. V. Igumenshchev, D. T. Michel, D. H. Edgell, R. Follett, V. Yu. Glebov, V. N. Goncharov, J. Kwiatkowski, F. J. Marshall, P. B. Radha, W. Seka, C. Sorce, S. Stagnitto, C. Stoeckl, and T. C. Sangster, Phys. Rev. Lett. **108**, 125003 (2012).

53. P. W. McKenty, R. S. Craxton, A. Shvydky, F. J. Marshall, J. A. Marozas, S. Skupsky, D. D. Meyerhofer, and R. L. McCrory, Bull. Am. Phys. Soc. **56**, 341 (2011).

54. I. V. Igumenshchev, D. H. Edgell, D. H. Froula, V. N. Goncharov, T. J. Kessler, F. J. Marshall, R. L. McCrory, P. W. McKenty, D. D. Meyerhofer, D. T. Michel, T. C. Sangster, W. Seka, and S. Skupsky, "Improved Performance in Direct-Drive Implosions Using Beam Zooming," to be submitted to Physical Review Letters.

55. T. J. B. Collins, J. A. Marozas, K. S. Anderson, R. Betti, R. S. Craxton, J. A. Delettrez, V. N. Goncharov, D. R. Harding, F. J. Marshall, R. L. McCrory, D. D. Meyerhofer, P. W. McKenty, P. B. Radha, A. Shvydky, S. Skupsky, and J. D. Zuegel, Phys. Plasmas **19**, 056308 (2012).

56. I. V. Igumenshchev, D. H. Froula, D. H. Edgell, V. N. Goncharov, T. J. Kessler, F. J. Marshall, R. L. McCrory, P. W. McKenty, D. D. Meyerhofer, D. T. Michel, T. C. Sangster, W. Seka, and S. Skupsky, "Laser Beam Zooming to Mitigate Cross-Beam Energy Losses in Direct-Drive Implosions," to be submitted to Physical Review Letters.

57. D. H. Froula, I. V. Igumenshchev, A. Shvydky, J. H. Kelly, J. D. Zuegel, E. Hill, and V. N. Goncharov, "Mitigation of Cross-Beam Energy Transfer: Implicaitons of Two-State Optical Zooming on OMEGA," to be submitted to Plasma Physics and Controlled Fusion.

58. P. W. McKenty, V. N. Goncharov, R. P. J. Town, S. Skupsky, R. Betti, and R. L. McCrory, Phys. Plasmas **8**, 2315 (2001).

59. *LLE Review Quarterly Report* **79**, 121, Laboratory for Laser Energetics, University of Rochester, Rochester, NY, LLE Document No. DOE/SF/19460-317, NTIS Order No. DE2002762802 (1999).

60. B. Yaakobi, P.-Y. Chang, A. A. Solodov, C. Stoeckl, D. H. Edgell, R. S. Craxton, S. X. Hu, J. F. Myatt, F. J. Marshall, W. Seka, and D. H. Froula, Phys. Plasmas **19**, 012704 (2012).

61. D. H. Froula, B. Yaakobi, S. X. Hu, P.-Y. Chang, R. S. Craxton, D. H. Edgell, R. Follett, D. T. Michel, J. F. Myatt, W. Seka, R. W. Short, A. Solodov, and C. Stoeckl, Phys. Rev. Lett. **108**, 165003 (2012).

62. K. Y. Sanbonmatsu *et al.*, Phys. Rev. Lett. **82**, 932 (1999).

63. R. Yan, C. Ren, J. Li, A. V. Maximov, W. B. Mori, Z. M. Sheng, and F. S. Tsung, Phys. Rev. Lett. **108**, 175002 (2012).

64. V. A. Smalyuk, R. Betti, J. A. Delettrez, V. Yu. Glebov, D. D. Meyerhofer, P. B. Radha, S. P. Regan, T. C. Sangster, J. Sanz, W. Seka, C. Stoeckl, B. Yaakobi, J. A. Frenje, C. K. Li, R. D. Petrasso, and F. H. Séguin, Phys. Rev. Lett. **104**, 165002 (2010).

65. S. X. Hu, G. Fiksel, V. N. Goncharov, S. Skupsky, D. D. Meyerhofer, and V. A. Smalyuk, Phys. Rev. Lett. **108**, 195003 (2012).

66. G. Fiksel, S. X. Hu, V. N. Goncharov, D. D. Meyerhofer, T. C. Sangster, V. A. Smalyuk, B. Yaakobi, M. J. Bonino, and R. Jungquist, Phys. Plasmas **19**, 062704 (2012).

Stress-Radiation–Induced Swelling in Plastic Capsules

Introduction

Unique and distinctive features on the inner surface of plastic capsules used in deuterium–tritium (DT) inertial confinement fusion (ICF) experiments on OMEGA[1] were observed when the capsules were permeation filled to provide cryogenic ignition-scale targets. The features were not observed when deuterium (D_2) was substituted for DT nor were they observed in similar targets filled at the National Ignition Facility (NIF) with DT through a narrow fill tube (<10-μm inner diameter) (Ref. 2). The size and number of these features did not change when the capsules were warmed above 40 K. A capsule warmed to 300 K without rupturing was recovered and inspected using electron microscopy. The features were smaller than 100 nm high and are not expected to impair the hydrodynamic stability during the implosion.[3] Despite their small size, the features are sufficiently noticeable that their origin and magnitude should be understood and eliminated if possible.

The likely cause of these features was deduced through a process of elimination: the features were not present before the capsules were filled with DT and appeared once the targets were cold (19 K) and filled with DT. These features did not grow in size or number after they were first observed; they possessed a sizeable footprint (>20-μm diameter) and were less than 100 nm high. No pore structure or voids (>20 nm, the detection limit) were observed in or below the features, and no blisters were formed by subsurface pressurized voids. The best explanation for their origin is that they arise from the radiation dose imparted to the plastic, combined with the stresses experienced by the capsules during gas permeation and/or transfer of the capsule at cryogenic temperatures (25 to 40 K). While it is well known that β-radiation ruptures carbon–carbon and carbon–hydrogen bonds to generate volatile species,[4] it is postulated that at very high doses and while under stress, the high density of $C_xH_y^*$ radicals and dissolved deuterium–tritium gas present in the polymer structure may recombine to form a material with a lower density in localized areas. This would cause volumetric swelling, and buckling would be more likely to occur at the inner surface because that region receives the highest dose. This would be a soft-matter analogue to stress–corrosion behavior in metals where a combination of stress and a corrosive environment accelerates chemical changes. This article describes the observed features, the radiation doses, and stress levels that the capsule experiences when it is processed to produce a cryogenic DT target.

Observed Defects

All the targets discussed here were provided by General Atomics and processed through the OMEGA Cryogenic Target Handling System using permeation-filling, cooling, and transporting protocols that are well established.[5] Figure 132.8(a) shows a DT-filled target (0.86-mm outer diameter; 10-μm plastic wall; 95-μm ice layer) at 19.5 K with several distinctive features, two of which are the topic of this article. These features were subsequently identified to be on the inner surface of the plastic wall. Figure 132.8(b) shows that same target at 227 K with the features in the same location possessing the same shape, indicating that the features were not condensed gas that had formed on the capsule. Features with similar shapes and in similar numbers (1 to 5) were observed in most but not all of the DT-filled targets.

Attempts to recover DT-filled cryogenic targets from the cryostat had limited success; all the targets except one exploded as the target warmed and the DT evaporated. In this instance the rate of temperature (and therefore pressure) rise was slower than the rate at which gas permeated out of the capsule so that the burst pressure was not exceeded. The capsule was examined optically and then fractured to image the inner surface with electron microscopy.

Figure 132.9 shows electron microscopy images of the features on the inner surface. Two separate features were imaged using backscattered-electron [Figs. 132.9(a) and 132.9(c)] and secondary-electron [Figs. 132.9(b) and 132.9(d)] modes of operation. The backscattered signal arises from incident electrons elastically scattered off atoms at the surface and is more sensitive to the elemental composition of the surface than is the signal obtained from secondary electrons. Images from the backscattered signal show greater contrast between the

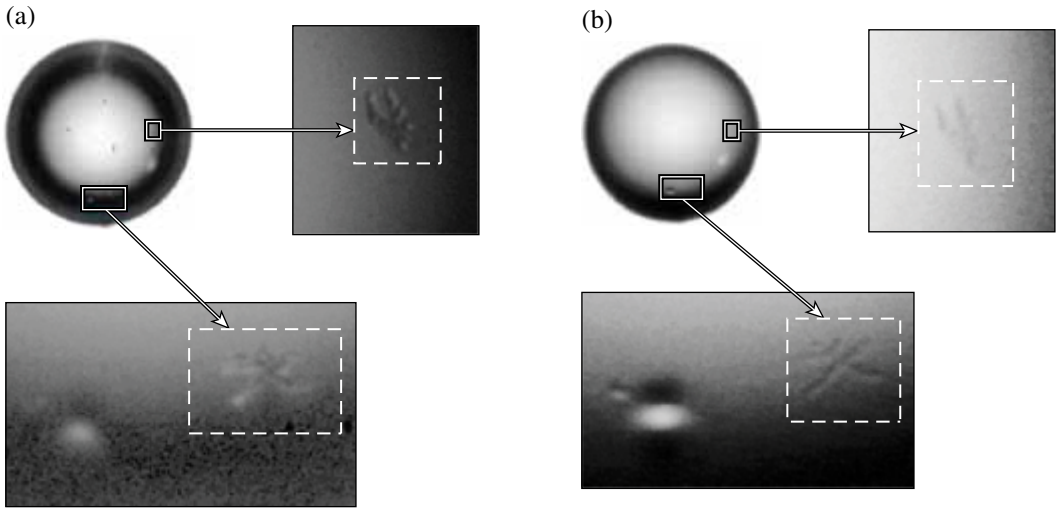

Figure 132.8
A DT-filled target is shown with two distinctive features at (a) 19.5 K and (b) 227 K. Both images were acquired while the target was inside the moving cryostat and were imaged using the existing shadowgraphy optical system. The insets show the features magnified digitally.

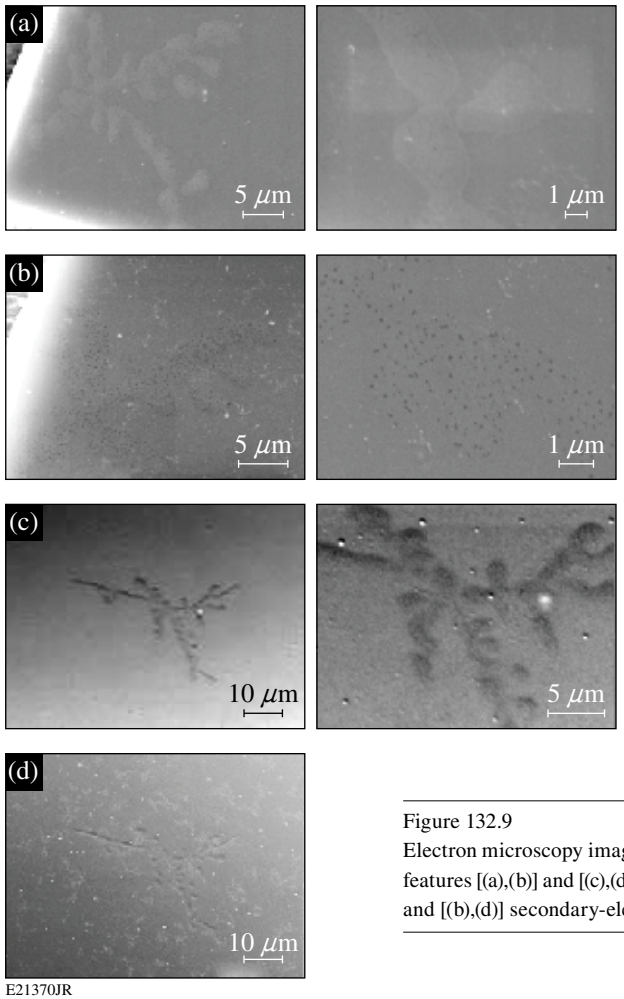

features and the plastic shell than could be obtained from the secondary-electron signal, suggesting that the feature could be associated with a difference in the elemental composition of the material; for example, a difference in the ratio of carbon to hydrogen atoms.

Viewing these features at an oblique angle (Fig. 132.10) provided topographic information: the two-dimensional (2-D) pattern seen in Figs. 132.8 and 132.9 is seen as a series of small domes less than 0.1 μm high when the surface is imaged from an angle of less than 50° to the surface. Imaging the edge of the shell wall at the location where the fracture intersects the dome features revealed no deep-level porosity or void structure [Figs. 132.10(a) and 132.10(b)]. No porosity was observed beneath the dome when a 0.5- × 0.5-μm-sq–shaped, 0.2-μm-deep depression was etched into the dome by repeatedly rastering the electron beam across the surface [Fig. 132.10(b)].

Figure 132.9
Electron microscopy images of the inner surface of the plastic shell recovered from the moving cryostat. Two features [(a),(b)] and [(c),(d)] were imaged and each image was acquired in both [(a),(c)] backscatter signal mode and [(b),(d)] secondary-electron mode. The insets show the features at higher magnifications.

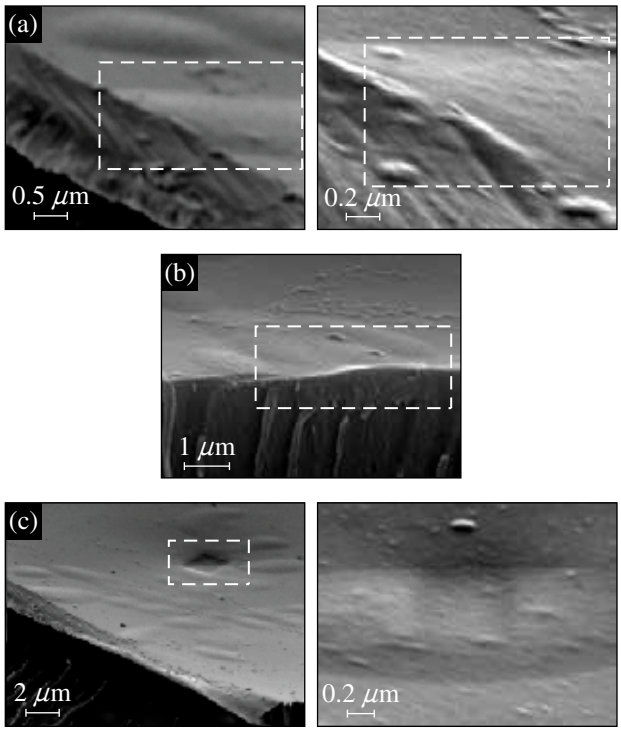

E21371JR

Figure 132.10
The secondary-electron images of the features taken at oblique angles. [(a),(b)] Images are of cross sections through the plastic wall and two domed features (highlighted in the box). The areas highlighted by the rectangular boxes are the regions where the domes intersect the fractured edge of the plastic capsule. (c) A square indentation (denoted by the rectangular box) was etched into the plastic and imaged to see if subsurface porosity was present (it was not).

Radiation Dose and Damage to the Plastic Capsule

Tritium has a half-life of 12.3 years and decays into ^{3}He, releasing an electron with a mean energy of 5.7 keV and a maximum energy of 18.6 keV (Ref. 6). The electron loses energy due to ionization and excitation as it propagates through a medium according to Bethe's relationship:[7]

$$dE/dx = 2\pi e^4 nZ\left[\ln\left(E/I\right)/E\right],$$

where E is the kinetic energy of the electron at position x, n is the number density, Z is the atomic number, and I is the average ionization and excitation energy of the absorber. The effect is that the electron flux to the plastic wall is, to the first order, independent of the DT-gas pressure: electron generation and self-absorption are equally proportional to the tritium density, so increasing the tritium density decreases the shell thickness of tritium near the capsule wall that generates the electron flux that strikes the plastic. The penetration range of the mean and the maximum electron energies in DT and plastic are shown in Table 132.II.

Calculating the dose to the plastic wall assumes that the attenuation of the electron energy is linear with distance. The electron flux (ϕ) to a surface is

$$\phi = \left(1/6\right)\int_0^R \left(1 - x/R\right)\lambda n\,dx,$$

where x is the distance traveled normal to the plastic surface, R is the range of the electron, n is the tritium number density, λ is the probability of tritium atom decay, and the dose (D) is

$$D = E\phi/\rho_m R_m = En\left[\lambda/\left(\rho_m R_m\right)\right]R_T/4,$$

where m is the mass of the absorbing region, ρ_m is the density of the region, R_m is the range in the absorbing region, and R_T is the average range of a 5.7-keV electron in the tritium gas.[8]

The plastic capsules experienced a dose of 259 Mrad during the 17.3 h required to permeation fill the target to 700 bar and the 16.3 h to cool the target to 26 K [Fig. 132.11(a)]. The plastic experienced an additional dose of 136 Mrad during the subsequent 34 h required to form and characterize the ice layer [Fig. 132.11(b)]. Increasing the time to fill the capsule to provide a thicker ice layer, or to permeate through a thinner plastic wall increased the dose to the plastic proportionally. A

Table 132.II: Electron ranges in relevant material.

Material	Density (g/cm^3)	Range for 5.7-keV electrons (μm)	Range for 18.6-keV electrons (μm)
DT (1 bar)	0.000223	2786	35571
DT (10 bar)	0.00223	280	3557
DT (50 bar)	0.0115	57	711
DT (700 bar)	0.156	4	50
DT (ice at 19.7 K)	0.25	2.3	29
Plastic	1.06	0.4	5

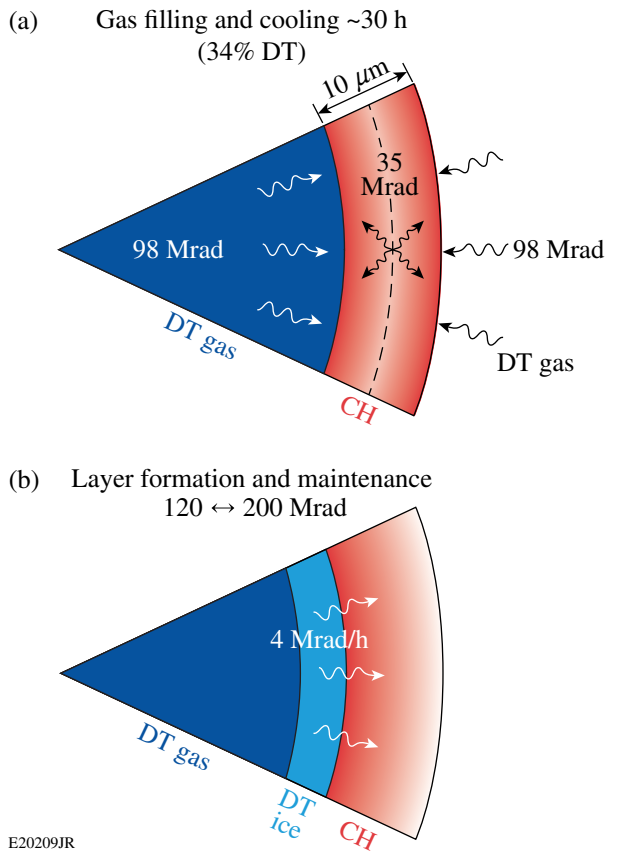

Figure 132.11
A schematic showing the electron dose to the plastic surface from (a) the gas inside and outside the capsule and the gas dissolved in the plastic during the permeation and cooling phase, and (b) the gas/liquid/ice inside the capsule during the layer formation and target storage period before the target is imploded.

portion of this dose was delivered to the plastic from the tritium dissolved in the plastic wall. This dose was

$$D = n\left(1/\rho\right)\lambda E,$$

where n is the concentration of tritium atoms in the material, ρ is the material density, and E is the mean β energy that varied during the pressure ramp as the amount of DT dissolved in the plastic is ~10% of the surrounding gas density. The solubility of deuterium in the plastic was not known; however, it may be estimated from the known solubility of hydrogen in polymers with comparable densities and elemental composition: neoprene has a solubility of 0.014 scc/cc-atm, corresponding to a dose of 35 Mrad for the 30-h–duration filling and cooling process.

Features attributed to tritium damage were present when the target was first observed after filling. No additional features developed while the ice layer was formed and until the target was imploded (up to 3 weeks). This suggests that a radiation dose alone is not a sufficient condition for the formation of features, but the absence of these features in D_2-filled shells indicates that it is a necessary condition.

These calculations are a conservative estimate since they assume an average electron energy of 5.7 keV, whereas the actual energy distribution is non-Gaussian and is skewed to higher energy values.

Stresses that Develop During Permeation Filling and Cryogenic Transport

The process of filling targets by permeation, cooling them, and transporting them from the permeation cell to individual moving cryostats subjects the capsules to compressive and tensile stress that approaches the limits for the plastic material (~60 MPa).

DT is permeated into the capsule at 295 K over a 24-h duration and subjects the capsules to a constant compressive stress. The magnitude of the compressive stress is limited by the buckling pressure of the shell, which is ~0.3 to 1 MPa for capsules with the dimensions used here (wall thickness was 5 or 10 μm) (Ref. 9). These stress levels are a worst-case instantaneous load averaged over the entire shell wall and the time-averaged compressive stress is ~0.2 MPa. Compressive stresses greater than 1 MPa could arise from near-instantaneous pressure spikes that occur as a result of isolated events (such as compressibility changes in the hydraulic fluid or rapid volume changes associated with valves closing) over a time interval that is shorter than the measurement duration of the pressure sensor (~2 s). Further, regions of the plastic wall that deviate from perfect circularity could experience approachably higher localized stress as the compressive hoop stress becomes increasingly a shear stress depending on the deviation from circularity.

Cooling the target from 300 K to 26 K (to recover the gas inside the pressure vessel but outside the capsule) takes 18 h and subjects the capsule to a maximum burst pressure of 0.8 bar (Ref. 10), equivalent to a tensile stress of 0.081 MPa (Fig. 132.12). As the target approaches 26 K, a compressive load forms (~0.1 MPa) on the capsule wall. This buckle pressure is an unavoidable consequence of the construction of the equipment that requires the pressure vessel to be sealed with a valve at 300 K (to avoid leakage), and the lower density of the warm gas near the valve results in a higher gas pressure outside the capsule than inside it. Removing the DT gas surrounding the capsule removes the compressive stress in the

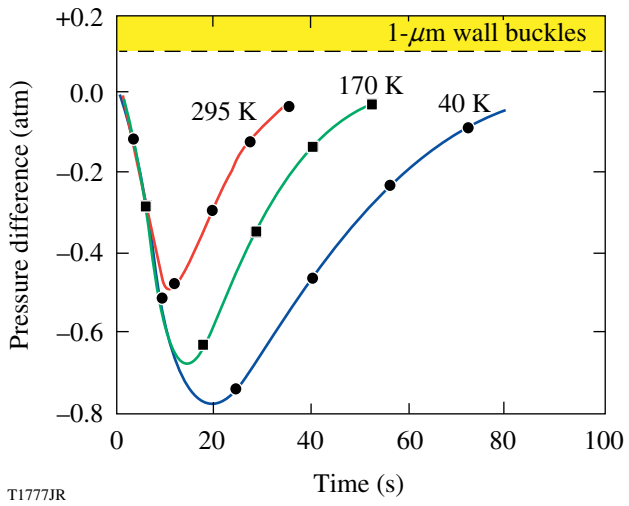

Figure 132.12
Time-dependent average burst pressure exerted on the plastic capsule wall when it was cooled by 1 K. The three curves show the effort of the 1-K temperature step at three separate temperatures: 295 K, 170 K, and 40 K.

plastic and replaces it with a 0.16-MPa tensile stress, resulting from the vapor pressure of liquid DT inside the capsule. A prolonged cyclic stress in the plastic that varies between compressive and tensile is a consequence of these permeation and cooling operations.

Once the capsule has the desired DT inventory, there is a constant heat source inside the capsule from β decay (up to 9 μW) and a heat-exchange gas cools the target. The pressure of the gas must be greater than 100 Pa for cooling to be most effective. The temperature of the capsule (and therefore the pressure in the capsule) depends on the temperature of the boundary (the permeation cell or cryostat) and the distance between the capsule and the boundary. Capsules are maintained below 19 K inside the permeation cell and at an external pressure of 250 Pa (helium). Transferring capsules to the moving cryostat is the process that induces the greatest known stress in the capsule wall, which approaches, and in some cases exceeds, the ultimate yield strength of the plastic. This occurs because the cooling process is inefficient [the helium cooling gas pressure in the cryostat is low (7 Pa), and the distance between the capsule and the cold surface is large (>15 cm)] and the process is lengthy. The capsule begins the transfer process at ~16 K and has taken up to 45 min to be inserted into the moving cryostat and cooled back to 19 K. The calculated rate of increase in the pressure inside the capsule during this process is shown in Fig. 132.13. This calculation includes the temperature-dependent heat capacity, heat-of-fusion, and heat-of-evaporation of DT. Figure 132.14 shows a target that overheated and ruptured during a transfer process that took too long to complete; a portion of the plastic shell is missing and features in the plastic wall appear similar to those imaged with the electron microscope.

One experiment that demonstrated the importance of stress on the formation of the features was to include a capsule with a

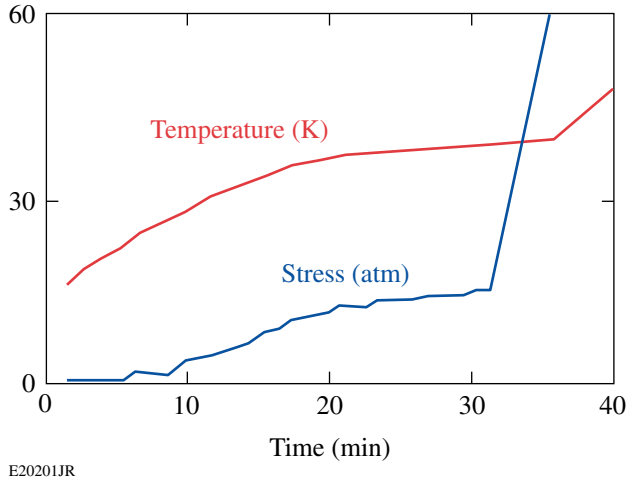

Figure 132.13
Calculated rise in temperature and pressure of a DT target when it was transferred from the permeation cell to the moving cryostat inside the Fill/Transfer Cryostat. β decay is the sole heat source.

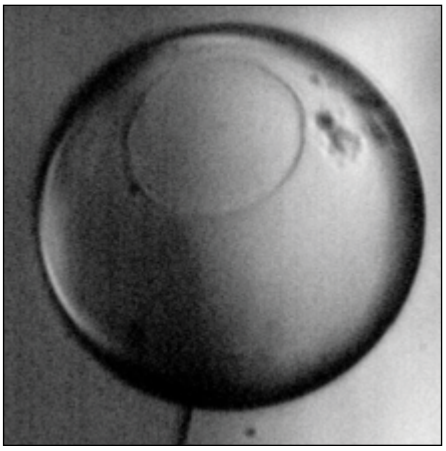

Figure 132.14
Image of a ruptured target inside the moving cryostat that overheated during transfer. A circular portion of the capsule is missing. Note the presence of a sizeable feature near the rupture area that is similar to the features identified as domes in the target (Fig. 132.8) that was recovered.

hole in it with other intact capsules in a fill cycle. This subjected all the capsules to the same radiation dose but the capsule with the hole did not experience the stresses experienced by the other capsules during the permeation, cooling, and transport phases. No evidence of these features was observed in the capsule containing the hole.

Improvements in the equipment and process used to transfer targets to the moving cryostat decreased the time required for the transfer and allowed for a higher helium gas pressure to be used in the moving cryostat. This substantially reduced the number of defects in the capsules.

Radiation-Relevant Properties and Behavior of ICF Capsules

Plastic capsules for ICF experiments are made using a vapor-phase, glow-discharge polymerization process where hydrocarbon radicals are formed in a low-temperature plasma and deposited on a mandrel that is subsequently removed.[11] The carbon-to-deuterium atomic-percent ratio is 0.53:0.47. The fraction and distribution of carbon–hydrogen and carbon–carbon single, double, and triple bonds throughout the capsule wall are stochastic. The polymer cannot be characterized by a molecular weight and the material is better defined as an amorphous hydrocarbon structure where on average one carbon atom is bonded to at least two other carbon atoms to form the structural backbone, and one carbon is bonded to two or three deuterium atoms to form branching side chains. No information regarding the radiation toughness of this material is available, although the material may be expected to have slightly higher radiation toughness than materials with comparable elemental ratios (such as polystyrene) because of the higher carbon-to-deuterium ratio and greater fraction of carbon–carbon double and triple bonds. It is speculated that the regions of the plastic wall that exhibit the domed features possess a locally higher fraction of species that are more likely to experience a density change when the chemical bonds are broken and subsequently rearranged.

Radiation damage from β electrons will rupture carbon–carbon and carbon–deuterium bonds (bond energies are 3.3 eV/bond and 3.9 eV/bond, respectively) at a high rate given the 5.7-keV mean energy of the electrons and flux of 7.4×10^9 electrons/s, which equates to 10^{13} bond ruptures per second. The majority of the bonds subsequently reform; however, carbon atoms may reform with neighboring carbon atoms rather than the ones from which they separated (possibly making double or triple bonds), or they may bond with nearby deuterium atoms formed in the D–T → D + ^{3}He + e$^-$ (5.7-keV) dissociation process. Should sufficient changes occur in a localized region of the capsule wall, the density and mechanical properties of the area will be altered. The behavior of an alternative plastic material with an estimated lower radiation toughness [poly(α-methyl)styrene (PAMS)] based on its structure was tested by filling a comparably dimensioned PAMS capsule with DT. (Capsules made from PAMS and glow-discharge polymerizations are the only ones available for testing and neither material has known radiation toughness values.) A feature larger than those typically observed in standard GDP (glow-discharge plasma) shells was observed in the PAMS capsule (Fig. 132.15).

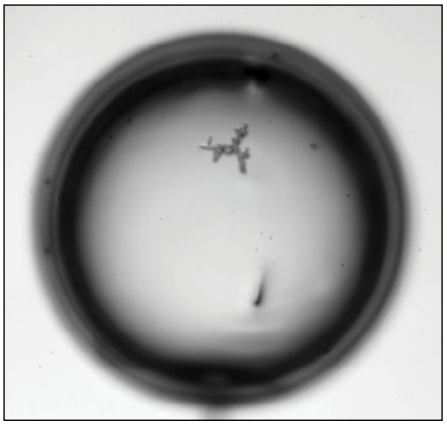

E21373JR

Figure 132.15
Image of a feature in a PAMS [poly(α-methyl)styrene] shell that was filled with DT along with standard GDP (glow-discharge plasma) shells.

Conclusion

Domed-shaped defects with large footprints (>20 μm) and small heights (<0.1 μm) were observed on the inside surface of plastic ICF shells that were permeation filled with DT and cooled to form ignition-scale targets. These features were not present on targets that were processed similarly and filled with D_2 instead of DT nor were they present on targets filled through a fill tube. A combination of high-radiation doses and stress levels inside the plastic wall were required for their formation. It is unclear which stage of the permeation filling, cooling, and transfer steps was responsible for their formation; however, it is clear that these features do not propagate in size or number once the ice layer has formed. There was no evidence of any porosity in these features nor were these features a result of blistering. These observations, combined with data from backscatter- and secondary-electron microscopy, suggest that the scission and reformation of carbon–carbon and carbon–hydrogen bonds may cause a localized decrease in the density of the material

that is manifested as a small-scale swelling. Other possible causes are not precluded, although no other mechanism has been identified that is consistent with all the data.

ACKNOWLEDGMENT

Electron microscopy of the tritium-contaminated plastic capsule was performed by General Atomics using dedicated equipment configured for handling radiation-exposed materials. We thank Abbas Nikroo and David Wall for their support.

This work was supported by the U.S. Department of Energy Office of Inertial Confinement Fusion under Cooperative Agreement No. DE-FC52-08NA28302, the University of Rochester, and the New York State Energy Research and Development Authority. The support of DOE does not constitute an endorsement by DOE of the views expressed in this article.

REFERENCES

1. V. N. Goncharov, T. C. Sangster, T. R. Boehly, S. X. Hu, I. V. Igumenshchev, F. J. Marshall, R. L. McCrory, D. D. Meyerhofer, P. B. Radha, W. Seka, S. Skupsky, C. Stoeckl, D. T. Casey, J. A. Frenje, and R. D. Petrasso, Phys. Rev. Lett. **104**, 165001 (2010).

2. E. Mapoles, Lawrence Livermore National Laboratory, private communication (2011).

3. T. J. B. Collins, J. A. Marozas, K. S. Anderson, R. Betti, R. S. Craxton, J. A. Delettrez, V. N. Goncharov, D. R. Harding, F. J. Marshall, R. L. McCrory, D. D. Meyerhofer, P. W. McKenty, P. B. Radha, A. Shvydky, S. Skupsky, and J. D. Zuegel, Phys. Plasmas **19**, 056308 (2012).

4. E. A. Evans, *Tritium and Its Compounds*, 2nd ed. (Wiley, New York, 1974).

5. D. R. Harding, T. C. Sangster, D. D. Meyerhofer, P. W. McKenty, L. D. Lund, L. Elasky, M. D. Wittman, W. Seka, S. J. Loucks, R. Janezic, T. H. Hinterman, D. H. Edgell, D. Jacobs-Perkins, and R. Q. Gram, Fusion Sci. Technol. **48**, 1299 (2005).

6. K. C. Jordan, B. C. Blanke, and W. A. Dudley, J. Inorg. Nucl. Chem. **29**, 2129 (1967).

7. G. F. Knoll, *Radiation Detection and Measurement*, 3rd ed. (Wiley, New York, 2000).

8. Canadian Fusion Fuels Technology Project, Ontario, Canada, CFFTP Report I-9219 (1992).

9. A. Nikroo *et al.*, Fusion Sci. Technol. **45**, 229 (2004).

10. E. L. Alfonso, R. Q. Gram, and D. R. Harding, Fusion Sci. Technol. **45**, 218 (2004).

11. S. A. Letts *et al.*, Fusion Technol. **28**, 1797 (1995).

Time-Resolved Carrier Dynamics in Si-on-Glass Absorbers for Photovoltaic Cells

The first amorphous silicon (a-Si) photovoltaic (PV) solar cell was fabricated in 1974 (Ref. 1). By the 1980s, commercial a-Si modules were limited to about 5% efficiency[2] because of a light-induced degradation called the Staebler–Wronski (SW) effect, which diminishes the efficiency of a-Si cells over time due to the creation of recombination centers.[3,4] While the impact of the SW effect could be minimized by reducing the intrinsic absorber thickness to below 250 nm, this also limited the conversion efficiency. Therefore, double-junction cells, such as a-Si–a-Si (Refs. 5 and 6) or a-Si–a-SiGe (Ref. 7), were the obvious path around the above limitations. Independently, the successful growth of microcrystalline silicon (mc-Si), a viable absorber material, was made possible by improvements in gas purification and the implementation of very high frequency (VHF) discharges. As a result, the commercialization thrust of thin-film Si PV cells has been focused on the a-Si–mc-Si tandem.[8] Recently reported stabilized efficiencies of a-Si–mc-Si tandem cells have been as high as 11.9% as a result of cell-design optimization and the use of light-management techniques throughout the device stack.[9] Further improvements, however, require better control of the growth process of the a-Si and mc-Si films to enhance their electron-hole recombination time, via reduced defect formation,[10] improved grain-boundary passivation, and minimized unwanted contaminants.[11] While the empirical approach to determining the optimized deposition is preferred, it would be time consuming and cost prohibitive to use the actual completed cell characterization and analysis as a feedback mechanism. In this work, we demonstrate that a time-resolved, optical pump–probe technique provides an effective means for determining the nonequilibrium carrier dynamics for feedback on the Si growth process. We have collected a large family of normalized reflectivity change ($\Delta T/T$) waveforms of various a-Si and mc-Si films, deposited under different conditions, to determine the optimum deposition parameter space.

The basic structure of a thin-film Si tandem cell, designed in a superstrate geometry on a transparent conductive oxide (TCO)–coated glass, is shown schematically in Fig. 132.16 (Ref. 12). Presently, the most common is low-iron, soda-lime float glass with a fluorinated tin oxide as a TCO material

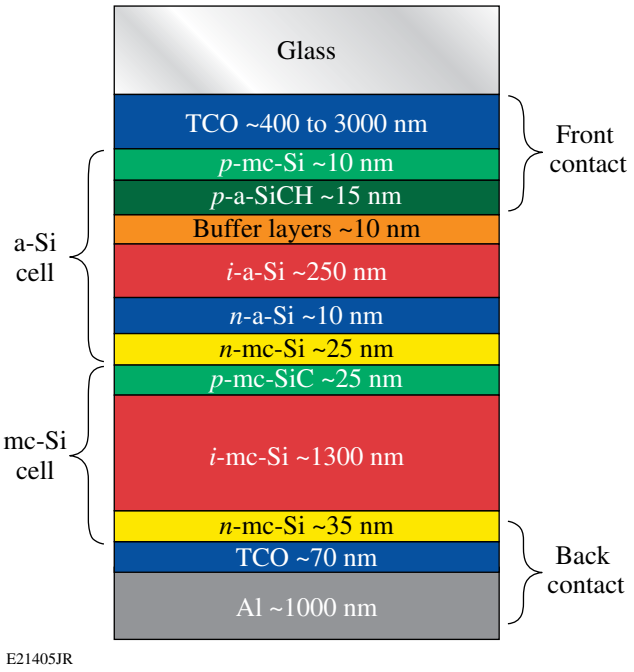

Figure 132.16
Schematic showing the layer structure of a typical Si tandem cell.

applied in-line on the float-glass process by atmospheric pressure chemical vapor deposition (APCVD).[13] In addition, other materials, such as boron-doped, aluminum-doped, or gallium-doped zinc oxide coatings, are utilized in the Si tandem PV cells. Both the a-Si cell and the mc-Si cell are *p-i-n* structures and drift-type devices with highly doped *p* and *n* layers to set up a built-in field. Therefore, for the *i* region, the a-Si and mc-Si materials with the best-possible electron lifetime and mobility are required to ensure an efficient drift under the built-in field of the *p* and *n* contacts, particularly for the a-Si film characterization by a very low hole mobility.[14]

Two sets of Si-on-glass samples were deposited for this study, and the growth conditions, band gap E_G, and optical properties (complex index of refraction; *n* and *k*) are listed in Table 132.III. The first set ("S" samples) was deposited using a plasma-enhanced CVD method, and the fabricated films

Table 132.III: Deposition conditions and measured index and band gap of a-Si films used in this study. The doping type, deposition conditions [hydrogen dilution ratio, radio frequency (rf) power, and pressure], and measured index and bandgap are listed.

		Deposition conditions				Spectroscopic ellipsometry measurements at 632 nm		
Sample	Type	Ratio $\left(H_2/SiH_4\right)$	rf power (W)	Pressure (mtorr)	Thickness (nm)	E_G (eV)	n	k
H032811S1	p	0.75	15	300	251.8	1.773	3.181	0.022
H032811S2	n	0.75	15	350	521.6	1.671	3.586	0.051
B032811S3	i	0.25	15	375	455.7	1.705	3.730	0.044
B032811S4	i	5	20	1000	342.4	1.680	3.864	0.057
B032811P3	i	5	20	1000	390.3	1.676	3.910	0.058
B032811P4	i	10	50	1000	506.9	1.818	3.651	0.015
B032811P5	i	1	15	1000	291.3	1.650	3.850	0.066

were primarily p-type SiCH and n-type a-Si films. Of notable interest, sample H032811S1 was deposited with a CH_4/SiH_4 ratio of 0.85 and a BF_3/SiH_4 ratio of 1. The "P" samples were deposited by the CVD method with no dopants. Intrinsic Si films grown by this system actually produced better solar cells with lower free-carrier concentration in the i layer. The film thickness and optical properties were determined by measuring the fringe fitting with an n and k analyzer and spectroscopic ellipsometry. The samples were 250 to 500 nm thick. Fits were performed by first fixing the optical model and surface roughness and getting thickness to fit, then fitting the material model, and finally the surface roughness. This method was required to overcome the instability inherent in the n and k fitting routines. Spectroscopic ellipsometry was performed using a commercial ellipsometer, and the data were fitted with JV's DeltaPsi2 software.[15] The a-Si was fit with the Jellison model,[16] and the mc-Si was fit as a crystalline Si using the standard JV's built-in model. Measurements were performed at a 70° angle over an energy range of 1.5 to 6.0 eV.

The carrier lifetime of our femtosecond pump–probe spectroscopy was characterized in a two-color setup using an optical system analog similar to that used by Zhang *et al.*[17] The pump beam had a 400-nm wavelength and an 800-nm probe. Special care was taken to ensure proper alignment of the beams to avoid any beam "walking" since, contrary to most femtosecond pump–probe experiments, we were interested not only in the early, fastest time evolution of the photoresponse, but also in the long relaxation tail. The latter was required in order to properly resolve the Shockley–Read–Hall recombination process,[18,19] and, correspondingly, our delay stage had a traveling range of over 30 cm. A large family of normalized transmissivity change ($\Delta T/T$) waveforms was measured at room temperature. Each sample was tested at least three times at three different spots in order to average any film inhomogeneities. All collected transients had the same general shape and consisted of a pump-pulse–limited rising edge and a bi-exponential decay. An example, in this particular case a recorder for the S3 sample, is shown in Fig. 132.17. Based on our phenomenological fitting, the initial fast relaxation was ascribed to electron–optical phonon cooling of highly excited electrons with the corresponding characteristic time constant τ_{cool} varying from 2.4 ps and 25.7 ps for the S1 and S3 samples, respectively, to 79.2 ps for the P3 sample. We interpret the subsequent relatively slow relaxation as the Shockley–Read–Hall recombination with

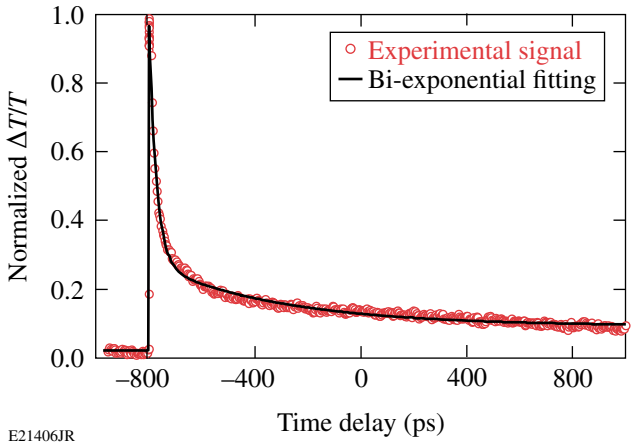

Figure 132.17
An experimental, normalized $\Delta T/T$ transient of the sample H032811S3 and a fit consisting of an error (erfc) function (rising edge) and bi-exponential relaxation (falling part).

the recombination time τ_{rec} varying from 76.4 ps and 490.5 ps for the S1 and S3 samples, respectively, to 954 ps for the P3 sample. As a result, we can see that both τ_{cool} and τ_{rec} vary substantially with the Si deposition process, with the P-type samples exhibiting the longest and most-desired τ_{rec} values.

Although the above phenomenological model provided direct indication of the desired growth conditions for maximized electron lifetime in Si PV absorbers, it did not provide physical insight into the actual carrier relaxation dynamics. It is well known that in a-Si and mc-Si materials, trapping centers strongly influence the carrier dynamics of the material.[20–22] The early trapping model for a-Si was proposed by Tiedje *et al.* based on drift-mobility measurements.[23] The underlying concept for the model consists of a continuum of energy states instead of a discrete set. In a perfect crystal, the valence and conduction band gap edge energies are well defined. In disordered semiconductors, however, the distribution of energy states begins with transport states occupying the energy levels of the material, i.e., the conduction and valence bands. This distribution continues into the energy gap as trap states. These states form a so-called band tail, and their distribution decreases exponentially near the band edge. The widths of these exponential distributions for both the conduction and valence band tails are asymmetrical. In fact, for a-Si, the width of the valence band tail is roughly twice that of the conduction tail.[24,25] For a-Si, the above model has been confirmed through electron photoemission[26,27] and optical absorption[28] measurements.

Jepsen *et al.*[29] proposed a dynamical model that involves shallow trap sites in the band gap to reproduce the transient photoresponse of carriers in optically excited and pulsed THz-probed mc-Si wafers. A schematic of the proposed relaxation process is illustrated in Fig. 132.18. After absorption of a femtosecond laser pulse, the excited electrons achieve the quasi-equilibrium Fermi distribution very rapidly (within ~10 fs). Next, they lose their energy via relaxing toward the bottom of the conduction band through the electron–optical phonon interaction. After that, electrons are very likely to be trapped by the band-tail sites near the conduction-band edge. However, after all these traps are filled, the remaining photoexcited electrons are forced to directly decay to the valence band through the nonradiative electron-hole recombination, i.e., the Shockley–Read–Hall process. Independently, over time, the trapped electrons can also be released to the valence band by recombination on a time scale that cannot be distinguished from the across-the-band gap recombination time τ_{rec}. Mathematically, the above scenario corresponds to a set of linear rate equations for concentrations of photoexcited electrons (N_{hot}),

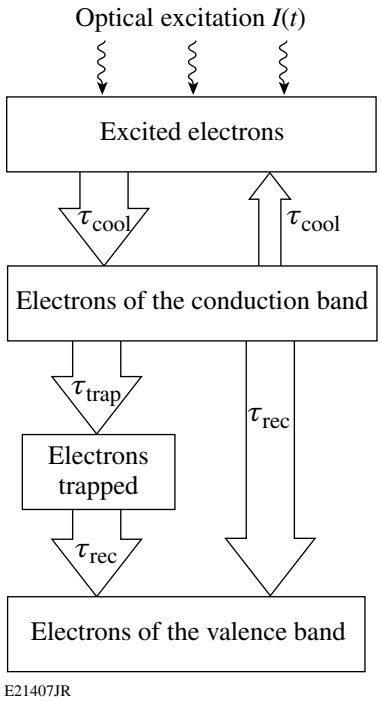

Figure 132.18
Schematic diagram of the dynamics of the carrier relaxation process for a-Si.

electrons at the bottom of the conduction band (N_{con}), and trap states N_{trap}, listed below:

$$\frac{dN_{hot}}{dt} = I(t) - \frac{N_{hot} - N_{con}}{\tau_{cool}}, \tag{1}$$

$$\frac{dN_{con}}{dt} = \frac{N_{hot} - N_{con}}{\tau_{cool}} - \left(\frac{1}{\tau_{trap}} + \frac{1}{\tau_{rec}}\right)N_{con}, \tag{2}$$

$$\frac{dN_{trap}}{dt} = \frac{N_{con}}{\tau_{trap}} - \frac{N_{trap} - N_{trap,e}}{\tau_{rec}}, \tag{3}$$

$$\tau_{trap} = \frac{\tau_{trap,max}}{1 - N_{trap}/N_{trap,max}}, \tag{4}$$

where $I(t)$ is the optical pump-pulse intensity and is assumed to be Gaussian with a width of 100 fs, τ_{trap} is the trap lifetime, and $N_{trap,e}$ is the final concentration of electrons in the trap sites. We stress that τ_{trap} actually depends on a function of the number of available trap sites and their individual lifetimes and is given by Eq. (4), with the $N_{trap,max}$ and $\tau_{trap,max}$ representing the maximum concentration of trap sites in the sample and the

longest trapping time, respectively. As compared to the equations introduced in Ref. 22, we added an extra term in Eq. (1) that is responsible for the re-exciting of some of the cooling electrons by nonequilibrium optic phonons.

Figure 132.19 shows experimental $\Delta T/T$ transients (red circles) and corresponding, simulated temporal evolutions for N_{hot} (dashed blue line), N_{con} (solid green line), and N_{trap} (solid black line) densities for four selected samples, namely, S1, S3, P5, and P3. First of all, we note that in each case the overall relaxation dynamics of photoexcited carriers, N_{hot}, fits the experimental data extremely well. At the same time, there is a considerable difference in the behavior of concentrations of trapped electrons, N_{trap}, among the various samples, providing crucial information on the difference in the density of trap sites and their trapping efficiency in samples fabricated using various methods. Figures 132.19(a) and 132.19(b) show that in both cases (samples S1 and S3), the densities of trapped electrons are large and the trapping is clearly very efficient and effective; for the S1 sample, it reaches approximately 90% with the direct across-the-band gap recombination channel, N_{con}, representing just the background. For the S3 samples, the proportions are less dramatic, even though most of the photoexcited electrons are trapped. For these samples, traps are filled fast and remain occupied (N_{trap} almost constant) at the end of our >1-ns-wide observation window. We believe that, actually, $\tau_{trap,max}$ for these a-Si samples is very likely to be longer than the pulse repetition time of our laser (~13 ns) and in our experiments the traps are being emptied by the next incoming ultraviolet (400-nm) pump pulse. In contrast to the S-type samples, for the P5 sample [Fig. 132.19(c)], the density of trapped electrons is low, while for the P3 sample [Fig. 132.19(d)], it can be neglected. Especially in this latter case, the hot carrier dynamics N_{con} is clearly governed by the

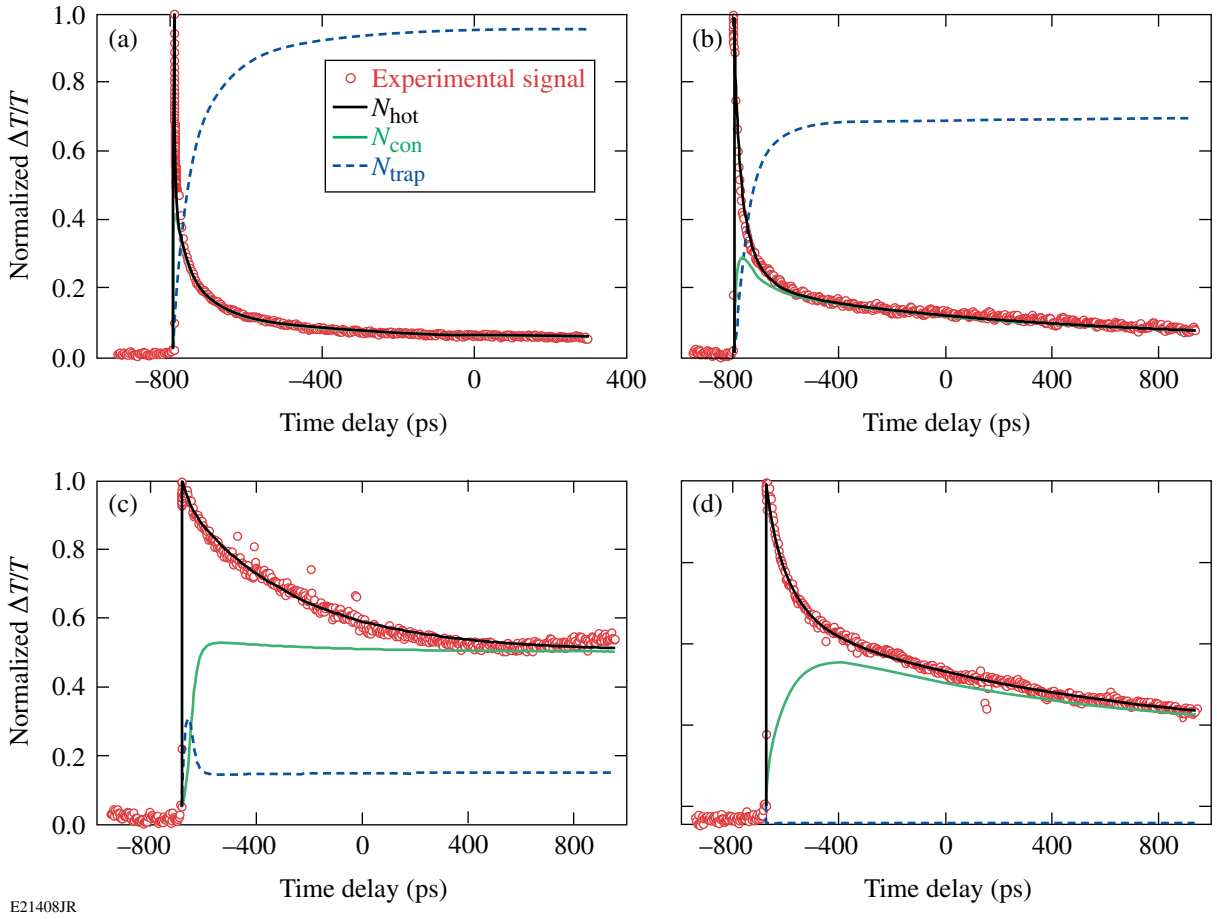

Figure 132.19
Experimental, normalized $\Delta T/T$ transients of the samples (a) H032811S1, (b) H032811S3, (c) B032811P5, and (d) B032811P3 and the corresponding simulation results based on Eqs. (1)–(4).

electron-hole recombination process, resulting in the longest value of the experimental τ_{rec} time.

The film growth conditions presented in Table 132.III corroborate with our observations. Sample H032811S1 is *p* type; therefore, its trap density is expected to be very large. The other three samples are intrinsic films with no doping; therefore, the number of trap sites should be lower. Samples B032811P5 and B032811P3 were fabricated using a growth apparatus in which the hydrogen dilution was increased as compared to the growth with the S-type samples. Since increasing hydrogen dilution shifts the material deposition from a-Si to mc-Si, we can conclude that the trap site's density has been significantly reduced in mc-Si specimens.

Finally, our S4 sample represents a very interesting case, as shown in Fig. 132.20. In this case, a significant portion of electrons is initially trapped; however, the trap lifetime is shorter than our measurement window. Therefore, we observe that at longer times, traps start to release electrons that, subsequently, "drop" to the valence band through the recombination process.

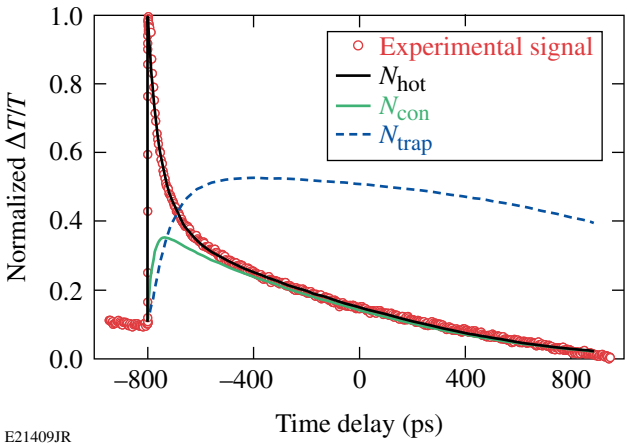

Figure 132.20
Experimental, normalized $\Delta T/T$ transients of the sample H032811S4 and the corresponding simulation results based on Eqs. (1)–(4).

Our femtosecond spectroscopy pump–probe experimental studies and subsequent simulations have proved that shallow trap sites in the band-tail states play a very important role in the relaxation of excited carriers in both a-Si and mc-Si samples. The relaxation dynamics reflects the trap-site densities and trapping lifetime in the samples, providing much-needed feedback on the control of wafer growth conditions. The latter is a crucial element for designing and optimizing new generations of Si-absorber–based PV solar cells with higher efficiencies.

ACKNOWLEDGMENT

This work is supported in part by the Corning, Inc., grant to the University of Rochester and by the New York State NYSTAR grant to the University of Rochester Center for Emerging and Innovative Sciences. J. Serafini acknowledges support from the Frank Horton Graduate Fellowship Program at the University of Rochester's Laboratory for Laser Energetics, funded by the U.S. Department of Energy Office of Inertial Confinement Fusion under Cooperative Agreement No. DE-FC52-08NA28302 and the New York State Energy Research and Development Authority. The support of NYSTAR and DOE does not constitute their endorsement of the views expressed in this article.

REFERENCES

1. D. E. Calson, U.S. Patent No. 4,064,521 (20 December 1977).
2. D. E. Carlson *et al.*, J. Mater. Res. **13**, 2754 (1998).
3. D. L. Staebler and C. R. Wronski, Appl. Phys. Lett. **31**, 292 (1977).
4. P. Stradins, Sol. Energy Mater. Sol. Cells **78**, 349 (2003).
5. R. Platz *et al.*, Sol. Energy Mater. Sol. Cells **46**, 157 (1997).
6. B. Rech, C. Beneking, and H. Wagner, Sol. Energy Mater. Sol. Cells **41/42**, 475 (1996).
7. E. Maruyama *et al.*, Sol. Energy Mater. Sol. Cells **74**, 339 (2002).
9. J. Bailat *et al.*, in *25th European Photovoltaic Solar Energy Conference and Exhibition* (Valencia, Spain, 2010), pp. 2720–2723.
10. P. Torres *et al.*, in *13th European Photovoltaic Solar Energy Conference*, edited by W. Freiesleben *et al.* (Nice, France, 1995), pp. 1638–1641.
11. U. Kroll *et al.*, J. Vac. Sci. Technol. A **13**, 2742 (1995).
12. J. Müller *et al.*, Sol. Energy **77**, 917 (2004).
13. C. Beneking *et al.*, Thin Solid Films **351**, 241 (1999).
14. R. Brenot *et al.*, Thin Solid Films **383**, 53 (2001).
15. DeltaPsi2 ©2006, HORIBA Jobin Yvon, Inc., Edison, NJ 08820-3012.
16. G. E. Jellison, Jr., M. F. Chisholm, and S. M. Gorbatkin, Appl. Phys. Lett. **62**, 3348 (1993).
17. J. Zhang, A. Belousov, J. Karpiński, B. Batlogg, G. Wicks, and R. Sobolewski, J. Appl. Phys. **110**, 113112 (2011).
18. R. N. Hall, Phys. Rev. **87**, 387 (1952).
19. W. Shockley and W. T. Read, Jr., Phys. Rev. **87**, 835 (1952).
20. S. Brehme *et al.*, Mater. Sci. Eng. B **69–70**, 232 (2000).
21. W. Fuhs, P. Kanschat, and K. Lips, J. Vac. Sci. Technol. B **18**, 1792 (2000).
22. E. A. Schiff, J. Phys.:Condens. Matter **16**, S5265 (2004).

23. T. Tiedje *et al.*, Phys. Rev. Lett. **46**, 1425 (1981).

24. X. Deng and E. A. Schiff, in *Handbook of Photovoltaic Science and Engineering*, edited by A. Luque and S. Hegedus (Wiley, Chichester, England, 2003), Chap. 12, pp. 505–566.

25. Q. Gu *et al.*, Phys. Rev. B **52**, 5695 (1995).

26. L. Ley, J. Non-Cryst. Solids **114**, 238 (1989).

27. W. B. Jackson *et al.*, Phys. Rev. B **31**, 5187 (1985).

28. G. D. Cody *et al.*, Phys. Rev. Lett. **47**, 1480 (1981).

29. P. Uhd Jepsen *et al.*, Appl. Phys. Lett. **79**, 1291 (2001).

Proton Emission from Cone-in-Shell Fast-Ignition Experiments at the Omega Laser Facility

Introduction

The fast-ignition concept[1,2] has been described thoroughly in literature as one alternative to direct-drive hot-spot ignition. In this scheme a high-energy, high-intensity (10^{15} W/cm^2) laser is used to compress a cold shell containing fusion fuel to high areal densities ($\rho R \sim 1$ g/cm^2). A short-pulse, ultrahigh-intensity laser (10^{19} W/cm^2) is then used to generate megavolt electrons to heat the core of the dense fuel assembly in a time that is short compared to hydrodynamic time scales. The use of two independent laser drivers to compress the fuel assembly and subsequently heat the core allows for higher target gains, in principle, for the same amount of driver energy. This is because high fuel-areal-density cores can be assembled with slow implosion velocities and ignition is achieved by efficiently coupling the short-pulse beam energy to the dense core.[1] In comparison to conventional hot-spot ignition, the symmetry requirement of the fuel assembly in fast ignition is not as stringent; this relaxes the illumination uniformity and power-balance constraints of the driver.

The success of this approach relies on the effective energy coupling between the short-pulse laser and the pre-assembled dense fuel. A high coupling efficiency (CE) depends on the generation of hot electrons and their transport and energy deposition to the dense fuel core. A potential problem is that the generation of energetic electrons will also inevitably accelerate ions. Any energy coupling to ions is a direct-loss channel that must be examined.

The acceleration of ions, and in particular protons, by electrostatic sheath fields set up by hot electrons generated by laser–plasma interaction (LPI) has been observed in both direct-drive[3] and indirect-drive[4] configurations with high-intensity (~10^{14}-W/cm^2) long-pulse beams. Protons and heavier ions produced by ultra-intense (~10^{18} to 10^{19} W/cm^2) short-pulse laser–plasma interactions have also been studied extensively using flat-foil and cone targets. In short-pulse scenarios, laser-to-proton energy conversion efficiency, angular emission of protons from flat-foil targets, focused emission of proton beams, and effects of plasma scale length on proton acceleration have been studied.[5–7] Proton measurements have also been used, in conjunction with ion expansion models,[8–10] to infer the temperature of the LPI-generated hot-electron distribution that accelerates these protons.[11,12]

This article presents the first measurements of fast protons in surrogate cone-in-shell fast-ignitor experiments conducted at the Omega Laser Facility.[13,14] In these experiments, a short-pulse laser was focused into gold cones to generate hot electrons and subsequently heat a pre-assembled dense D_2 core, with the aim to increase the DD-neutron yield by raising the ion temperature.[15] For these experiments, the neutron-yield enhancement caused by core heating has been measured to be a factor of ~4, corresponding to a CE of 3.5% (Ref. 15).

In the context of proton acceleration, these experiments differ from previous work with cone targets and short-pulse lasers in that protons have been used here as a diagnostic tool to (1) assess effectiveness of fast-ignitor coupling to the dense core and (2) determine the energy coupling to protons, a loss mechanism in fast-ignition experiments.

The following sections provide an overview of the experimental setup and charged-particle diagnostics used to measure proton spectra; present proton spectra and maximum energies; discuss where and how the protons are generated; and relate how protons are used to infer the hot-electron temperature for these experiments. The article concludes with a summary of results.

Experiments

The experiments were performed at LLE using both the OMEGA (long-pulse) and OMEGA EP (short-pulse) lasers. OMEGA is a 60-beam neodymium-glass laser capable of focusing 30 kJ of frequency-tripled light at a wavelength of 351 nm to on-target intensities greater than 10^{15} W/cm^2. OMEGA EP consists of four beams, two of which are short pulse, each capable of delivering 1 kJ of 1053-nm light in 10 ps, while the other two are long pulse. In these experiments,[15] 54 OMEGA beams delivering 18 kJ of UV light to the capsule were used to compress the target along a low adiabat ($\alpha \approx 1.5$), which

was achieved using a short single picket, followed by a main drive pulse with a duration of approximately 2.7 ns. A single short-pulse (~10-ps), Gaussian-shaped OMEGA EP beam was then brought to focus inside the OMEGA target chamber. At best focus, 80% of the beam energy was contained within a diameter of approximately 50 μm, resulting in a maximum, beam-averaged on-target intensity of $\approx 6 \times 10^{18}$ W/cm^2. For these experiments, the OMEGA EP power and energy contrast were of the order of 10^6 and 10^4, respectively.[15] Details on the targets can also be found in Ref. 15. In summary, the targets for these experiments were re-entrant gold cones inside 40-μm-thick, deuterated-plastic (CD) shells with a nominal diameter of 870 μm. The cones were either 1.2 or 1.8 mm in length and had an opening half-angle of 17°. The cone tips were flat with a variable tip thickness (5 to 15 μm) and a tip diameter of 10 μm. The cone walls were 10 μm thick inside the shell and 50 μm thick outside. The shells were not gas filled, leaving only the CD shell and the ablated material from it to undergo fusion.

Proton energy spectra were measured using both magnet-based charged-particle spectrometers (CPS1 and CPS2) and wedged-range-filter (WRF) spectrometers.[16] These instruments utilize CR-39 solid-state nuclear track detectors (SSNTD's), which are known to provide information about the energy and species of the detected charged particles.[16] It has been shown recently, however, that there exists CR-39 piece-to-piece variability in its response to charged particles.[17] Therefore, CR-39 alone cannot be used to accurately measure charged-particle spectra and must be paired with an additional particle dispersion mechanism. In addition, CR-39 is immune to electromagnetic pulse and, to some extent, to x rays, making it ideal for short-pulse experiments such as those presented here.

The CPS's feature a 0.1-mm slit and a 7.6-kG magnet to disperse charged particles onto CR-39 detectors. These spectrometers are capable of measuring proton energy spectra in the range of 200 keV to 30 MeV. The low-energy limit is set by filtering (directly in front of the CR-39), which is required to mitigate a very large flux of low-energy charged particles that would otherwise scatter within the diagnostic and saturate the detector. The high-energy limit is set by the magnet dispersion and detector arrangement. The CPS systems are fixed to the OMEGA target chamber at two different polar angles, as shown in Fig. 132.21. In practice, the exponential energy spectra of short-pulse accelerated protons result in a large on-detector proton fluence at lower energies. This may cause saturation of the CR-39 detector at these energies, effectively raising the low-energy limit of this diagnostic. It is worth noting that the CPS cannot resolve heavy ions because of the degeneracy between charge state, mass, and energy that exists for magnetic spectrometers.[16] Filters constructed of mylar and aluminum are overlaid on the CR-39 to filter out these ions. Furthermore, any energetic heavy ions that penetrate the filters are separated from protons on the basis of the contrast and diameter of the tracks they leave on the CR-39.

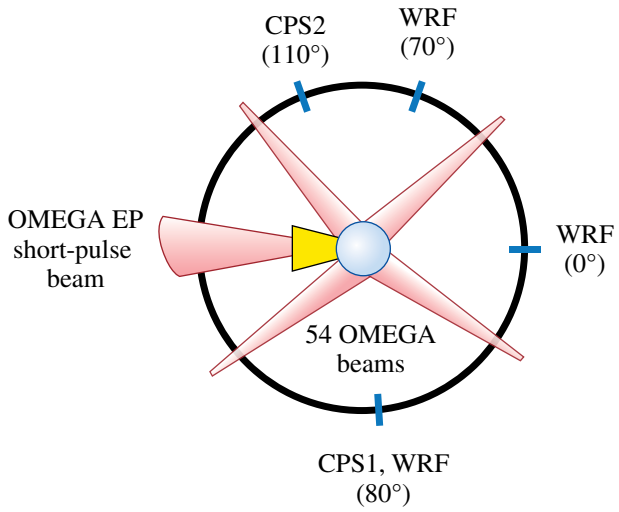

Figure 132.21
Schematic of the experimental setup. The charged-particle spectrometers (CPS1 and CPS2) and wedged-range-filter (WRF) spectrometers positioned at different azimuthal angle were used in these experiments. The coordinate system is defined such that the pole (0°) corresponds to the direction of the short-pulse laser. The OMEGA beams were used to first compress the CD shell, after which the short-pulse OMEGA EP beam was used to produce energetic electrons to heat the deuterium fuel.

The WRF spectrometers use CR-39 overlaid with a piece of wedge-shaped zirconia ceramic (ZrO_2), in which the minimum particle energy required to penetrate the wedge varies along the thickness (dispersion) direction. Since the zirconia wedge cannot be made thinner than 40 μm, the low-energy instrument cutoff for measurement of protons is approximately 3 to 4 MeV. The WRF's are compact (5 cm across) spectrometers that are ideal in probing the implosion at several locations. Several (either three or five) WRF modules, each consisting of two WRF's, were used at a single measurement location to obtain good statistics. Figure 132.21 shows the azimuthal projection of these spectrometers in the OMEGA target chamber relative to the short-pulse beam and target. The coordinate system is defined such that the pole (0°) corresponds to the direction of the short-pulse laser.

The WRF spectrometers were the primary proton diagnostic. They were fielded on nearly every shot, while the CPS was fielded on a handful of shots to corroborate the WRF measurements and provide additional details of the spectrum at energies below the WRF low-energy cutoff. The spectrometers were pointed to the target chamber center, which coincides with the center of the spherical shell. The spectrometers also subtend small solid angles (1 μsr for the CPS and 100 μsr for the WRF). As a result, they measured protons accelerated normal to the CD shell surface for each of the locations shown in Fig. 132.21. In addition, when fielded at 70° and 80°, the spectrometers measured protons accelerated nearly normal to the cone surface since that surface is nearly parallel to the spectrometer aperture because of the 17° cone opening half-angle.

Proton Spectra and Maximum Energies

A typical proton energy spectrum from integrated experiments, acquired using CPS1 (OMEGA shot 56971), is shown in Fig. 132.22. Alongside this spectrum is the proton spectrum for a neutron reference implosion (OMEGA shot 56976), where a similar target was imploded using the same long-pulse configuration (~20 kJ, 54 OMEGA beams) without any short-pulse core heating. It has been well established that long-pulse LPI generates protons up to ~1 MeV (Refs. 3 and 18), consistent with the data shown from the reference implosion. Nearly all of the observed energetic protons, however, arise from short-pulse LPI. These spectra exhibit a high-energy cutoff corresponding to the maximum path-integrated electric fields seen by the ions.

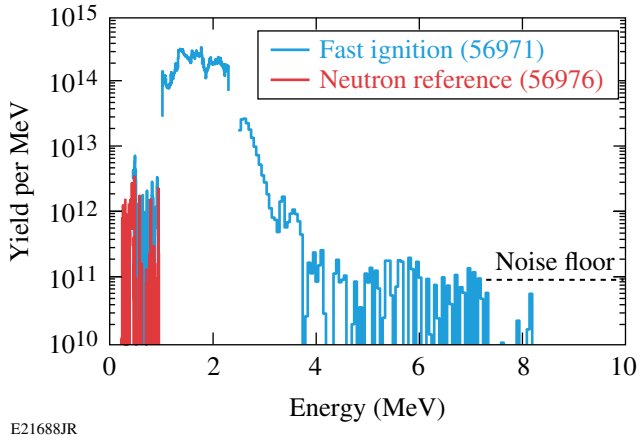

Figure 132.22
Proton spectra measured with CPS1 (80°) on fast-ignition experiments and neutron reference experiments. In both cases, a gold cone-in-shell target was compressed using 54 OMEGA beams (~20 kJ) and a low-adiabat laser drive. For the fast-ignition case, the OMEGA EP short-pulse laser was fired, at peak compression of the target, to generate hot electrons and heat the dense core. These energy spectra were background subtracted, although some residual background is observed in the 4- to 7-MeV range. The gaps in the spectrum at ~1 MeV and ~2.3 MeV are due to the instrument.

Proton energy spectra were measured down to approximately 200 keV using the CPS. As proton emission was anisotropic, it was difficult to precisely measure the total energy lost to protons. On the basis of measurements such as the one shown in Fig. 132.22, we estimate that the total energy carried by these protons is typically of the order of 10 J, or just about 1% of the incident short-pulse laser energy. This number can be compared to the previously inferred 20% coupling efficiency of short-pulse laser energy to hot electrons.[19] Therefore, approximately 5% of the short-pulse laser energy coupled to hot electrons is lost to the acceleration of ions.

The fact that the observed ions were protons (and not deuterons or heavier ions) was confirmed by simultaneous charged-particle measurements using CPS and WRF spectrometers. Since the CPS's use magnetic fields for ion dispersion, it can be shown that the inferred energy of an ion depends inversely on the assumed ion mass.[16] Therefore, the CPS-inferred energy of a deuteron mistakenly identified as a proton will be twice as large as the actual particle's energy. The WRF's have an opposite energy-mass dependence, whereby the inferred energy of a deuteron mistakenly identified as a proton will be lower than the actual particle's energy. It is therefore possible to constrain the particle species using these measurement techniques on the same shot and same polar angle. In particular, CPS1 and the WRF's measure particles at the same polar angle (80°) but different azimuthal angles.

Since the target is composed of a CD shell and Au cone, these protons originate predominantly from hydrocarbon contaminants on the surface of the target. The implications are that the protons do not significantly interact or scatter with the compressed shell. The cone-in-shell target conditions at the time when the short-pulse laser interacts with the cone are schematically illustrated in Fig. 132.23, which shows the cone, the compressed D_2 core (~50-μm diameter), the blowoff plasma surrounding the core, the generated hot electrons, and the accelerated surface protons. The relative timing between the short-pulse laser and the start of the long-pulse compression lasers was varied from shot to shot, but it is typically 3 ns. At this point in time, the blowoff plasma from the ablated shell has expanded for this same amount of time at the ion sound speed $\left(c_s \equiv \sqrt{T/m_i}\right)$, resulting in a characteristic scale length of about 400 μm to 1 mm for typical coronal temperatures of ~2 keV. The blowoff plasma scale length is therefore comparable to the length of the cone, and it is expected that the

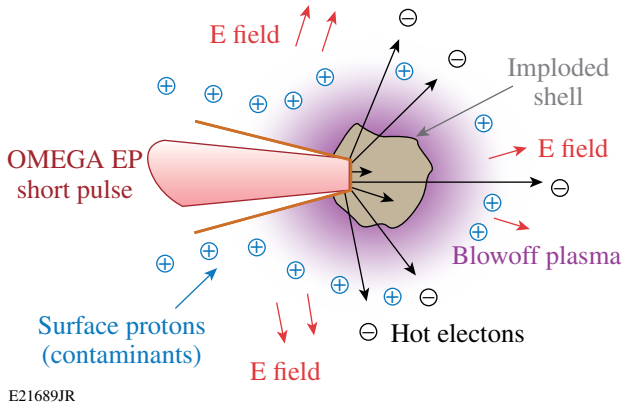

Figure 132.23
Schematic of the target conditions when the short-pulse OMEGA EP laser interacts with the cone tip. The CD shell has been compressed to a diameter of ~50 μm and is surrounded by blowoff plasma from the ablated shell (~1-mm scale length). Interaction of the short-pulse laser with the cone generates hot electrons that accelerate surface-contaminant protons from the ablated plasma.

protons from the target are accelerated in the presence of this long-scale-length plasma.

The maximum proton energy for each shot is of interest since it scales directly with the temperature of short-pulse–generated hot electrons.[20,21] Direct measurements of the maximum energy can therefore be used to qualitatively infer how the hot-electron temperature varies with experimental parameters. The maximum proton energy was measured at various locations around the implosion using the compact WRF spectrometers on several shots (Fig. 132.24). These data incorporate measurements from gold cones with 5-μm-, 10-μm-, and 15-μm-thick tips and 10-μm tip diameters. The data obtained in the direction transverse to the short-pulse beam (80° and 70°) scale with intensity. A χ^2 analysis of the data indicates that these data fit a normalized ponderomotive scaling ($\propto I^{1/2}$) at both 80° (reduced $\chi^2 = 0.96$) and 70° (reduced $\chi^2 = 0.71$). This is further confirmation that these protons are accelerated by short-pulse–generated hot electrons. In addition, since the maximum energies scale with intensity as expected from theory, these protons can be used to estimate a hot-electron temperature, albeit with some caveats (see **Inferred Hot-Electron Temperature**, p. 209).

In contrast to the transverse direction, the maximum energies of forward-going protons (0°) show neither such scaling nor a dependence on cone-tip thickness. In addition, the maximum energies of forward-going protons are lower compared to the transverse-going protons. This is consistent with simulations, which indicate that for these experiments, the hot electrons are emitted in two lobes with half-angles of 57° (with a minimum

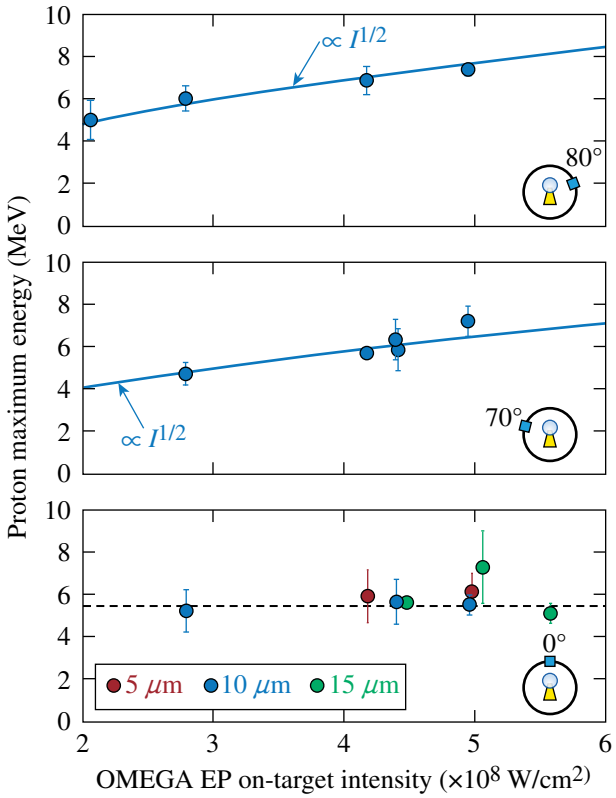

Figure 132.24
Maximum proton energies measured by WRF spectrometers at 80°, 70°, and 0° with respect to the forward short-pulse beam direction. The data points shown are averages over many WRF measurements at one location. The error bars (within 95% confidence limits) were computed from the standard deviation of these multiple measurements. At both 80° and 70°, the data show reasonable agreement with the known ponderomotive hot-electron scaling. The maximum proton energies for the forward beam direction (0°) show neither scaling with intensity nor dependence on cone-tip thickness.

in the forward direction).[22] In this case, it is expected that fewer and less-energetic protons would be observed in the forward direction even when the cone tip is intact, which is consistent with these observations.

In addition, forward-going protons are accelerated by hot electrons that have interacted with the compressed core and lost a significant amount of energy (Fig. 132.23). Some of the slower electrons are even ranged out in the core. The inferred electron temperatures and ρR of the compressed shell (~150 mg/cm^2) are consistent with this notion, as discussed further in **Inferred Hot-Electron Temperature**, p. 209. As a result, the distribution of forward-going electrons has a lower maximum energy and empty regions in velocity space, thereby reducing the energies of forward-going protons relative to transverse protons.

Several WRF's were used to obtain the average maximum proton energies at each location. The standard deviations of these measurements were used to compute the error bars (within 95% confidence limits) shown in Fig. 132.24. Since the spatial separation between adjacent WRF's is of the order of several centimeters, the observed uncertainties in the data arise from both the absolute measurement uncertainty of each WRF (~200 to 300 keV) and possible spatial variations in the maximum energy. For the case of forward-going protons, the uncertainties are as large as ±2 MeV, which is larger than the absolute measurement uncertainty of the WRF spectrometers. Therefore, we conclude that there are real spatial modulations of the maximum proton energy for forward-going protons. These observed larger spatial variations could be the reason why the scaling with intensity is not readily apparent. Furthermore, these variations are consistent with the presence of a stochastic process, such as hot electrons scattering in the compressed shell. For these reasons, it is difficult to infer a hot-electron temperature from forward-going protons, as additional physics must be unfolded from the proton measurement, and we defer to only transverse-going protons when inferring hot-electron temperatures in **Inferred Hot-Electron Temperature**, p. 209.

Source of the Protons

There is evidence that the observed protons are accelerated from the cone walls rather than from the cone tip, where the laser interacts with the cone. The data presented throughout this article consist primarily of cones 1.2 mm in length, with 10-μm or 40-μm tip diameters and variable tip thicknesses. On a few shots, cones with a length of 1.8 mm (but otherwise identical) were also shot. A comparison of 1.2-mm and 1.8-mm cones showed that the proton yields scale with the square of cone length (and therefore the surface area of the cone, for a fixed cone-opening angle). This suggests that the protons are accelerated from the entire surface of the cone rather than from the tip alone. Since charged-particle spectra were not available for these shots, proton yields could not be directly measured. Instead, relative proton yields were inferred from the neutron time-of-flight (nTOF) data in Fig. 132.25, which shows the raw signals from the nTOF liquid scintillator.[23] For these two shots, the nTOF settings, laser drive, and target parameters were identical with the exception of the cone length. The x-ray flash, which occurs when the short-pulse beam hits the cone, and the 2.45-MeV DD-neutron signals are characteristic of these implosions, as shown in Fig. 132.25. In between these signals are a number of smaller peaks associated with neutrons from (p,n) reactions in the surrounding material. Their arrival time is generally consistent with the maximum energies of the protons

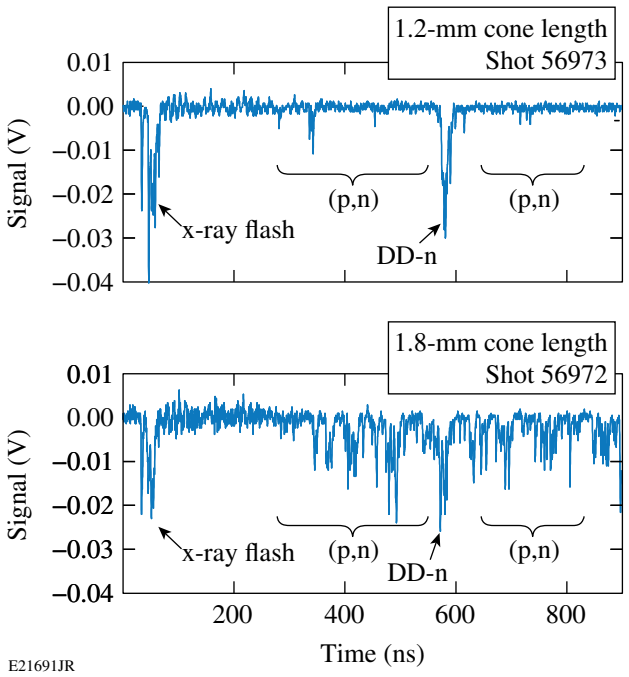

Figure 132.25
Neutron time-of-flight signal (Channel 2), showing the x-ray flash, 2.45-MeV DD-n signal, and neutrons from (p,n). For these two shots, all laser and target parameters were identical with the exception of the cone length, which was 50% greater, corresponding to 2.25× more surface area. The ratio of the total (p,n) signal of these two cone lengths is ~2 to 3, roughly proportional to the ratio of the cone surface areas. This suggests that the protons are emitted over the entire cone surface as opposed to just the tip alone.

shown in **Proton Spectra and Maximum Energies** (p. 206). The integral of these signals from the proton-arrival time (e.g., ~300 ns for 7.5-MeV protons) through 900 ns (excluding the DD-n peak) was computed for three shots: two with 1.2-mm cones and one with a 1.8-mm cone. The ratio of the integrals between the 1.2- and 1.8-mm cones' data were found to be 2.0±0.5 and 3.0±0.3, respectively. These ratios are comparable to the increase in surface area of the two cones (an increase of 2.25×). Since the number of (p,n) neutrons and, therefore, fast protons scale with the area of the cone, it is likely that they are accelerated over the entire surface of the cone.

Throughout the course of these experiments, the timing between the long-pulse OMEGA and short-pulse OMEGA EP beams was varied to find the optimal timing of the OMEGA EP beam for maximum core heating and yield. Optimal timing corresponds to core heating at peak compression of the cold, dense core.[15] For effective coupling of the short-pulse laser energy to the dense core, the cone tip must be intact when the

short-pulse laser is fired. Shock waves launched into the fuel during compression by the long-pulse OMEGA lasers will eventually reach the cone tip, break through, and leave the tip physically destroyed.[15] In this scenario, we expect poor hot-electron production, and, therefore, less-energetic protons. The cone tip was intact for the data shown in Fig. 132.24. For two shots, the timing between OMEGA and OMEGA EP was such that the tip was broken when the short pulse arrived at the tip. Figure 132.26 shows data taken at 80° using CPS1, alongside data from WRF's (80°) and CPS2 (110°). The CPS1 data are generally in excellent agreement with the WRF data. This is expected since these instruments are at the same polar angle. The two shots where the tip was broken are indicated by the open circles; WRF's were not fielded at 80° for these shots. The maximum proton energies were significantly lower (~40%) at 80° and 70° (not shown) when the tip was not intact.

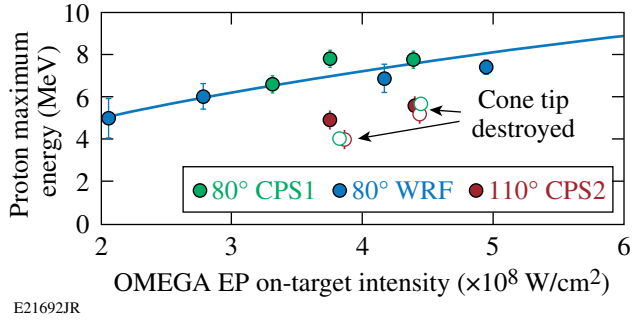

Figure 132.26
Maximum proton energies measured by CPS1, CPS2, and WRF's. The different CPS1 and WRF measurements (at 80°) show good agreement with one another, despite the fact that they sample different azimuthal angles. The solid line is a fit to the data ($\propto I^{1/2}$, with reduced $\chi^2 = 0.72$). The maximum energies of the transverse protons depend on whether the cone tip is intact when the OMEGA EP short-pulse laser arrives at the tip. When not intact (open circles), the maximum energy of the transverse protons (and therefore the fields that accelerate them) are smaller and similar to measurements and large angles (110°), as shown by the CPS2 measurement.

Since the acceleration of transverse-going protons upstream of the cone tip is affected by the presence of the tip, these data suggest that return currents associated with the initial hot-electron production could be responsible for the acceleration of these protons. We speculate that destruction of the tip affects the formation of return currents and could mitigate proton acceleration.

The drastic effect of the cone tip's destruction on electron production and subsequent proton acceleration was not observed in the forward direction, as shown in Fig. 132.27. For two shots, the 10-μm-thick cone tip was shocked before the

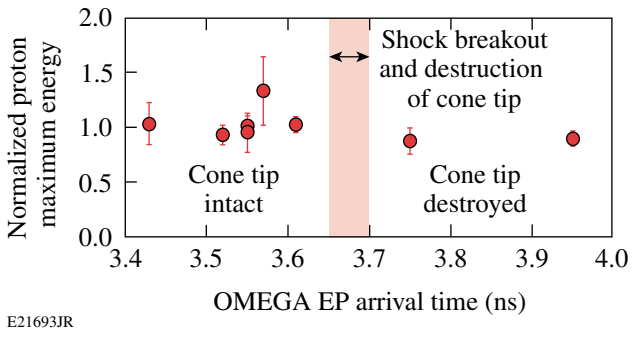

Figure 132.27
Maximum energies of forward-going protons as a function of the OMEGA EP arrival time at the cone tip relative to the start of the long-pulse drive. For comparison, the maximum energies were normalized to the mean of the data shown. Forward-going protons show no significant dependence on whether the cone tip is intact when the OMEGA EP short-pulse laser arrives at the cone tip. The shock-breakout time at the cone tip, which depends on cone-tip thickness, occurs between 3.65 ns and 3.7 ns, as shown schematically.

short pulse arrived at the cone tip. The previously measured shock-breakout time,[15] which varies with tip thickness, is indicated in Fig. 132.27. Therefore, neither the presence of the cone tip nor the thickness of the tip (per Fig. 132.24) affects the acceleration in the forward direction.

Inferred Hot-Electron Temperature

It has been suggested that the presence of a significant preformed plasma inside the cone can lead to filamentation and self-focusing of the short-pulse laser, leading to higher hot-electron temperatures.[15,24] In particular, simulations suggest that for these experiments, a preformed plasma with a scale length of 100 μm is present within the cone at the arrival time of the short-pulse OMEGA EP laser. The large preformed plasma, if present, is due to the laser prepulse that arises from amplified spontaneous emission (ASE). The prepulse is characterized by the laser contrast, defined as the amplitude ratio of the main drive to the prepulse.

Hotter electron temperatures, due to either self-focusing or another physical mechanism, result in more-energetic electrons that would not stop in the core as intended, thereby lowering the overall CE. The average ρR for spherical implosions with comparable laser and target parameters has been previously measured to be approximately 150 mg/cm^2 (Ref. 25). Given this dense core, electrons generated on one side near the cone tip would need energies of 500 keV to penetrate and escape the core, thereby accelerating surface ions in the forward direction. Therefore, we require temperatures of a few hundred kilo-electron volts, which are the expected temperatures in these experiments given the on-target intensities and the ponderomo-

tive scaling.[24] Using the proton data presented in this work, we can place a lower bound on the initial hot-electron temperature to see whether the electrons are hotter than expected from the ponderomotive scaling. The hot-electron temperature is inferred using a plasma expansion model, which links the temperature of an initial hot-electron distribution to the proton maximum energies measured here (80°). In particular, $E_M = \alpha T_H$ (Ref. 21), where α depends on the expansion model.[8–10,26] In general, α has a logarithmic dependence on the hot-electron density (n_0) and the laser pulse duration. The expansion process can be described as isothermal, adiabatic, or two phase, as described shortly. The choice of an appropriate model depends only on the relative time scales of the laser-pulse duration (τ_L) and the transit time of electrons through the target (τ_e) (Ref. 9). For these experiments, $\tau_L \sim 20\ \tau_e$. Therefore, during the first part of the laser pulse, the cone tip is completely populated with hot electrons generated from the preformed plasma on the inside of the cone. For the remainder of the pulse duration, the laser maintains the temperature of these electrons. After the pulse turns off, the electrons expand adiabatically, giving their energy to the ions. A one-dimensional (1-D) fluid model has been previously used to describe this process. This so-called two-phase fluid model[9,26] treats the laser as a source term that acts to maintain a steady temperature during the pulse (isothermal expansion) and then conserves energy between electrons, ions, and the accelerating field thereafter (adiabatic expansion).

The two-phase model relates the hot-electron temperature to the maximum proton energy by the relation

$$T_H = E_M \times \left[2.5 + 0.92 \ln\left(\omega_{pi}\tau_L\right)\right]^{-1}, \qquad (1)$$

where T_H, E_M, ω_{pi}, and τ_L are the hot-electron temperature, maximum proton energy, ion plasma frequency [$\omega_{pi} \equiv (n_{e0}e^2/m_p\varepsilon_0)^{1/2}$], and the laser-pulse duration, respectively. This formula was interpolated from numerical simulations[26] and applies for $\omega_{pi}\tau_L$ in the range of 5 to 100. The maximum energies and laser-pulse duration were measured for each shot, while the plasma frequency was estimated. To estimate n_{e0} and therefore ω_{pi}, we used a variation of a known method.[11] First, we determined the number of hot electrons generated by the short-pulse laser. Recent experiments on OMEGA EP showed that the laser-energy conversion efficiency to hot electrons is 20% for such kilojoule-class short-pulse lasers,[19] and is independent of the laser intensity. The number of hot electrons is then found by dividing the energy converted to hot electrons by the average energy of the electrons, as given by the hot-electron temperature. For the experiments presented in this work, we estimate (self-consistently, from the results of this calculation) that N_e is about 10^{14} to 10^{15}. Next, we obtained the volume by taking the product of the surface area of the cone and the characteristic scale length along the expansion dimension, given by $\approx c \times \tau_L$. The hot-electron density is then just the ratio of the number of hot electrons to volume. Since the plasma frequency ultimately depends on the hot-electron temperature through the density, Eq. (1) is transcendental and must be solved numerically.

It is important to recognize that the density computed here ($n_{e0} \sim 10^{17}$ cm^{-3}) is an overestimate. As discussed in **Source of the Protons** (p. 208), these protons are accelerated from the surfaces of the cone, possibly by hot-electron return currents. In the calculation, we assumed that the hot-electron density is uniform, which is generally not the case. We expect the hot-electron densities to be lower upstream of the cone tip, where the ions are accelerated. In addition, if the protons are indeed accelerated by hot-electron return currents, we expect these currents to be colder and less dense than the initial forward current. From Eq. (1), it is evident that for a given maximum proton energy, an upper bound on n_{e0}, and therefore on ω_{pi}, corresponds to a *minimum* inferred hot-electron temperature.

Even though these ion expansion models apply primarily to thin-foil experiments,[11,12] they can be used in the context of this work. A major distinction, however, between thin-foil experiments and those presented here must be considered to allow for a correct interpretation of the data taken in this work. The scale length of the ion front where the protons are accelerated is very different in these experiments. The two-phase model used here assumes that the initial scale length of this front is small in comparison to the hot-electron Debye length. While this is true for typical thin-foil experiments with short-pulse lasers, in our case the scale length of the blowoff plasma in front of the cone is ~400 μm to 1 mm due to the long-pulse laser's interaction with the capsule. The effective scale length seen by the accelerating protons is roughly of this order, whereas the hot-electron Debye length is ~20 μm. In this case, the maximum proton energy scales inversely with the initial density scale length at the ion front;[27] therefore, the proton energies shown in Fig. 132.24 are significantly lower than that expected by the model. To quantify this difference to some extent, it has been shown that the addition of a 100-μm-scale-length plasma at the ion expansion front (in a scale length otherwise dominated by the much smaller hot-electron Debye length), reduced the observed maximum proton energies by about 4× (Ref. 27). Therefore, in applying the expansion model to these experiments, it is expected that the actual temperatures are much higher than the temperature inferred using the model.

We used protons at 80° to infer the hot-electron temperature. For each shot, Eq. (1) was solved numerically for the minimum inferred hot-electron temperature, shown in Fig. 132.28. The error bars correspond to the uncertainty of the maximum proton energy measurement. The ponderomotive vacuum scaling (for the case of negligible pre-plasma) is shown alongside these data. The minimum inferred temperatures are factors of 2 to 3 higher than the vacuum scaling. If this inferred increase in temperature is due entirely to laser self-focusing in the pre-plasma, this result corresponds to a 3 to 10× enhancement of the incident laser intensity.

It is worth noting that OMEGA EP is known to produce maximum proton energies that are higher in comparison to those of other laser systems.[28] In particular, it has been shown that for a fixed laser intensity (~2 to 8×10^{18} W/cm^2), the maximum proton energy increases as the pulse duration is increased from 1 ps to 10 ps (Ref. 29). Observations indicate that the maximum proton energy increases faster with the laser-pulse duration than models [for example, Eq. (1)] predict. At present, there is no explanation for this observation. We speculate that the effect itself could be caused by hotter electron temperatures (for instance, enhanced absorption or hot-electron refluxing) for longer pulses (10 ps) or by additional physics of the ion acceleration process that is not incorporated into the models at this point. In the context of this work, the effect of the former would be to reinforce our argument about enhanced temperatures. The effect of the latter, if present, would be to compete with the effect of the initial scale length on maximum energies; if taken into account, it would act to lower the minimum temperatures inferred in this work.

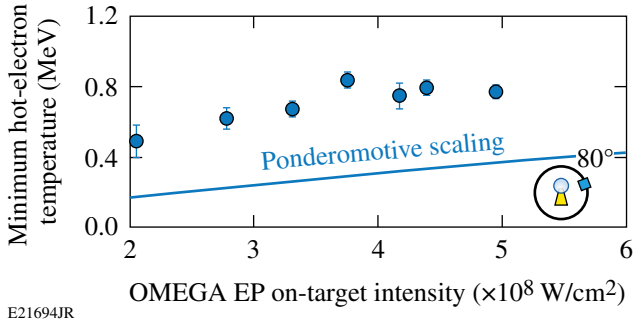

Figure 132.28
Proton-inferred hot-electron temperatures as a function of the incident short-pulse laser intensity. These temperatures are an underestimate and therefore represent the minimum initial hot-electron temperature. Shown alongside the data is the ponderomotive prediction of the hot-electron temperature for the case of negligible preformed plasma inside the cone. These inferred temperatures are 2× to 3× higher than expected.

Conclusion

This work has for the first time characterized the energy loss to fast protons in cone-in-shell fast-ignitor experiments. We estimate that of the order of 10 J, or 1% of the short-pulse laser energy, is lost to fast protons. It has been shown that these protons are accelerated from the entire surface of the cone, rather than from the cone tip alone. Since these protons are accelerated far upstream from where the short-pulse laser interacts with the tip, one possibility is that they are accelerated by hot-electron return currents. This notion is further corroborated by the fact that proton acceleration depends on the integrity of the cone tip.

Finally, these protons have been used to estimate a lower bound on the initial hot-electron temperature. These minimum, proton-inferred hot-electron temperatures (500 to 900 keV) are hotter than predicted from the ponderomotive scaling by factors of 2 to 3. If the enhancement of the hot-electron temperature is due entirely to laser self-focusing, this result corresponds to a minimum enhancement of 3× to 10× the incident laser intensity.

ACKNOWLEDGMENT

This work was supported in part by the Fusion Science Center (Rochester Sub Award PO No. 415023-G), National Laser Users' Facility (DOE Award No. DE-NA0000877), U.S. DOE (Grant No. DE-FG52-09NA29553), Laboratory for Laser Energetics (LLE) (No. 414090-G), and Lawrence Livermore National Laboratory (No. B580243).

REFERENCES

1. N. G. Basov, S. Yu. Gus'kov, and L. P. Feokistov, J. Sov. Laser Res. **13**, 396 (1992).
2. M. Tabak *et al.*, Phys. Plasmas **1**, 1626 (1994).
3. D. G. Hicks, C. K. Li, F. H. Séguin, J. D. Schnittman, A. K. Ram, J. A. Frenje, R. D. Petrasso, J. M. Soures, D. D. Meyerhofer, S. Roberts, C. Sorce, C. Stoeckl, T. C. Sangster, and T. W. Phillips, Phys. Plasmas **8**, 606 (2001).
4. A. B. Zylstra *et al.*, Phys. Plasmas **19**, 042707 (2012).
5. P. McKenna *et al.*, Phil. Trans. R. Soc. A **364**, 711 (2006).
6. S. S. Bulanov *et al.*, Phys. Rev. E **78**, 026412 (2008).
7. K. A. Flippo *et al.*, Phys. Plasmas **15**, 056709 (2008).
8. P. Mora, Phys. Rev. Lett. **90**, 185002 (2003).
9. P. Mora, Phys. Rev. E **72**, 056401 (2005).
10. P. Mora, Phys. Plasmas **12**, 112102 (2005).
11. J. Fuchs *et al.*, Nat. Phys. **2**, 48 (2006).

12. L. Robson *et al.*, Nat. Phys. **3**, 58 (2007).

13. T. R. Boehly, D. L. Brown, R. S. Craxton, R. L. Keck, J. P. Knauer, J. H. Kelly, T. J. Kessler, S. A. Kumpan, S. J. Loucks, S. A. Letzring, F. J. Marshall, R. L. McCrory, S. F. B. Morse, W. Seka, J. M. Soures, and C. P. Verdon, Opt. Commun. **133**, 495 (1997).

14. L. J. Waxer, D. N. Maywar, J. H. Kelly, T. J. Kessler, B. E. Kruschwitz, S. J. Loucks, R. L. McCrory, D. D. Meyerhofer, S. F. B. Morse, C. Stoeckl, and J. D. Zuegel, Opt. Photonics News **16**, 30 (2005).

15. W. Theobald, A. A. Solodov, C. Stoeckl, K. S. Anderson, R. Betti, T. R. Boehly, R. S. Craxton, J. A. Delettrez, C. Dorrer, J. A. Frenje, V. Yu. Glebov, H. Habara, K. A. Tanaka, J. P. Knauer, R. Lauck, F. J. Marshall, K. L. Marshall, D. D. Meyerhofer, P. M. Nilson, P. K. Patel, H. Chen, T. C. Sangster, W. Seka, N. Sinenian, T. Ma, F. N. Beg, E. Giraldez, and R. B. Stephens, Phys. Plasmas **18**, 056305 (2011).

16. F. H. Séguin, J. A. Frenje, C. K. Li, D. G. Hicks, S. Kurebayashi, J. R. Rygg, B.-E. Schwartz, R. D. Petrasso, S. Roberts, J. M. Soures, D. D. Meyerhofer, T. C. Sangster, J. P. Knauer, C. Sorce, V. Yu. Glebov, C. Stoeckl, T. W. Phillips, R. J. Leeper, K. Fletcher, and S. Padalino, Rev. Sci. Instrum. **74**, 975 (2003).

17. N. Sinenian *et al.*, Rev. Sci. Instrum. **82**, 103303 (2011).

18. D. G. Hicks, C. K. Li, F. H. Séguin, A. K. Ram, J. A. Frenje, R. D. Petrasso, J. M. Soures, V. Yu. Glebov, D. D. Meyerhofer, S. Roberts, C. Sorce, C. Stöckl, T. C. Sangster, and T. W. Phillips, Phys. Plasmas **7**, 5106 (2000).

19. P. M. Nilson, A. A. Solodov, J. F. Myatt, W. Theobald, P. A. Jaanimagi, L. Gao, C. Stoeckl, R. S. Craxton, J. A. Delettrez, B. Yaakobi, J. D. Zuegel, B. E. Kruschwitz, C. Dorrer, J. H. Kelly, K. U. Akli, P. K. Patel, A. J. Mackinnon, R. Betti, T. C. Sangster, and D. D. Meyerhofer, Phys. Rev. Lett. **105**, 235001 (2010).

20. S. P. Hatchett, C. G. Brown, T. E. Cowan, E. A. Henry, J. S. Johnson, M. H. Key, J. A. Koch, A. B. Langdon, B. F. Lasinski, R. W. Lee, A. J. MacKinnon, D. M. Pennington, M. D. Perry, T. W. Phillips, M. Roth, T. C. Sangster, M. S. Singh, R. A. Snavely, M. A. Stoyer, S. C. Wilks, and K. Yasuike, Phys. Plasmas **7**, 2076 (2000).

21. S. C. Wilks *et al.*, Phys. Plasmas **8**, 542 (2001).

22. J. Li, J. Davies, C. Ren, A. Solodov, W. Theobald, J. Tonge, and W. Mori, Bull. Am. Phys. Soc. **56**, 222 (2011).

23. C. Stoeckl, M. Cruz, V. Yu. Glebov, J. P. Knauer, R. Lauck, K. Marshall, C. Mileham, T. C. Sangster, and W. Theobald, Rev. Sci. Instrum. **81**, 10D302 (2010).

24. A. A. Solodov, K. S. Anderson, R. Betti, V. Gotcheva, J. F. Myatt, J. A. Delettrez, S. Skupsky, W. Theobald, and C. Stoeckl, Phys. Plasmas **16**, 056309 (2009).

25. C. D. Zhou, W. Theobald, R. Betti, P. B. Radha, V. A. Smalyuk, D. Shvarts, V. Yu. Glebov, C. Stoeckl, K. S. Anderson, D. D. Meyerhofer, T. C. Sangster, C. K. Li, R. D. Petrasso, J. A. Frenje, and F. H. Séguin, Phys. Rev. Lett. **98**, 025004 (2007).

26. P. Mora, in *Asian Summer School on Laser Plasma Acceleration and Radiation*, edited by Z.-M. Sheng and J. Zhang (AIP, New York, 2007), Vol. 920, pp. 98–117.

27. A. J. Mackinnon *et al.*, Phys. Rev. Lett. **86**, 1769 (2001).

28. K. Flippo, T. Bartal, F. Beg, S. Chawla, J. Cobble, S. Gaillard, D. Hey, A. MacKinnon, A. MacPhee, P. Nilson, D. Offermann, S. Le Pape, and M. J. Schmitt, J. Phys., Conf. Ser. **244**, 022033 (2010).

29. L. Gao, P. M. Nilson, W. Theobald, C. Stoeckl, C. Dorrer, T. C. Sangster, D. D. Meyerhofer, L. Willingale, and K. M. Krushelnick, Bull. Am. Phys. Soc. **55**, 377 (2010).

The Fourth Omega Laser Facility Users' Group Workshop

Introduction

A capacity gathering of 115 researchers from over 25 universities and laboratories and 9 countries met at the Laboratory for Laser Energetics (LLE) for the Fourth Omega Laser Facility Users' Group (OLUG) Workshop. The purpose of the 2.5-day workshop was to facilitate communications and exchanges among individual Omega users and between users and the LLE management; to present ongoing and proposed research; to encourage research opportunities and collaborations that could be undertaken at the Omega Laser Facility and in a complementary fashion at other facilities [such as the National Ignition Facility (NIF) or the Laboratoire pour l'Utilisation des Lasers Intenses (LULI)]; to provide an opportunity for students, postdoctoral fellows, and young researchers to present their research in an informal setting; and to provide feedback to LLE management from the users about ways to improve the facility and future experimental campaigns. The interactions were wide ranging and lively, as illustrated in the accompanying photographs.

OLUG consists of 304 members from 33 universities and 25 centers and national laboratories; their names and affiliations can be found at **www.lle.rochester.edu/media/about/documents/OLUGMEMBERS.pdf**. OLUG is by far the largest users' group in the world in the field of high-energy-density (HED) physics and certainly one of the most active.

During the first two mornings of the workshop, seven science and facility talks were presented. The facility talks proved especially useful for those not familiar with the art and complexities of performing experiments at the Omega Laser Facility. But since the facility is constantly changing and improving, even experienced users significantly benefited from these updates. The overview science talks, given by leading world authorities, described the breadth and excitement of HED science undertaken at the Omega Laser Facility.

Approximately 50 students and postdoctoral fellows participated in the workshop; 42 of these participants were supported

U1458JR

Figure 132.29
A capacity gathering of 115 researchers from 25 universities and laboratories around the world participated in this year's workshop. OLUG has 304 members who come from 33 universities and 25 laboratories, making it by far the largest users' group in the world in high-energy-density physics. The next annual OLUG Workshop will occur on 24–26 April 2013.

U1459JR

Figure 132.30
Nearly all of the 50 students and postdoctoral fellows who attended made poster presentations; 42 of these attendees received travel assistance from an NNSA grant. Travel assistance has already been arranged for the 2013 workshop. The workshop places tremendous emphasis on the participation and involvement of young researchers.

by travel grants from the National Nuclear Security Administration (NNSA). The content of their presentations ranged from target fabrication to simulating aspects of supernovae; the presentations generated spirited discussions, probing questions, and friendly suggestions. In total, there were 75 contributed posters, including 11 that focused on the Omega Facility. The invited and facility presentations, as well as OLUG's Findings and Recommendations, can be found at **www.lle.rochester.edu/about/omega_laser_users_group.php**.

An important function of the workshop was to develop a set of findings and recommendations to help set future priorities for the Omega Laser Facility. These findings were grouped into four areas: 60-beam OMEGA, OMEGA EP, general facility improvements, and accessibility of OMEGA operational information. These categories comprise a report to be given to the Omega Facility management. Twenty presentations were made by researchers deeply involved in HED science. LLE management uses these recommendations as a guide for making decisions about Omega Laser Facility operations, priorities, and future changes. In addition, the status of these OLUG findings and recommendations were updated and reviewed at a satellite evening meeting during the 2012 APS–DPP Conference. They will also form the grist for the forthcoming workshop.

One highlight of the workshop, as in past workshops, was a panel of students and postdoctoral fellows who discussed their experiences at the Omega Laser Facility and their thoughts and recommendations on facility improvements. The engaging discussions that were sparked by this forum resulted in student/postdoctoral recommendations for the facility.

Another important event at the end of the workshop was a panel of experts who gave an overview of the HED opportunities at national laboratories, universities, and LLE itself. These discussions are very useful for young researchers who may not know all the capabilities and HED research occurring at these different institutions.

U1460JR

Figure 132.31
Registration for OLUG 2012 was a busy time. MIT's seven Ph.D. students worked the registration desk, demonstrating that they are capable of doing more than just physics!

Finally, one of the important decisions made at the workshop was the selection of 24–26 April 2013 as the date of the next users' workshop. Plans are already well underway for this event.

The photographs on the following pages provide a representative sampling of the workshop's talks, interactions, and ambience.


U1461JR

Figure 132.32
University of Rochester Provost Ralph Kuncl (above), along with LLE Director Dr. Robert L. McCrory (not shown), welcomed and thanked the OLUG members for their active involvement in helping to guide and formulate the priorities and activities of the Omega Laser Facility.

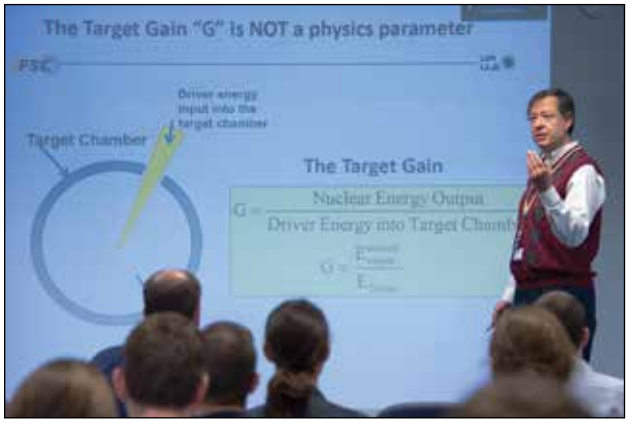

U1462JR

Figure 132.33
Invited presentations of OLUG 2012 were made by world-class physicists, such as LLE's Riccardo Betti, who talked about frontier research in inertial confinement fusion (ICF) and, more generally, in HED physics.


U1463JR

Figure 132.34
General Atomics' Joe Kilkenny, head of NIF diagnostics, presented many examples of the critical role that OMEGA and OLUG play in developing and fielding essential NIF diagnostics and platforms.


U1464JR

Figure 132.35
Nino Landen [Lawrence Livermore National Laboratory (LLNL)] presented two talks: one highlighting the National Ignition Campaign's (NIC's) scientific progress and challenges; the other regarding the HED opportunities available at the Jupiter facility, in which a wider but smaller-scale spectrum of research was described.

U1465JR

Figure 132.36
Hans Herrmann also presented two talks: one on gamma-ray spectroscopy at the Omega Laser Facility and the NIF; the other on the broader HED activities at Los Alamos National Laboratory. Hans is one of the leaders in the nascent field of plasma nuclear science.

U1466JR

Figure 132.37
During the workshop's numerous question and discussion sessions, animated and spirited discussions were the norm. Here LLNL postdoctoral fellow Nathan Kugland humorously (but seriously) raises a technical issue of widespread concern that impacts many OLUG members (i.e., imaging detectors for multi-MeV protons).

U1467JR

Figure 132.38
During three different poster sessions, 75 posters were presented, the majority by students and postdoctoral fellows.

The 11 "Facility" posters (available online), many addressing findings and recommendations of OLUG, were widely lauded by the users. "Incredibly useful" was the universal sentiment for this session.

Another critical finding and recommendation of OLUG was the appointment of a key technical contact with whom the users can interact to help implement their complex experiments.

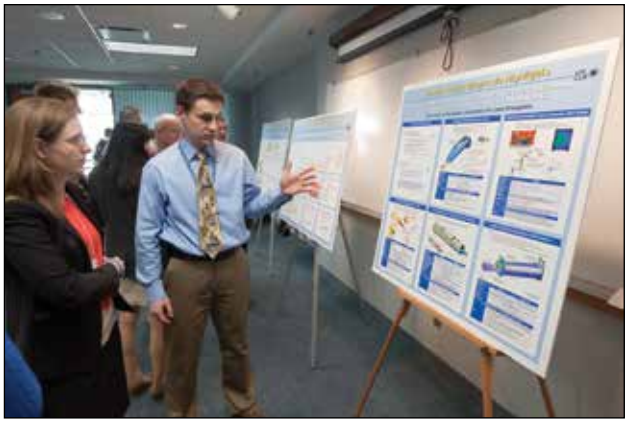

U1468JR

Figure 132.39
Chuck Sorce, shown here talking with Carolyn Kuranz of the University of Michigan, was subsequently appointed head of the Experimental Support Group with a staff to address this issue. OLUG thanks LLE for such responsiveness.


U1469JR

Figure 132.40
The student/postdoc panel and town meeting is one of OLUG's most important sessions, highlighting many of the challenges faced by young researchers at the Omega Laser Facility and elsewhere. Their findings and recommendations often highlight infrastructure and operational issues, many of which have been addressed by LLE.


U1471JR

Figure 132.42
Princeton Physics Laboratory's Ken Hill presented, in a Findings and Recommendations session, a unique concept and proposal for an OMEGA high-resolution x-ray imaging spectrometer. OLUG recommends that we actively pursue further exploration and development of Dr. Hill's promising concept.


U1470JR

Figure 132.41
Rutherford-Appleton Laboratory's Peter Norreys chaired a session on findings and recommendations. Here he shares a light moment during Tammy Ma's presentation on the student/postdoc findings and recommendations. Tammy, a LLNL postdoctoral fellow, chairs that group.


U1472JR

Figure 132.43
One of OLUG's 2011 Findings and Recommendations focused on the development of a robust magnetized HEDLP platform. LLE's Gennady Fiksel (right) and Professor Peter Norreys of Rutherford Appleton Laboratory (left) talked about these recent implementations, which OLUG found truly impressive! Thank you, LLE and Gennady!


U1473JR

Figure 132.44
In a session chaired by University of Nevada's Roberto Mancini (left), DOE technical manager Lois Buitano praised the OLUG/LLE working relationship: "This is an excellent model" for all NNSA facilities.

Questions Addressed in the General Workshop Sessions

What new avenues of research should we be pursuing at the Omega Laser Facility?

What facility improvements, large or small, can improve current research and help us pursue science at the cutting edge?

How can the administrative organization and the infrastructure at LLE better support ongoing and groundbreaking research?

What additional platforms/experiments/diagnostics might advantageously be built and coordinated, e.g., between OMEGA and the NIF, and/or between OMEGA and Trident or Jupiter?

The next Omega Laser Users' Group Workshop will be held at LLE on 24–26 April 2013.

ACKNOWLEDGMENT

This Omega Laser Facility Users' Workshop is made possible in part by the generous support of the National Nuclear Security Administration for travel expenses of students and postdoctoral fellows; by the Office of Fusion Energy Sciences for support of general workshop costs; by the Fusion Science Center; by the MIT/Plasma Science and Fusion Center; and by the Laboratory for Laser Energetics for the use and availability of critical resources and support. In addition, OLUG especially thanks LLE Director Dr. Robert L. McCrory and the LLE management and technical staff for their responsiveness to OLUG's findings and recommendations and for providing a superb and dynamic HED facility in which to conduct state-of-the-art experiments. For capturing through his lens the workshop ambiance, OLUG thanks Eugene Kowaluk. R. D. Petrasso is the editor for this Proceeding.


U1474JR

Figure 132.45
The banquet at the Meliora on the University of Rochester's campus offered workshop attendees a wonderful opportunity for socializing and good cuisine.

LLE's Summer High School Research Program

During the summer of 2012, 16 students from Rochester-area high schools participated in the Laboratory for Laser Energetics' Summer High School Research Program. The goal of this program is to excite a group of high school students about careers in the areas of science and technology by exposing them to research in a state-of-the-art environment. Too often, students are exposed to "research" only through classroom laboratories, which have prescribed procedures and predictable results. In LLE's summer program, the students experience many of the trials, tribulations, and rewards of scientific research. By participating in research in a real environment, the students often become more excited about careers in science and technology. In addition, LLE gains from the contributions of the many highly talented students who are attracted to the program.

The students spent most of their time working on their individual research projects with members of LLE's technical staff. The projects were related to current research activities at LLE and covered a broad range of areas of interest including experimental concept development and diagnostics modeling, computational modeling of implosion physics, materials science, laser system development and diagnostics, isotope separation, and database development (see Table 132.IV).

The students attended weekly seminars on technical topics associated with LLE's research. Topics this year included laser physics, fusion, holography, nonlinear optics, shape memory polymers, electronic paper, and scientific ethics. The students also received safety training, learned how to give scientific presentations, and were introduced to LLE's resources, especially the computational facilities.

The program culminated on 29 August with the "High School Student Summer Research Symposium," at which the students presented the results of their research to an audience including parents, teachers, and LLE staff. The students' written reports will be made available on the LLE Website and bound into a permanent record of their work that can be cited in scientific publications.

Two hundred and ninety-seven high school students have now participated in the program since it began in 1989. This year's students were selected from over 60 applicants.

At the symposium LLE presented its 16th annual William D. Ryan Inspirational Teacher Award to Ms. Sage Miller, a mathematics and computer science teacher at Webster Schroeder and Webster Thomas High Schools. This award is presented to a teacher who motivated one of the participants in LLE's Summer High School Research Program to study science, mathematics, or technology and includes a $1000 cash prize. Teachers are nominated by alumni of the summer program. Ms. Miller was nominated by Troy Thomas and Avery Gnolek, participants in the 2011 program, both of whom credit her for their decisions to major in computer science. Troy wrote, "I get most inspired by the way Ms. Miller teaches computer science…I had not realized how intricate and complex this subject was, and I now know that I will definitely study this in college…Ms. Miller is completely responsible for this decision as she showed me the true nature of computer science, and inspired me to pursue this more closely as a possible career option." Avery wrote, "As my math teacher Ms. Miller inspires many of her students and also displays a passion for teaching…She went out of her way to help students succeed, even when it used her own time…She would frequently meet after school with students to help them make up missed work or understand topics better…Her enthusiasm and attitude made class both informative and enjoyable…I believe that I would have never chosen such a career path had it not been for Ms. Miller's teaching and assistance." Ms. Miller also received strong support from Mr. Joe Pustulka, principal of Webster Schroeder High School, who described her as "a wonderful math and computer science teacher" who "is very devoted to her students, and is well respected and admired by her colleagues."

Table 132.IV: High School Students and Projects—Summer 2012.

Name	High School	Supervisor	Project Title
Emily Armstrong	Mercy	M. Barczys, B. E. Kruschwitz	Wavefront Measurements of High-Power UV Lasers with a Hartmann Sensor
Virginia Boy	East Rochester	R. W. Kidder	Integrating Semantic Technology with Legacy Databases
Christa Caggiano	Victor	K. L. Marshall, C. Dorrer	Fabrication of Radial Polarization Converters with Photo-aligned Liquid Crystals
Ian Gabalski	Webster Thomas	P. B. Radha	Polar-Drive Target Designs for Early Experiments on the National Ignition Facility
Mary Kate Hanchett	Fairport	W. T. Shmayda	Oxygen Uptake Using a Nickel Catalyst
Aaron Jo	Victor	W. T. Shmayda, N. Redden	Hydrogen Isotope Separation Using Gas Chromatography
Alec Kirkley	Pittsford Sutherland	G. Fiksel	Magnetic-Field Penetration into a Conducting Hohlraum
Evan Lustick	Canandaigua Academy	R. S. Craxton, M. D. Wittman	Modeling Density Change Inside a Cryogenic Target Using a Fabry–Perot Interferometer: A Feasibility Study
Aimee Owens	Home School	T. Z. Kosc, S. D. Jacobs	Performance Degradation of OMEGA Liquid Crystal Polarizers
Jesse Pan	Webster Thomas	S. X. Hu	Examination of Opacity Effects in Inertial Confinement Fusion Implosions
Mitchell Perry	Brighton	J. Qiao	Deformable-Grating Design Evaluation and Optimization for Large-Aperture Pulse-Compressor Systems
Raz Rivlis	Brighton	R. Boni	Optical Modeling and Analysis of a High-Throughput and High-Temporal-Bandwidth Spectrometer
Lucas Shadler	West Irondequoit	W. D. Bittle	Prediction of Getter Bed Regeneration Intervals Through Absolute Humidity and Flow Rate
Julia Tucker	Brighton	R. Epstein	The Dependence of Plasma Ionization Equilibrium on Electron and Radiation Temperatures
Jack Valinsky	Brighton	W. R. Donaldson, D. H. Froula	Electronic Analysis of Pulse Propagation Through an X-Ray Framing Camera
Charles Wan	Penfield	K. L. Marshall	Dynamic Mechanical Analysis of Cryogenic Target Materials

FY12 Laser Facility Report

During FY12, the Omega Laser Facility conducted 1494 target shots on OMEGA and 426 target shots on OMEGA EP for a total of 1920 target shots (see Tables 132.V and 132.VI). OMEGA averaged 11.2 target shots per operating day with Availability and Experimental Effectiveness averages for FY12 of 94.2% and 96.7%, respectively.

OMEGA EP was operated extensively in FY12 for a variety of internal and external users. A total of 356 target shots were taken in the OMEGA EP target chamber and 70 joint target shots were taken in the OMEGA target chamber. OMEGA EP averaged 6.1 target shots per operating day with Availability and Experimental Effectiveness averages for FY12 of 88.0% and 95.5%, respectively.

Table 132.V: OMEGA Laser System target shot summary for FY12.

Laboratory	Planned Number of Target Shots	Actual Number of Target Shots	NIC	Shots in Support of NIC	Non-NIC
AWE	10	12	0	0	12
CEA	35	43	0	0	43
CRASH	20	18	0	0	18
LANL	200	244	361	0	183
LBS	170	202	0	0	202
LLE	347	411	13	398	0
LLNL	300	335	116	8	211
NLUF	172	215	0	0	215
SNL	10	14	14	0	0
Total	1264	1494	204	406	884

Table 132.VI: OMEGA EP Laser System target shot summary for FY12.

Laboratory	Planned Number of Target Shots	Actual Number of Target Shots	NIC	Shots in Support of NIC	Non-NIC
LBS	45	71	0	0	71
LLE	120	172	0	172	0
LLNL	105	121	39	0	82
NLUF	55	62	0	0	62
Total	325	426	39	172	215

Highlights of achievements in FY12 include the following:

Multi-FM Beam Smoothing on OMEGA EP

A one-dimensional smoothing by spectral dispersion (SSD) demonstration system using multiple modulation frequencies (multi-FM 1-D SSD) was commissioned on one long-pulse beamline of OMEGA EP. The modified OMEGA EP beamline has supported experiments to validate this novel beam-smoothing capability prior to implementation at the National Ignition Facility (NIF) to enable polar-drive ignition. The fiber-laser–based seed-pulse system design greatly increases the laser pulse–shaping flexibility and is compatible with the NIF front-end laser design. Multi-FM SSD modulation is selectively applied to portions of the laser pulse required for polar-drive ignition on the NIF. The output seed pulse is injected into the NIF preamplifier module (PAM) with a custom SSD grating inserted into the PAM's multipass amplifier section. The dispersion of the SSD grating was selected to cleanly propagate the dispersed SSD bandwidth through the spatial-filter pinholes in the system while providing the required focal-spot smoothing performance. A series of equivalent-target-plane measurements was conducted that confirmed the expected time-integrated smoothing of the focal spot when combined with a distributed phase plate (DPP).

Equivalent-Target-Plane Diagnostics on OMEGA EP

An equivalent-target-plane (ETP) diagnostic has been activated on Beamline 4 to characterize the UV laser pulse spot on target through DPP's. The UV diagnostic package receives a sample of the laser pulse after frequency conversion. A mount has been added to install a DPP into this diagnostic arm. A far-field camera is configured to observe the entire intensity profile in low-resolution mode with 1-μrad/pixel resolution and also features a fine-resolution mode to study details of the speckle pattern with 0.3 μrad/pixel.

OMEGA EP Short-Pulse Contrast Improvement

The primary source for prepulse in the OMEGA EP short-pulse laser has historically been the amplified stimulated emission (ASE) in the optical parametric amplifiers. In FY12, the seed oscillators were upgraded to include an ultrafast optical parametric amplifier (UOPA) prior to the pulse stretcher. With this equipment, the seed energy into the next stage of amplification is increased, allowing a redistribution of the system gain to realize reduced ASE. This upgrade resulted in an improvement in the short-pulse (SP) contrast of over two orders of magnitude. (See Fig. 132.46 for representative short-pulse contrast measurements before and after this upgrade.)

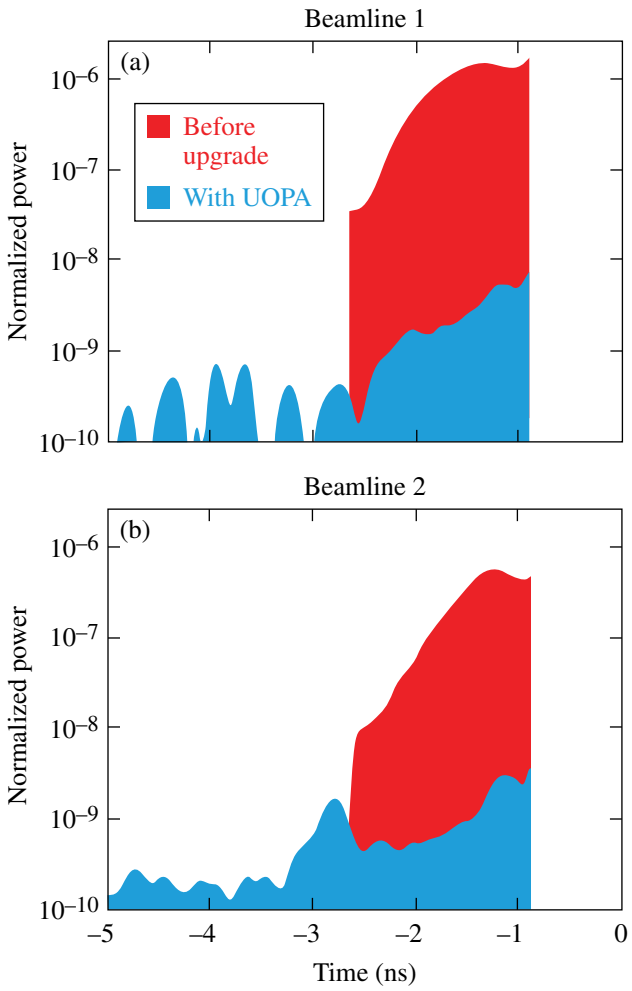

Figure 132.46
Short-pulse contrast measurements from Beamlines 1 and 2. The red curves show previously normal contrast results. The blue curves are characteristic of contrast measurements after the UOPA upgrade. On-shot power contrasts higher than 10^9 at best compression have been measured, translating into intensity contrasts higher than 10^{10}.

OMEGA EP Spatial Profile Improvements on Beamlines 3 and 4

Programmable spatial light modulators (PSLIM's) have been installed and activated in the front ends of Beamlines 3 and 4. The PSLIM system consists of a spatial light modulator installed at an image plane. The spatial light modulator applies a phase term in a 2-D array to the beam such that a prescribed amount of energy is removed at the next spatial filter in the system. A dedicated wavefront sensor (employing a novel routine for calculating the spatial profile) is used to provide feedback and achieve the desired near field without adversely affecting the wavefront.

OMEGA Ultraviolet Pulse-Shape-Measurement Capabilities

A precision ultraviolet pulse (PUVP) shape measurement diagnostic has been commissioned on the OMEGA laser to improve the resolution of pulse-shape measurements. The PUVP is a streak camera with 6-ps resolution that is free-space coupled to Beamlines 47, 57, and 67. This is twice the resolution offered by the fastest sweep speed of the P-510 streak cameras. This diagnostic also offers longer sweep speeds to ensure data collection when the beamline timings are requested to be within 13-ns separation.

A 33-ns sweep speed was added to complement existing 6-ns and 20-ns options on the P-510 timing diagnostic for all six clusters. The extended acquisition duration gives new capability to capture reference fiducials when large timing offsets are employed on individual beams or between multiple drivers. The longer sweep speed was specifically tailored to provide improved timing analysis for several campaigns that routinely employ such offsets. Standard automated analysis gives a reported timing accuracy of 350 ps and a precision of 100 ps. Additional manual processing can be performed to further improve these results when necessary.

4ω Probe Laser System

The source laser for the 4ω probe diagnostic has been installed and activated in the OMEGA EP Target Bay. This system produces a 10-ps pulse of 263-nm light, which will be used to investigate laser–plasma interactions in the OMEGA EP target chamber. The seed laser is a mode-locked oscillator that is synchronized to the short-pulse lasers by the hardware timing system to less than 5 ps. The pulse is stretched to a length of 10 ps and amplified by two stages of regenerative amplifiers before being frequency quadrupled. The energy at the target interaction (currently >20 mJ available) will exceed the background UV in the diagnostic systems. A shadowgraphy and schlieren diagnostic package is under construction to accurately

characterize the plasma densities based on the refracted light from the source.

Thomson-Scattering Spectrometer System on OMEGA

The Thomson-scattering spectrometer diagnostic has proven to be a valuable resource for characterizing the electron and ion temperatures during a target interaction. During FY12, the Thomson-scattering spectrometer system was upgraded to improve the resolution, increase the signal to noise, and add functionality. In this diagnostic, the scattered light from a probe beam is collected by an improved optical system in TIM-6 and relayed to diagnostic tables where an ion-acoustic wave spectrometer, electron plasma wave spectrometer, and the new two-plasmon-decay imager reside. Both of the spectrometers have a resolution of 20 lp/mm (increased from 7 lp/mm).

Experimental Operations and Diagnostics

In FY12, 26 new target diagnostics were commissioned on OMEGA and 8 on OMEGA EP. These included a suite of TIM-based scattered-energy calorimeters, the SXS crystal spectrometer for x-ray streak cameras, the first of the new PJX-2 streak cameras, a new high-speed video target viewing system, and an additional x-ray pinhole camera. The streaked optical pyrometer diagnostic measures the time-resolved laser-driven shocks on OMEGA. This system has been upgraded with a ROSS streak camera system and improved optical relay for higher resolution in increased signal strength. As in previous years, many of the new instruments were developed by or in collaboration with other laboratories, including LLNL, LANL, CEA, and General Atomics.

Experimental facility improvements included the introduction of an image plate scanning capability on OMEGA, the addition of a second image plate scanner on OMEGA EP, and the commissioning of a set of fully integrated TIM-based target positioning systems on both OMEGA and OMEGA EP. Two of the OMEGA TIM's were retrofit with new EMI-resistant, OMEGA EP–type control systems, and updated TIM vacuum system operating software was installed on both OMEGA and OMEGA EP.

National Laser Users' Facility and External Users' Programs

Under the facility governance plan that was implemented in FY08 to formalize the scheduling of the Omega Laser Facility as an National Nuclear Security Administration (NNSA) User Facility, Omega Facility shots are allocated by campaign. The majority (67.6%) of the FY12 target shots were allocated to the National Ignition Campaign (NIC) conducted by integrated teams from the national laboratories and LLE and to the high-energy-density campaigns conducted by teams led by scientists from the national laboratories.

Nearly 29% of the facility shots in FY12 were allocated to basic science experiments. Half of these were dedicated to university basic science under the National Laser Users' Facility (NLUF) Program, and the remaining shots were allotted to the Laboratory Basic Science (LBS) Program, comprising peer-reviewed basic science experiments conducted by the national laboratories and by LLE including the Fusion Science Center (FSC).

The Omega Facility is also being used for several campaigns by teams from the Commissariat à l'Énergie Atomique (CEA) of France and the Atomic Weapons Establishment (AWE) of the United Kingdom. These programs are conducted at the facility on the basis of special agreements put in place by DOE/NNSA and participating institutions.

The facility users during this year included 11 collaborative teams participating in the NLUF Program; 12 teams led by Lawrence Livermore National Laboratory (LLNL) and LLE scientists participating in the LBS Program; many collaborative teams from the national laboratories conducting experiments for the NIC; investigators from LLNL and Los Alamos National Laboratory (LANL) conducting experiments for high-energy-density-physics programs; and scientists and engineers from CEA, AWE, and the Center for Radiative Shock Hydrodynamics (CRASH) of the University of Michigan.

In this section, we briefly review all the external user activity on OMEGA during FY12.

FY12 NLUF Program

In FY12, the Department of Energy (DOE) issued a solicitation for NLUF grants for the period FY13–FY14. A record of 23 proposals were submitted to DOE for the NLUF FY13–FY14 program. An independent DOE Technical Evaluation Panel reviewed the proposals on 11 July 2012 and recommended that 11 proposals receive DOE funding and 28 days of shot time on OMEGA in each of FY13 and FY14. Table 132.VII lists the successful NLUF proposals for FY13–FY14.

FY12 was the second of a two-year period of performance for the NLUF projects approved for the FY11–FY12 funding and OMEGA shots. Eleven NLUF projects were allotted Omega Laser Facility shot time and conducted a total of 277 target shots at the facility. This work is summarized in this section.

Systematic Study of Fast-Electron Transport in Imploded Plasmas

Principal Investigators: F. N. Beg (University of California, San Diego) and M. S. Wei (General Atomics)
Co-investigators: R. B. Stephens (General Atomics); H. Sawada, C. McGuffey, and B. Qiao (UCSD); A. A. Solodov, W. Theobald, C. Stoeckl, J. A. Delettrez, and R. Betti (LLE); M. H. Key, P. Patel, and H. McLean (LLNL); and T. Yabuuchi and H. Habara (Osaka University)
Lead Graduate Student: L. C. Jarrott (UCSD)

Understanding fast-electron generation inside the cone and its subsequent transport into hot dense plasmas is crucial to the success of the cone-guided fast-ignition (FI) scheme of inertial confinement fusion. The goal of the University of California, San Diego (UCSD) NLUF project is to investigate the coupling efficiency and spatial energy deposition of fast electrons into an imploded CH/CD shell attached to a re-entrant gold cone target in joint OMEGA and OMEGA EP experiments. The Au cone has a 34° opening angle, 10-μm inner tip diameter, 15-μm cone-tip thickness, with 44-μm offset distance from the tip to the shell center, while the CH/CD shell has an 870-μm outer

Table 132.VII: NLUF proposals approved for shots at the Omega Laser Facility for FY13–FY14.

Principal Investigator	Institution	Project Title
F. N. Beg	University of California, San Diego	Systematic Study of Fast-Electron Energy Deposition in Imploded Plasmas with Enhanced OMEGA EP Laser Contrast and Intensity
R. P. Drake	University of Michigan	Experimental Astrophysics on the OMEGA Laser
T. Duffy	Princeton University	Dynamic Compression of Earth and Planetary Materials Using OMEGA
W. Fox	University of New Hampshire	Dynamics and Instabilities of Magnetic Reconnection Current Sheets in High-Energy-Density Plasmas
P. Hartigan	Rice University	Astrophysical Dynamics in the Laboratory: Mach Stems and Magnetized Shocks
R. Jeanloz	University of California, Berkeley	Journey to the Center of Jupiter, Recreating Jupiter's Core on OMEGA
H. Ji	Princeton University	Study of Particle Acceleration and Fine-Scale Structures of Collisionless Magnetic Reconnection Driven by High-Energy Petawatt Lasers
B. Qiao	University of California, San Diego	Dynamics of High-Energy Proton Beam Focusing and Transition into Solid Targets of Different Materials
R. D. Petrasso	Massachusetts Institute of Technology	Studies of Laboratory Astrophysics, Inertial Confinement Fusion, and High-Energy-Density Physics with Nuclear Diagnostics
A. Spitkovsky	Princeton University	Generation of Collisionless Shocks in Laser-Produced Plasmas
R. B. Stephens	General Atomics	Investigation of the Dependence of Fast-Electron Generation and Transport on Laser Pulse Length and Plasma Materials

diameter consisting of a 15-μm-thick outer CH ablator and a 23-μm-thick inner CD layer. A Cu dopant (at ~1% atomic number density of CD) is added to the CD layer of the shell, which allows one to characterize the fast electrons' transport via their induced Cu K-shell fluorescence radiation. The CH ablator prevents direct heating of the CD layer by the OMEGA driver beam and also reduces the neutron background from the corona plasmas. In this experiment, 54 (with a total energy of ~18 kJ) of the 60 OMEGA beams with a low-adiabat pulse shape [LA241701P with smoothing by spectral dispersion (SSD) off] were used to compress the shell. The 10-ps OMEGA EP backlighter beam (BL2) was tightly focused at the inner cone tip with various time delays relative to the OMEGA driver. The primary diagnostics were a monochromatic spherical crystal imager (SCI) (centered at 8048 eV with 6-eV bandwidth) to image the Cu K_α emission and a zinc Von Hamos (ZVH) x-ray spectrometer tuned to measure the Cu K-shell and ionic line emission spectrum. Several other diagnostics including broadband x-ray imaging diagnostics such as pinhole cameras and Kirkpatrick–Baez (KB) microscopes, neutron time-of-flight detectors, and a multichannel magnetic electron spectrometer were also employed. Figure 132.47 shows the target and diagnostic setup for the experiment.

In this second-year (FY12) NLUF experiment, with the improvement made to the SCI diagnostic that was newly implemented on the OMEGA chamber in FY11 for the first-year NLUF experiment, we have obtained for the first time clear images of fast electrons' spatial energy deposition in the imploded plasmas. Figure 132.48 depicts the background-subtracted SCI images showing that the OMEGA EP beam produced fast-electron–induced Cu K_α emission. The images show the imploded shell's center region from three joint shots with the OMEGA EP beam at ~500-J energy injected at three different time delays (i.e., 3.65 ns, 3.75 ns, and 3.85 ns) relative to the OMEGA driver. These SCI images clearly show that fast electrons penetrated through the cone (wall and tip) into the compressed shell, producing strong Cu K_α emission from the region of the imploded high-density plasmas. The observed decreasing fluorescence emission spot size in the SCI images with increasing OMEGA EP time delay is consistent with the simulated density profiles of the imploded shell at the

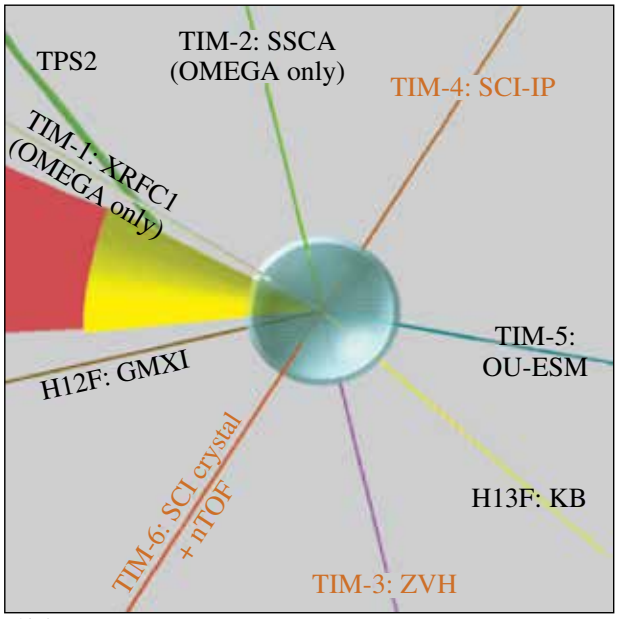

Figure 132.47
VisRad view of the cone-in-shell target and diagnostics layout. Primary diagnostics for this experiment were the SCI and ZVH for Cu K-shell measurements, OU-ESM (multichannel magnetic spectrometer) for electron spectra, and nTOF (LaCave) for neutron measurement.

corresponding implosion time in the 2-D radiation–hydrodynamic modeling results (also shown in Fig. 132.48) using the *DRACO* code. It should be pointed out that the peak emission from the dense shell outside the side cone wall is ~100 μm farther away from the cone tip, which can be caused by the pre-plasma filling of the cone as a result of the intrinsic 3-ns-long prepulse with an energy of ~20 mJ prior to the main pulse. It was also observed that the Cu K_α emission was reduced in the hot region of the core in front of the cone tip, which can be explained by the reduced collection efficiency of the SCI due to the shifting and broadening of the Cu K_α spectral line at plasma temperatures increasing above the order of 150 eV. The ZVH spectrometer provided spatially integrated Cu K_α-yield measurements. As seen in Fig. 132.49, the total Cu K_α yield (due to both OMEGA EP–produced MeV fast electrons and OMEGA driver–produced superthermal electrons with an energy of 20 to 30 keV) increased significantly (up to 60%) in the joint shots compared to the OMEGA-only implosion shots as a result of fast electrons propagating into the high-density plasma. Fast-electron energy coupling to the compressed core was found to increase with the OMEGA EP beam energy injected into the cone up to the time the cone tip broke out by the implosion-driven shocks. It is worth noting that at the latest delay, 3.85 ns, the yield decreased because the cone filled

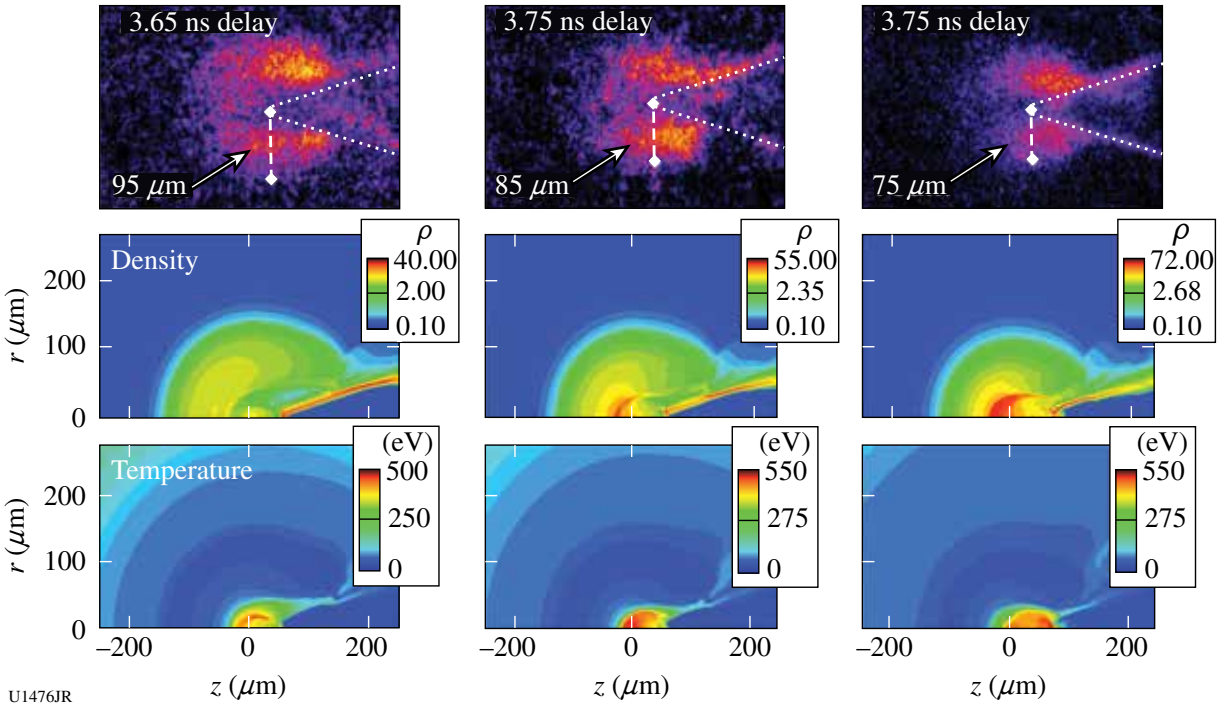

Figure 132.48
(Top) Cu K_α images show the emission from the vicinity of the cone tip at various delays with the OMEGA EP beam energy at ~500 J. The dotted lines are added to visualize the cone position, and the dashed lines show the estimated emission spot radius. The middle and bottom plots are the calculated mass density (in units of g/cm^3) and temperature (eV) maps from the *DRACO* simulations above.

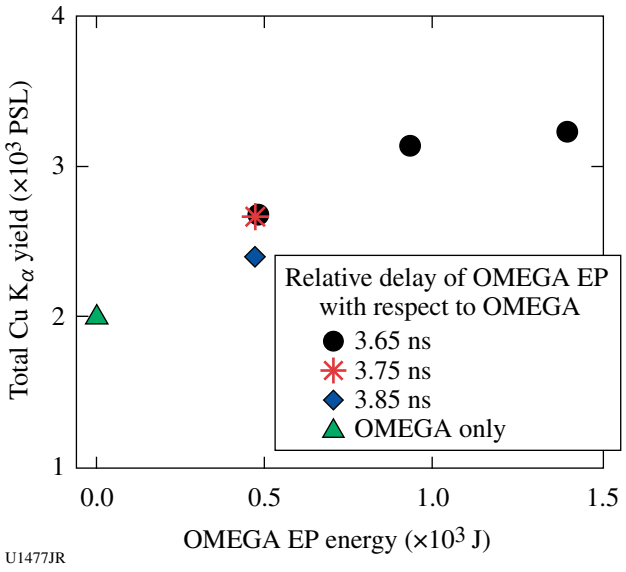

Figure 132.49
Total Cu K_α yield from the joint shots and OMEGA-only shots showing increasing yield with increasing OMEGA EP energy. Also note the significant reduction in Cu K_α yield at 3.85 ns for the OMEGA EP delay corresponding to after the cone-tip breakout by the implosion.

with plasma after the implosion-driven shock destroyed the cone tip—consistent with the *DRACO*-simulation prediction.

In summary, the FY12 UCSD-led NLUF fast-electron transport experiment with cone-in-shell (with Cu doping) targets has made the first direct measurements of the spatial energy deposition of fast electrons into an imploded high-density plasma core in the cone-guided FI configuration. The Cu fluorescence images show a clear signature of fast electrons heating the high-density plasma core and an increase in fast-electron energy coupling with OMEGA EP beam energy. Further work is in progress to combine these measurements with simulations to deconvolve the quantitative spatial information of fast-electron distribution, core plasma density, and temperature.

Experimental Astrophysics on the OMEGA Laser
Principal Investigator: R. P. Drake (University of Michigan)
Co-investigators: B. Loupias and E. Falize (CEA); J. Holloway, C. Kuranz, P. Keiter, and K. Powell (University of Michigan); T. R. Boehly and D. H. Froula (LLE); T. Plewa (Florida State University); and B. A. Remington, S. Ross, H.-S. Park, and S. H. Glenzer (LLNL)

Recreating aspects of astrophysical phenomena on OMEGA provides the ability to quantitatively test observations and models in an experimental setting and is a long-term goal of our research there. The OMEGA laser makes this feasible due to the very high-energy-density (>10-MBar) conditions it can create in millimeter-scale areas. This project includes various experiments exploring either the contribution of hydrodynamic instabilities to the structure in astrophysical systems such as supernovae or the dynamics of radiative shock waves. Here we discuss a continuation of successful campaigns at LLE that investigate the contribution of radiative shock waves to the evolving dynamics of binary star-accretion disk systems in which they reside.

Radiative shock waves produce shocked matter so hot that it radiates away most of its thermal energy. This radiation causes variable structure to develop depending on the optical properties of the material on either side of the shock. In an attempt to control these properties and understand the shock-front emission, this experiment produces an accelerating plasma flow into vacuum that becomes strongly shocked when the flow is impeded. We study the three-dimensional shock structure and the developing dynamics around it using stereoscopic x-ray radiography.

The experiments on OMEGA employ a laser configuration of ten UV beams with a 1-ns square pulse. They are focused on the 10-μm plastic ablator whose opposite face is coated with 5 μm of Sn. The beams deposit a total energy of ~4.5 kJ, giving an average irradiance of $\sim 1.2 \times 10^{15}$ W/cm^2. After an ablative shock breaks out of the rear of the foil, the Sn plasma will expand, cool, and accelerate down the evacuated target cylinder at an average velocity of the order of 150 km/s. About 4 mm from the laser drive surface, the Sn ejecta impact a 100-μm-thick, cold Al foil. In response, a reverse shock develops in the flow. The traditional "upstream" velocity in the shocked system is defined by the Sn flow, which is fast enough that the reverse shock will reach temperatures of a few hundred eV. As it radiatively cools, a thin dense layer of Sn will form, showing compressions much above the adiabatic limit of about 4. Additional sets of four OMEGA laser beams each irradiate zinc foils on orthogonally placed backlit pinhole targets for 1 ns, creating the x-ray sources used to radiograph the reverse shock onto film and image plates. Figure 132.50 shows a pair of images from a single experimental target shot, taken ~34 ns after the drive laser pulse was turned off.

Ramp Compression for Studying Equations of State, Phase Transformations, and Kinetics on OMEGA
Principal Investigator: T. Duffy (Princeton)
Co-investigators: R. Smith, J. H. Eggert, J. Hawreliak, C. Bolme, and D. Braun (LLNL); and T. R. Boehly (LLE)

The aim of this campaign was to measure powder diffraction of MgO under ramp compression. We used the PXRDIP diagnostic

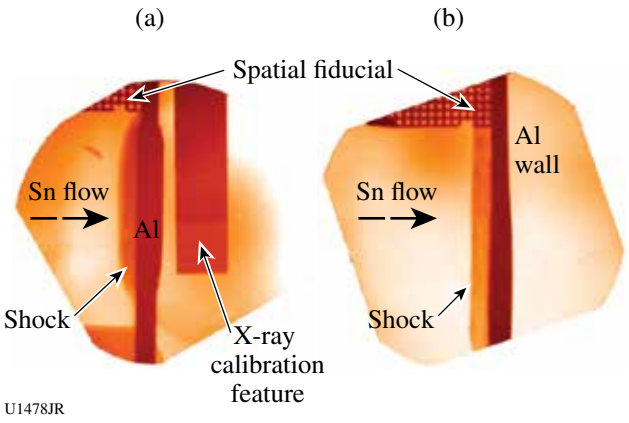

Figure 132.50
Orthogonal x-ray radiographs of a radiative reverse shock in a Sn plasma. The Al obstacle in the collision region of the experiment is 1 mm × 2 mm × 100 μm. (a) The rebounding flow from the 1-mm side, in which we see the shock wave as well as the flow moving above and below it. (b) The orthogonal view along the 2-mm Al edge where it and the reverse shock span the field of view of the diagnostic. Both radiographs were taken at the same time.

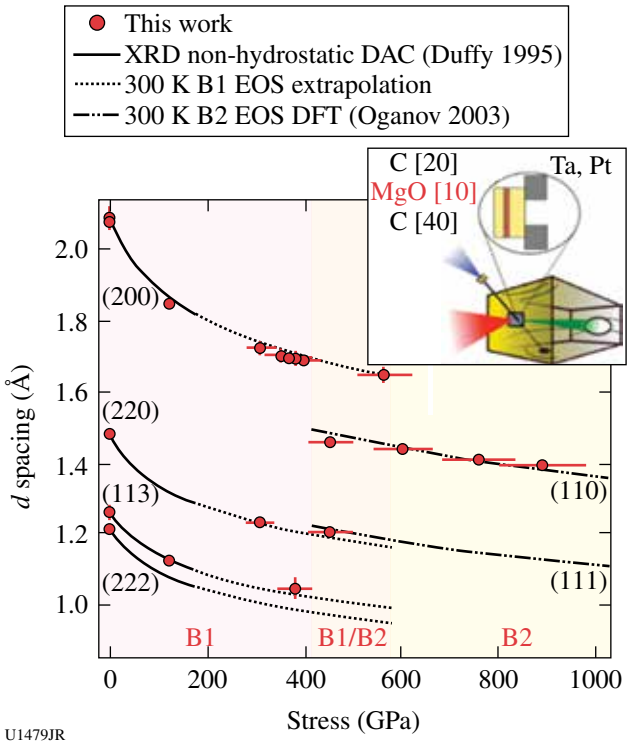

Figure 132.51
Measured d spacing of ramp-compressed MgO. The red dots indicate our experimental data and the black curves indicate our data compared with data from the literature.[1] Below 400 GPa our data indicate that the B1 phase of MgO is the stable one. Above 600 GPa a new solid phase is observed and is consistent with the B2 phase.[2]

reported in the inset of Fig. 132.51 to perform the experiments. Four OMEGA beams were focused on the main target (H7) to drive and compress the MgO powder (sandwiched between two diamonds) and up to ten beams were focused on a Fe or Cu backlighter (H2) to generate x-ray emission for diffraction measurements. We used a 3.5-ns ramp (rm3501) followed by a 1-ns square pulse (sg1018) to drive the main target and a 1-ns square to drive the backlighter. The active shock breakout [velocity interferometer for any reflector (VISAR)] was used to estimate the pressure by measuring the free-surface velocity of the diamond.

MgO was ramp compressed to about 900 GPa and diffraction patterns were recorded. The measured d spacings are shown in Fig. 132.51 as a function of the applied stress. Below 400 GPa, our data (red dots) are in good agreement with static compression experiments (black line)[1] and their extrapolation to higher pressure (black dashed line). The clear discontinuity observed between 400 and 600 GPa is the first experimental evidence for the occurrence of a phase transition in solid MgO. Analysis of the diffraction data shows that the observed solid–solid transformation is consistent with the expected B1–B2 transition[2] (from the six-fold–coordinated NaCl structure to the eight-fold–coordinated CsCl structure).

Detailed In-Situ *Diagnostics of Higher-Z Shocks: Angularly Resolved Quasi-Elastic XRTS of Shocked Al Using 18-keV X Rays*

Principal Investigator: L. Fletcher (University of California, Berkeley)

Co-investigators: T. Ma, A. Pak, H. J. Lee, T. Döppner, C. Fortmann, O. L. Landen, S. H. Glenzer, and R. Falcone (LLNL)

Molybdenum He$_\alpha$ (18-keV) x rays have been used to probe Al foils that have been compressed using both single and double (counter-propagating) shocks in a forward, small-angle scattering platform with very high angular precision.

In this experiment two scattering platforms, demonstrated in Fig. 132.52, have been used. In one configuration [Fig. 132.52(a)], 125-μm-thick Al targets were shock compressed up to 3.5× solid density using nine beams with a total energy of 4.5 kJ using stacked 1-ns pulses. In the second configuration [Fig. 132.52(b)], 200-μm-thick Al targets were shock compressed, under a counter-propagating shock geometry, up to 7× solid density using 18 beams (nine stacked 1-ns pulses on each side), resulting in a total energy of 9 kJ delivered to the Al foil. Both experiments used SG4 distributed phase plates to achieve a smooth 800-μm focal spot, yielding a total

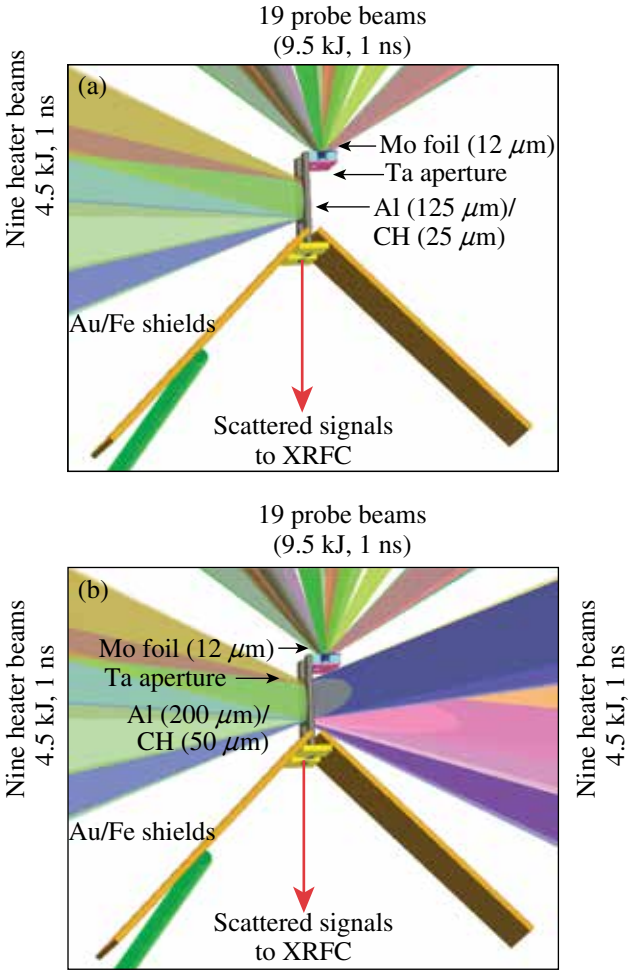

Figure 132.52
The experimental setup for HiZShk-12A. (a) A 125-μm-thick Al target and beam configuration; (b) a 200-μm-thick Al target and beam configuration; (c) a photo of the Al scattering target.

drive intensity of 3×10^{14} W/cm^2 on each irradiated surface. Nineteen beams were incident on a thin Mo foil to generate Mo He$_\alpha$ x rays at 17.9 keV used to probe the compressed targets.

Figure 132.53 shows the predicted shift of the calculated elastic x-ray scattering amplitudes to higher wave numbers with increased density. Therefore, for higher densities, the mean separation between ions decreases while the wave number k increases, making it possible to observe the structure's peak shift. The width and shape of the angularly resolved scattering feature can provide additional information on temperature and the ionization state. By directly measuring the frequency-integrated, quasi-elastic contribution to the dynamic structure factor using angularly resolved x-ray Thomson scattering (XRTS), it is possible to infer the electron densities, electron temperatures, and ionization states of double- and single-shocked Al foils with one experimental platform. Our initial analysis of the scattered data demonstrates good agreement with the predicted quasi-elastic contribution.

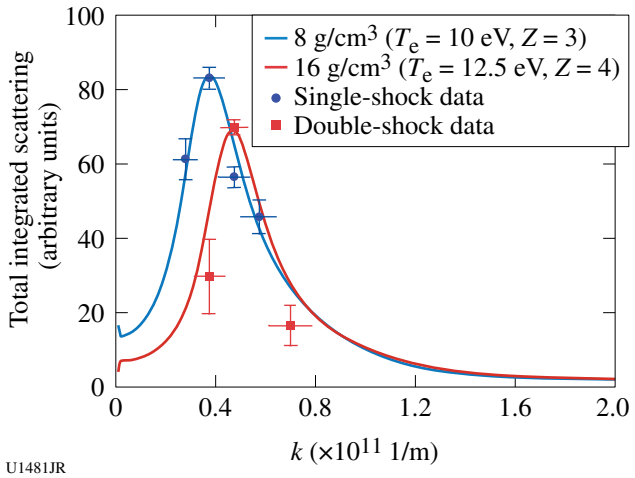

Figure 132.53
Preliminary data analysis shows the total integrated signal of the scattering data as a function of k, following the trends predicted by the SOCP or OCP models using the frequency-integrated, quasi-elastic contribution to the dynamic structure factor of single-shocked (ρ = 8 g/cm^3) and double-shocked (ρ = 16 g/cm^3) aluminum.

Measuring the Compression of Multishocked CH Ablators Using X-Ray Scattering

Principal Investigator: L. Fletcher (University of California, Berkeley)
Co-investigators: A. Kritcher, A. Pak, T. Ma, T. Döppner, C. Fortmann, R. W. Lee, J. J. Lee, O. L. Landen, R. W. Falcone, and S. H. Glenzer (LLNL)

We have performed measurements of the electron densities, electron temperatures, and ionization states of spherically compressed multishocked CH capsules by using spectrally resolved x-ray Thomson scattering. Forty-five beams (13.5 kJ at 300 J/beam incident on a CH shell) compress the 70-μm-thick CH shell above solid-mass density using a laser pulse shape comprised of three precisely timed coalescing shocks. Separately, a laser-produced, high-energy zinc He_α x-ray source at 9 keV, delayed approximately 200 ps to 800 ps in time after maximum compression (full shock coalescence), is used to probe the plasma under a noncollective 135° scattering geometry.

Figure 132.54 shows a schematic of the experimental configuration and the target geometry. In addition, hydrodynamic simulations performed with Helios [Fig. 132.54(c)] demonstrate the possibility of compressing 70-μm-thick CH ablators up to 8.75 g/cm^3 using three co-propagating coalescing shocks. A mass density of approximately 8× the initial solid density (ρ_{CH} = 1.1 g/cm^3) can be achieved using a pulse shape [Fig. 132.54(c)] with three timed steps of 1 ns, 1.5 ns, and 500 ps in duration along with precisely controlled amplitudes of 0.67 TW, 6.85 TW, and 15.5 TW, respectively. Figure 132.54(c) shows the measured radii of the CH shell superimposed on radiation–hydrodynamic simulations of the shell mass density as a function of time and shell radius. In the figure, t = 0 ns indicates the start of the drive beams and t = 3 ns indicates when the laser pulse has turned off. The simulations predict peak compression at the end of the 3-ns-long laser drive, at which time laser-produced x rays are used to probe the plasma by varying the delay between the drive laser beams (used to heat the CH capsule) and the probe laser beams incident on a Zn foil (used to produce high-energy zinc He_α x rays).

The best fits to theoretical spectra shown in Fig. 132.55 allow one to infer the temperature, electron density, and ionization state of shock-compressed CH. The changing shape of the Compton feature with respect to time, as seen in Fig. 132.55, shows that the electron density and the electron temperature change with shock propagation. The Compton feature at each time of 3.4 ns, 3.5 ns, 3.6 ns, and 3.8 ns represents the response

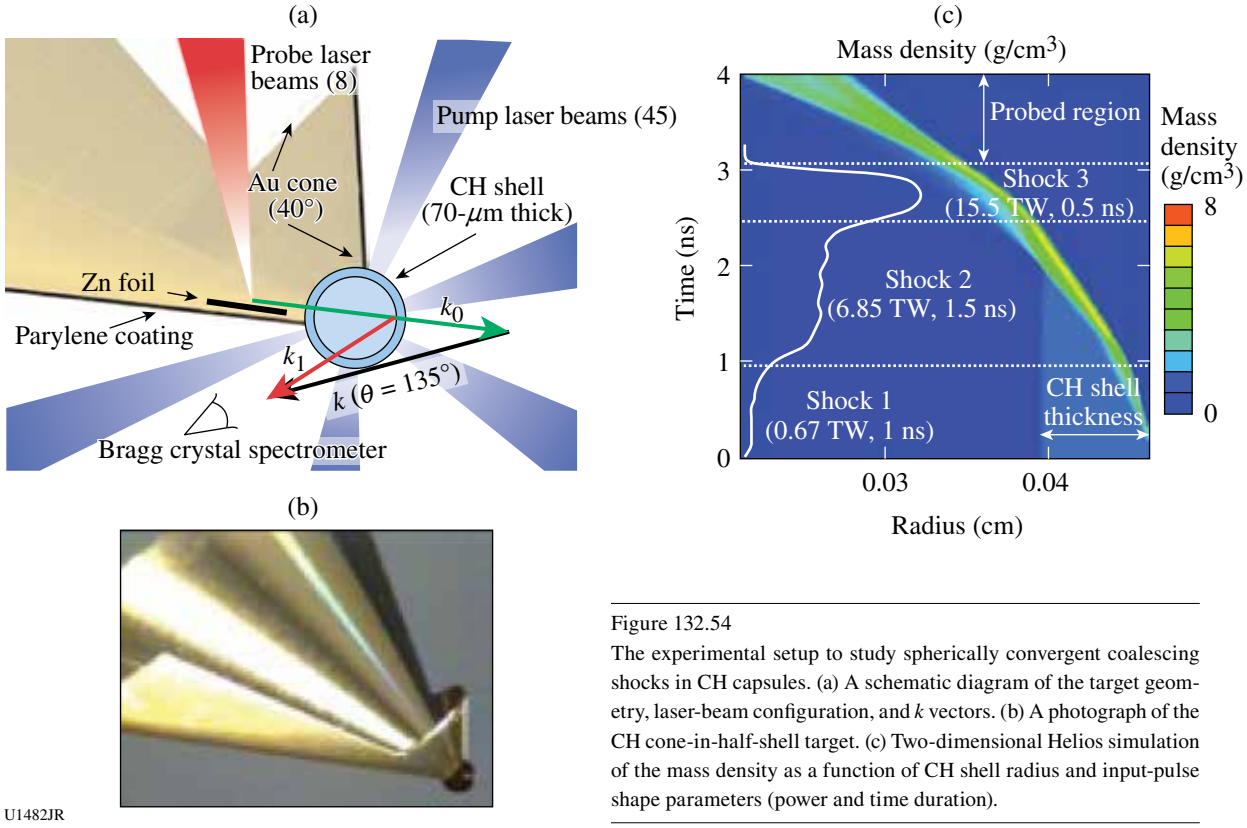

Figure 132.54
The experimental setup to study spherically convergent coalescing shocks in CH capsules. (a) A schematic diagram of the target geometry, laser-beam configuration, and k vectors. (b) A photograph of the CH cone-in-half-shell target. (c) Two-dimensional Helios simulation of the mass density as a function of CH shell radius and input-pulse shape parameters (power and time duration).

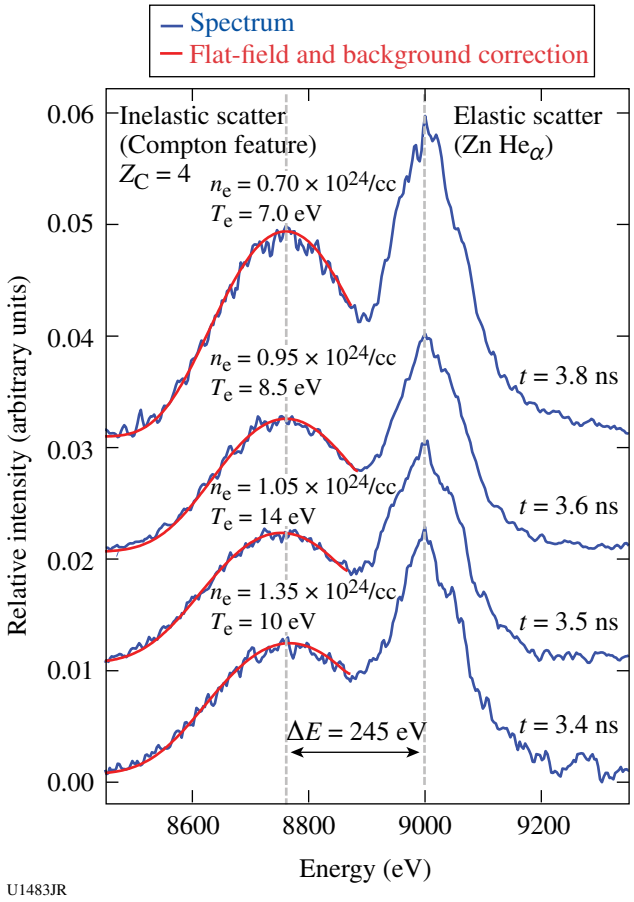

Figure 132.55
Thomson-scattering curve fit analysis. Measured scattered spectra (blue) and best fit (red) to the Compton x-ray scatter features from multishocked CH ablators at t = 3.4 ns, 3.5 ns, 3.6 ns, and 3.8 ns, yielding n_e, T_e, and Z.

of the compressed state during shock coalescence. Our analysis, which provides a full characterization of the heating process, will enable us to completely describe the time-dependent hydrodynamic evolution of shock-compressed CH capsules. It can also be used as a platform to study current equation-of-state models of CH under similar extreme conditions.

Clumpy Environments and Interacting Shock Waves: Realistic Laboratory Analogs of Astrophysical Flows
Principal Investigator: P. Hartigan (Rice University)
Co-investigators: J. Foster and P. Rosen (AWE); K. Yirak, B. Wilde, and M. Douglas (LANL); D. Martinez (LLNL); A. Frank (Rochester); and B. Blue (General Atomics)

Motivated by recent astrophysical images from the Hubble Space Telescope (HST) that were taken as part of a previous NLUF program, our focus in the past year has been to recreate laboratory analogs of some of the shock structures present in jets from young stars. Hot spots appear at the intersection points of overlapping shocks in the HST images, and it is possible that these represent transient normal shocks known as Mach stems. In the laboratory, one can study Mach stems when a strong shock wave moves along a surface. Mach stems may either grow, remain static, or vanish, depending on the intersection angle between the shock front and the surface. Our goals have been to quantify how easily Mach stems form and how fragile they are once formed.

In the last year we have been fielding a suite of experiments that control the angle of interaction between a shock wave and a reflecting surface. We do this by altering the shape of a cone embedded in foam into which we drive a strong shock front. One goal has been to study hysteresis, a phenomenon that allows a Mach stem, once formed, to persist even when the interaction angle decreases below the critical angle for formation. Another project has been to embed irregularities in the surface of the cone to determine how rough surfaces disrupt the growth and survival of Mach stems. We are also quantifying effects of preheating and ablation of the surface by radiation in the shock. A third goal has been to develop a second test bed that involves gas targets to study a system with a lower value (down to about 1.2) at gamma, the specific heat ratio. Theoretical work predicts that critical angles depend on gamma, and we will be testing that prediction. In the astrophysical case, the shock radiates and effectively lowers gamma, so it is important to understand how the system behaves when gamma deviates from the typical value of 5/3.

Examples of data from experiments fielded in the last year appear in Figs. 132.56–132.58. At the end of the campaign, we will have enough data taken at different delay times and with differently shaped cones to be able to measure growth rates for Mach stems under a variety of conditions and compare these results with predictions from simulations. These experiments are being designed using the LANL hydrocode *RAGE*. On the most-recent shot day we experimented with a design for the low-gamma gas targets that produced the expected behavior, but the image contrast was not sufficient to accurately measure Mach-stem sizes. After a modest redesign, we are ready to attempt this again with the next set of shots, where we will continue to fill out the parameter space of angles and delay times, as well as quantify the effects of preheating.

On the astrophysical side, we have discovered a way to image irradiated interfaces in regions of massive star formation. The technique involves taking narrowband images of fluoresced molecular hydrogen at near-infrared wavelengths

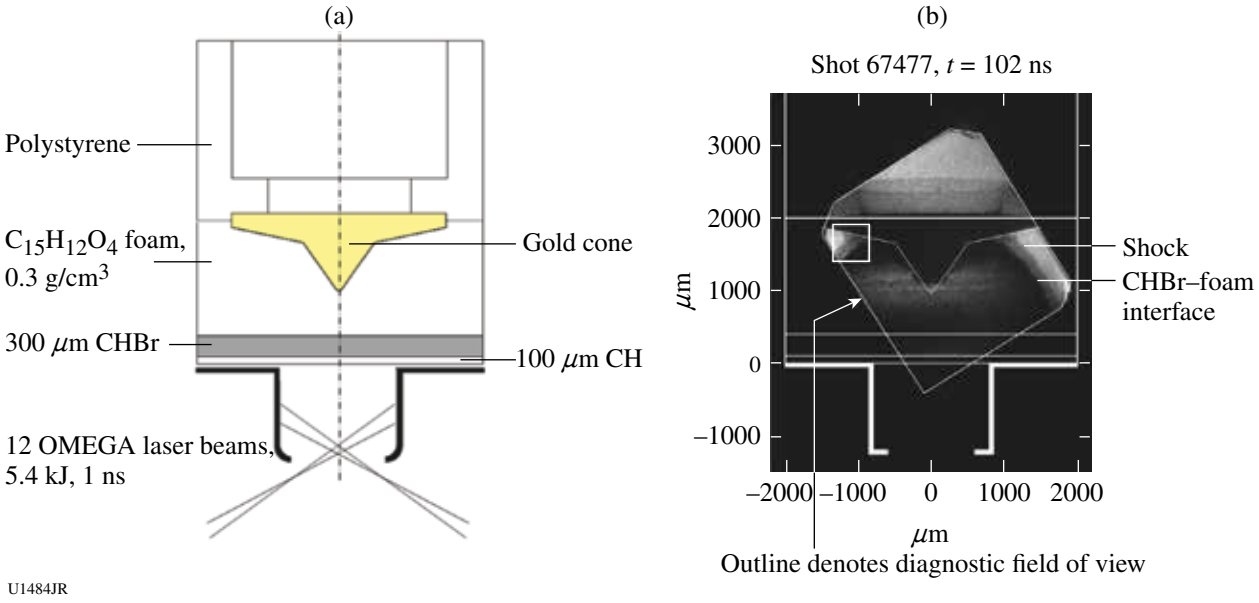

Figure 132.56
(a) Experiment to investigate hysteresis in the development of the Mach stem generated by reflection of a shock at the surface of a gold cone embedded in hydrocarbon foam. Radiation from a laser-heated hohlraum results in ablation of a CH and CHBr pusher that then drives a shock into foam containing the gold cone. (b) The experiment is diagnosed using point-projection backlighting radiography. The small, 500-μm-sq region (surrounded by a white line) identifies the position of the Mach stem, shown in detail in Fig. 132.57. The profile of the gold cone is chosen to provide a specific trajectory of the angle of the incident shock at the cone's surface, as a function of time and radial position.

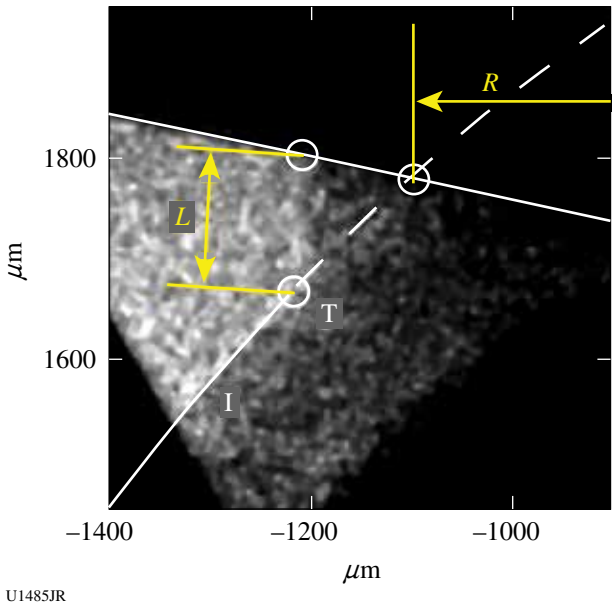

Figure 132.57
Detail taken from Fig. 132.56 showing the incident shock (I) and triple point (T). Metrics of the experiment are the length (L) of the Mach stem, and the radial position (R) at which the incident shock meets the surface of the cone. The 30-μm-diam white circles identify the triple point and the points at which the Mach stem and the extrapolation of the incident shock meet the surface of the cone.

and subtracting off a suitable continuum image. The result shows where molecular clouds absorb ultraviolet radiation and allows us to observe any radiation-driven instability that may be present. It is impossible to do this observation directly at ultraviolet wavelengths because ambient dust causes the entire region to be opaque. An example of such an image, also used on the cover of the 2012 annual report of the NNSA Stewardship Science Academic Alliance program, appears in Fig. 132.59. Observations such as these provide a wonderful opportunity to study the physics of ablated interfaces, a subject of great interest in the laboratory as well.

Results from this work have appeared in several major journals, including High Energy Density Physics and the Astrophysical Journal. A status report on the Mach-stem work, including an analysis of the growth-rate information obtained thus far, was given by co-investigator K. Yirak at the most-recent HEDLA meeting, and a paper is in press to High Energy Density Physics. Additional papers on shock waves overrunning clumps (J. Foster *et al.*, in preparation) and irradiated interfaces (P. Hartigan *et al.*, High Energy Density Physics in press; P. Hartigan *et al.*, Astrophysical Journal in preparation) are forthcoming.

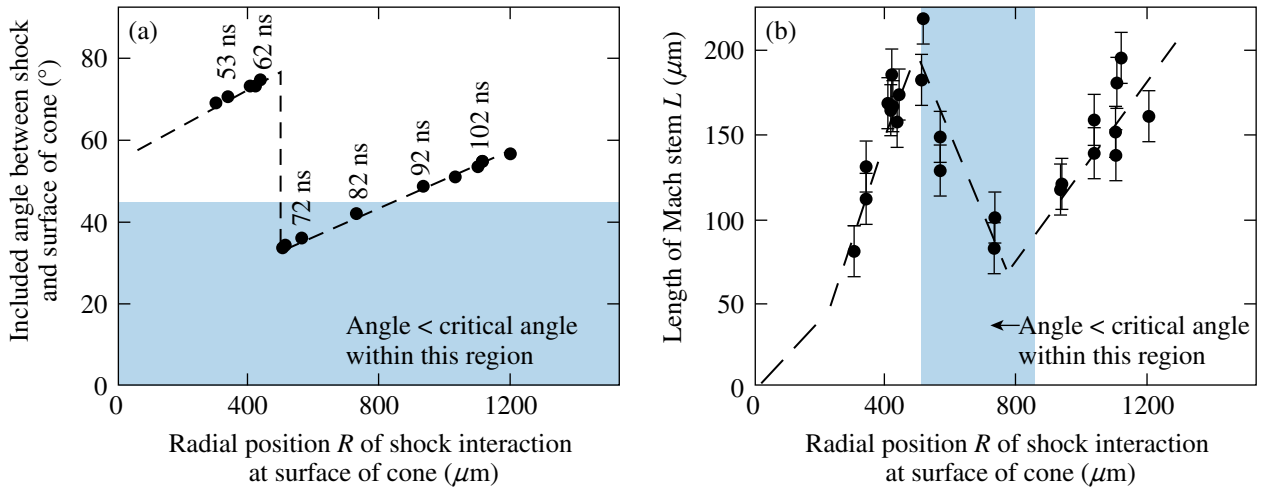

Figure 132.58
(a) Included angle between the incident shock and the surface of the cone and (b) length of Mach stem, both as functions of the radial position of the interaction of the incident shock with the reflecting surface. The growth, destruction, and later re-growth of the Mach stem are evident.

Figure 132.59
A color composite (red = H2, green = HI, blue = OIII) of a small portion of the Carina star formation region. The image reveals spectacular structures that arise when radiation from massive stars interacts with molecular globules that harbor newborn stars.

Recreating Planetary Core Conditions on OMEGA

Principal Investigator: R. Jeanloz (University of California, Berkeley)
Co-investigators: P. Loubeyre (CEA); J. H. Eggert, D. G. Hicks, and G. W. Collins (LLNL); and T. R. Boehly (LLE)

We have extended the determination of the equation of state of dense fluid hydrogen by measuring the Hugoniot of D_2 precompressed in a diamond anvil cell to 6 GPa. We have also collected an extended pressure–density–temperature data set on hydrogen–helium mixtures precompressed to 4 GPa. Two He concentrations have been studied: 20 mol.% He and 50 mol.% He. A strong difference is observed between the shock temperature curves of these two concentrations. As illustrated in Fig. 132.60,

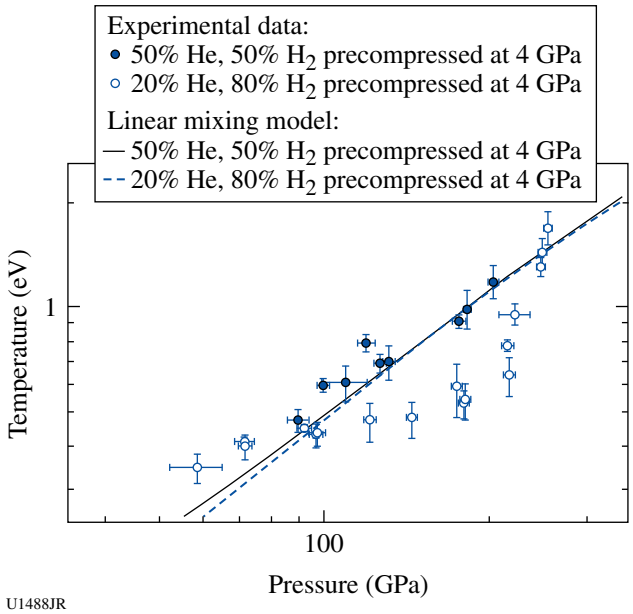

Figure 132.60
In FY12, the OMEGA laser was used to study hydrogen–helium mixtures at planet-core conditions. The H_2, D_2, and H_2–He shock pressure and density were inferred by shock-velocity measurements impedance matched to a quartz standard. The temperature along the Hugoniot data for two different helium contents (20 mol.% He: open symbols; 50 mol.% He: solid symbols) provide evidence for demixing at 20 mol.% He by a drop of the temperature below the expected linear-mixing behavior that describes well the 50-mol.%-He mixture.

for a 20-mol.% He mixture, a strong *relative-cooling* effect is observed, whereas for 50 mol.%, the ideal mixing behavior is followed. We interpret this *relative-cooling* effect as the signature of the phase separation along the shock Hugoniot between 100 and 250 GPa. This result is important because it provides the first experimental evidence for a longstanding theoretical prediction that warm dense H–He fluid mixtures can undergo *unmixing*. This has direct astrophysical implications: a helium-rich phase may separate from hydrogen inside giant planets (so-called "helium rain"). This *differentiation* process releases gravitational energy that is thought to have greatly influenced the evolution of Saturn relative to Jupiter.

Investigation of Hydrodynamic Stability and Shock Dynamics in OMEGA Direct-Drive Implosions Using Spectrally Resolved Imaging

Principal Investigator: R. C. Mancini (University of Nevada, Reno) and R. Tommasini (LLNL)
Co-investigators: J. A. Delettrez, S. P. Regan, and W. Theobald (LLE)

The multimonochromatic (MMI) x-ray imager instrument records arrays of spectrally resolved images whose interpretation and analysis have created a new era for x-ray spectroscopy of inertial confinement fusion plasmas. The MMI data are based on spectrally, spatially, and time-resolved x-ray images because of the emission and/or absorption of radiation by a tracer element added to the plasma. The instrument combines pinhole-array imaging with the dispersion of a Bragg multilayer mirror and the time resolution provided by a framing (gated) camera detector. The MMI data are rich in information and its processing permits the extraction of narrow and broad images as well as space-integrated and space-resolved spectra.[3] The simultaneous and self-consistent analysis of sets of spatially resolved spectra observed along quasi-orthogonal directions has led to the demonstration of a new type of tomography, i.e., *polychromatic tomography*, which, unlike standard tomography, relies on data recorded along a limited number of lines-of-sight (LOS) but employs the information encoded in multiple wavelengths.[4] In this project, we apply spectrally resolved imaging to investigate the hydrodynamic stability and shock dynamics of low-adiabat, direct-drive implosions on OMEGA. In low-adiabat implosions, a nearly isentropic compression is launched by a shaped laser pulse drive that starts from a low intensity, gradually leading to a high intensity. By minimizing preheat, higher compressions are achieved in low-adiabat implosions compared to high-adiabat implosions, therefore making fundamental studies on the stability of low-adiabat implosions relevant to high-energy-density-plasma hydrodynamics and, in particular, inertial confinement fusion. Furthermore, benchmarking of hydrodynamic codes with data from well-characterized implosions is important since these codes are also used to model and design low-adiabat cryogenic implosions and advanced ignition concepts.

The experiments on OMEGA consist of spherical implosions where the 60 OMEGA laser beams symmetrically illuminate a spherical shell filled with deuterium gas. The plastic shell has a 0.5-μm-thick, plastic tracer layer doped with Ti at the 6% (atomic) level of concentration and initially located on the inner surface of the shell. Three identical MMI instruments fielded on TIM-3, TIM-4, and TIM-5 of the OMEGA chamber are used to record the x-ray signal of this spectroscopic tracer. Figures 132.61–132.63 illustrate some of the data processing and analysis results.

Figure 132.61 shows gated narrowband images reconstructed from spectrally resolved image data recorded in frame 1 of OMEGA shot 62086 with the MMI instrument mounted on TIM-3. In addition to the narrowband image based on the Ti Ly$_\alpha$ line transition ($1s$–$2p$, $h\nu$ = 4979 eV), an x-ray image of the same bandwidth based on the nearby continuum is also displayed. The fact that MMI data afford the extraction of images based on spectral signatures of the tracer, and the nearby continuum is important since it permits the removal of the underlying continuum from the line transition image and, therefore, produces a better approximation to the image due to just the line emission of the tracer; this image is also included in Fig. 132.61. In turn, the intensity distribution observed on the line emission image allows us to track the spatial localization of the tracer originally placed on the inner surface of the shell. Since in a perfectly stable, one-dimensional spherical implosion the tracer remains on the inner surface of the shell (i.e., core–shell boundary), the observation of the actual spatial distribution of tracer in the core (through its line emission) provides information about the stability and mixing of the implosion. In this regard, Fig. 132.62 displays the time evolution of the Ti Ly$_\alpha$ line emissivity radial profiles in the core obtained from Abel inversion of angle-averaged narrowband images from data of the same OMEGA shot and TIM shown in Fig. 132.61. Results from two frames, i.e., frames 1 and 3, are shown that are characteristic of early and late times through the collapse of the implosion. The separation in time between frames 1 and 3 is approximately 200 ps. Early in time the tracer emission is localized away from the core center. Later in time, the tracer emission is seen to peak at the center of the core.

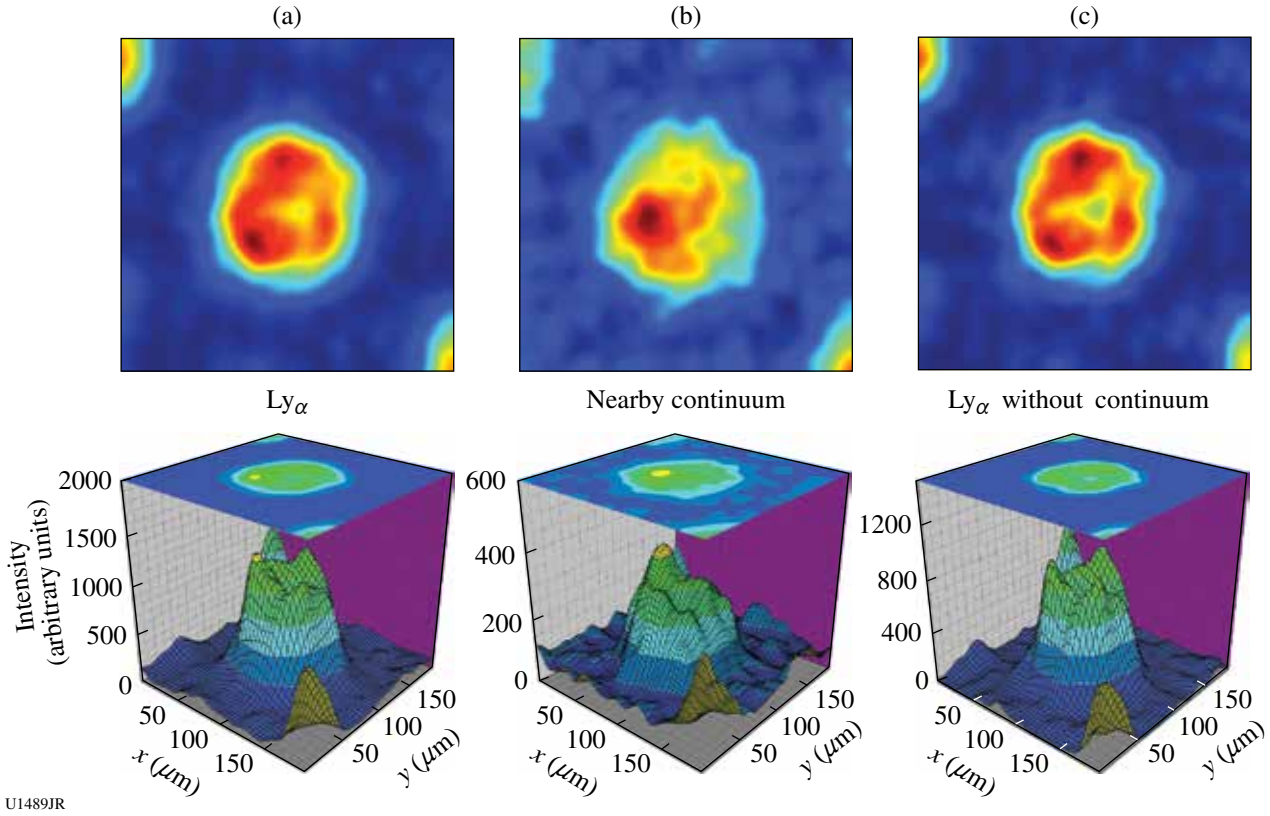

Figure 132.61
Gated narrowband images reconstructed from spectrally resolved image data recorded in frame 1 of OMEGA shot 62086 with the MMI instrument mounted on TIM-3. (a) Intensity map and surface plot of the Ti Ly$_\alpha$ image; (b) intensity map and surface plot of the nearby continuum image; (c) intensity map and surface plot of the Ly$_\alpha$ with the continuum removed.

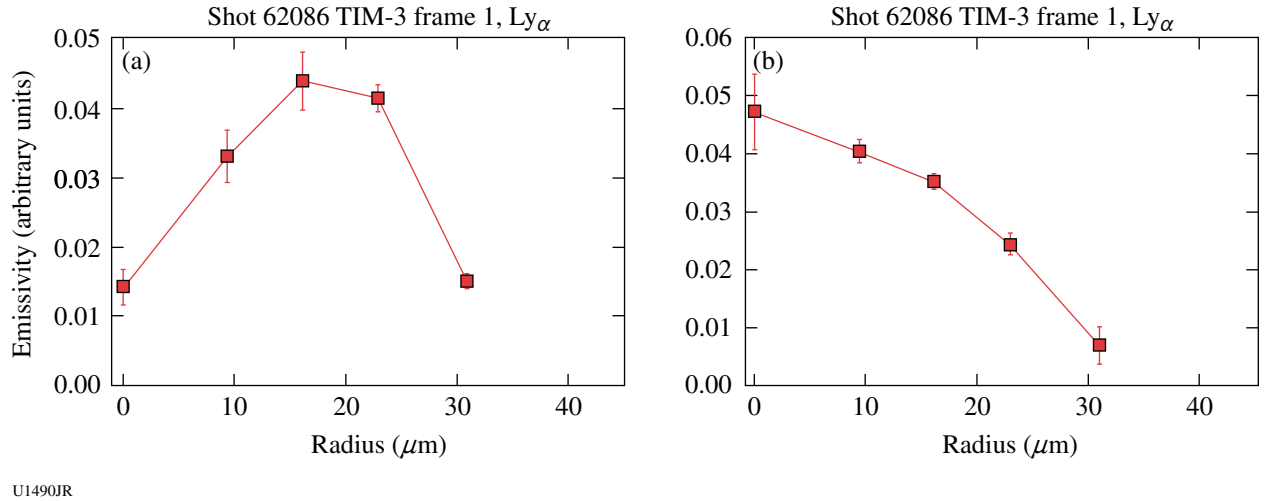

Figure 132.62
Time evolution of the Ti Ly$_\alpha$ line emissivity radial profiles in the core obtained from Abel inversion of angle-averaged narrowband images recorded on OMEGA shot 62086 with the MMI instrument mounted on TIM-3. (a) Early-in-time emissivity profile based on image data recorded in frame 1. (b) Later-in-time emissivity profile based on image data recorded in frame 3. The separation in time between frames 1 and 3 is ~200 ps.

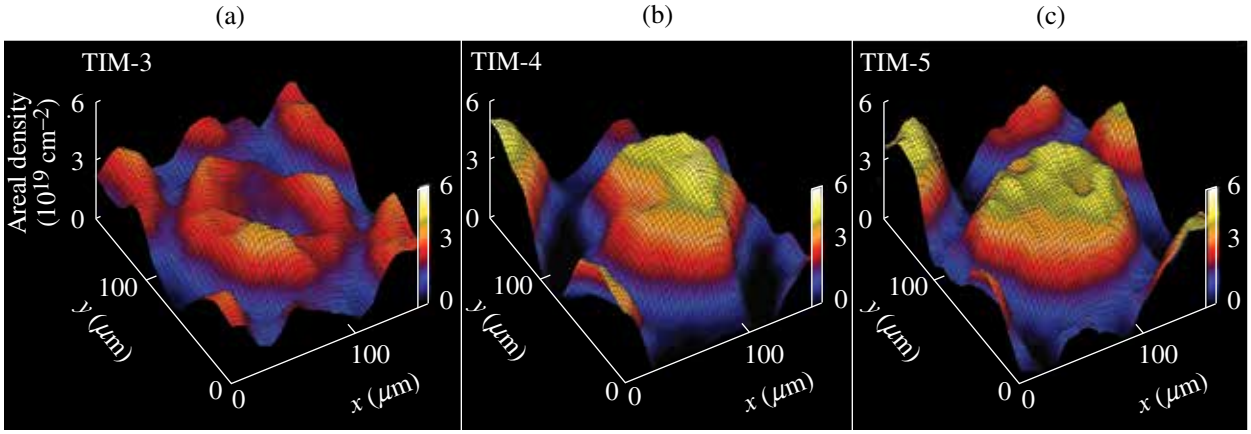

Figure 132.63
Areal-density surface plots extracted from the absorption signature of a Ti-doped tracer layer embedded in the plastic shell, initially located 3 μm from the shell's inner surface. The data were recorded on OMEGA shot 49953 with three identical MMI instruments mounted on TIM-3, TIM-4, and TIM-5. The x and y axes' ranges of the surface plots are from 0 μm to 160 μm, and the z-axis range is from 0 Ti-atoms/cm^2 to 8×10^{19} Ti-atoms/cm^2, or ~45 mg/cm^2 of plastic areal density. This areal density is due to only the compressed plastic of the Ti-doped tracer layer.

Another important aspect of the stability and symmetry of the implosion is the uniformity of the compression of the (unablated) shell confining the implosion core. In this connection, Fig. 132.63 shows areal-density surface plots extracted from the absorption signature of a Ti-doped plastic tracer layer embedded in the plastic shell, 1 μm thick with a 2% atomic concentration level and initially located 3 μm from the shell's inner surface. In this case, the absorption is due to 1s–2p line transitions in F- through He-like Ti ions that are backlit by continuum radiation coming from the hot spot in the core. The photon-energy range of these transitions spans the range from 4450 eV to 4750 eV. The data were recorded in OMEGA shot 49953 with three identical MMI instruments mounted on TIM-3, TIM-4, and TIM-5. We emphasize that this areal density is due to only the compressed plastic of the Ti-doped tracer layer and not the entire compressed shell. We also note that the areal-density maps are extracted in two different ways and checked against each other for consistency: on the one hand, from ratios of images based on the (attenuated) absorption feature and the (unattenuated) nearby continuum; on the other hand, from the analysis of sets of spatially resolved absorption spectra. The results displayed in Fig. 132.63 clearly show the modulations in areal density along a given LOS as well as the differences along different LOS. These results provide information about the stability and symmetry of the implosion.

Charged-Particle Probing of Inertial Confinement Fusion Implosions and High-Energy-Density Plasmas

Principal Investigators: R. D. Petrasso and C. K. Li (MIT)
Co-investigators: F. H. Séguin and J. A. Frenje (MIT); T. C. Sangster, V. Yu. Glebov, D. D. Meyerhofer, and R. Betti (LLE); and O. L. Landen (LLNL)

In FY12 MIT work included a wide range of experiments applying proton radiography, charged-particle spectrometry, and neutron spectrometry methods developed by MIT and collaborators to the study of high-energy-density physics (HEDP) and inertial confinement fusion (ICF) plasmas. Eighteen NLUF-related papers were published in FY12,[5–22] including four papers in Physical Review Letters,[5,10–12] and there were many invited talks and contributed talks at conferences. Our NLUF experiments also provided unique research opportunities in HEDP for eight MIT graduate students, who will use (or have already used) resultant data in major parts of their theses, and for several undergraduates.

Topics studied on the OMEGA[23] and OMEGA EP[24] lasers included the imaging, identification, and measurement of electric and magnetic fields generated in direct- and indirect-drive ICF plasmas[9,12,13,17,19,21] and other laser-generated plasmas;[7,9,10] Rayleigh–Taylor[7,10] and other[12,13] instabilities; the characterization of ICF capsule implosions;[8,11,13] ions accelerated by laser–plasma interactions;[6,8] plasma nuclear science;[5] and diagnostic development.[14–20,22] The work successfully addressed basic physics issues and issues directly relevant to the future success of ignition experiments at the National Ignition Facility (NIF) as well as general issues of importance to HEDP and the physics of fields generated by laser–plasma interactions.

As described in Physical Review Letters[10] and illustrated in Fig. 132.64, monoenergetic, charged-particle radiography[17,25] was used to make the first measurements of magnetic fields generated by Rayleigh–Taylor (RT) instabilities.[10] Experiments were performed using laser-irradiated plastic (CH) foils with pre-imposed surface perturbations to stimulate the instability at a known spatial wavelength. Path-integrated field measurements were compared directly with benchmarked hydrodynamic simulations, and it was shown that diffusion processes were necessary to explain the observations.[10] Figure 132.64(a) illustrates that RT-induced fields are generated near the ablation front, where local resistivity is high; therefore, magnetic fields of the measured strength, shown in Fig. 132.64(b), will have a minimal impact on thermal heat conduction. This evidence demonstrated for the first time that RT-induced magnetic fields do *not* significantly reduce heat conduction in directly driven targets until perturbation growth reaches the hotter, more-conductive region near the critical surface.[7]

Work described in Physical Review Letters[12] and illustrated in Fig. 132.65 provided novel physics insight into the effects of hohlraum fill gas on x-ray–driven implosions. The first time-gated proton radiography showing spatial structure and temporal evolution of fields and plasma in the hohlraum interior demonstrated that fill gas compresses wall blowoff, inhibits plasma jet formation, and impedes plasma stagnation. The important roles of spontaneously generated electric and magnetic fields in the hohlraum dynamics and capsule implosion were demonstrated. Interpenetration of blowoff and fill gas occurs as a result of the classical RT instability as the lighter, decelerating ionized fill gas pushes against the heavier, expanding gold wall blowoff. The results will have an important impact on the ongoing ignition experiments on the NIF.

Two other papers in Physical Review Letters[5,11] described important studies of basic nuclear physics and ICF dynamics. Neutron spectrometry was used to diagnose implosions of deuterium–tritium (DT)-gas–filled capsules on OMEGA. The neutron spectrum from the T(t,2n)^{4}He (*tt*) reaction was measured[5] and used to study the *tt* reaction in thermonuclear plasmas at low reactant center-of-mass (c.m.) energies. When compared to accelerator experiments at higher c.m. energies

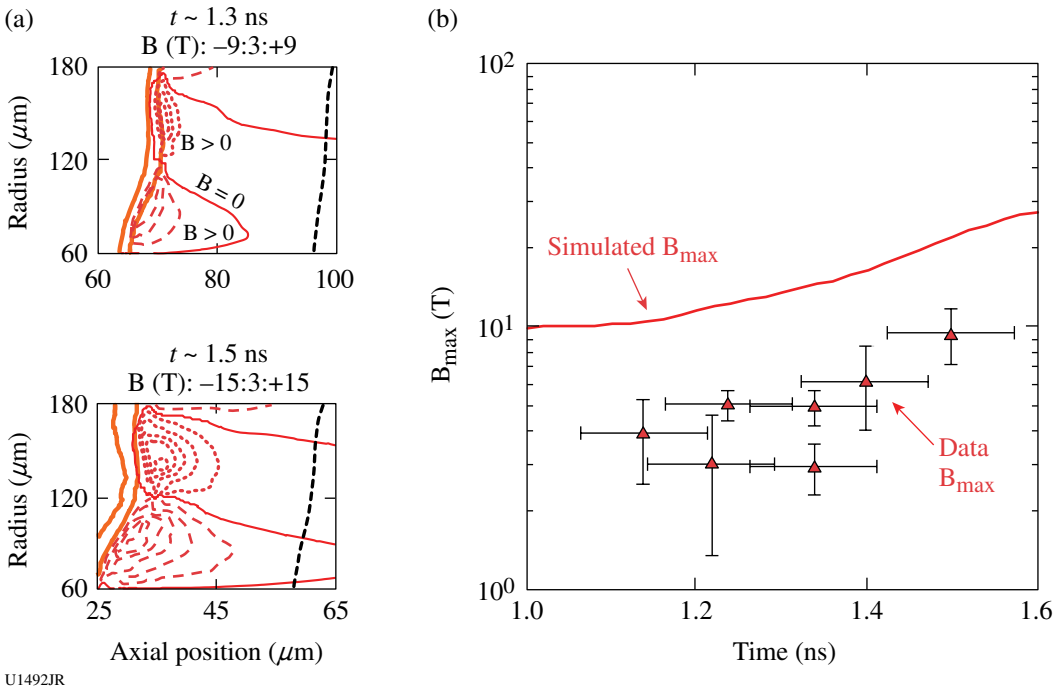

Figure 132.64
(a) Contour plots of magnetic fields from hydrodynamic simulations of a growing Rayleigh–Taylor instability in a laser-driven plastic foil that had machined grooves with a wavelength of 120 μm (thick solid orange). The times corresponding to the two plots are 1.3 and 1.5 ns during a 2-ns laser pulse. Magnetic-field contour levels are identified at the top of each plot and contours are indicated as follows: negative (into page) (red dots); positive (out of page) (red dashes); and zero contour (thin red solid line). Maximum field strength is clearly shown to occur near the ablation front, far from the hotter critical surface (short black dashes). (b) Comparison of measured and simulated peak magnetic fields. The factor of ~2 discrepancy is due to exclusion of collisional terms (diffusion) in the model. For more information, see Refs. 7 and 10.

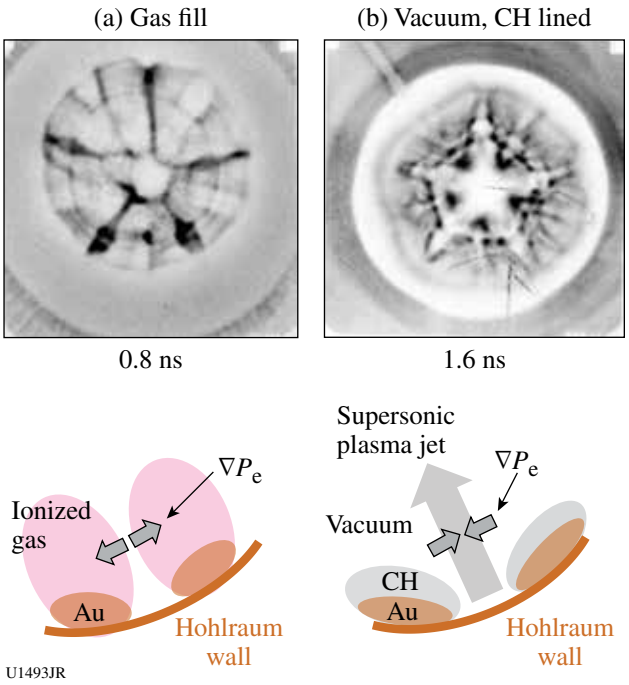

Figure 132.65
Some differences between plasma behavior in laser-driven hohlraums (a) with gas fill and (b) without gas fill but with a CH liner, shown by proton radiography images. The images were recorded during indirect-drive ICF experiments, looking down the hohlraum axis from a CR-39 detector toward a monoenergetic, 15-MeV proton backlighter. The proton fluence distributions in these images show a proton surplus in the regions between pairs of expanding plasma plumes in (a) a gas-filled, Au hohlraum but a proton deficit in (b) a CH-lined, vacuum Au hohlraum, indicating opposing directions of the self-generated electric fields as illustrated schematically by the corresponding cartoons. For details, see Ref. 12.

(above 100 keV), the results indicate an energy-dependent n + ^{5}He reaction channel branching ratio not previously recognized. In addition, D(d,p)T (*dd*) and T(t, 2n)^{4}He (*tt*) reaction yields were measured and compared[11] with those of the D(t,n)^{4}He (*dt*) reaction yield. Absolute spectral measurements of *dd* protons and *tt* neutrons were measured. It was concluded that the *dd* yield is anomalously low and the *tt* yield is anomalously high relative to the *dt* yield, an observation that we conjecture to be caused by a stratification of the fuel in the implosion core. This effect may be present in ignition experiments planned on the NIF.

Collisionless Shocks in Laboratory High-Energy-Density Plasmas

Principal Investigator: A. Spitkovsky (Princeton)
Co-investigators: L. Gargate (Princeton); H.-S. Park, B. A. Remington, S. Pollaine, and D. Ryutov (LLNL); J. P. Knauer, G. Fiksel, and R. Betti (LLE); Y. Sakawa, T. Ide, T. Kato, Y. Kuramitsu, T. Morita, and H. Takabe (Osaka University); T. Bell (University of Oxford); M. Koenig and A. Ravasio (Ecole Polytechnique); and E. Liang (Rice University)

This NLUF program studies the creation of collisionless shocks in counter-propagating laser-produced plasmas. Collisionless shocks are of great importance in astrophysical and space plasmas and occur when the mean free path to Coulomb collisions is large compared to the size of the shock transition. The shock is then mediated by collective plasma effects as the result of the interaction between plasma particles and the self-generated electromagnetic fields. Collisionless plasma conditions can now be created on OMEGA and OMEGA EP, where the laser-driven plasmas propagate at speeds of ~1000 km/s and densities of ~10^{18} to 10^{19} cm^{-3}. The experiments in this program collide two streams of high-speed plasma and study the formation of shocks as a function of an externally applied magnetic field that is generated by a set of Helmholtz coils at the interaction region (Fig. 132.66). The theoretical expectation is that at low external fields the shock is mediated by the filamentation (Weibel) instability, while at higher fields magnetic reflection of ions will form the shock. These regimes are representative of the conditions encountered in a range of astrophysical environments, including supernova remnant shocks and solar wind shocks. The experiments on OMEGA are testing these shock-formation mechanisms and addressing the open questions of astrophysical collisionless shock physics such as the presence of particle acceleration and the mechanisms of magnetic-field amplification in shocks.

In FY12, we performed shock experiments in a joint OMEGA/OMEGA EP shot day on 24 April 2012. In this experiment, we used the OMEGA laser to initiate two ablated plasma

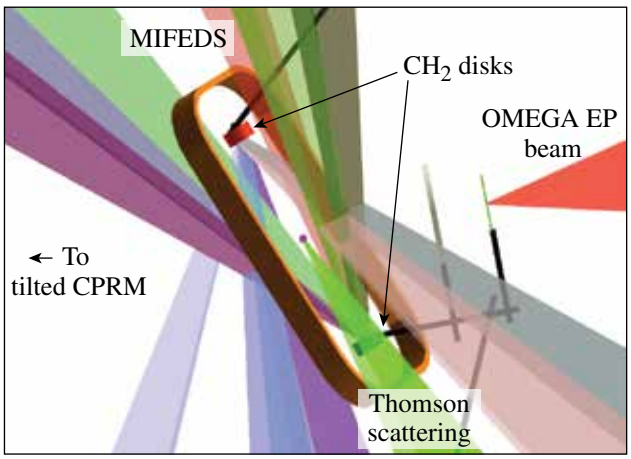

Figure 132.66
Diagram of the experimental setup for NLUF MagShock-12a.

flows from CH foils. OMEGA EP was used to provide a short pulse for proton radiography of the interaction region. The new configuration of the magnetic coil was fielded (fabricated by G. Fiksel's group at LLE). The new design used a single coil, which delivered a higher peak magnetic field of 5 T (compared to 1 T in 2011). The diagnostics included Thomson scattering and proton radiography (delivered by a short pulse from OMEGA EP). We moved the radiochromic film pack (CPRM) closer to the target to obtain a wider field of view than in 2011. We performed seven shots (five joint) and are very thankful to the facility for providing outstanding support during this challenging experiment.

We studied the Thomson signal and proton images as a function of the external magnetic field and tried several time offsets for diagnostics to build a time series. The Thomson signal was fairly insensitive to the magnetic field. The proton signal showed characteristic filamentation that we observed in 2011. It is important that this signal is reproducible. The field had a moderate effect on the early time signal [Figs. 132.67(a) and 132.68(a)]. Analysis of later snapshots (5 ns) is still continuing and requires additional shots to completely fill out the time series. This will be performed in 2013.

We modeled the proton signal using particle-in-cell (PIC) simulations. We concentrated on the unmagnetized 3-D PIC simulations of interpenetrating flows, tracing orbits of test protons through the simulation domain to accumulate proton images. The results (Fig. 132.69) show that we can reproduce main features of the interaction–turbulent ripples with horizon-

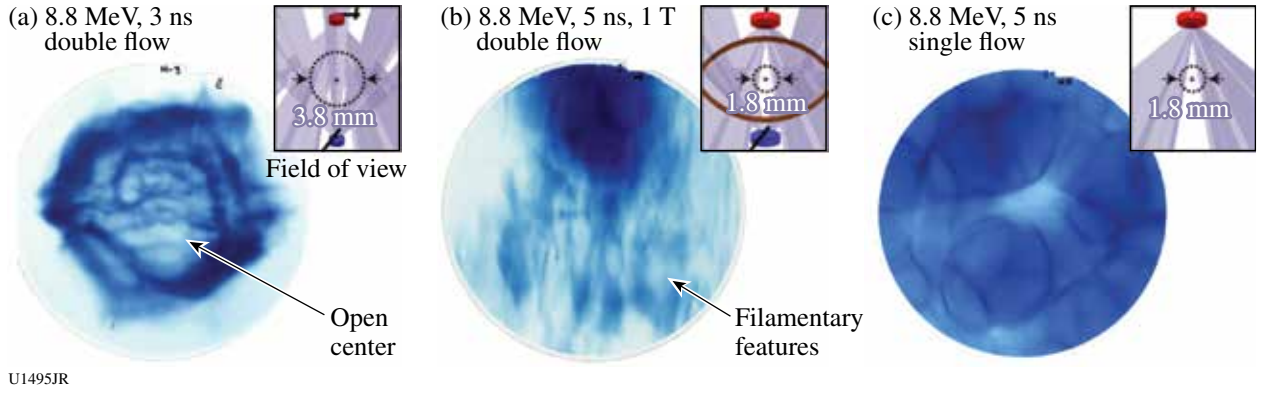

Figure 132.67
Proton images of plasma flows with little or no external magnetic field. (a) 3-ns counter-streaming flows, (b) 5-ns counter-streaming flows, and (c) 5-ns single-plasma flow. Insets: experimental configuration and proton-image field of view.

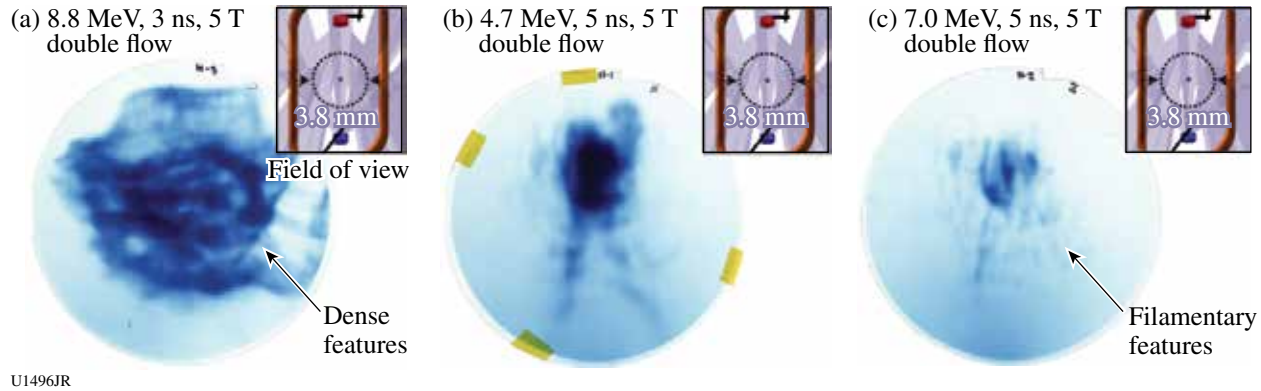

Figure 132.68
Proton images of counter-streaming plasma flows with a moderately strong external B field of 5 T. Both foils are illuminated. (a) 3 ns with 8.8-MeV protons, (b) 5 ns with 4.7-MeV protons, and (c) 5 ns with 7.0-MeV protons. Insets: experimental configuration and proton-image field of view.

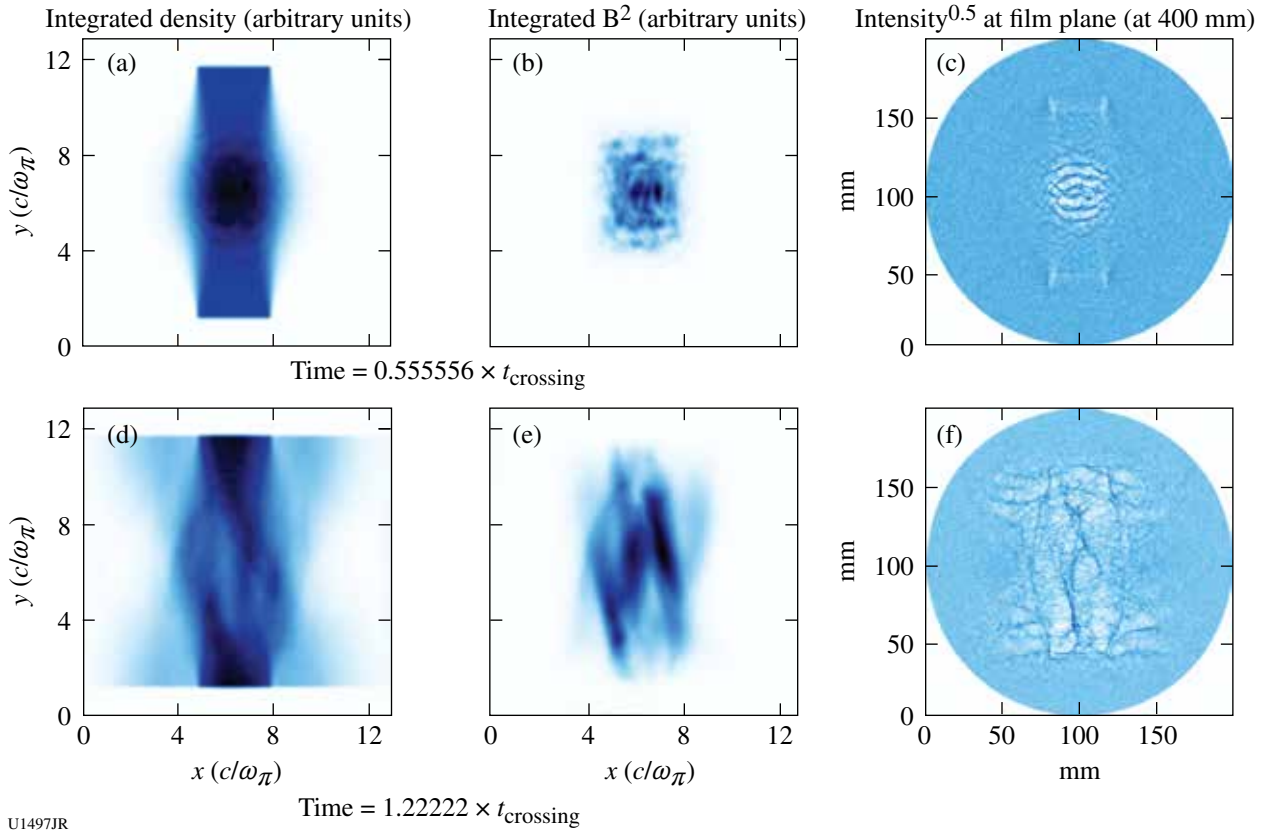

Figure 132.69
Simulated proton imaging using PIC simulations. Plasmas collide along the *y* axis. [(a),(d)] Time evolution of the integrated density and [(b),(e)] magnetic-energy profiles. [(c),(f)] Simulated proton imaging signal as collected on the film plate 400 mm from the proton source. These images show horizontal and bubble-like features at early times and filamentary features at late times. The field of view in (c) is 2× larger than in (f).

tal features at early times and longitudinal filaments at later times. The ripples are caused by electrostatic fields that are created in the first moments of collision, while the later filaments are driven by the magnetic field from the Weibel instability. We are currently exploring how the flow parameters can be better approximated in the simulation and checking whether any of the structures observed in the experiment are a result of electrostatic shocks.

We developed a suite of post-processing diagnostics for the PIC simulation code that allows us to calculate Thomson and radiography signals based on the full distribution function from the simulations. Preliminary analysis of the data and PIC simulations indicates that the next experiment in this program in FY12 will require stronger magnetic fields. The design work on increasing the magnetized inertial fusion energy delivery system (MIFEDS) magnetic fields is currently underway, and we expect another increase by a factor of 2 after the upgrade of MIFEDS.

This NLUF research has been reported in three peer-reviewed publications,[26–28] five invited papers,[29–33] and one contributed paper.[34]

Investigation of Laser-to-Electron Energy Coupling Dependence on Laser Pulse Duration and Materials Composition

Principal Investigators: M. S. Wei and R. B. Stephens (General Atomics)
Co-investigators: F. N. Beg, R. Mishra, H. Sawada, L. C. Jarrott, and J. Peebles (University of California, San Diego); H. McLean and P. Patel (LLNL); W. Theobald and C. Stoeckl (LLE); and Y. Sentoku (University of Nevada, Reno)
Lead graduate student: A. Sorokovikova (University of California, San Diego)

Efficient conversion of laser energy to fast electrons (1 to 3 MeV) and their subsequent energy transport to the compressed fuel are extremely important for the success of fast ignition.

Energy coupling is controlled by the nature of the plasma (i.e., density profile, ionization, etc.) at the laser–plasma-interaction (LPI) interface and the dynamic response of the transport material, which both evolve with time, therefore dependent on laser pulse length. For full-scale fast ignition, the high-intensity ignitor pulse duration will be of the order of 10 ps. So far, most of the electron source and transport studies have been limited to subpicosecond pulses with energies ~100 J. The goal of the General Atomics NLUF project is to extend such investigation to fast-ignition (FI)–relevant pulse durations using the high-energy (>1-kJ) OMEGA EP laser. In this second-year NLUF experiment in FY12, our study is focused on the effect of the laser pulse length on LPI and fast-electron source generation and the transport by systematically varying laser pulse duration from 0.7 ps up to 10 ps at a constant laser intensity and using identical multilayered planar-foil targets. Figure 132.70 shows the schematics of the target and experimental setup on the OMEGA EP laser. The planar multilayered foil targets consist of an Al substrate with a Cu x-ray tracer layer (20 μm thick) buried ~100 μm below the front surface and a large, thick (5-mm × 5-mm × 1-mm) conductive carbon layer at the back to minimize fast-electron refluxing. The OMEGA EP backlighter beam was normally incident onto the front target surface. The beam was tightly focused with a spot radius of ~20 μm within which contained 80% of the laser energy. The experiment was performed with identical targets at the same laser intensity ($I_{peak} \sim 2 \times 10^{19}$ W/cm^2) for three different laser pulse lengths, i.e., 0.7 ps, 3 ps, and 10 ps, with main pulse energies of 100 to 150 J, 400 J, and 1500 J, and prepulse energies of 5 mJ, 16 mJ, and 110 mJ, respectively. Fast electrons were characterized by the induced K-shell fluorescence from the Cu tracer layer and high-energy bremsstrahlung x rays from the whole target. Two-dimensional Cu K_α spot and the total K_α yield were measured with a spherical quartz crystal imager (SCI) and a calibrated x-ray spectrometer using a highly oriented pyrolytic graphite (HOPG) diffraction crystal, and the high-energy bremsstrahlung spectrum was monitored at two angles behind the targets with two fixed-port bremsstrahlung MeV x-ray spectrometers (BMXS), which were recently implemented in the OMEGA EP chamber by the PI and project team.

The measured bremsstrahlung spectrum data suggest a hotter energy distribution in the 10-ps interaction case. Figure 132.71 shows the inferred fast-electron temperature from the Monte Carlo modeling analysis fitting a synthetic electron energy distribution (one temperature exponential) to the measured bremsstrahlung spectrum. The slope temperature increased by a factor of 2, i.e., ~1.5 MeV in 10-ps LPI compared to 0.7 MeV in the 0.7-ps case. The 2-D Cu K_α images (Fig. 132.72) showed a large change in LPI-produced electron-beam spatial distribution with increasing laser pulse duration. The fast-electron beam evolved from a single beam with a beam spot size of about 160 μm in a subpicosecond interaction into multiple narrow (~70-μm) filaments over a 10-ps pulse dura-

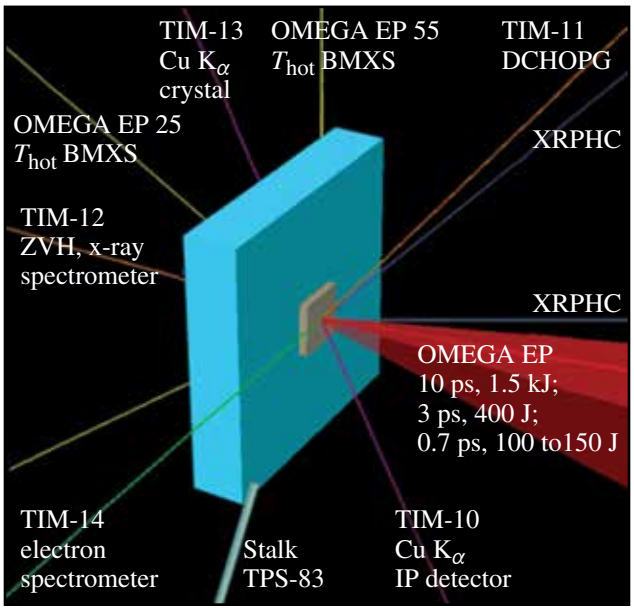

U1498JR

Figure 132.70
Schematic of the experimental setup.

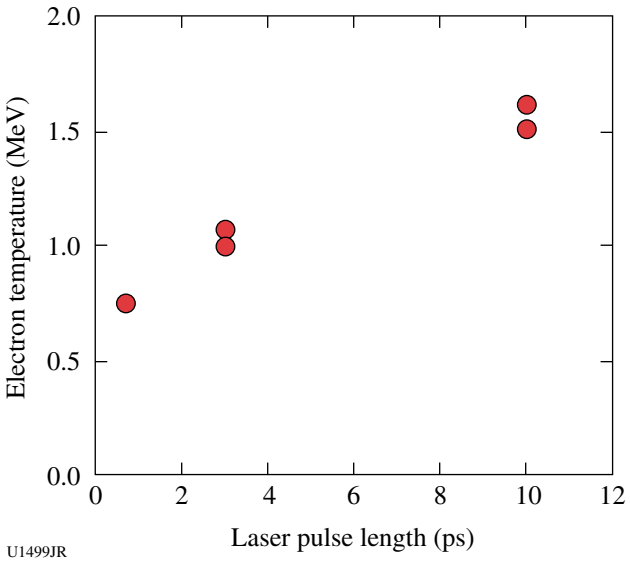

U1499JR

Figure 132.71
Inferred fast-electrons' energy spectrum slope temperature from the measured bremsstrahlung spectrum data.

tion. The very large angular separation (~45°) between these distinct filaments in the 10-ps case is quite unusual, indicating a significant deviation of energy flow directions from the original laser propagation axis. The observed new phenomena such as hotter energy distributions and multiple widely separated filaments can be caused by the presence of an extended pre-plasma in the 10-ps case. It is well known that LPI in a longer pre-plasma can produce fast electrons with a hotter electron spectrum as the result of stochastic heating. Extended pre-plasmas can also result in strong nonlinear LPI processes such as filamentation, hole boring, and hosing instabilities, which can develop over a longer pulse duration leading to the formation of widely separated electron-beam filaments. Preliminary collisional particle-in-cell (PIC) simulations to examine LPI and fast-electron generation over 2 ps using the PICLS (PIC simulations for large-scale plasmas) code have suggested that these widely separated electron filaments could be initiated by the filamented and self-focused laser beam [Fig. 132.73(a)] in the long-scale-length pre-plasma, injecting electrons into solid plasmas at particular angles. These electron filaments could be further pinched by self-generated resistive magnetic fields inside the high-density plasmas as shown in Figs. 132.73(b)

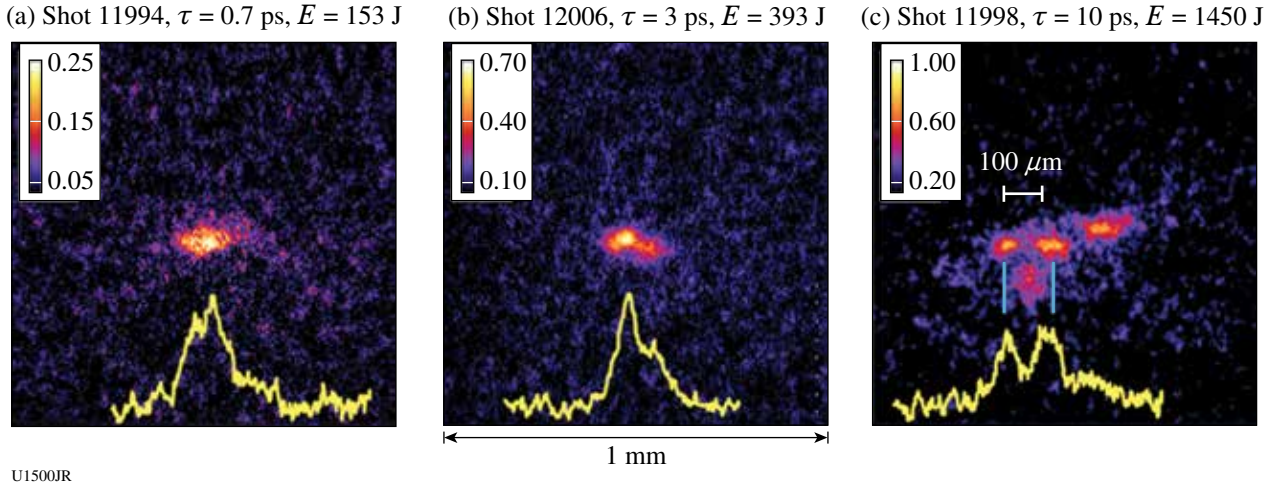

Figure 132.72
Cu K_α fluorescence images showing a fast-electron beam cross section ~100 μm below the generating point using a laser pulse of (a) 0.7 ps, 153 J, (b) 3 ps, 393 J, and (c) 10 ps, 1450 J in the OMEGA EP experiment. All images are to the same spatial scale and compressed vertically because of the view angle. The yellow lines at the bottom of each image are plots of the pixel intensity along a horizontal line through the points.

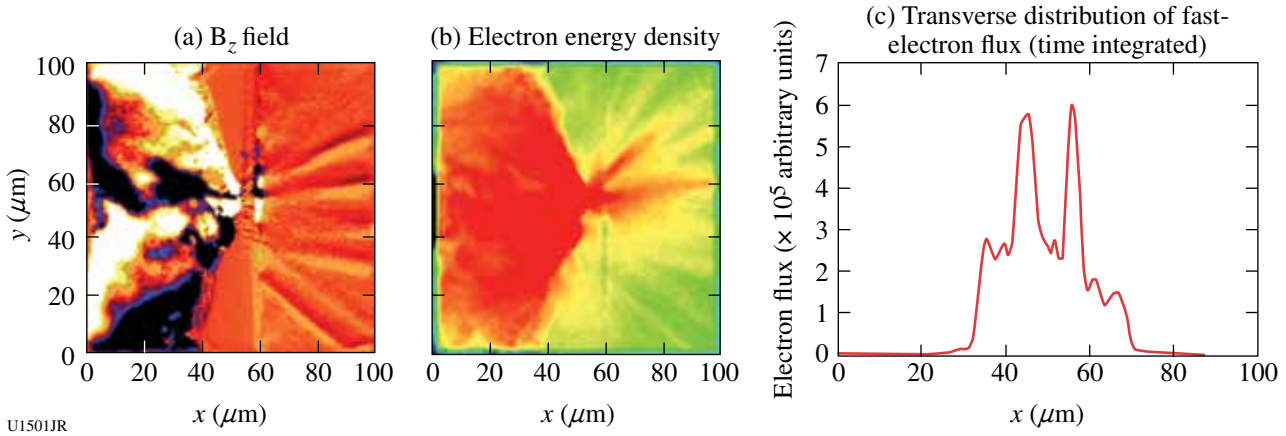

Figure 132.73
Preliminary 2-D PIC modeling results of LPI and fast-electron generation over a 2-ps pulse duration. The semi-infinite high-intensity laser with a focal-spot size of 30 μm rises to peak intensity (10^{20} W/cm^2) in 330 fs and stays constant. The target is a planar Al slab with a pre-plasma (8-μm density scale length) in front of the solid Al. (a) Quasi-static azimuthal B_z field; (b) electron energy density at 2 ps; and (c) the transverse profile of the time-integrated fast-electron flux taken in a 2-μm-thick, 100-μm-wide sampling box at x = 65 μm.

and 132.73(c). Although this simulation was performed with a much higher laser intensity, the pre-plasma scale length is of a similar order as that in our experiment and the observed phenomena may be applicable to the observed electron filaments in our experiment. Simulations with the realistic laser and pre-plasma parameters are underway, which will examine the dependence of beam filaments on pre-plasma scale length and pulse duration.

In summary, the FY12 GA-led NLUF experiment has systematically investigated the dynamics of the LPI-produced fast-electron source generation and transport from subpicosecond to over 10-ps pulse durations. We observed formation of multiple electron filaments in LPI with a longer scale length of pre-plasma over 10 ps. Future experiments using the newly available ultrahigh-contrast OMEGA EP pulses are planned to further examine the LPI and electron-beam dynamics in an initially pre-plasma free condition to help identify the roles of the pre-plasma and pulse length on the laser filaments and resistive beam filamentation.

Intense Laser Interactions with Low-Density Plasma Using OMEGA EP

Principal Investigator: L. Willingale, C. Zulick, A. G. R. Thomas, A. Maksimchuk, and K. Krushelnick (University of Michigan); P. M. Nilson, R. S. Craxton, C. Stoeckl, V. Yu. Glebov, and T. C. Sangster (LLE); H. Chen (LLNL); J. Cobble (LANL); and P. Norreys (RAL)

The study of high-intensity laser interactions with low-density plasma is of interest to many phenomena such as channeling,[35] electron and ion acceleration, and neutron and x-ray production. The focus of the low-density plasma campaign this year has been to investigate electron acceleration and neutron production. To generate an underdense target, a long-pulse beam (2.5 ns, ~1200 J in an 800-μm-diam focal spot) is used to create a plasma plume from a plastic-foil target. The main interaction beam is then focused into the plasma plume, with the laser propagating parallel to the target surface so that it sees an approximately Gaussian density profile (2-D *SAGE* modeling estimates the plasma-density profile).

Electron spectra along the laser axis were measured using the electron positron proton spectrometer (EPPS). High-energy electrons with an effective beam temperature many times greater than the ponderomotive potential were measured under several different laser pulse-length and energy conditions. Since the channels are almost completely cavitated at OMEGA EP laser intensities, a plasma wakefield cannot be responsible for the electron acceleration. Instead, particle-in-cell simulations indicate that a direct laser acceleration (DLA) mechanism is responsible.[36] For the electrons to be accelerated via DLA, they must be injected into the cavitated channel with some initial momentum. Based on proton probe data showing the channel formation, periodic modulations are observed at the channel wall [Fig. 132.74(d)], which are consistent with surface wave formation. Particle-in-cell simulations indicate the surface waves can act as the required injection mechanism for DLA.[37]

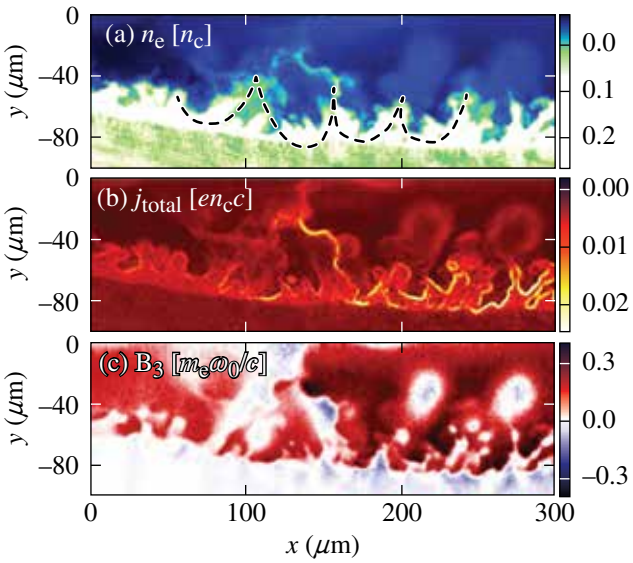

(d) Experimental proton probe image of the channel

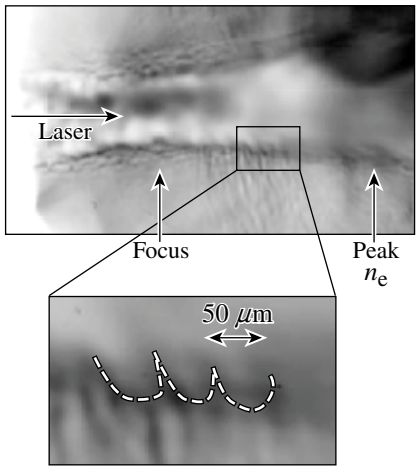

U1502JR

Figure 132.74
Particle-in-cell simulation data showing the modulations in the channel wall region in (a) electron density, (b) the total current, and (c) the transverse magnetic field. (d) Experimental proton probe image of the channel wall illustrating the periodic modulations.

Figures 132.74(a)–132.74(c) show simulation data illustrating the surface wave modulation that has been driven in the channel walls. High-temperature electron spectra are also observed in the simulations.

The shape of the neutron spectra from underdense plasma interactions can enable us to estimate the ion heating within the channel.[38] For the neutron-production experiment, deuterated polyethylene (CD_2) targets were used instead of the regular CH_2 targets. To measure the neutrons, a time-of-flight scintillator diagnostic that was gated using a microchannel plate to reduce the signal from the prompt gamma flash. Simultaneously, the transverse ion spectrum was measured using the Thomson parabola ion spectrometer (TPIE). Figure 132.75(a) shows an example of a time-of-flight trace and indicates the main features. Figure 132.75(b) shows the uncalibrated neutron spectra comparing the signal from CH and CD plasma at the same plasma density and under the same laser conditions. The residual signal from the prompt γ flash means that it is not possible to measure neutrons with energies >12 MeV. A plasma density scan was also performed and indicated higher neutron yield for higher plasma density as would be expected [shown in Fig. 132.75(c)]. Analysis is underway to address calibration and saturation effects for the neutron diagnostic so that comparison with the measured ion spectra and qualitative conclusions can be made.

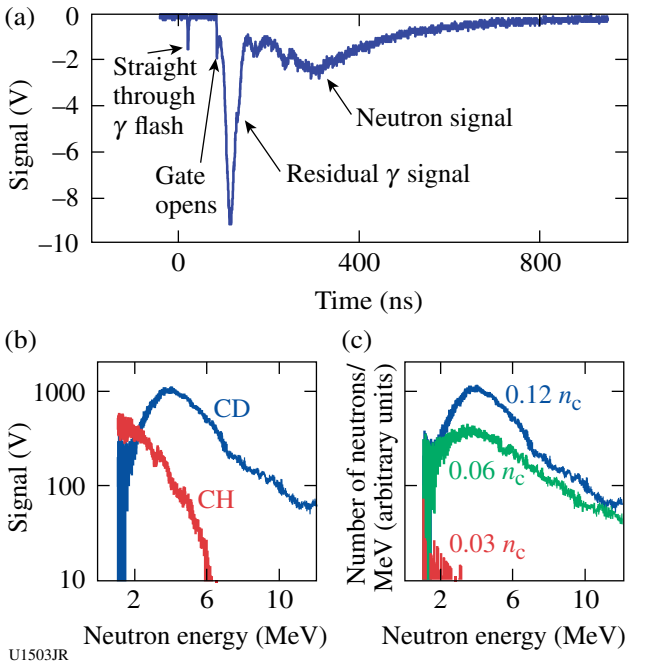

Figure 132.75
(a) Time-of-flight trace showing the main features of the signal. Uncalibrated, preliminary neutron spectra comparing (b) CH with CD plasma shots and (c) different peak CD plasma density shots.

The authors gratefully acknowledge the *OSIRIS* consortium for the use of the *OSIRIS* 2.0 code.

FY12 Laboratory Basic Science Programs

In FY12, LLE issued a solicitation for LBS proposals to be conducted in FY13. A total of 32 proposals were submitted. An independent review committee reviewed the proposals and recommended that 16 proposals receive 28 shot days at the Omega Laser Facility in FY13. Table 132.VIII lists the successful LBS proposals.

Fifteen LBS projects were allotted Omega Facility shot time and conducted a total of 273 target shots at the facility in FY12. This work is summarized in this section.

Measurements of the Viscosity of Shock-Compressed Fluids: Studies of Water and Silica

Principal Investigators: P. M. Celliers and M. A. Barrios (LLNL)

This is the second in a series of experiments that aims to demonstrate a method for determining the viscosity of a high-pressure fluid created by the propagation of a strong shock front through an initially transparent sample. The measurement technique is based on observing the evolution of a spectrum of perturbations imposed on a multi-Mbar shock front passing through the sample material. The viscosity of the liquid state just behind the shock front is expected to influence the decay rate of the perturbations as the shock front propagates; detailed measurements of the perturbation state can be compared with calculations to assess the viscosity. The sample under study is liquid silica (SiO_2), produced by propagating the shock through samples of either alpha-quartz or fused silica. The viscosity of high-pressure liquid silica has obvious geophysical relevance, and measurements in the Mbar domain are impossible with conventional methods. An earlier campaign in 2010 examined the shock response to a perturbation spectrum that was generated by an etched array of shallow pits a few microns deep and 10 μm in diameter that were created on the sample surface at the interface with the ablator. The 2012 campaigns examined the response to a random distribution of surface perturbations generated by roughening the silica surface with a grinding technique. Initial experiments in October 2011 used the active shock breakout (ASBO)/streaked optical pyrometer (SOP) to perform hohlraum drive characterization measurements in preparation

Table 132.VIII: Approved FY13 LBS proposals.

Principal Investigator	Affiliation	Project Title
P. M. Celliers	LLNL	Equation of State and Optical Properties of Dense Silica: Shock Study of Coesite and Stishovite
H. Chen	LLNL	Exploring Pair Plasma and Their Applications Using OMEGA EP
J. R. Davies	LLE	Fast-Electron Control with Magnetic Field in Hohlraum
J. H. Eggert	LLNL	HED Condensed Matter: Magnesium and Aluminum
G. Fiksel	LLE	Magnetic Reconnection and Particle Energization in High-Energy-Density Plasmas in the Presence of an External Magnetic Field
G. Fiksel	LLE	Magnetized ICF Implosions on OMEGA
R. F. Heeter	LLNL	"Gattling Gun" Long-Duration Radiation Sources on OMEGA EP for Sustained-Drive Hydrodynamics and Low-Density Atomic Physics Applications on OMEGA EP and the NIF
B. R. Maddox	LLNL	Direct Measurements of Dislocation-Based Plastic Flow in Quasi-Isentropically Compressed bcc Metals
H.-S. Park	LLNL	Astrophysical Collisionless Shock Generation by Laser-Driven Experiments
P. K. Patel	LLNL	Areal-Density Measurements of Cone-in-Shell Implosions Using Compton Radiography for Fast Ignition
Y. Ping	LLNL	Long-Term Dynamics of Hole Boring and Target Heating at Fast-Ignition-Relevant Conditions
S. P. Regan	LLE	Collective X-Ray Scattering from Shocked Liquid Deuterium
J. R. Rygg	LLNL	Extreme Chemistry, Equation of State, and Optical Properties of Dense Water at Terapascal Pressure
A. A. Solodov	LLE	Fast-Ignition Integrated Experiments with Low-Z Cone-Tip Targets
C. Stoeckl	LLNL	Spectroscopy of Neutrons Generated Through Nuclear Reactions with Light Ions in Short-Pulse Laser-Interaction Experiments
W. Theobald	LLE	Laser Channeling in Long-Scale-Length, Overdense Plasmas

for the rippled shock measurements carried out in May 2012. The second campaign in May used the OMEGA high-resolution velocimeter (OHRV) to observe the velocity perturbations directly on the surface of the reflecting shock front.

The shocks were driven using a hohlraum coupled to a 50-μm poly(methylmethacrylate) (PMMA) ablator followed by the sample. As the shock passed through this interface, the perturbations were transferred to the shock front, which were detected and measured quantitatively by the OHRV. An example of a 2-D velocity spectrum recorded on these experiments is shown in Fig. 132.76. Examples of averaged velocity spectra for ~170-GPa shocks driven into fused silica are shown in Fig. 132.77, along with model calculations of the expected velocity spectra assuming a viscosity of 35 poise. The model calculations employ an analytical expression derived by Miller and Ahrens.[39] Detailed analysis of these data is at a preliminary stage; the goal is to fit the data set to the analytical model in order to estimate the viscosity. Initial indications suggest that the viscosity is in the range of a few poise to tens of poise.

Exploring Pair Plasma and Its Applications Using OMEGA and OMEGA EP

Principal Investigator: H. Chen (LLNL)

In FY12, an LLNL/LLE team performed a Laboratory Basic Science (LBS) experiment on OMEGA EP to study positron production during high-intensity laser interactions with high-Z targets. This experiment was a follow-up on to those of 2010 and 2011. In the previous experiments, a record number of positrons were produced using the 1-kJ, 10-ps OMEGA EP backlighter interacting with a 1-mm-thick Au target.[40] It was deduced that a non-neutral pair plasma was made in those shots.[41] In FY11, the laser energy was extended to 1400 J for the backlighter beam, and a seemingly faster increase in positron number was observed once the laser energy exceeded 1 kJ. In

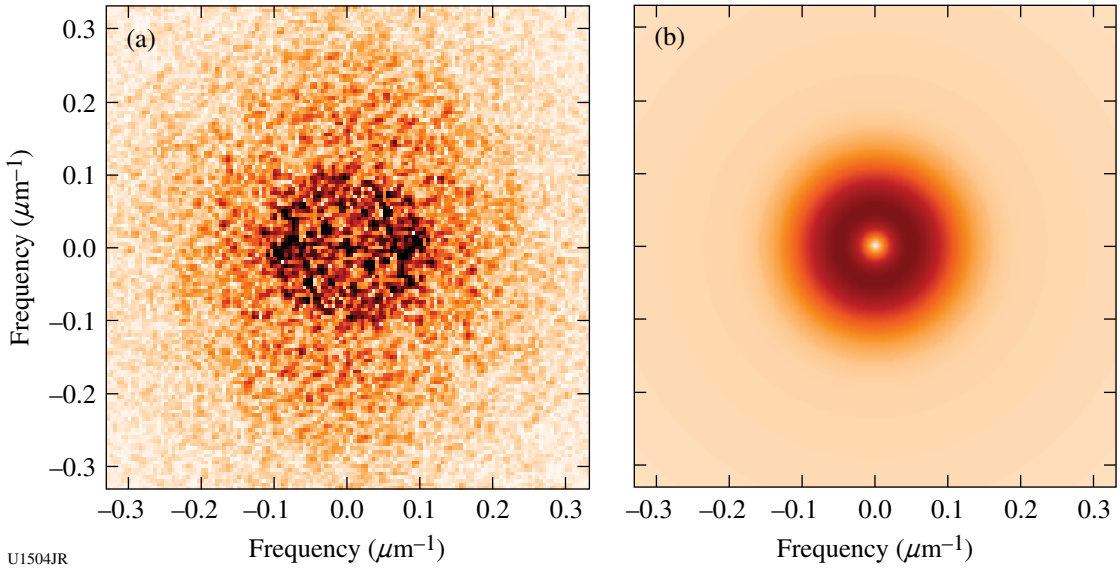

Figure 132.76
(a) An example of a 2-D velocity spectrum on a rippled shock front generated at a roughened interface between a PMMA ablator and a fused-silica sample recorded 650 ps after the passage of the shock through the interface (shot 66008). The gray scale is proportional to mode amplitude. (b) A velocity spectrum computed for similar conditions as in the experiment using the analytical expression provided in Ref. 39.

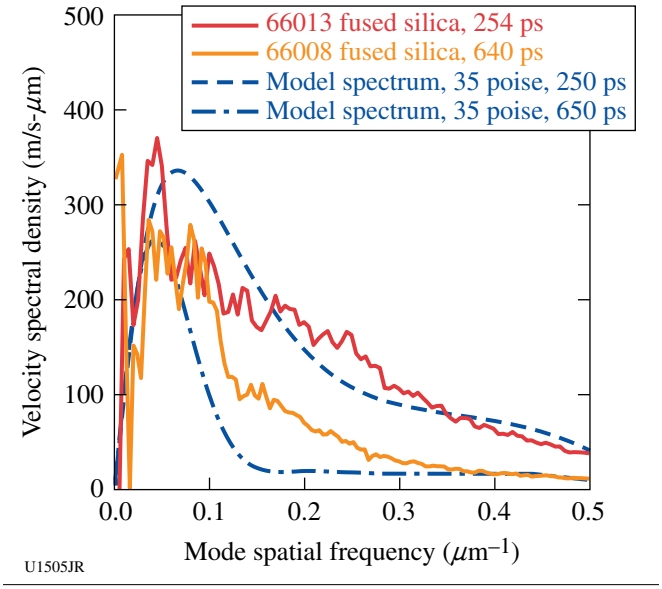

Figure 132.77
Averaged velocity spectra for ~170-GPa shocks in fused silica recorded at 250 ps and 650 ps after passing through the interface, compared with calculations of the expected spectra assuming 35-poise viscosity. More precise fits to the model are in progress.

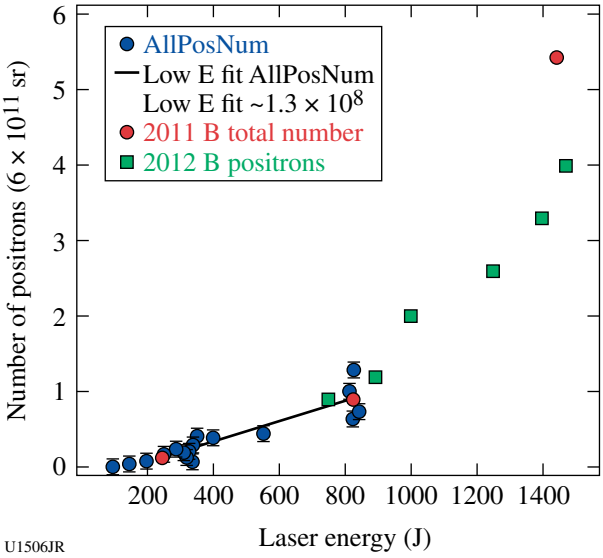

Figure 132.78
Positron yield is nonlinear at higher laser energies (green squares) in 2012B, confirming the conclusion from previous OMEGA EP experiments.

FY12, we carried out systematic experiments to confirm this finding. The preliminary results are shown in Figs. 132.78 and 132.79. At a higher laser-contrast condition (10^9 versus 10^7 in FY11), the positron scaling remains "nonlinear" at laser energies greater than 1000 J. The effect of laser contrast to fast electrons and positrons was also observed. Further data analysis is in progress to evaluate the laser–electron conversion efficiency as a result of enhanced contrast. Positron research extends over diverse fields ranging from particle physics and astrophysics to medical application. This often requires the production of

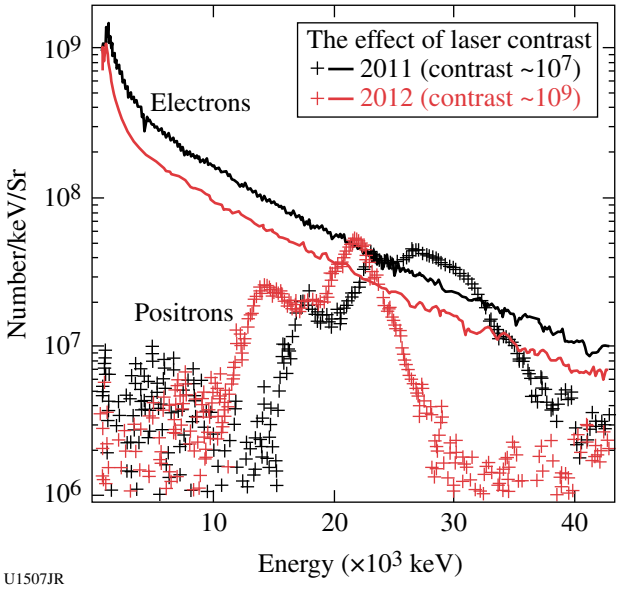

Figure 132.79
Fewer electrons were made in 2012B apparently due to a higher contrast laser condition, resulting in fewer and lower-energy positrons.

large numbers of positrons on a short time scale, which has been difficult to supply. The new OMEGA EP results could alter the direction of the quest to establish a laser-produced positron source for research in these fields.

Magnetic-Field Compression in Spherical Implosions on OMEGA

Principal Investigators: G. Fiksel, M. Hohenberger, J. P. Knauer, and P.-Y. Chang (LLE); R. Betti, K. S. Anderson, and J. R. Davies (FSC/LLE); and F. H. Séguin (MIT)

Project objective: The main goal of the experiments was to measure the compressed magnetic field in spherically imploded targets embedded in an externally generated seed field. These experiments will establish the scientific basis for magnetizing high-energy-density (HED) plasmas and enhancing the performance of inertial fusion implosions through the use of magnetic fields.

Experimental setup: The experimental setup is illustrated in Fig. 132.80. A spherical CH target is embedded in a seed magnetic field generated by a single-loop coil powered by the magnetized inertial fusion energy delivery system (MIFEDS) generator. The target is then imploded by 40 OMEGA beams with a square 1-ns pulse at maximum power. The shell is filled with 5 atm of deuterium gas. The shell's outer diameter is 860 μm, and the shell's thickness is 24 μm. The compressed magnetic field will be measured by the proton radiography

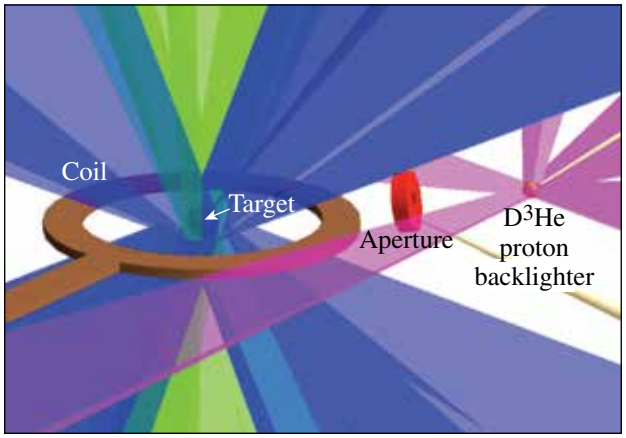

Figure 132.80
Experimental setup to measure magnetic-field compression.

technique. The 14.7-MeV fusion protons, used to radiograph the compressed core and field, are produced by the D + ^{3}He fusion reactions from an imploding glass microballoon filled with an 18-atm D^{3}He gas mix. The implosion of the proton backlighter is driven by ten OMEGA beams. The protons are recorded on a CR-39 nuclear track detector stack that allows for both spatial and energy resolution (via the track diameter) of the particles incident on the surface. The backlighter implosion can be timed so the backlighter proton beam passes through the target at the desired time of peak compression (e.g., "bang" time).

Preliminary results and future plans: Despite good laser performance and excellent MIFEDS operations, the obtained proton radiography images did not indicate the presence of deflected fast protons. After analyzing the results, a conclusion was made that the fast-proton fluence was too low and because the compressed magnetized spot has a diameter of less than 20 μm, the number of deflected protons was low as well, comparable to the background noise level of the CR39 detectors. In future experiments we plan to use fast protons generated from the interaction of OMEGA EP with a thin metal foil. The OMEGA EP–generated fast-proton fluence is at least three orders of magnitude higher than that from the D^{3}He source.

Magnetic Reconnection in High-Energy-Density Plasmas in the Presence of an External Magnetic Field

Principal Investigators: G. Fiksel and P. M. Nilson (LLE); and W. Fox and A. Bhattacharjee (University of New Hampshire)

Project objectives: The primary goals for the magnetic-reconnection experiments are to (1) demonstrate that an

extended reconnection current sheet can be formed in the gap between two laser-irradiated foils by the collision of the high-conductivity blowoff plasmas, (2) show that this interaction can be well diagnosed using proton radiography and x-ray imaging, and (3) observe basic properties of the reconnection, such as inflow and outflow rates, the geometry of the current sheet, and the magnitude of the magnetic field in the current sheet.

Experimental setup: Figure 132.81 shows a simplified diagram of the experiment on OMEGA EP. The experiment was carried out in close collaboration with the computational plasma physics group at the University of New Hampshire. This group has recently conducted particle simulations of reconnection in LLE and Rutherford (UK) laser-driven reconnection experiments.

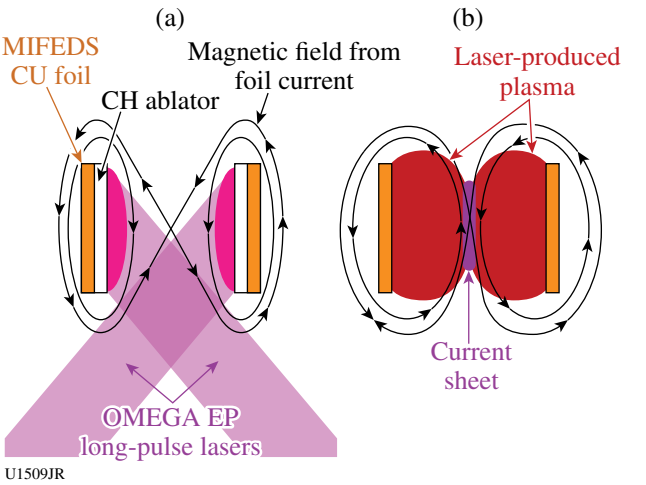

Figure 132.81
A simplified diagram of the proposed reconnection experiments. (a) Laser-driven plasma blowoff drives the collision of two magnetized plasma flows and reconnection of the (b) seed magnetic fields from the MIFEDS current generator.

For the first series of shots (5 September 2012) the magnetic coils were not energized. The main goal of that experiment was to establish proper parameters of the drive lasers and investigate the dynamics of the colliding plasmas with the proton radiography diagnostic. The actual experimental setup is shown in Fig. 132.82.

Preliminary results and future plans: One of the proton images of the colliding plasma interface is shown in Fig. 132.83. The result indicates the presence of a long-lived, self-organized structure similar to what was recently described in a Nature Physics publication.[26] A new series of experiments on characterization of the reconnection magnetic field and particle energization is planned.

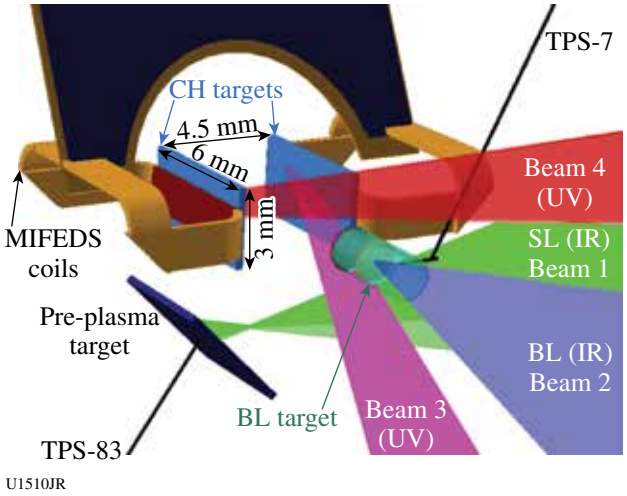

Figure 132.82
The experimental setup showing MIFEDS coils with the support structure and the attached CH targets. The colliding plasmas are generated with 1.8-kJ, 2-ns OMEGA EP Beams 3 and 4. The proton backlighter beam is generated by the 800-J, 10-ps OMEGA EP Beam 2. The protons are detected with a radiochromic film (RCF)-based detector situated 8 cm away from the target. Also shown is a target for prefilling the intercoil region with pre-plasma.

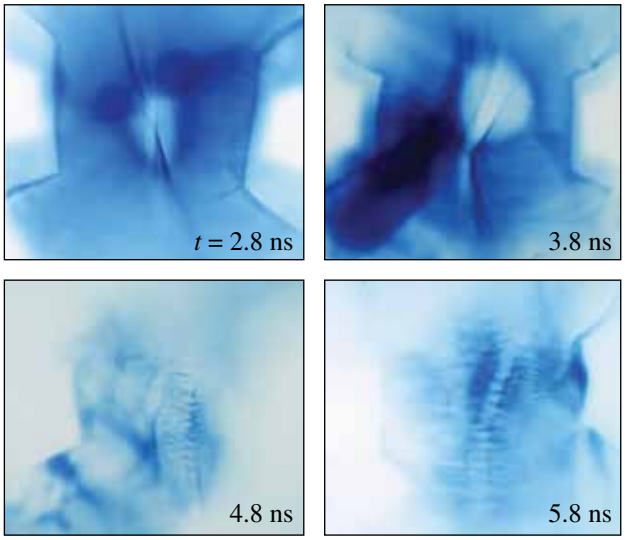

Figure 132.83
A series of images of the colliding plasmas obtained with the proton radiography diagnostic.

Measurements of Linear, Nonlinear, and Turbulent Mixing Regimes in Kelvin–Helmholtz Instability in the Subsonic Regime

Principal Investigators: O. A. Hurricane and V. A. Smalyuk (LLNL)

A Kelvin–Helmholtz (KH) growth experiment was performed using a platform successfully developed in earlier OMEGA experiments.[42–44] Figure 132.84 shows a target schematic that consists of a plastic ablator and a shock tube. In the shock tube the interface between low-density foam and high-density plastic was either flat or had pre-imposed sinusoidal modulation at a 400-μm wavelength and a 30-μm amplitude, as in previous experiments. The central part of the plastic target contained a layer of I-doped CH to increase the contrast to 5-keV backlighter x rays. The ablator of the target was directly driven with laser light, producing a strong shock that propagated through the target. The shock produced a velocity gradient at the interface between foam and plastic. This velocity difference between two materials resulted in the KH growth of the surface modulations. The density of foam was 100 mg/cm^3. Previous experiments detected a mixing layer development caused by the growth of 3-D, short-scale modulations in addition to pre-imposed, 2-D, 400-μm-wavelength modulations. New experiments performed with flat CH–foam interfaces were aimed at measurements of 3-D turbulent mixing since in previous experiments the growth of large 400-μm-wavelength modulations could have modified the growth of 3-D, short-scale modulations.

Figure 132.85 shows the experimental data. Figures 132.85(a) and 132.85(b) present flat-interface data at 35 ns and 75 ns, respectively. Figure 132.85(c) shows data with 2-D pre-imposed modulation at 75 ns, taken to confirm evolution measured in previous experiments. The shock traveled from left to right, so the modulations at the left-hand side of the image had more time to grow than the modulations at the right-hand side. The

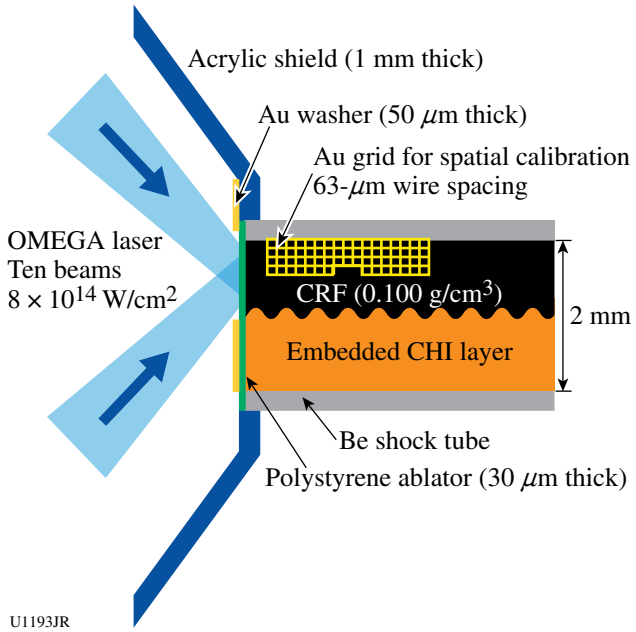

Figure 132.84
Experimental configuration. The interface between lower-density CRF foam and higher-density I-doped plastic was either flat or had a pre-imposed 2-D modulation with a 400-μm wavelength, as in previous experiments. The surface roughness at the interface had a rms amplitude of 100 nm. The density of the CRF foam was 100 mg/cm^3.

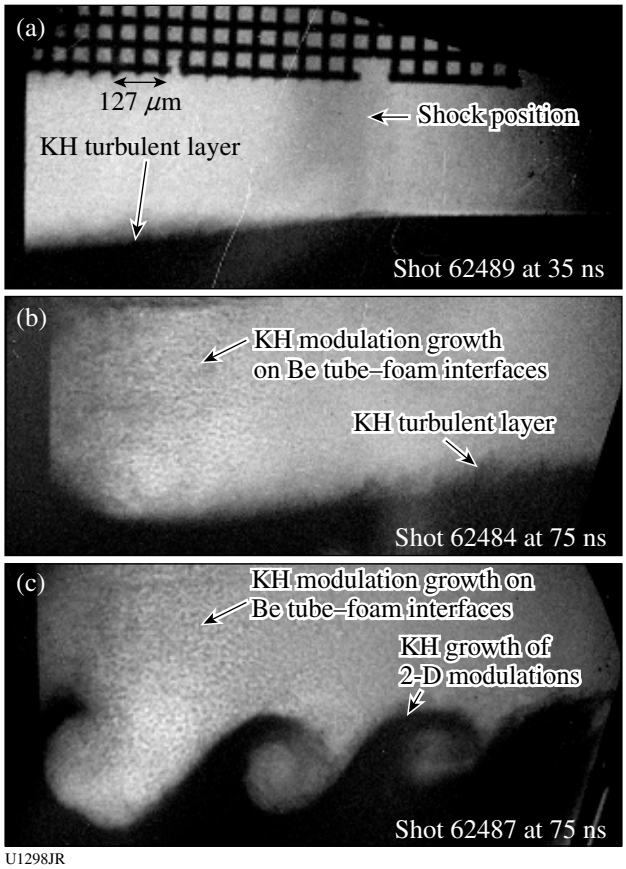

Figure 132.85
X-ray radiographs of KH growth with a flat CHI–foam interface were taken at (a) 35 ns, (b) 75 ns, and (c) with an interface having a 2-D modulation at 75 ns. The areas on the right-hand side of the images experienced less KH growth than the areas on the left-hand side.

light color in the image corresponds to foam material, while the dark color corresponds to plastic. A mixing layer developed behind the shock front, as expected since the Reynolds number was high in this experiment, Re ~ 1×10^6. The mix width was ~60 μm at ~700 μm behind the shock front, inferred from the measured image at 35 ns, close to mix-model predictions. Growth of 2-D pre-imposed modulations [Fig. 132.85(c)] was similar to previous experiments, confirming the repeatability of the drive. In addition, growth of 3-D modulations at the Be tube–foam interfaces was also detected, as shown in both 75-ns images. These experimental data are used to develop and validate mix models that are based on post-processing of hydrodynamic simulations.[45–47]

Nuclear-Atomic–Plasma Interactions in Laser-Produced Plasmas (NEEC and NEET)

Principal Investigator: A. L. Kritcher (LLNL)

Plasma coupling to nuclei in high-energy-density plasmas, or nuclear–plasma physics, is a cutting-edge field that traverses the areas of nuclear physics, plasma physics, and atomic physics. Nuclear–plasma interactions occur in hot and dense plasmas such as inertial confinement fusion environments and astrophysical bodies. The effect of high-energy-density-plasma (HEDP) environments on astrophysical nucleosynthesis, the formation of heavy elements from pre-existing nucleons in astrophysical plasmas, is expected to play a significant role.[48] Nuclei in stellar plasmas reach a thermal population of low-lying excited nuclear states from photoexcitation, free electrons in the plasma (NEEC),[49–52] excitation from atomic transitions (NEET),[53–55] and inelastic electron scattering in the dense plasma. In these experiments at the Omega facility, we investigate the NEEC process in underdense plasmas by illuminating mini hot hohlraums (400 or 600 μm in diameter) with ~15 kJ of laser light (Fig. 132.86).

The goal of these first experiments was to identify the plasma conditions of hot Tm hohlraums with spectral line emission analysis and optical Thomson scattering, measure the energy and time-resolved atomic emission background, investigate this experimental platform to study nuclear lifetime shortening in hot plasmas, and determine the possibility to investigate nuclear–plasma interactions. We collected high-quality data and are in the process of analyzing the results. Future campaigns will continue to measure plasma conditions of hot hohlraums and investigate nuclear–plasma interactions in HEDP plasma environments. We will also field additional isotopes in this configuration.

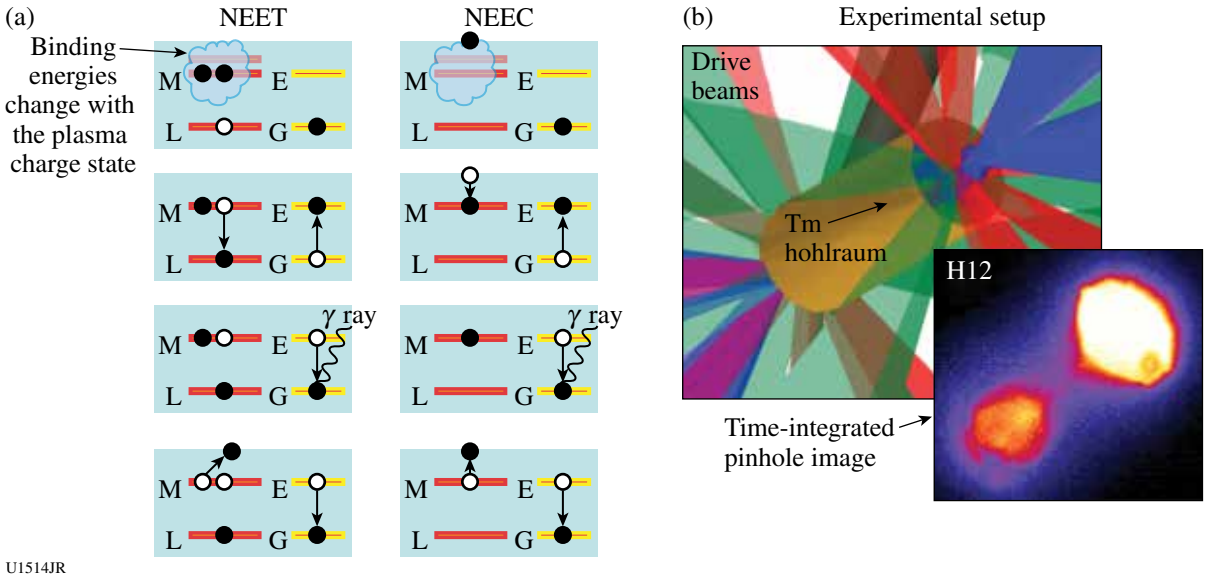

Figure 132.86

(a) Schematic of the NEET and NEEC processes. The red levels on the left-hand side denote the atomic shells; the yellow levels on the right-hand side denote the nuclear excited and ground states. First, the nucleus in the ground state and atomic shell vacancies are present (and/or free electrons are present). Electrons either transition or are captured into atomic states and the nucleus becomes excited. The nucleus radioactively decays by γ-ray emission or internal conversion. (b) A schematic of the experimental configuration. Tm hohlraums, 400 and 600 μm in diameter, are illuminated by 40 drive beams with a total of 15 to 20 kJ.

Astrophysical Collisionless Shock Generation by Laser-Driven Laboratory Experiments on OMEGA and OMEGA EP

Principal Investigators: N. Kugland, S. Ross, and H.-S. Park (LLNL)

The goal of this experiment is to study astrophysical collisionless shocks with counter-streaming plasmas from high-power lasers. Astrophysical "collisionless" shocks form via plasma instabilities and self-generated magnetic fields. Laboratory experiments at large laser facilities can achieve the conditions necessary for the formation of collisionless shocks and will provide a unique avenue for studying the nonlinear physics of shock waves. We are performing a series of experiments on the OMEGA and OMEGA EP lasers in which collisionless shock conditions will be generated by the two high-speed plasma flows resulting from the laser ablation of solid targets using 10 kJ to 20 kJ of laser energy. The experiments will aim to answer several questions of relevance to collisionless shock physics: the importance of the electromagnetic filamentation (Weibel) instability in shock formation, the self-generation of magnetic fields in shock collisions, the influence of external magnetic fields on shock formation, and the signatures of particle acceleration in shocks.

Our second year of OMEGA EP experiments (EP-ACSEL-12A and EP-ACSEL-12B) continued proton imaging to visualize the electromagnetic fields produced by two counter-streaming plasmas. As shown in Fig. 132.87, these plasmas were made by two UV beams that irradiated plastic or carbon drive targets with 2200 J (per target) in 3 ns. These interpenetrating plasmas were then probed from the side by short-pulse laser-generated protons.

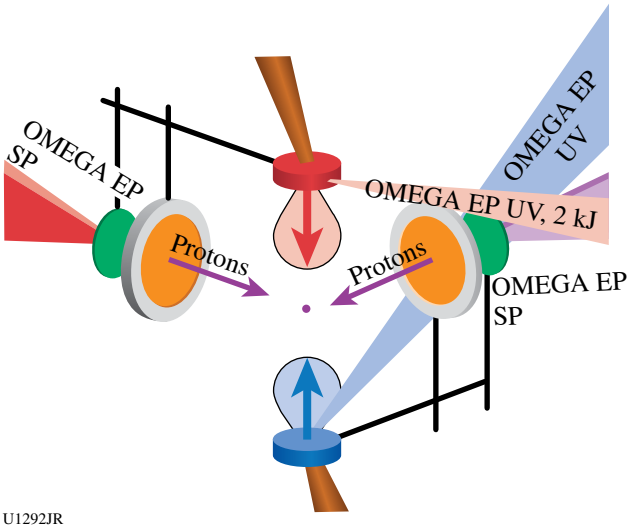

Figure 132.87
EP-ACSEL experimental setup.

EP-ACSEL-12A confirmed the presence of the large self-organized fields first observed in our FY11 OMEGA EP shots. These surprising structures, formed by a yet unexplained mechanism, are much larger than the intrinsic plasma spatial scales and persist for much longer than the plasma kinetic time scales. Now in press in Nature Physics[26] as a cover figure article, this finding provides a new way to understand how electromagnetic order emerges from chaos in the cosmos, such as in the plasma flows that emerge from young stars.

EP-ACSEL-12B explored the sensitivity of these self-organized fields to changes in the laser-drive conditions and target type. Figure 132.88 shows the dramatic difference in the fields that develop in counter-streaming CH_2 flows (a hydrogenated multi-species plasma), and pure C plasmas. The C flows develop much less turbulence. We are currently exploring the origin of these features using basic plasma theories and numeric simulations.

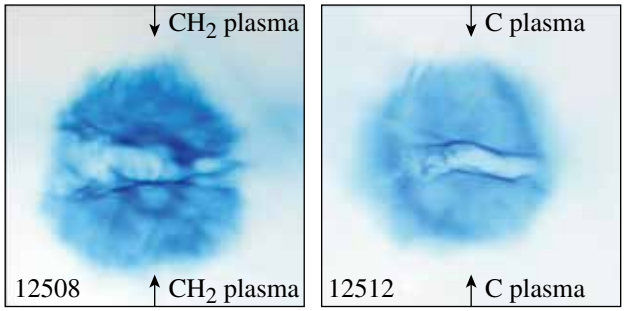

Figure 132.88
Proton images of the counter-streaming plasmas from the collisionless shock experiments of July 2012.

The results have been presented at many conferences.[56–59] Seven papers[26–28,59–62] have been published and additional papers are in preparation.[63–65]

The ACSEL-12A/B on OMEGA-60 campaigns focused on characterizing plasma conditions in the interaction region of two high-velocity plasma flows. The target geometry is similar to previous ACSEL campaigns with two foil targets separated by 8 mm. The targets are heated with 5 kJ of laser energy per foil, producing high-velocity plasma blowoff. The target material is pure carbon, CH_2, or beryllium. Thomson scattering is then used to measure the plasma conditions. High-quality data

were obtained, providing plasma parameters that have never before been measured, as seen in Fig. 132.89.

The electron temperature and density are measured from the electron feature; then the ion feature can be used to measure the ion temperature and flow velocity. The ion temperature is shown in Fig. 132.90 for all three target materials. The ion temperatures were similar for the targets containing carbon and significantly lower for the beryllium target. A detailed understanding of the counter-streaming heating mechanism is currently being developed.

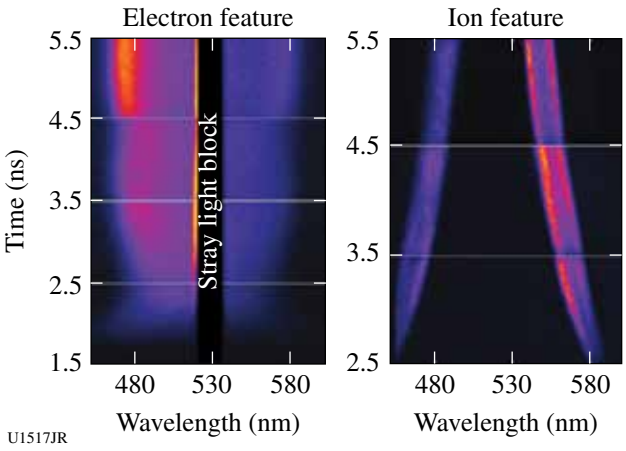

Figure 132.89
Thomson-scattered light from the plasma is measured on a series of carbon target shots.

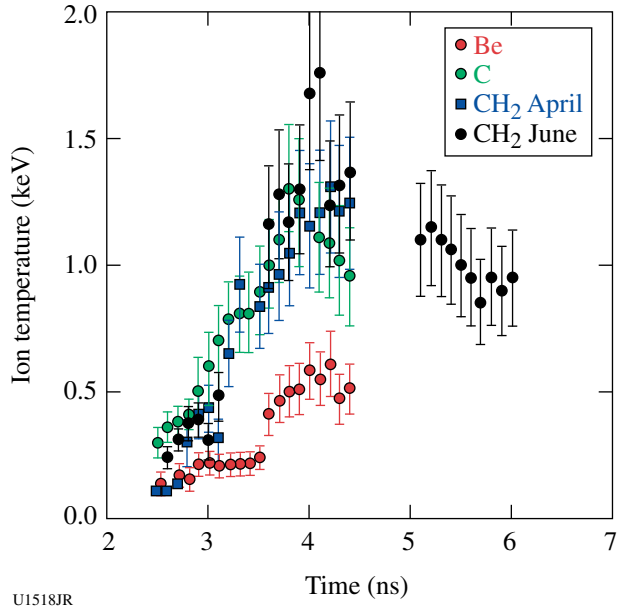

Figure 132.90
Compilation of ion temperatures of counter-streaming plasmas from different target materials of Be, carbon, and CH_2. The differences are important to understanding the collisionless shock-creation regime.

Our work and collaboration produced numerous invited talks and high-profile papers including Nature Physics (cover figure),[26] Physics of Plasmas (highlight research), and Review of Scientific Instruments (invited article).

Dislocations and Twinning at High Pressures and Strain Rate on bcc Metals

Principal Investigators: B. R. Maddox, A. Comley, and C. Wehrenberg (LLNL)

In TaRDiff-2012 our goal was to study twinning and dislocation motion in shock-compressed tantalum. The experimental configuration used the broadband x-ray diffraction diagnostic on TIM-4 as the primary diagnostic for studying twinning. Alternatively, a recovery tube was fielded on TIM-1, to allow for the study of recovered micro-indented samples. Samples were driven using a 1-ns square pulse with laser energy in the 15- to 65-J range. High-quality diffraction data were obtained and Ta samples were successfully recovered. Initial analysis did not show driven diffraction signal for the (110) Ta samples, which were expected to show larger amounts of twinning. However, high-contrast–driven Laue spots were observed for (100) oriented Ta crystals, and these data were used in Ta strength measurements. Recovered Ta samples will be examined by a transmission electron microscope (TEM) to measure the dislocation motion originating from the micro-indents.

Thermonuclear Reactions in Stellar Plasmas and High-Resolution Measurements of Three-Body Breakup in Isobaric Analogue Reactions

Principal Investigators: D. P. McNabb (LLNL); R. D. Petrasso (MIT); and T. C. Sangster (LLE)

The starting point for this project was to design a series of direct-drive, exploding-pusher implosions to measure particle production spectra for the $T(t,2n)^4He$ fusion reaction. The $T(t,2n)^4He$ reaction is important for NIF diagnostics and is the charge-symmetric reaction to $^3He(^3He,2p)^4He$—a key reaction in the solar proton–proton chain. Our initial goal is to compare these results with those predicted by nuclear theory calculations to gain insight into the reaction mechanism. We will be measuring the neutrons with an improved neutron time-of-flight (nTOF) detector system, with the magnetic recoil spectrometer optimized for lower-energy neutrons and high resolution, and different activation systems. The Thomson parabola ion

energy (TPIE) analyzer has also been optimized to attempt to measure the continuum alpha particle spectrum in addition to the emitted neutrons. Due to difficulties getting capsules filled with high-purity tritium, the shot day was deferred until Q1FY13. There is a renewed interest in these experiments on OMEGA given the recent high-quality TT symcap nTOF data obtained on the NIF and the discrepancy between these neutron spectral measurements and previous experiments. In addition to fielding the TPIE spectrometer, the OMEGA measurements are expected to take place at a higher temperature than the new NIF data.

Compton Radiography Fast Ignition (CRFI) Campaign

Principal Investigators: P. Patel (LLNL) and H. Sawada (University of California, San Diego)

Co-investigators: C. D. Chen, R. Tommasini, H. S. McLean, and M. H. Key (LLNL); L. C. Jarrott and F. N. Beg (University of California, San Diego); W. Theobald, A. A. Solodov, J. A. Delettrez, V. Yu. Glebov, and C. Stoeckl (LLE); and M. S. Wei and R. B. Stephens (General Atomics)

The goal of the Compton radiography fast ignition (CRFI) campaign is to measure the 2-D areal-density map of an imploded cone-in-shell target using a high-energy bremsstrahlung x-ray backlighter. In cone-guided fast ignition, the formation of a high-density compressed core near the cone tip is critical for efficient fast-electron core heating. The areal density, core shape, and standoff distance from the cone tip provide important parameters for experimentally estimating the energy coupling of an ignition laser to the core. In our joint OMEGA experimental campaign, a 40-μm-thick deuterated carbon (CD) shell was imploded by 54 18-kJ OMEGA beams with a low-adiabat shaped drive pulse. A backlighter target consisting of a 10-μm-diam Au wire embedded on a 300-μm × 300-μm CH foil was irradiated with a 250- to 1500-J, 10-ps OMEGA EP beam in a 100-μm focal spot to produce high-energy bremsstrahlung x rays. The hard x rays with an energy greater than 20 to 30 keV transmitting through CD plasmas were dominated by Compton scattering and the mass attenuation coefficient was weakly sensitive to the plasma density. The bremsstrahlung spectrum and spatial resolution were estimated to be an ~160-keV x-ray slope and 7-μm half width at half maximum (HWHM), respectively, from a radiograph of a 200-mm-diam solid tungsten sphere using 10-ps, 250-J OMEGA EP beam energy. Figure 132.91 shows the radiographic images of an imploded cone-in-shell target at 4.0 ns from the start of the drive pulse with an OMEGA EP energy of 1.5 kJ. Figures 132.91(a) and 132.91(b) show the same image but in different color scales. A preliminary analysis shows a

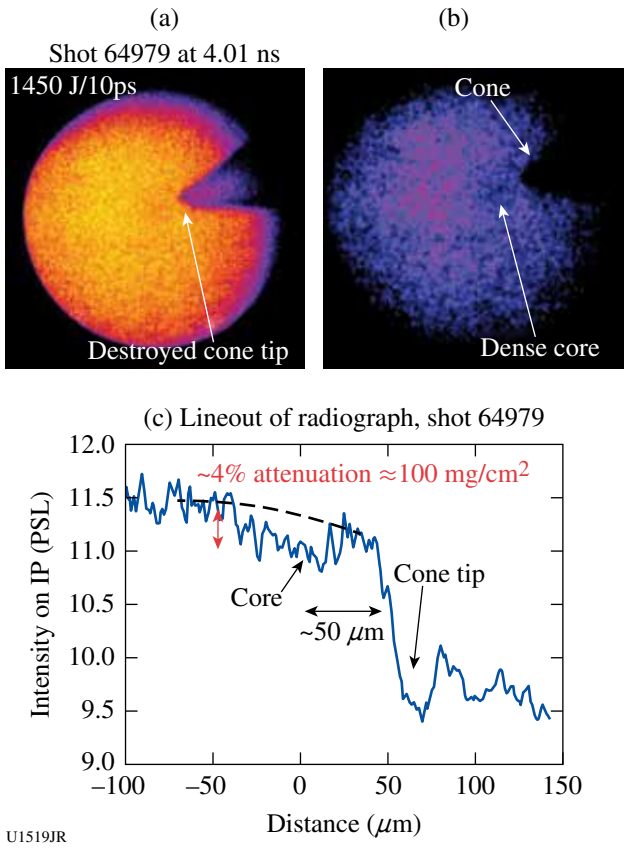

Figure 132.91
[(a) and (b)] Radiographic images of an imploded cone-in-shell target 4.0 ns from the start of the drive pulse. (c) Analysis of images to deduce areal density and standoff distance.

peak areal density of ~100 mg/cm^2 and a standoff distance of ~50 μm as shown in Fig. 132.91(c). Further analysis is underway to estimate the core size and errors caused by uncertainties in the backlighter spectrum and source size. The inferred areal density from the radiographic images will be compared to a 2-D radiation–hydrodynamic *DRACO* simulation to validate the simulation results.

Probing Shocked Liquid H, H/He, CH_4, N_2, and NH_3 with Inelastic X-Ray Scattering and Shock-Velocity Measurements: Toward the Equation of State of Planetary Interiors

Principal Investigator: S. P. Regan (LLE)

The Fermi-degenerate plasma conditions created in liquid deuterium by a laser-ablation–driven shock wave were probed with noncollective, spectrally resolved, inelastic x-ray Thomson scattering (XRTS) employing Cl Ly$_\alpha$ line emission at 2.96 keV (Ref. 66). These first XRTS measurements of the microscopic

properties of shocked deuterium show an inferred spatially averaged electron temperature of 8±5 eV, an electron density of 2.2 (±0.5) × 10^{23} cm^{-3}, and an ionization of 0.8 (−0.25, +0.15). Two-dimensional hydrodynamic simulations using equation-of-state (EOS) models suited for the extreme parameters occurring in inertial confinement fusion research and planetary interiors are consistent with the experimental results.

The scattered spectrum of the Cl Ly$_\alpha$ emission taken at t = 5 ns with a 250-μm slit in the scattering channel is shown in Fig. 132.92(a). The measurement taken without the slit is shown in Fig. 132.92(b), and the incident spectrum is shown in Fig. 132.92(c). The observed noise in the measured scattered x-ray spectrum is consistent with the estimated signal level. The incident spectrum is measured by irradiating a parylene D foil target on a separate laser shot. The scattered spectrum has a strong Rayleigh peak around 2960 eV and a Compton-downshifted feature. Scattered x-ray spectra were calculated using the x-ray scattering (XRS) code, which uses the finite-temperature random-phase approximation with static local field corrections to obtain the spectral shape of the inelastic (Compton) feature caused by scattering from free electrons.[67] The elastic scattering intensity strongly depends on the degree of ion–ion correlations in the plasma via the structure factor S_{ii} (Ref. 68). To constrain the value for S_{ii}, density functional theory molecular dynamics (DFT-MD) simulations were performed using the Vienna *ab initio* simulation package (VASP).[69,70] The simulations indicate weak ionic correlations for the conditions similar to the average of the plasma probed. This means the ion–ion structure factor S_{ii} at the relevant scattering wave number is close to unity for most of the conditions probed. With this information, the elastic scattering feature can be used to constrain the temperature and the ionization degree of the system. Structure factors close to unity are also found for the unshocked deuterium liquid. In addition to Doppler broadening, the width and position of the inelastic feature depend on the density for $\alpha_s \sim 1$. This fact allows us to bracket the electron density and estimate the ionization charge based on the initial mass density of the sample. The simulated scattering spectra computed using XRS provided the best fit to the spectrum measured with the slit for the following plasma conditions: T_e = 8±5 eV, $Z \sim 0.8$ (−0.25, +0.15), and n_e = 2.2 (±0.5) × 10^{23} cm^{-3}. The *DRACO* simulations are in close agreement with the experimental results. These plasma conditions were repeatable on a subsequent laser shot. The plasma conditions inferred from the spectrally resolved x-ray spectrum recorded without the slit in the x-ray scattering channel are lower with T_e = 3±2 eV, $Z \sim 0.6 \pm 0.2$, and n_e = 2.0 (±0.5) × 10^{23} cm^{-3}. The lower plasma pressure created by the lower-intensity portion of the laser drive causes bowing of the shock front (see Fig. 131.7 in Ref. 66). When the slit is placed in the scattering channel, the x rays scattered from this underdriven portion of the target are blocked from the detector. This leads to higher inferred values of T_e, Z, and n_e, which is more representative of the uniformly shocked region.

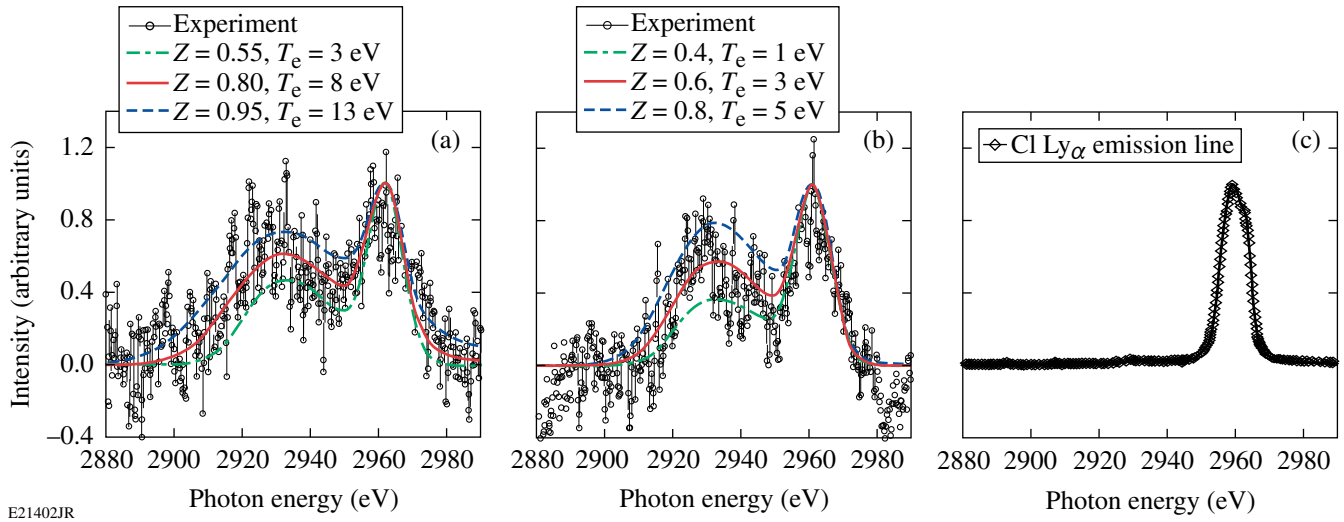

Figure 132.92
Measurement of (a) Cl Ly$_\alpha$ emission scattered from shocked liquid deuterium with a 250-μm slit in the scattering channel and simulated scattering spectra, (b) Cl Ly$_\alpha$ emission scattered from shocked liquid deuterium without a 250-μm slit in the scattering channel and simulated scattering spectra, (c) Cl Ly$_\alpha$ emission incident on the shocked liquid deuterium. The inferred plasma conditions in (a) are T_e = 8±5 eV, $Z \sim 0.8$ (−0.25, +0.15), and n_e = 2.2 (±0.5) × 10^{23} cm^{-3} and in (b) are T_e = 3±2 eV, $Z \sim 0.6 \pm 0.2$, and n_e = 2.0 (±0.5) × 10^{23} cm^{-3}.

Unlike previous velocity spectrometer for any reflector (VISAR) measurements, the x-ray scattering experimental platform offers the considerable advantage of probing off-Hugoniot states. This experimental result is a significant step toward achieving accurate measurements of all thermodynamic variables needed to provide stringent tests of EOS models, which would require at least three thermodynamic variables like pressure, mass density, and temperature.

Extreme Chemistry of Precompressed Nitrogen

Principal Investigator: J. R. Rygg (LLNL)

Experimental measurement of the N_2 Hugoniot was extended to 850 GPa by launching shocks into N_2 samples precompressed in diamond anvil cells to ~2 GPa (see Fig. 132.93). VISAR and streaked optical pyrometry (SOP) measurements of the N_2 shock front in comparison to concomitant measurements in quartz were used to infer pressure, density, reflectance, and temperature of shocked N_2. Compressibility, optical reflectivity, and temperature measurements show that N_2 undergoes a complex dissociation–polymerization transition, in good agreement with first principle calculations.

Measurements of the Ablative Richtmyer–Meshkov Instability in the Nonlinear Regime

Principal Investigator: V. A. Smalyuk (LLNL)

Figure 132.94 shows a schematic of the experimental setup for the nonlinear Richtmyer–Meshkov (RM) instability experiments on OMEGA. Planar CH targets (15, 30, and 50 μm thick) were driven with three UV beams using a 6-ns square pulse shape, a total energy of ~0.7 kJ, and a laser intensity of ~5×10^{13} W/cm^2. Initial target modulations were imposed by laser imprinting using a beam with a special 2-D phase plate with a modulation wavelength of ~70 μm. The timing of this beam was advanced by ~200 ps, relative to other drive beams that have regular SG4 distributed phase plates (DPP's). Figure 132.95 shows laser-beam images with an SG4 DPP [Fig. 132.95(a)] and a special 2-D DPP [Fig. 132.95(b)]. Growth of target modu-

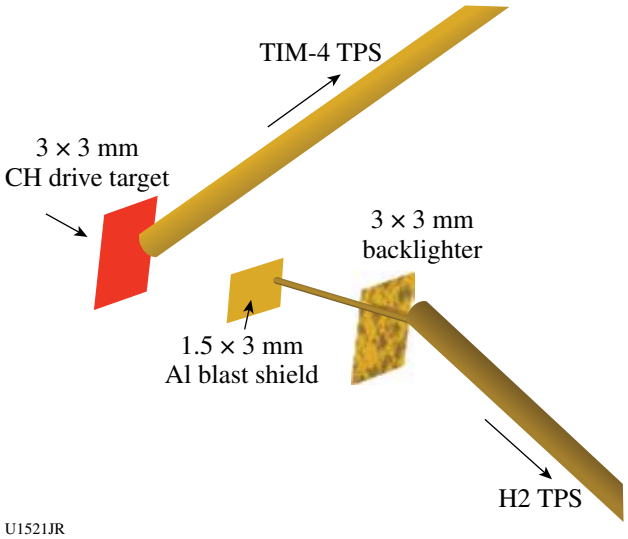

Figure 132.94
Experimental setup.

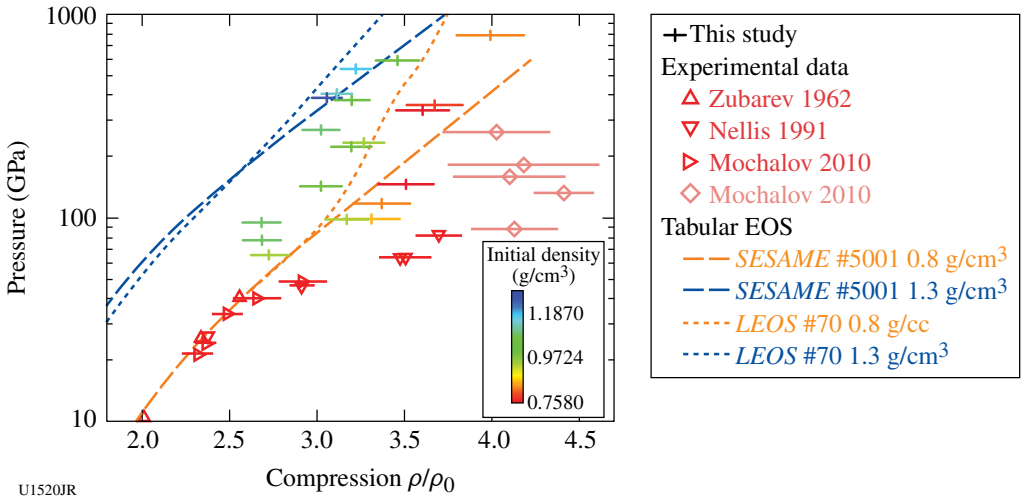

Figure 132.93
In FY12, the OMEGA laser was used to extend the N_2 Hugoniot from 100 to 850 GPa (crosses). The N_2 shock pressure and density were inferred by shock-velocity measurements impedance matched to a quartz standard.

lations was measured with x-ray radiography using uranium (~1.3-keV), samarium (~1.8-keV), and tantalum (~2.2-keV) backlighters on a framing camera with 10-μm spatial resolution and 80-ps temporal resolution. The backlighter targets were driven with a 2-ns square pulse shape and an intensity of ~3×10^{14} W/cm^2 using seven additional UV beams. Figure 132.96 shows an example of a measured image at 1.1 ns (near the end of the RM phase) taken with a 50-μm-thick CH foil and tantalum backlighter. Evolution of 2-D broadband modulations was observed in the RM phase for all target types during a shock transit time before the onset of acceleration and subsequent RT growth. Figure 132.97 summarizes the areal-density evolution of 2-D modulation at a wavelength of 70 μm for the 30- and 50-μm-thick foils and compares data with predictions of the 2-D hydrocode *DRACO*. The vertical dashed lines show expected times of the end of the RM phase and the beginning of the RT phase for these types of foils. Blue data points and curves correspond to 30-μm-thick foils, while black curves and data points correspond to 50-μm-thick foils. Areal-density modulations grow throughout the RM phase, and their evolution is similar to code predictions, validating the simulations.

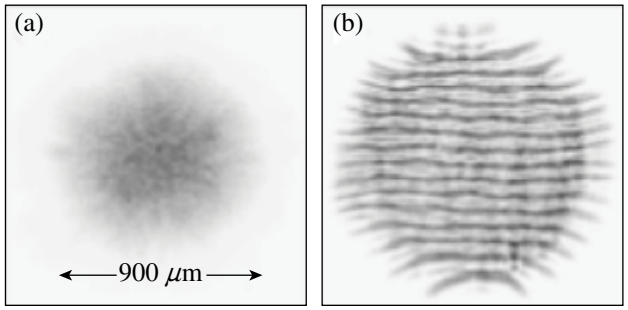

U1522JR

Figure 132.95
Laser-beam images with (a) regular SG4 DPP and (b) special 2-D DPP.

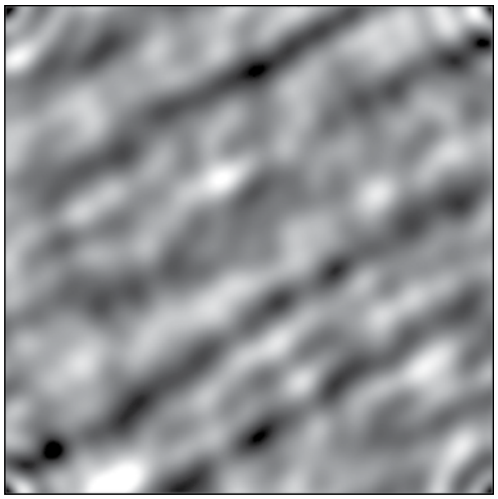

U1523JR

Figure 132.96
X-ray images of 2-D broadband modulations near the end the Richtmyer–Meshkov instability growth phase measured in 50-μm-thick CH targets.

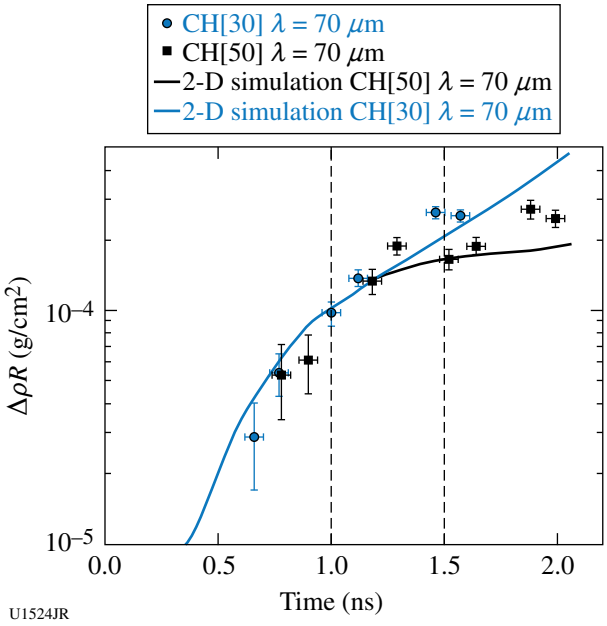

U1524JR

Figure 132.97
Evolution of 2-D areal-density modulations at a wavelength of 70 μm measured in 30-μm-thick foils (blue circles) and in 50-μm-thick foils (black squares). Solid curves correspond to 2-D *DRACO* simulations, while vertical dashed lines correspond to times of the end of the RM phase and beginning of the RT phase in 30-μm-thick foils (blue curves) and 50-μm-thick foils (black curves).

Spectroscopy of Neutrons Generated Through Nuclear Reactions with Light Ions in Short-Pulse Laser Interaction Experiments

Principal Investigators: C. Stoeckl, V. Yu. Glebov, and T. C. Sangster (LLE)

The experimental objective of this project is to study nuclear reactions in light ions by measuring the spectrum of neutrons generated in short-pulse laser interaction experiments and compare them with simulated spectra based on the published cross sections.

Planar targets are irradiated with one short-pulse beam focused at the target's front surface. Charged particles from the back side of the target create neutrons and charged particles through nuclear reactions in a second converter target placed closely behind the primary interaction target. The spectrum of the neutrons generated in the converter target is measured using a scintillator/photomultiplier–based neutron time-of-flight (nTOF) detector. Charged-particle detectors are used to measure the spectra of the primary particles.

In FY12 three new nTOF detectors were installed on OMEGA EP (see Fig. 132.98). One in the laser forward direction on port 82, one at 90° to the laser on port 90, and one in the laser backward direction on port 73. Each of these detectors is heavily shielded with lead and gated to suppress the signal from the prompt hard x rays generated in the laser–plasma interaction processes on the primary target.

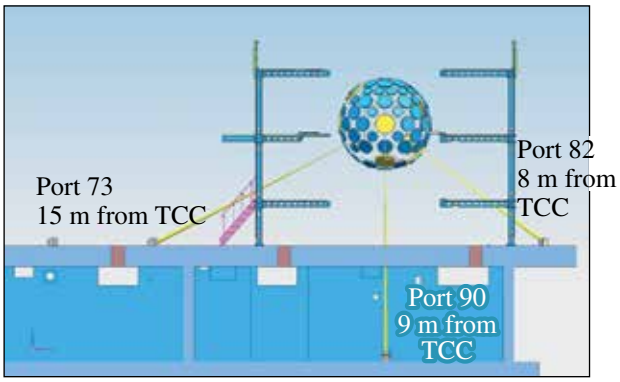

Figure 132.98
Location map of the three neutron detectors installed in FY12.

In FY12 one shot day (19 September) was available for experiments. Copper foils were used as primary targets to generate protons and irradiated with 10- and 100-ps OMEGA EP pulses and energies of up to 2.0 kJ. A container target was developed to place ~100 mg of LiD inside a stainless-steel container ~2.5 cm behind the primary target. High-quality nTOF spectra were recorded on all detectors for all shots during the day. Figure 132.99 shows data from all three detectors.

No specific spectral features like DT fusion neutrons are visible in the recorded data. The analysis of this data is ongoing. The current working hypothesis is that the measured neutron spectrum is dominated by p–n reactions in the LiD container and the target chamber. Efforts to reduce this background are currently under consideration.

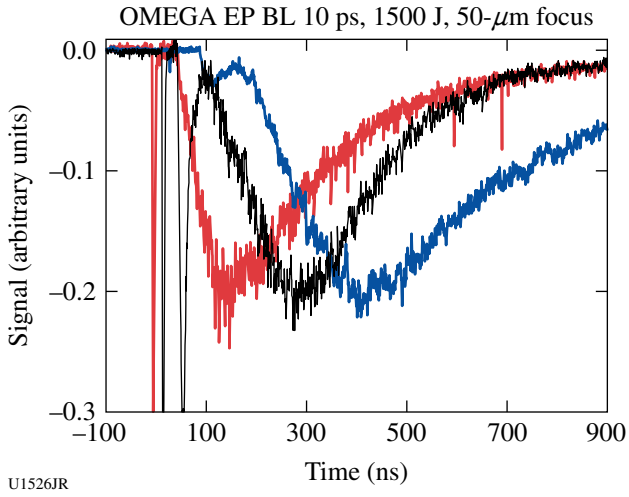

Figure 132.99
Neutron time-of-flight data from the detectors in ports 82 (red), 90 (black), and 73 (blue). The first peak in the data corresponds to the arrival of the prompt hard x rays. Gating suppresses this peak by at least five orders of magnitude.

Integrated Fast-Ignition Experiments

Principal Investigators: W. Theobald and A. A. Solodov (LLE)
Co-investigators: C. Stoeckl, R. Epstein, V. Yu. Glebov, G. Fiksel, S. Ivancic, F. J. Marshall, G. McKiernan, C. Mileham, P. M. Nilson, and T. C. Sangster (LLE); L. C. Jarrott and F. N. Beg (University of California, San Diego); E. Giraldez, R. B. Stephens, and M. S. Wei (General Atomics); H. McLean (LLNL); H. Sawada (University of Nevada, Reno); H. Habara (ILE); and J. J. Santos (CELIA)

Integrated fast-ignition experiments with cone-in-shell targets on OMEGA have demonstrated ~3.5% coupling efficiency of short-pulse laser energy into a compressed target.[71] The goals of this Laboratory Basic Science (LBS) proposal were to study the short-pulse laser/fast-electron coupling efficiency using an improved OMEGA EP laser and to validate the 2-D radiation–hydrodynamic modeling predictions of a new aluminum cone-tip target design with a backlighter experiment. The new target design has been modeled with detailed hydrodynamic simulations. Figure 132.100 shows a *DRACO*[72] simulation of the cone-in-shell target with an aluminum block mounted in front of a gold cone for different times during the implosion. This design is more resilient against the strong shock from the implosion than a previous design with a gold-only cone.[71] Shock breakout is predicted to be delayed by ~80 ps in the new target design. Figure 132.100(c) shows that the interior of the cone volume is free of plasma up to the time when the shock breaks through. A new backlighter platform has been developed

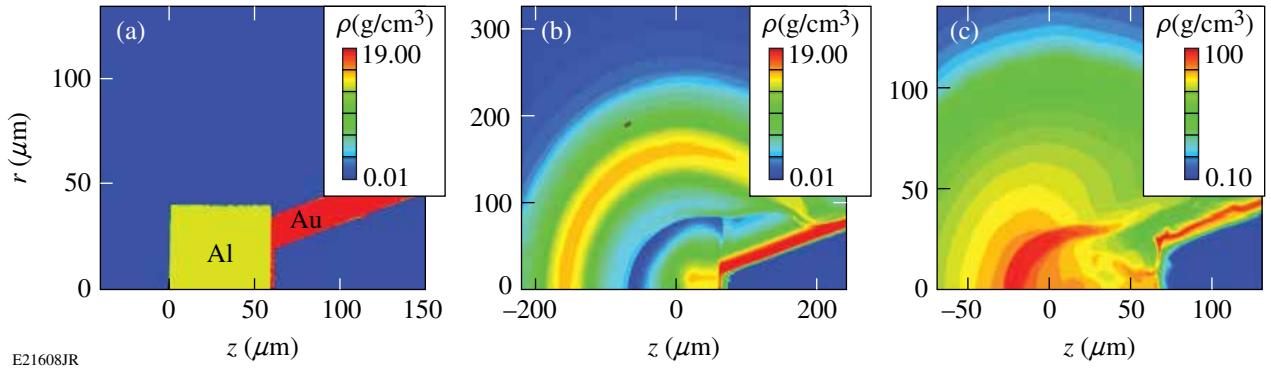

Figure 132.100
Two-dimensional hydrodynamic *DRACO*[72] simulation of a new cone-in-shell target design. (a) Detail of the target tip showing the gold cone with an aluminum tip. (b) Imploding shell before peak compression at 3.25 ns. Simulations predict thermal expansion of the cone material due to radiation preheat. The aluminum tip expands faster than the gold material. (c) Density map at 3.87 ns (~0.19 ns before peak compression) showing better shock resilience of this design than the previous[71] Au cone tip target.

and was tested during the first shot day in FY12 to characterize the fuel assembly of cone-in-shell targets close to peak compression and to validate the 2-D radiation–hydrodynamic modeling predictions. This was done with flash radiography[73] using a monochromatic 8.05-keV x-ray source that radiographed the target that was imploded by 54 OMEGA beams. A thin Cu foil was irradiated by the 1.5-kJ, 10-ps OMEGA EP short-pulse laser and generated a bright Cu K_α backlighter source. The laser was defocused to an ~20-μm spot that provided an intensity of ~5×10^{17} W/cm^2. The fast electrons refluxed in the Cu foil and generated K_α radiation over the ~1-mm foil, which provided an ideal area backlighter source. A spherical Bragg crystal located on the opposite side of the target imaged the implosions onto an image plate detector.[74] Figure 132.101 shows measured images of the implosion at various times around peak compression over a time range of ~0.4 ns and over a region of 500 μm × 500 μm. Note that each image was taken with a different shot. Figure 132.101(a) shows an image of an undriven target, where the Al tip is clearly visible and less opaque than the gold cone. The false color scheme represents the measured optical density. The frame in Fig. 132.101(b) shows an implosion at 3.75 ns after the start of the drive pulse. The fuel starts to assemble in front of the tip and the Al tip is compressed in the radial and longitudinal directions to a higher density. The following frames were taken at successively later times: Fig. 132.101(c) at 3.82 ns, Fig. 132.101(d) at 3.93 ns, Fig. 132.101(e) at 4.05 ns, and Fig. 132.101(f) at 4.15 ns. At later times the Al tip is more deformed and eventually completely destroyed and the fuel assembly reaches higher density. The radiographs show how the implosion destroys and pushes back the cone tip. Peak compression was reached close to the time of the frame in Fig. 132.101(e), while the last frame was

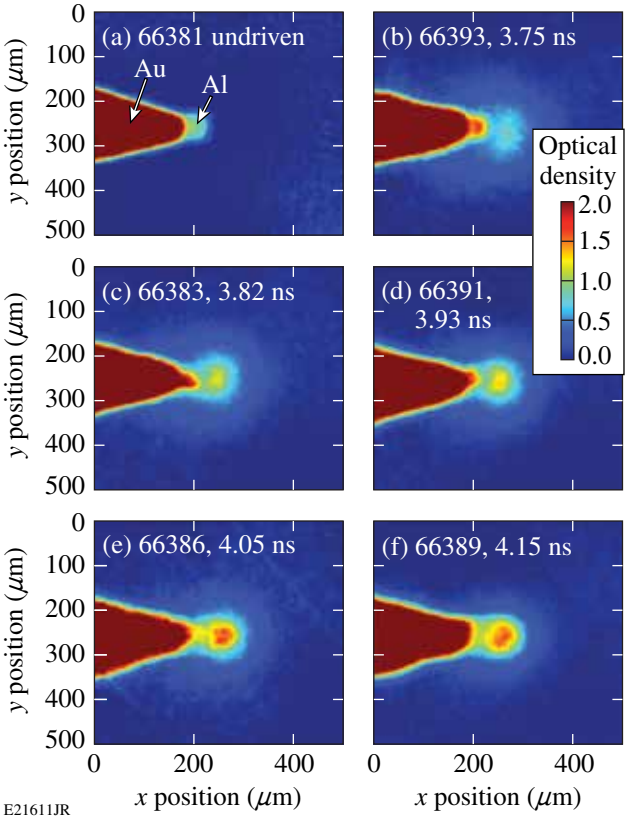

Figure 132.101
(a) Radiography images of an undriven target and imploded cone-in-shell targets at various stages of the implosion: (b) 3.75 ns, (c) 3.82 ns, (d) 3.93 ns, (e) 4.05 ns, and (f) 4.15 ns after the start of the UV drive laser pulse.

after peak compression. The measured time of peak compression (~4.10±0.05 ns) compares well to the time (4.06 ns) predicted from 2-D *DRACO* simulations. The measured peak

areal density is 330±50 mg/cm^3 using a calculated average mass absorption coefficient from the *DRACO* simulation along the line of sight. The predicted peak value of 360 mg/cm^3 shows that the measured value is close to the 2-D prediction. Interleaved with joint shots, the shock-breakout measurements were performed with OMEGA-only beams. The measured shock-breakout time agrees with the predicted breakout time within ~60 ps. The experiments confirm the improved shock resilience of the target. The second shot day at the end of FY12 studied the fast-electron coupling of the new target. The OMEGA EP laser was significantly improved with a smaller focus (R_{80} = 15 μm), a higher energy (1.35 kJ), and a higher contrast (~0.5-mJ prepulse energy). Compared to the previous experiment,[71] the average intensity increased about four times to $\sim 2 \times 10^{19}$ W/cm^2. The laser contrast was sufficiently high so that no significant pre-plasma formation is expected. The data of the integrated experiment are still being analyzed.

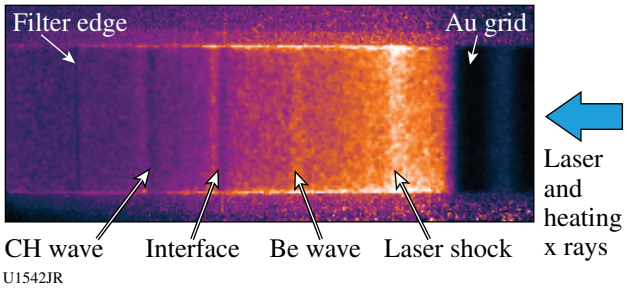

Figure 132.102
A radiograph of the heated CH/Be target. The delay between the heater and the backlighter was 5 ns. The laser beams and heating x rays were incident from the right side. Three fringes show up in the image: the middle fringe representing the interface and two side fringes corresponding to the waves propagating in CH and Be, respectively. The shock driven by the laser, traveling from right to left, is also visible.

FY12 LLNL OMEGA Experimental Programs

In FY12, LLNL conducted several campaigns on the OMEGA and OMEGA EP lasers, as well as campaigns that jointly used the OMEGA and OMEGA EP beams. Overall, LLNL led 335 target shots involving OMEGA and 121 target shots involving OMEGA EP. Approximately 38% of the total number of shots (124 OMEGA shots and 39 OMEGA EP shots) supported the National Ignition Campaign (NIC). The remaining 211 OMEGA shots and 82 OMEGA EP shots were dedicated to experiments for high-energy-density (HED) physics.

National Ignition Campaign Experiments

Thermal Conductivity Study of CH/Be and CH/D_2 Interfaces by Refraction-Enhanced X-Ray Radiography

Principal Investigator: Y. Ping
Co-investigators: O. L. Landen, J. A. Koch, R. Wallace, and G. W. Collins

The Atwood#12A&B campaigns are based on the technique of time-resolved, refraction-enhanced x-ray radiography that was successfully demonstrated in FY11. The evolution of the density profile at a cylindrical CH/Be interface isochorically heated by Ag L-band radiation has been measured to infer the thermal conductivity under inertial confinement fusion (ICF)-relevant conditions. In addition to observing the density evolution caused by thermal conduction, a counter-propagating shock wave and rarefaction wave were also observed as shown in Fig. 132.102. The velocities of these waves were measured simultaneously, providing constraints on the temperature after heating. Preliminary analysis of the data and hydrodynamic simulations shows that the thermal conductivity is higher than most models predict. The measurements of the CH/D_2 interface in cryogenic targets were complicated by leaking in the cryo cells, limited rotation movement, and condensation on the backlighter, which significantly reduced the brightness. A list of potential improvements has been provided to LLE for future experiments with cryogenic targets.

High-Resolution Measurements of Velocity Nonuniformities Created by Microscopic Perturbations in NIF Ablator Materials

Principal Investigator: P. M. Celliers
Co-investigator: M. A. Barrios

In May 2012, a full day was dedicated to the CAPSEED campaign. This campaign is a continuation of earlier campaigns that studied the performance of National Ignition Facility (NIF) ablators. The latest capsule designs using glow-discharge–polymer (GDP) ablators for the NIC currently employ Si doping layers as preheat shielding for the fuel; the earlier NIC designs employed Ge-doping layers. In response to this design change, most of the CAPSEED-12A campaign was devoted to assessing the performance of the newer Si-doped design (as compared to the previous Ge-doped designs). Results from this campaign (see Fig. 132.103) show that the performance of the Si-doped material matches that of the Ge-doped material.

Three additional shots were devoted to studying double-shocked nanocrystalline diamond [or "high-density carbon" (HDC)]. In current capsule designs employing diamond ablators, the initial shock strength is sufficient to only partially melt the capsule. Shock strengths much higher than this will set the fuel adiabat higher than the design goal of current designs.

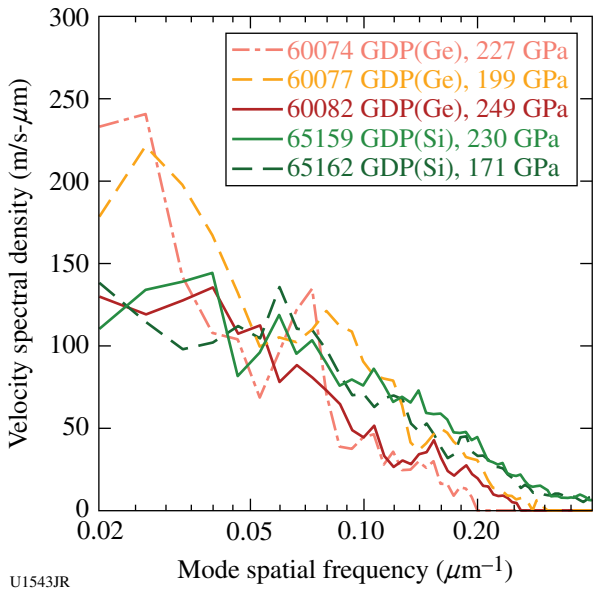

Figure 132.103
Velocity-fluctuation spectra measured for Ge-doped GDP in 2011 (shots 60074, 60077, and 60082) and Si-doped GDP in 2012 (shots 65159 and 65162). The velocity spectra for all cases appear to be equivalent within the range of statistical fluctuations.

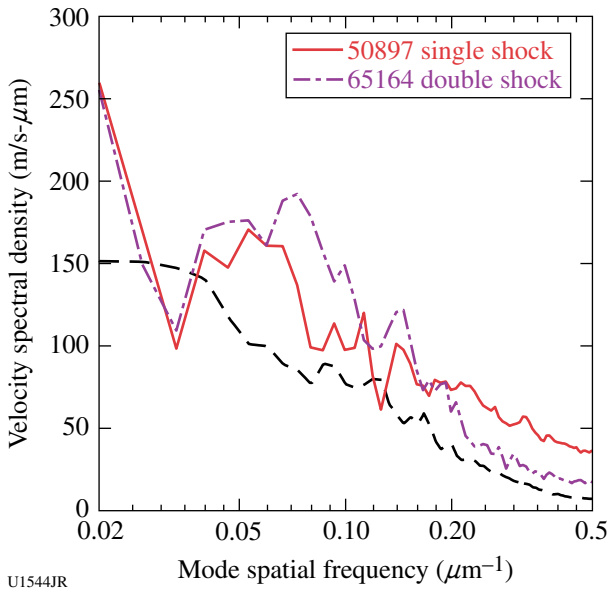

Figure 132.104
Velocity-fluctuation spectra measured for single-shocked and double-shocked HDC ablators. The black dashed curve represents the noise floor of the measurement (which is higher than for the measurements in Fig. 132.103). The fluctuation levels behind the second shock appear comparable to those behind the first shock.

Velocity fluctuations on the first (leading) shock are known to diminish significantly when the shock melting starts. The purpose of the double-shock test is to see whether the second and third shocks that follow in the compression sequence accumulate further velocity fluctuations, owing to the mixed-phase state of the diamond ablator following passage of the first shock. An initial double-shock test performed during the CAPSEED-12A campaign suggests (Fig. 132.104) that subsequent shocks appear to have similar fluctuation levels as the initial shock. Further tests are needed to extend the data set.

Measuring the Adiabatic Index of Polystyrene Using Counter-Propagating Shocks and X-Ray Thomson Scattering

Principal Investigator: A. Pak
Co-investigators: T. Ma, L. Fletcher, T. Döppner, and S. H. Glenzer

The adiabatic index of a material γ is an important quantity in determining a material's equation of state (EOS), which describes the response in density and temperature of a material to a change in pressure (such as that created by a strong shock). Understanding the EOS of polystyrene, a material similar to the NIF ablator, at high densities (>4× solid) and at temperatures of several eV, is of interest since it may inform the design and performance of current implosion experiments. In the CH-HeatCap campaign on OMEGA, the electron density, temperature, and charge state of shocked polystyrene (CH) were directly measured with x-ray Thomson scattering (XRTS). Using the Hugoniot relationships for a single strong shock, γ can be experimentally determined by measuring the mass density of the shocked material. Additionally, the use of colliding shocks in this experiment allowed for γ to be measured at higher mass densities and temperatures than could be obtained using a single shock.

Figure 132.105(a) shows the experimental setup, in which six drive beams on each side drove counter-propagating shock waves into an initially 200-μm-thick polystyrene foil. The drive beams were each 1 ns long and delayed with respect to one another to create an ~3-ns-long pulse with an 800-μm spot diameter at an intensity of $\sim 1 \times 10^{14}$ W/cm^2. An additional eight co-timed laser beams with a 1-ns pulse width and a focused intensity of $\sim 1 \times 10^{15}$ W/cm^2 created a probe of zinc He$_\alpha$ x rays. The x rays scattered through the shocked CH and to the ZSPEC crystal spectrometer onto the framing-camera detector. The timing of the probe with respect to the drive was varied to probe the CH before, during, and after shock collision.

Figures 132.105(b) and 132.105(c) show the scattering spectrum at two different times: just before and after shock collision,

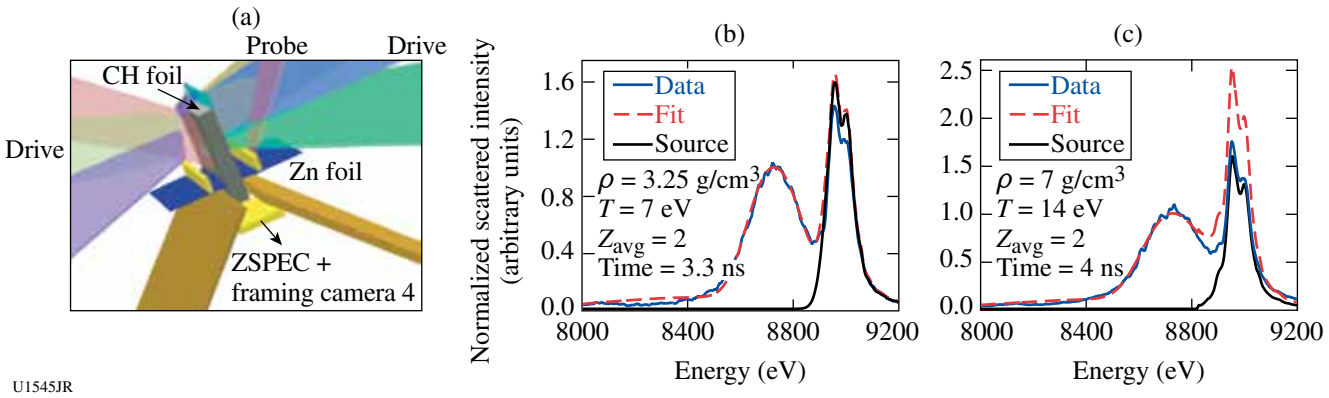

Figure 132.105
(a) Experimental setup. Two drive bundles compress the CH foil, while a probe bundle creates a burst of Zn He_α x rays that scatter through the target. Scattered x rays are collected via ZSPEC onto a framing camera detector in TIM-3. The normalized source and scattered x-ray intensity versus energy are shown (b) before and (c) after shock collision, respectively.

respectively. An increase in the width of the lower-energy, downshifted Compton feature indicates an increase in the material's electron density. Initial fits of the data indicate that a single shock density of 3.25±0.5 g/cm^3 and a 7±0.5 g/cm^3 density after shock collision have been reached. From this preliminary data analysis, the γ measured at the single- and double-shock density is 1.7 to 2.1 and 1.57 to 2.36, respectively. Additional data analysis is in progress.

In a second set of experiments, this time using OMEGA EP, a new experimental platform was developed to pursue similar physics. This year a total of four shot days in the BeXRTS and CH HeatCap campaigns were spent developing an experimental platform utilizing counter-propagating shocks and XRTS on OMEGA EP. One unique property of this class of experiments is that they allow for the adiabatic index γ of warm dense matter (WDM) to be directly measured. Additionally, counter-propagating shocks allow for materials to be compressed to higher densities and temperatures than single-shock experiments can create. A direct measurement of the γ of a material at densities and temperatures relevant to conditions existing in the ablator of NIF implosion experiments will contribute to the understanding, selection, and performance in ablator materials.

The experimental setup is shown in Fig. 132.106(a). In these preliminary experiments, a $200 \times 1000 \times 1400$-$\mu$m polystyrene (CH) foil was driven symmetrically from two sides by separate laser beams. Each drive beam had an ~351-nm wavelength, a 4-ns temporal width, and an average on-target intensity of ~1×10^{13} W/cm^2. Strong shocks, one from each of the two drive beams, counter-propagate with respect to one another and collide at the center of the CH foil. Two additional 1-ns-long UV laser beams are focused onto a zinc foil to create an

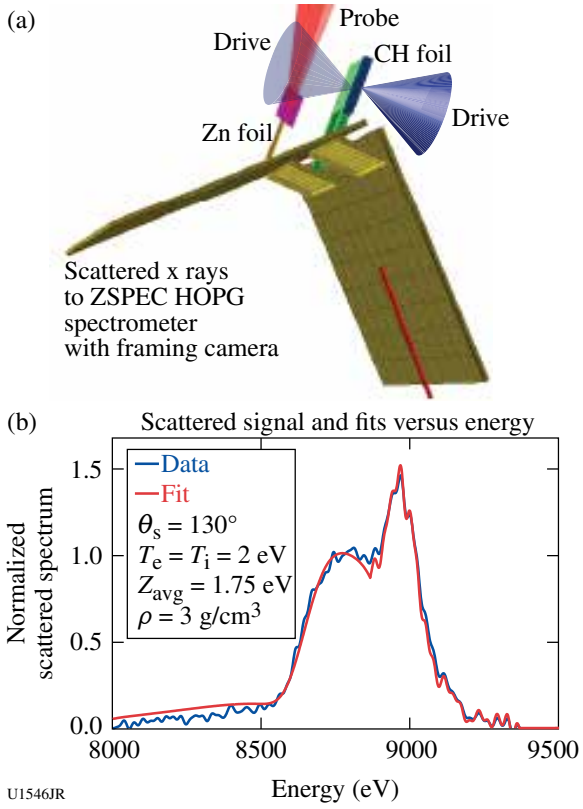

Figure 132.106
(a) The experimental setup for the XRTS OMEGA EP colliding-shock campaign. The CH foil is driven from the top and bottom by separate 4-ns-long UV laser beams with $I_0 \sim 1 \times 10^{13}$ W/cm^2. The counter-propagating shocks are diagnosed using Zn He_α x rays created from one or two probe UV laser beams. The scattered x rays travel through a target aperture to the ZSPEC highly oriented pyrolytic graphite (HOPG) crystal spectrometer and onto a framing camera. (b) An example of the measured scattered x-ray signal plotted versus energy taken 4.5 ns from the start of the laser drive. The fit of the scattered signal (red line) indicates that $\rho = 3$ g/cm^3, $T = 2$ eV, and $Z_{avg} = 1.75$ eV.

x-ray probe pulse. The Zn He_α x rays scatter from the shock-compressed CH foil through a gold aperture in the bottom of the target to the HOPG ZSPEC crystal spectrometer and onto a framing-camera detector that records the scattering signal over ~500 ps. Figure 132.106(b) shows an XRTS spectrum obtained at 4.5 ns after the laser drive had begun. The initial fit is in good agreement with predicted values for the density, temperature, and charge state from 2-D *HYDRA* simulations at this time. Additional analysis of the data is ongoing at this time.

Ablator Opacity Measurements

Principal Investigator: R. F. Heeter
Co-investigators: A. Graf, G. V. Brown, C. Mauche, R. E. Marrs, and B. Wilson

A new effort was initiated in FY12 to validate models of x-ray absorption and re-emission of capsule ablator materials, including germanium, silicon, and glow-discharge–polymer (GDP) plastic, over x-ray energies and material conditions typical of inertial confinement ablation plasmas. Experiments were undertaken using two platforms: First, the high-energy-density (HED) hohlraum-based opacity platform on OMEGA was used to assess the transmission opacity of Si, Ge, and GDP samples in LTE (local thermodynamic equilibrium) at T = 100 eV at densities around 0.03 g/cm^3. The second platform was launched in FY12 on OMEGA EP using dual short-pulse backlighters to measure the x-ray transmission of buried silicon layers embedded in plastic samples. This newer OMEGA EP technique is able to achieve both higher densities and higher temperatures than the OMEGA technique, but it requires tuning to achieve uniform sample conditions.

Sample data from the initial OMEGA experiments are shown in Fig. 132.107. For both Si and Ge samples, the transmission data for the spectral band from 250 to 1500 eV came in below the expected transmission calculated with standard opacity models using the plasma conditions predicted by 2-D radiation–hydrodynamic simulations. These plastic-tamped samples appear to be cooler and denser than expected, indicating either slower ablation and heating than predicted or a substantial error in the opacity models.

In late FY12, a series of follow-up shots were completed, including a tuned-up target design and independent characterization of the plasma conditions. Those data are currently being analyzed. Additional platform improvements, focused on reducing the noise in the transmission measurements, were implemented for beryllium-tamped, Si-doped GDP (plastic) opacity shots taken in early FY13.

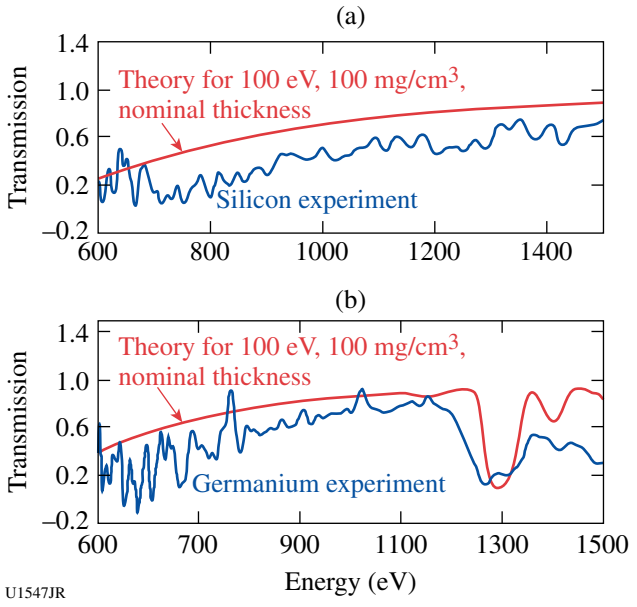

Figure 132.107
Initial results from (a) silicon and (b) germanium transmission experiments on OMEGA with comparison to expected transmissions.

Meanwhile, success was also achieved in obtaining dual-axis transmission spectra for silicon samples. In this new platform, up to two of the OMEGA EP UV beams are used to heat a CH-tamped Si foil with up to 200 J delivered in a Gaussian pulse shape with 100-ps FWHM (full-width-at-half-maximum). Peak sample temperatures of up to 400 eV are inferred from the time-integrated emission spectra of the embedded Si foil. Shortly after the UV heating pulse, a 10-ps IR laser drives a Zn wire backlighter, producing a bright continuum x-ray source with 16-ps FWHM duration and roughly 20-μm source size. This backlighter probes the expanding silicon plasma edge-on, measuring the sample expansion to yield the plasma density, and measuring the ionization state via absorption spectroscopy to provide information on the sample temperature. A second 10-ps continuum backlighter, synchronized to within 30 ps of the first, probes the sample face-on, delivering precise transmission spectral data for the measured temperature and density. Initial transmission measurements were completed in FY12 and are now being compared with theory.

Furthermore, by choosing a relatively thin tamper layer thickness, it is possible to tailor nonuniform density profiles and study the density of specific charge states as a function of position in an expanding ablated plasma. A sample of the latter data is shown in Fig. 132.108. In this case, 100 J of UV laser energy, arriving from the upper side of the image, heated the sample for 100 ps. The image was recorded roughly 400 ps

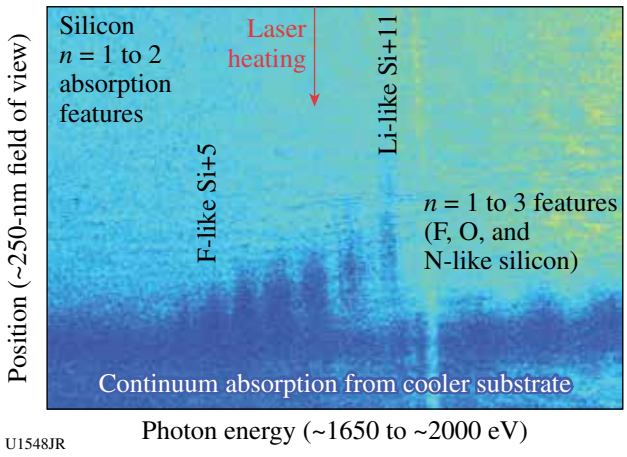

Figure 132.108
Space-resolved absorption spectrum obtained on OMEGA EP using edge-on broadband radiography of a silicon foil deposited on a carbon substrate and overcoated with a thin CH tamper layer.

after peak drive, during the cooling of the silicon plasma. The n = 1 to 2 absorption features of multiple ionization states of silicon are visible on the left (lower-energy) side of the spectrum, with additional n = 1 to n = 3 features on the right (higher-energy) side. The data show that 400 ps after peak sample drive, lithium-like Si persists on the low-density, laser-heated side of the plasma, while the various charge states of L-shell ions (Be- through F-like) are observed deeper into the plasma at higher density. The typical density at the location of the L-shell features is about 0.1 g/cm^3. The laser appears to not have fully heated the carbon substrate and perhaps some of the silicon, so continuum absorption from the rear of the sample is also visible. This technique is now being applied to study x-ray–ablated, silicon-doped GDP ablator plasmas in FY13.

Multipump Stimulated Raman Scattering

Principal Investigator: R. Kirkwood

The second campaign in this series was carried out to investigate the cooperative interaction of multiple beams in a cone to drive stimulated Raman scattering (SRS). The experiments used exploding-CH foil targets preheated by 11 heater beams to create a symmetric density profile. A normally incident seed beam was focused on the back side of the foil where it could produce SRS backscatter with a total power waveform as shown in the "seed beam only" case in Fig. 132.109. When (in a separate experiment) the seed beam was intersected by a cone of two to six pump beams that were pointed to cross the seed on the front side of the foil (where the density and temperature would allow further re-amplification of the SRS), a significant enhancement in the scattered power was observed. The

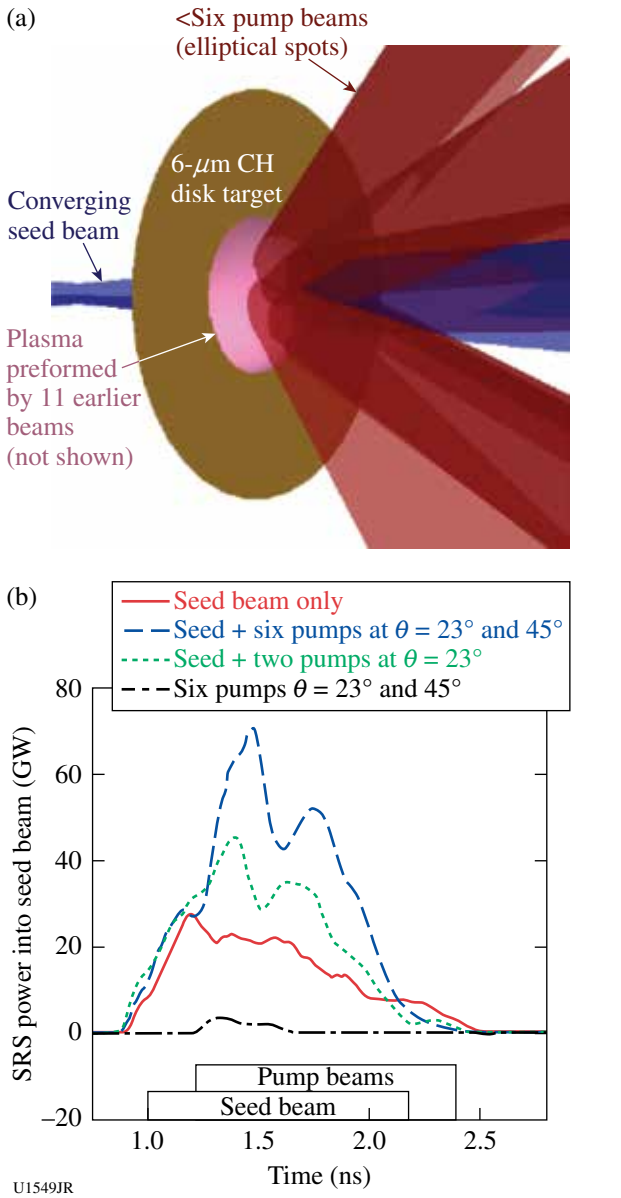

Figure 132.109
The geometry and measured SRS backscatter of a seed beam in the presence of different numbers of pump beams, from the SRS multipump experiments.

enhanced level of power was seen to increase with the number of pumps as expected from models of SRS re-amplification, and the total peak SRS was significantly greater than the sum of the SRS observed in both "seed only" and "six pumps" cases, as also shown in the figure. The overall increase in SRS with all beams cannot be explained by the simulated change in absorption by the plasma due to the pump beams and has the magnitude expected for SRS re-amplification. The experiment has provided an important benchmark for models of multibeam stimulated Raman scattering from ignition experiments.

Comparison of Plastic and High-Density Carbon Ablator Performance

Principal Investigator: S. Ross

The HDCEnerg-12A campaign successfully compared high-density carbon (HDC) and CH ablator performance. A series of OMEGA experiments with three distinct pulse shapes were used to investigate HDC and CH performance. The pulse shapes were designed to deliver different drive pressures during the foot of the laser pulse. The pulses delivered foot pressures ranging from ~1.7 Mb (LA234002) to ~7.5 Mb (LA190801) with an intermediate pressure of ~3.6 Mb (LA232301). The capsules were filled with either 40 atm or 20 atm of deuterium. The measured neutron yield is shown in Fig. 132.110.

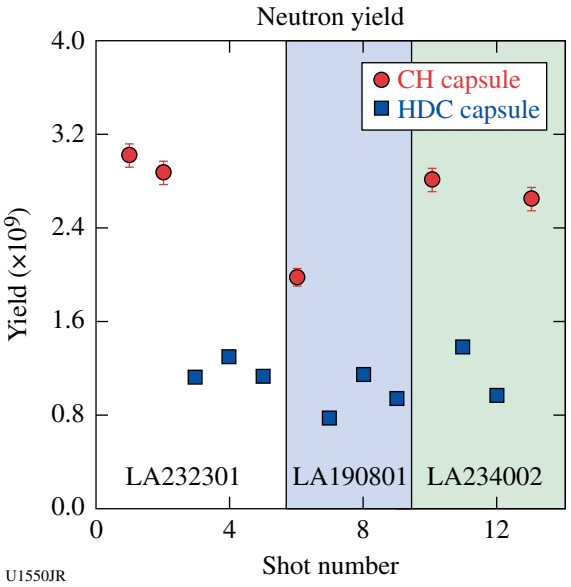

Figure 132.110
The measured neutron yield for different capsule materials and pulse shapes.

The HDC capsules showed very similar neutron yields for all three pulse shapes. This is evidence that the capsule's compression and performance are independent of the pressure in the laser foot for pressures ranging from 1.7 Mb to 7.5 Mb. The difference in HDC and CH yields are expected because of differences in capsule thickness. These results are being used to design future HDC experiments.

Shock Release of ICF-Relevant Materials

Principal Investigator: D. E. Fratanduono

Inertial confinement fusion (ICF) capsule implosions are driven by four shock waves. The strength and timing of each shock are controlled to maintain a low adiabat. High-pressure (>1-Mbar) equation-of-state (EOS) experiments on ICF ablators have been primarily limited to Hugoniot measurements. These experiments focus on developing a technique to measure the release isentropes of ICF-relevant materials in order to better constrain the EOS of ICF-relevant materials.

Experiments are performed at the Omega Laser Facility. Target design consists of a glow-discharge polymer (GDP, an ICF ablator), and a thin (~50-nm) silicon nitride film separated by a vacuum or gas-filled gap (~250 μm) as shown in Fig. 132.111. A strong shock (>250 GPa) is generated in the GDP ablator. When the shock breaks out of the sample and into vacuum, it releases and isentropically expands as it propagates across the gap. When the strong shock in the GDP enters the gas-filled void, a weak shock is generated and propagates across the gap. By measuring the shock state of the gas, a point on the GDP release isentrope is determined. The released material stagnates on the silicon nitride. The velocity of the silicon nitride is measured using a velocity interferometer system for any reflector (VISAR). Using the measured velocity profile, a momentum balance technique is employed to extract information regarding the release isentrope.

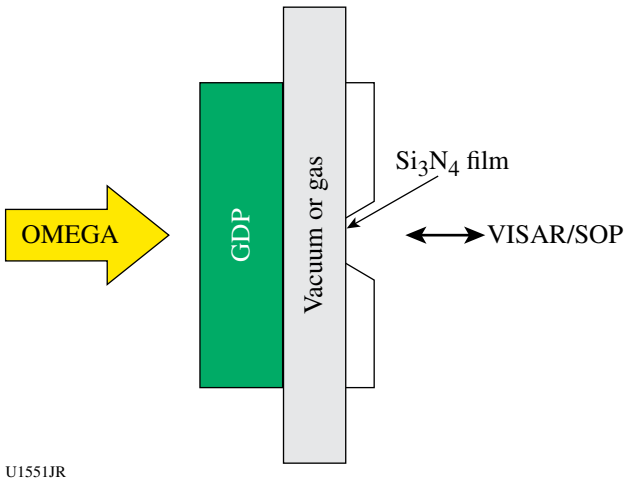

Figure 132.111
Target design.

The vacuum results indicate that the velocity of the leading edge of the release isentrope is traveling ~30% faster than predicted by the LEOS tables. This behavior has been observed on CH, GDP, and diamond. These results are shown in Fig. 132.112. The gas (methane)-filled results are consistent with Hugoniots generated from LEOS tables. However, the data at lower-pressure shock states are inconsistent with the vacuum measurements. Further experiments are being performed to examine this discrepancy. We are in the process of designing

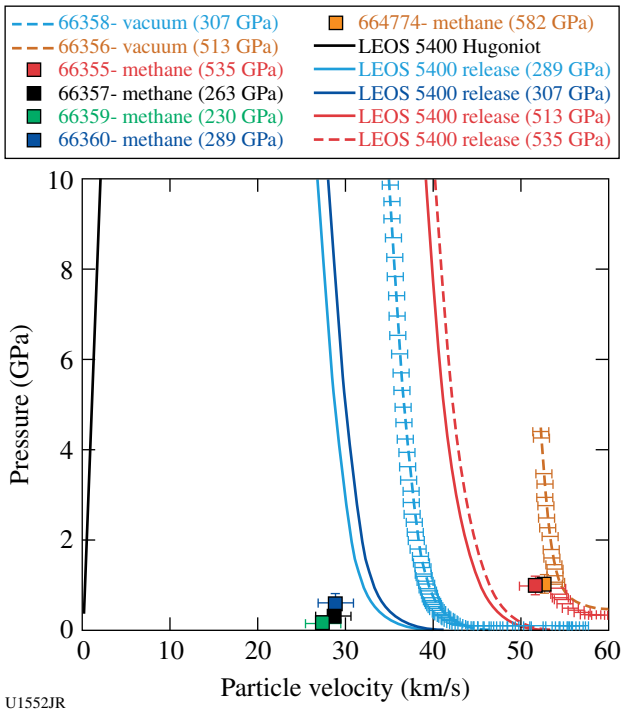

Figure 132.112
Glow-discharge–polymer release isentropes.

targets to measure the release of D_2 ice into low-density D_2 gas. Using this technique, we may be able to determine species separation for DT.

High-Energy-Density Experiments

1. Material Dynamics and Equation of State

Tantalum Rayleigh–Taylor Experiments

Principal Investigators: H.-S. Park and C. Plechaty

The focus of the ICETaRT campaign was to study Ta material strength at high pressure (>1 Mbar) and high strain rates (10^6 to 10^8 s^{-1}). To achieve these conditions in the experiment while keeping the temperature of the Ta sample well below melting, a reservoir and vacuum gap[75] configuration was employed to produce a quasi-isentropic pressure drive (see Fig. 132.113). The plasma drive was produced by ablating a hohlraum with 40 OMEGA beams to deposit a total energy of 20 kJ. Attached to the side of the hohlraum was an ablator/reservoir and a physics package, which were separated by a vacuum gap to produce ramped drive conditions onto the physics package.

The physics package consisted of a CH heat shield placed on a Ta sample. Sinusoidal perturbations were imposed on the

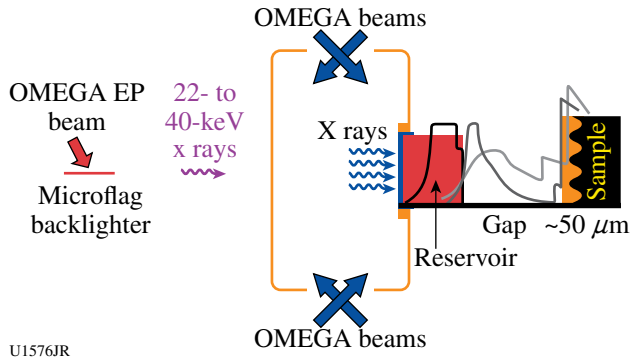

Figure 132.113
Experimental configuration employed for OMEGA EP joint shots. OMEGA beams deposited energy into the hohlraum, producing a plasma drive. Face-on high-energy radiography was employed on the rippled Ta sample by using a short-pulse OMEGA EP beam to ablate an Ag backlighter. For OMEGA shots, the rippled Ta sample was replaced by a VISAR witness sample to characterize the plasma drive.

surface of the Ta. As the plasma from the reservoir crosses the gap and stagnates on the sample package, the Ta ripples undergo an effective acceleration from the stagnating plasma drive. This acceleration actuates Rayleigh–Taylor (RT) growth of the pre-imposed sinusoidal pattern. Since the Ta material strength acts to suppress the amount of RT growth, measuring the RT ripple amplitude gives a measure of the material strength.[75–77] To measure the perturbation amplitude, face-on high-energy (22-keV Ag K_α) radiography was employed using an OMEGA EP short-pulse beam. We needed the OMEGA EP beam to employ a high-energy backlighter (22 keV) to probe the high-Z tantalum material. The amount of backlighter transmission through the ripples is governed by the quantity $\rho\Delta Z$, where ρ is the density of the driven ripples and ΔZ is the amplitude. The RT growth factor (GF) is determined by measuring the driven $\rho\Delta Z$:[75,78]

$$\mathrm{GF} = \frac{(\rho\Delta Z)_{\mathrm{driven}}}{(\rho_0 \Delta Z_0)_{\mathrm{undriven}}\,\mathrm{gMTF}}, \tag{1}$$

where ρ_0 and ρZ_0 are the initial density and ripple amplitude (determined from pre-shot metrology) and the MTF is the modulation transfer function, which characterizes the frequency response of the system and is measured by using a knife edge. To determine the properties of the plasma drive, separate shots without the backlighter were performed by replacing the physics package with a witness sample and taking VISAR measurements.

The FY12 ICETaRT campaign employed the experimental setup discussed above to study several aspects of Ta material

strength. The first topic studied was the Ta material failure threshold. In previous experiments, we observed (Fig. 132.114) that as the relative growth increased, defined as the ratio between the ripple amplitude and the Ta sample thickness, the measured relative growth deviated from that predicted by the multiscale model.[79] To study the threshold where the relative growth measured in the experiment deviates from that predicted by the multiscale model, or measure the threshold where failure occurs, a three-amplitude pattern was employed. The Ta sample was split into three regions, each with a 50-μm wavelength, but with a different amplitude—namely, 1.0, 2.0, and 3.5 μm. We found that failure occurred as the relative growth in experiment exceeded ~20%.

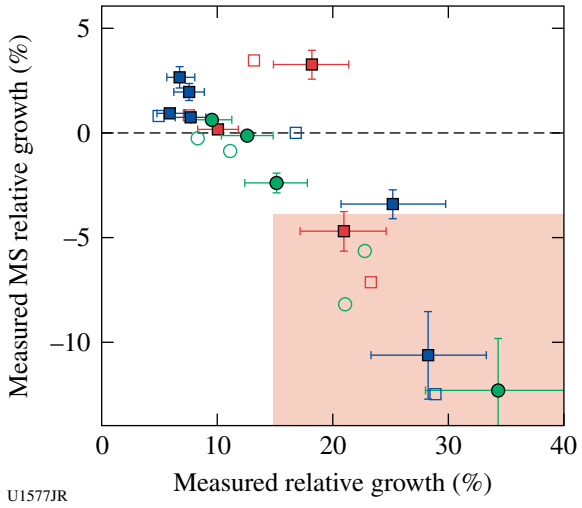

Figure 132.114
Plot of measured relative growth (RG) versus the deviation of the measured relative growth from that predicted by the multiscale (MS) model. The colored box in the lower right-hand corner denotes where the absolute value of this difference becomes >4%. This is defined as failure.

The second topic studied was a comparative material strength study between Ta [100] and Ta [111] crystal orientations. In previous studies[80] the target samples were predominantly in the [111] orientation. In the multiscale model, crystal orientation can affect material strength via the Taylor factor. To understand the effect of crystal orientation on the material strength, we placed the two samples side by side and compared the ripple growth for a given shot (see Fig. 132.115). Initial results from just a few shots suggest that the difference in the growth factor between these two crystal orientations is too small to be measured within our error bars of ~18%.

Lastly, the final topic of study undertaken in the FY12 ICETaRT campaign was the study of a new multimode configuration (Fig. 132.116). A superposition of two different sinusoidal ripple patterns was imposed on the Ta sample. The two modes employed had the same amplitude (1.85 μm) but different wavelengths (75 and 112 μm, respectively) and phases (210° and 24°, respectively). The purpose of this study was twofold. The first purpose was to study the coupling of RT growth between the modes. For example, the growth of the designed modes with wave vectors k_1 and k_2 induced growth at $|k_1 \pm k_2|$, $2k_1$, and $2k_2$. The exact details of the coupling are not fully understood. Second, by using multiple modes, the multimode configuration can be used to produce simultaneous Rayleigh–Taylor (RT) measurements, with corresponding strengths. A detailed analysis of this data is currently underway.

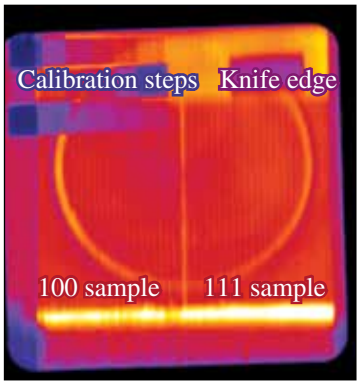

Figure 132.115
Radiography image of [100] and [111] target configuration. The 100 sample is on the left, and the 111 sample is on the right. The calibration steps are employed to relate the backlighter transmission to a specific value of $\rho\Delta Z$. The knife edge is used to determine the MTF. The circular structure in the middle is a hole in the hohlraum and indicates where the plasma drive can stagnate onto the sample, driving RT ripple growth.

Iron Rayleigh–Taylor Experiments
Principal Investigator: C. Plechaty

The ICEIronRT campaign focused on the study of iron material strength at high pressures and strain rates when a phase transition occurs at lower pressures (~100 kbar). The goal was to understand the strength parameter difference at high pressure when a phase transition occurs from the α-to-ε phase at a lower pressure level.

For ICEIronRT, we employed a quasi-isentropic plasma drive produced by a reservoir–gap–sample configuration.[76] A newly designed 6% BrCH reservoir was employed to achieve pressures up to ~1.5 Mbar. In the experiment, 40 OMEGA beams (with a total energy of 20 kJ) were employed to ablate a hohlraum with a side-mounted reservoir–gap–sample pack-

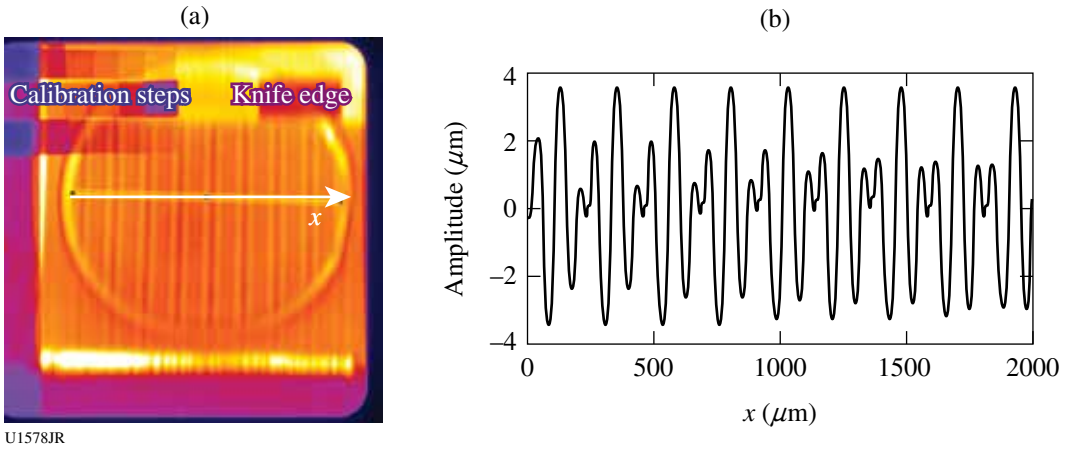

Figure 132.116
(a) The radiography image obtained for this multimode configuration; (b) an ideal plot of the ripple structure for $0 < x < 2000$ μm.

age in order to produce a plasma drive. As the plasma drive crossed the vacuum gap, it stagnated onto the Fe sample with an imposed sinusoidal pattern on the surface. The stagnation of the plasma drive onto the Fe sample drives Rayleigh–Taylor (RT) growth of the ripples where the observed RT growth rate is dependent on the strength.

To obtain the quantities listed in Eq. (1), $\rho_0\Delta Z_0$ was derived from pre-shot Veeco measurements and the MTF was measured using a knife edge (Fig. 132.117). To measure $\rho\Delta Z$ for the driven sample, face-on high-energy (22-keV) radiography was employed using an Ag microflag backlighter ($200 \times 200 \times 5$ μm). A short-pulse (100-ps) OMEGA EP beam was employed to ablate the backlighter with a 1.0-kJ pulse delivered with a given time delay in respect to the OMEGA drive beams. To resolve the ripple growth, the thinnest side of the backlighter was aligned along the direction of the ripples.

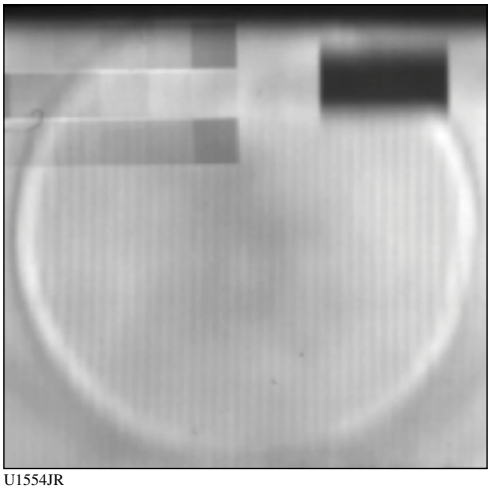

Figure 132.117
A radiograph for shot 67210 (60-ns delay). The iron calibration steps, located in the upper left-hand corner, are used to relate the backlighter transmission to a specific value of $\rho\Delta Z$. The knife edge located in the upper right-hand corner is used to measure the MTF. The circular feature in the middle of the image indicates the region of driven ripple growth.

In addition to joint OMEGA EP shots, OMEGA-only shots were performed to determine the properties of the plasma drive. In these shots, the Fe sample was replaced with a witness sample and VISAR measurements were performed.

Figure 132.118 compares the undriven ripple $\rho_0\Delta Z_0$ and the driven ripple $\rho\Delta Z$. As shown, $\rho\Delta Z > \rho_0\Delta Z_0$, indicating that the driven ripples have undergone RT growth. The GF, calculated

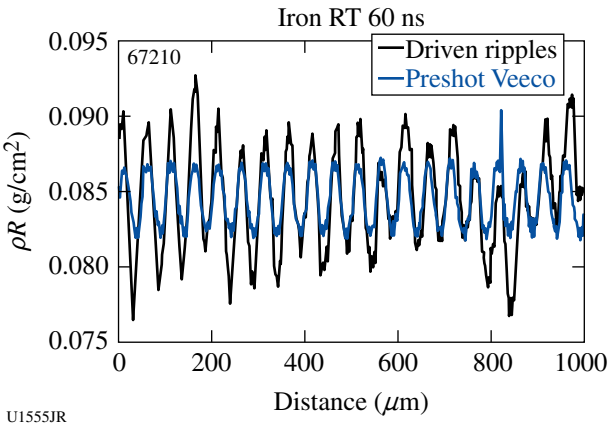

Figure 132.118
Comparison of the pre-shot values of $\rho_0\Delta Z_0$ and the shot values of $\rho\Delta Z$ for a 60-ns delay between the OMEGA drive and OMEGA EP backlighter beams.

with Eq. (1), is shown in Fig. 132.119 with error bars of ~±50%. An initial analysis indicates that the iron material strength is higher than that predicted using a hybrid α-to-ε phase-transiting Preston–Tonks–Wallace (PTW) strength model[81] calculated using our experimental condition of ~1.5-Mbar pressure and strain rate >10^6 s^{-1}.

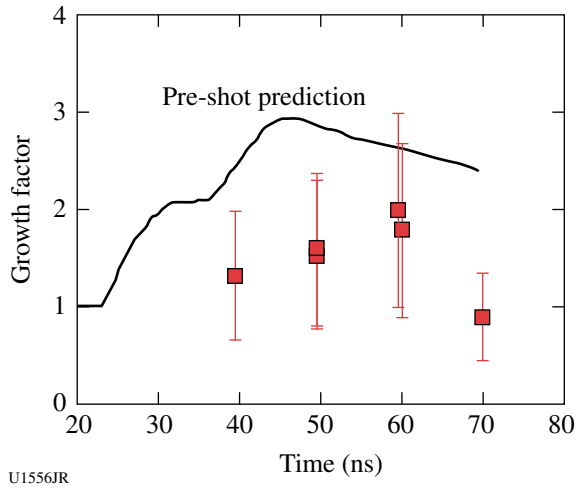

Figure 132.119
Comparison between the GF (with error bars of 50%) and the GF prediction obtained from a hybrid α-to-ε transition PTW model.

Double-Pulse Radiography Development

Principal Investigator: C. Plechaty

Laser-driven, high-energy (>22-keV) x-ray radiography has been employed as a diagnostic tool in many different types of high-energy-density (HED) experiments with applications ranging from material strength studies[75,78,82,83] to capsule implosion experiments. In FY12, the DBLPULSE campaign focused on the development of a new multiframe radiography technique that takes advantage of the multiple beams available at state-of-the-art laser facilities such as Omega and the NIF. This concept is of particular importance to the NIF and HED programs since it will yield twice the amount of data per shot.

Experiments were performed on OMEGA EP using two short-pulse (100-ps, 100-μm spot size) beams to independently ablate two 300 × 300 × 10-μm foils (Cu and Ag) placed 1.2 mm apart (Fig. 132.120). In the experiment a 1-kJ beam was employed to ablate the Cu backlighter. After delayed time t, the Ag backlighter target was irradiated by a 1.5-kJ beam. The performance of the two time-delayed x-ray pulses were tested by radiographing a Au grid pattern placed 10.3 mm from the foils. To obtain two distinct images of the grid pattern, a collimator was employed. The collimator consisted of a 1-mm-thick Au disk, with two tapered holes to act as pinholes for each backlighter. The surface of the collimator was placed 3.2 mm from the center of the foils. The angle of the holes was chosen such that two distinct and spatially separate images were produced at the location of the image plate (IP), placed ~500 mm from the foils.

To characterize the frequency response of the system, we employed a Au grid pattern that consisted of several orthogonal mesh elements, each with different spatial scales. The Au grid had 10-, 20-, 30-, 40-, and 80-μm mesh features, aligned along the horizontal and vertical axes of the grid. The Cu and Ag foils were mounted orthogonal to each other and the IP such that each backlighter would produce a 1-D orthogonal x-ray source aligned along either the vertical or horizontal axis of

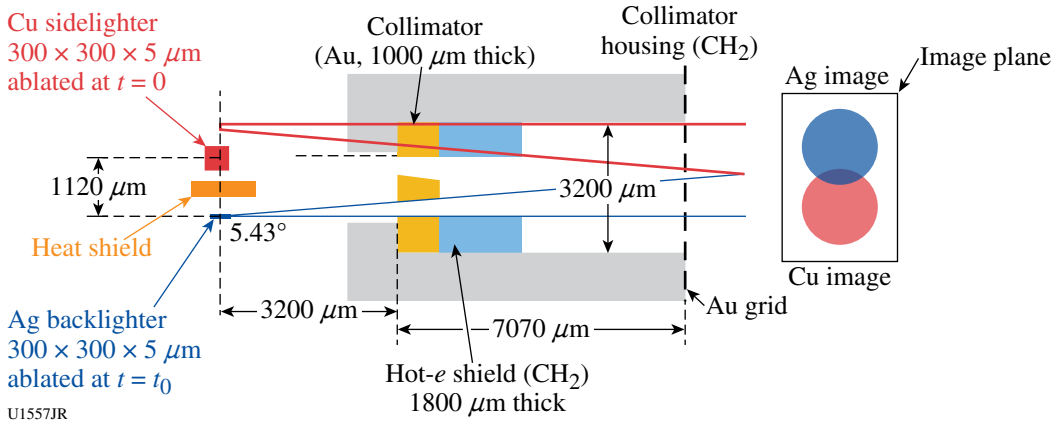

Figure 132.120
Schematic of experimental setup. X rays from the two independently ablated backlighter foils pass through a collimator assembly. This produces two temporally and spatially independent images of an Au grid on an image plate.

the Au grid. The IP was placed far enough away so that two spatially distinct images were captured.

To protect the second backlighter target from the hydrodynamic expansion and x-ray emission from the first backlighter, a heat shield was placed between the foils on a separate target positioner.

Radiography images captured using this configuration are shown in Fig. 132.121. In Figs. 132.121(a)–132.121(c), the heat shield employed was a 1000 × 1000 × 200-μm-thick CH heat shield. At $t = 0$ ns [Fig. 132.121(a)] the 10-, 20-, 30-, and 80-μm features are clearly visible in the Cu (top) image. In the Ag (bottom) image, the 10- and 30-μm features are observed, while the other features are located out of the instrument field of view. At $t = 5$ ns [Fig. 132.121(b)], the image produced by the delayed backlighter is observed to degrade; only the 30-μm features are visible. This trend continues when $t = 20$ ns [Fig. 132.121(c)], where the Ag backlighter resolution has degraded enough so that the grid features are not observed.

An explanation for the reduction in the image quality can be found by examining the time-integrated x-ray pinhole camera (XRPHC) images (Fig. 132.122). As shown by Fig. 132.122, the Ag backlighter x-ray source size becomes notably larger for the $t = 20$ ns case [Fig. 132.122(c)] when compared to the $t = 0$ ns case [Fig. 132.122(b)], causing the delayed image quality to degrade.

Since the CH heat shield employed for the images captured in Figs. 132.121(a)– 132.121(c) is transparent to laser backscatter and x-ray emission from the $t = 0$ ns backlighter, it was replaced by a 1000 × 1000 × 50-μm Au heat shield [Fig. 132.121(d)]. When employing this heat shield design, the resolution of the delayed backlighter only slightly increases. Employing an even thicker Au heat shield (1000 × 1000 × 200 μm) does not yield better system resolution.

Since the 50-μm-thick and 200-μm-thick Au heat shields prevent a significant portion of the low-energy x-ray emission from the Cu backlighter from reaching the Ag backlighter, the observed preheating of the Ag backlighter is likely caused by radiating plasma expansion. As the Cu backlighter is ablated, the resulting plasma expands past the heat shield and radiates. This causes the Ag backlighter to be preheated, producing plasma and increasing the x-ray source size once the backlighter is ablated. A future study will investigate this effect.

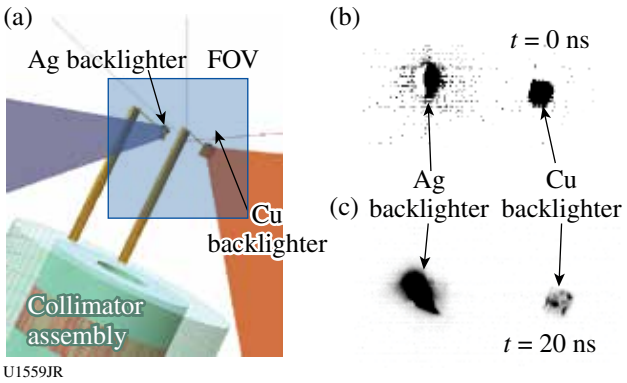

Figure 132.122
XRPHC images. (a) Image geometry showing the Cu beam and backlighter (on the right) and the Ag beam and backlighter (on the left). The field of view (FOV) for the XRPHC images is shown. The captured time-integrated images are shown in (b) for the case of $t = 0$ ns and (c) for the case of $t = 20$ ns.

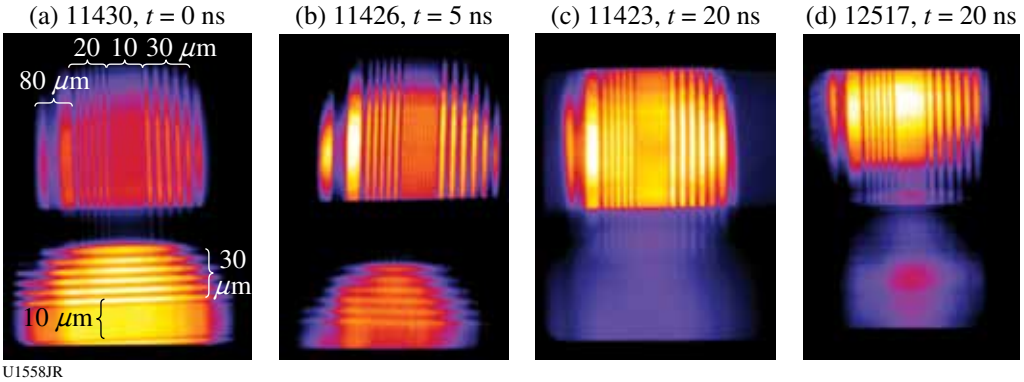

Figure 132.121
Images obtained with the HERIE. In these images, the top image was produced by the Cu backlighter, which is always taken at $t = 0$ ns. The bottom image was produced by the Ag backlighter, which ablates the foil at the time shown. [(a)–(c)] A 1000 × 1000 × 200-μm-thick CH heat shield was employed; (d) a 1000 × 1000 × 50-μm-thick Au heat shield was employed.

Diffraction Studies on Shocked Tantalum

Principal Investigators: B. Maddox, A. Comley, and C. Wehrenberg

Three distinct experiments were conducted to study the behavior of shocked and ramp-loaded tantalum.

StrDiff-12A: The goals of the StrDiff-12A campaign were to observe twin formation in single-crystal Ta shocked along the [110] direction, obtain large-pinhole diffraction for a quantitative temperature analysis of shocked Ta, extend out previous measurements of the lattice anisotropy of Ta shocked along [100] to lower peak pressure, verify our simulations using a stepped diamond drive target, and test a glueless target for future studies of shock- and ramp-compressed Ta. The experiment used the broadband x-ray diffraction diagnostic (BBXRD) on TIM-4 as the primary diffraction diagnostic, as well as the tilted VISAR. Crystal samples were driven using a single beam (Beam 18) with an SG8 phase plate. The x rays for diffraction were produced by an imploded CH shell driven by 44 beams with SG4 phase plates. All beams used a 1-ns square pulse. We achieved 12 shots and obtained excellent data. Due to the initial crystal sample quality of the Ta [110] samples, we were unable to observe any useful driven diffraction patterns for Ta shocked along [110] and, therefore, observed no twinning. However, all other experimental goals were met. In this campaign, we recorded our highest-quality Laue diffraction pattern to date, detecting up to seven compressed diffraction spots on a single side of the BBXRD detector (shown in Fig. 132.123).

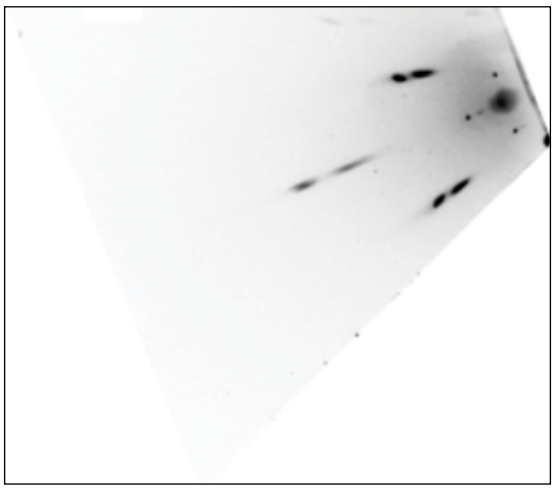

U1560JR

Figure 132.123
Example of high-quality Laue diffraction recorded from Ta single-crystal shock compressed to ~0.5 Mbar along the [100] direction.

ShkLaue-2012: In ShkLaue-2012 our goal was to extend previously successful strength measurements of shocked Ta using *in-situ* Laue diffraction to ramped-loading conditions, allowing us to compare our measurements to Rayleigh–Taylor strength experiments with similar strain rates. As in previous ShkLaue campaigns, the BBXRD diagnostic was used to record Laue diffraction data, giving a direct measurement of lattice anisotropy and shear strength of the material. A reservoir drive was developed in which a directly driven brominated-CH reservoir releases across a gap and creates a ramped stagnation shock on the Ta sample. A new glueless target design was also developed for this campaign, in which the Ta samples were kept on the MgO substrate and the substrate was polished down to the desired thickness. This design allowed us to record high-quality VISAR data simultaneously with Laue diffraction data. Initial analysis shows that the reservoir drive was successful in creating the ramped drive, which demonstrated highly repeatable behavior. High-contrast diffraction data were recorded for a range of drive times and show a range of lattice anisotropy ratios.

EP-TaBragg-2012: In EP-TaBragg-2012 our goal was to study shock-compressed Ta using *in-situ* Bragg diffraction, building on the successful BraggDiff-2011 campaign. The experimental configuration used the Lawrence Livermore diffraction imager as the primary diagnostic on TIM-13. Samples were driven using two defocused beams with a 10-ns pulse, while a short-pulse beam was used to drive a silver backlighter to create the high-energy x rays. There were a few issues in adjusting the drive-backlighter relative timing, producing an imbalance in the signal strength in either the driven or static diffraction signal in the initial shots. This issue was solved by comparing VISAR data with previous campaigns, resulting in a 0.5-ns shift from previous experiments. The data quality obtained was excellent and, combined with BraggDiff-2011 data, provides a range of pressures for Ta strength measurements.

Ta X-Ray Diffraction

Principal Investigators: A. Lazicki, J. H. Eggert, and J. R. Rygg

In FY12 powder x-ray diffraction experiments (Fig. 132.124) on solid ramp-compressed tantalum yielded additional data points confirming a high-pressure phase transition near 300 GPa (Fig. 132.125). The structure was determined to be consistent with a predicted simple hexagonal (ω) phase.[84,85] During the shot day, we ramp compressed Ta and Fe samples to pressures above 10 Mbar. The technical difficulties encountered while trying to measure x-ray diffraction at these high pressures

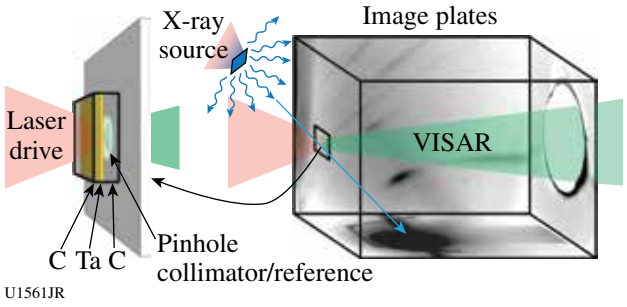

Figure 132.124
X-ray diffraction experimental setup. The target consisted of a 4-μm foil of Ta sandwiched between single-crystal diamond plates. The x-ray source was laser-excited He_α radiation from Fe or Cu thin foils. X rays diffracted off of the Ta sample were scattered onto the inner surfaces of a box lined with image plates, yielding crystal structure and volume. Target rear-surface velocities were detected using VISAR, yielding pressure.

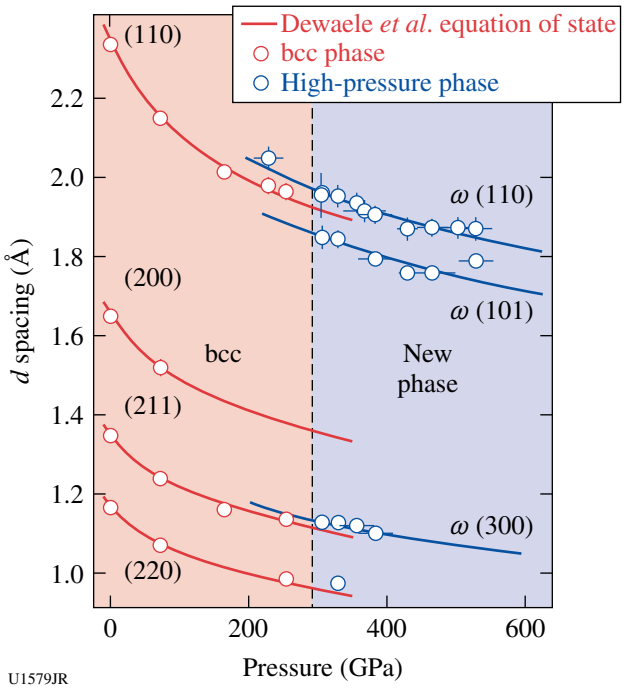

Figure 132.125
Shift of the d spacings of x-ray diffraction peaks under pressure showing evidence of a new phase at 300 GPa.

have provided critical feedback for our design of terapascal-range x-ray diffraction experiments on the NIF.

Hydrogen Equation of State

Principal Investigators: A. Lazicki, M. Millot, J. R. Rygg, and J. H. Eggert

The purpose of this study was to look for pressure-induced chemistry in deuterium by electron doping from an added ~5% of xenon, evidenced by the effects on the Hugoniot and the reflectivity, compared to pure deuterium. Gas mixtures were precompressed to fluid deuterium density in a diamond anvil cell prior to shock compression. Measurements (Fig. 132.126) reveal a Hugoniot shifted to higher density but not to the extent predicted by a simple linear mixing model, indicating chemical interaction between the species. There is, however, some uncertainty in the concentrations of gas captured in the diamond cells, so the conclusion awaits further experiments. Because of difficulties in sample preparation, some of the shots were devoted instead to the measurement of the Hugoniot of the hydrogen compound lithium hydride (Fig. 132.127), precompressed to 5 to 9 kbar in a diamond anvil cell. Results will aid in refinement of equation-of-state models.

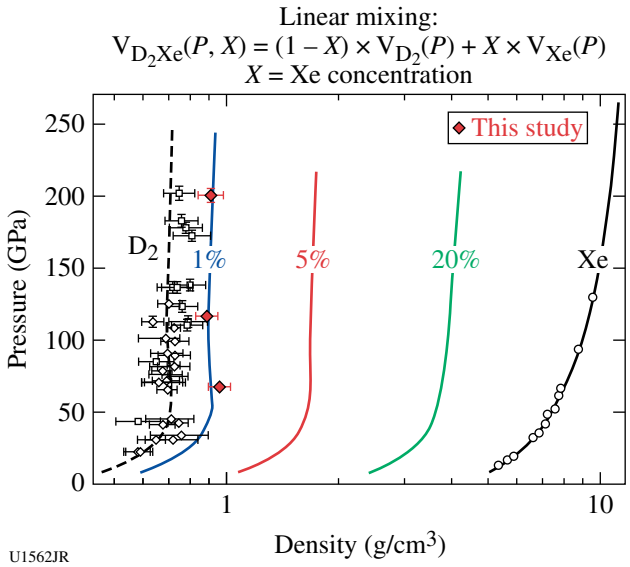

Figure 132.126
Hugoniot of D_2 (Ref. 86) and Xe (Ref. 87) compared with the data from this study. Curves predicting the behavior the mixture are based on the linear mixing model.

XAFS Study of Ramp-Compressed Fe, Ta, and Mo

Principal Investigator: Y. Ping
Co-investigators: F. Coppari, D. G. Hicks, D. E. Fratanduono, S. Hamel, J. H. Eggert, J. R. Rygg, R. F. Smith, D. C. Swift, and G. W. Collins (LLNL); B. Yaakobi and T. R. Boehly (LLE)

Extended x-ray absorption fine structure (EXAFS) measurements of dynamically compressed iron have been performed on OMEGA using an implosion backlighter. Iron is compressed in the solid state to 560 GPa (5.6 Mbar), the highest solid-state pressure for iron explored in the laboratory (Fig. 132.128). EXAFS measurements provide simultaneous density, tem-

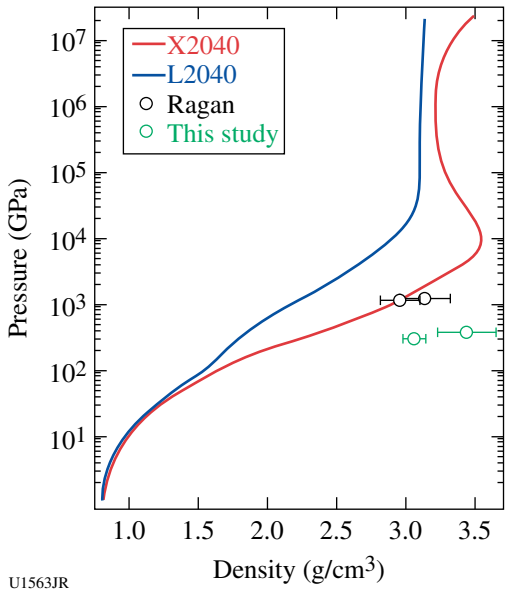

Figure 132.127
Hugoniot of LiH from EOS models, compared to experimental data.[88] The data shown from this study are for LiH precompressed to ~6.5 kbar.

perature, and local-structure data for compressed iron in this new regime—the first such data for constraining solid-state theory and evolution models for many newly discovered extra-solar terrestrial planets. The data show that the close-packed structure of iron is stable up to 560 GPa, the temperature at peak compression is significantly higher than expected from pure compressive work, and the strength of iron is many times greater than expected from lower-pressure data.[89]

Based on the success of EXAFS measurements of iron, we have extended this platform to study L edges of Ta and Mo. Data on Mo at ambient conditions, 2 Mbar, and 3 Mbar have been obtained, and EXAFS of undriven Ta has been observed for the first time on OMEGA. The last campaign in September 2012 demonstrated 2× enhancement in backlighter brightness and 4× enhancement in the spectrometer efficiency, making it possible to do single-shot EXAFS measurements of driven Ta in FY13.

Tin Melt

Principal Investigator: A. Lazicki

Campaigns investigating the high-pressure solid crystal structure and probing the melting curve of tin have continued in FY12, extending the measured diffraction up to 720 GPa (Fig. 132.129), and potentially yielding information about the melting curve up to 300 GPa (Fig. 132.130). The new x-ray diffraction data provide further evidence for a high-pressure, high-temperature phase transition near 200 GPa. The structure of this new phase differs from the hexagonal close-packed structure that arises near 200 GPa at ambient temperature.[90] We propose the simple hexagonal omega phase as a likely crystal structure for this new phase. The particle velocity histories of shock-melted and ramp-compressed tin show a plateau consistent with changing sound velocities at a phase transition such as recrys-

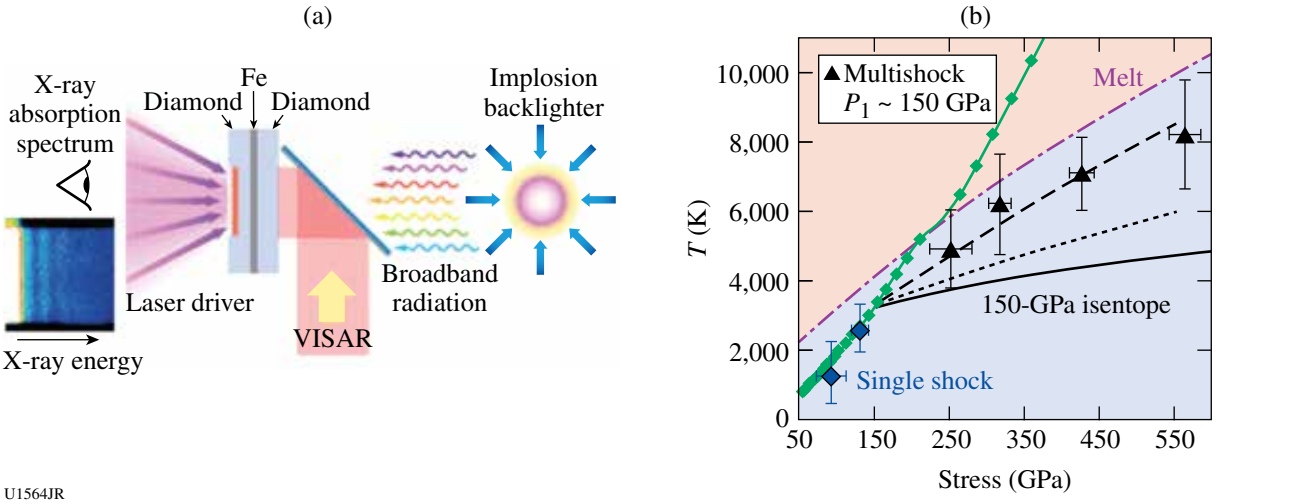

Figure 132.128
(a) Experimental schematic. The raw image of a typical x-ray absorption spectrum is displayed at the lower left corner, showing the intensity modulations above the K edge. (b) Temperature inferred from EXAFS data as a function of stress for the shock + ramp data with an initial shock of 150 GPa. The single-shock data are also shown (blue diamonds). The melting curve (dashed–dotted lines) and the Hugoniot (green solid lines with squares) are plotted for comparison. Also shown are isentropes (solid lines), isentropes with the temperature increase calculated using static strength Y_{sta} (dotted lines), and dynamic strength $Y_{dyn} = 3Y_{sta}$ (dashed lines).

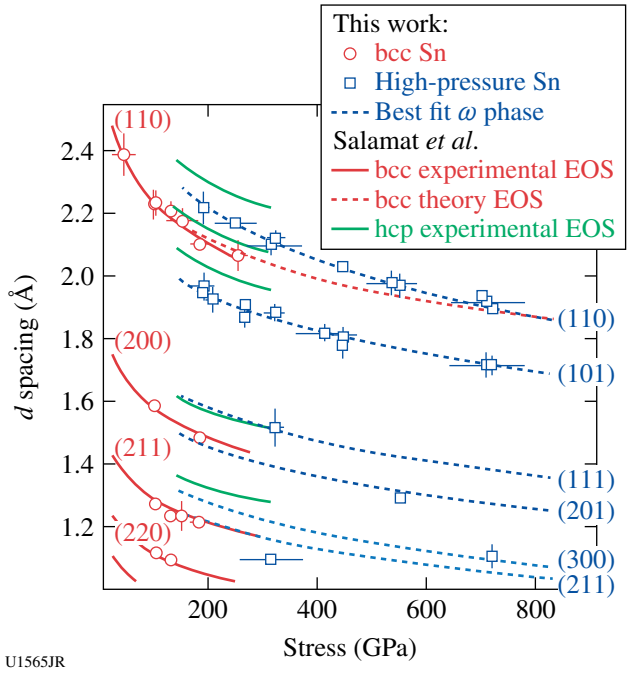

Figure 132.129
The *d* spacing of observed peaks, compared with known isothermal equation of state and phase transition from static experiments.[90,92,93] Our observed high-pressure *d* spacings fit a simple hexagonal (ω) phase. The line weight is proportional to the expected relative peak intensity.

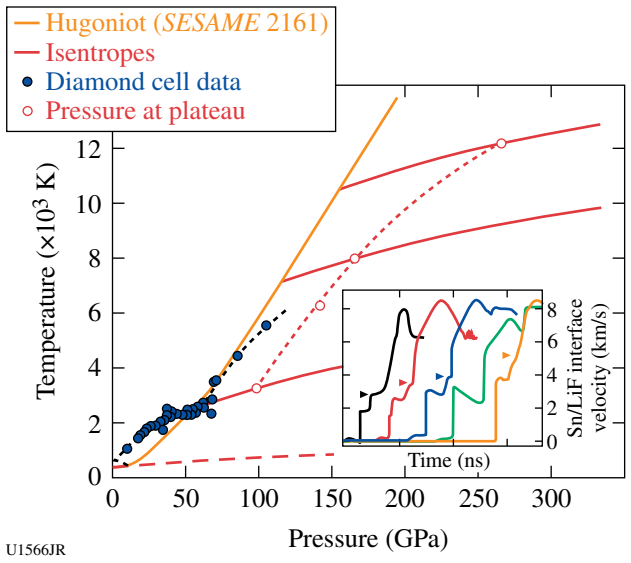

Figure 132.130
Melting curve of tin with new data from this study, determined from the pressure at which a plateau is seen in the ramp-compression wave profile (shown in the inset). Paths in phase space are approximated as shown, with the temperatures associated with the principle Hugoniot and subsequent ramp-compression pathways (modeled as isentropes) determined from the *SESAME* 2161 table.

tallization. Assuming recrystallization, a preliminary analysis shows the melting temperature rising steeply with pressure, in qualitative agreement with recent diamond anvil cell results.[91]

Gigabar Equation of State

Principal Investigator: J. Hawreliak

High-pressure equation-of-state (EOS) experiments using convergent compression of a solid spherical target have a geometric advantage over conventional planar techniques, in which a constant ablation pressure causes the propagating shock to maintain a constant pressure, because in the converging case the shock will increase in strength as it approaches the sphere's center. This approach makes it possible to achieve shock pressures >100 Mbar at the Omega Laser Facility. These experiments use *in-situ* gated radiography to measure the propagating shock speed and density. We will apply the Hugoniot relations to determine the pressure based on the measure shock front speed and density:

$$P = \rho_0 u_s^2 \left(1 - \frac{\rho_0}{\rho}\right)$$

$$\frac{\delta P}{P} = \sqrt{\left(\frac{2\delta u_s}{u_s}\right)^2 + \left[\left(\frac{\rho_0}{\rho - \rho_0}\right)\frac{\delta\rho}{\rho}\right]^2}, \qquad (2)$$

where ρ_0 is the initial density and δu_s, $\delta\rho$, and δP are the associated uncertainties in the shock speed, density, and pressure, respectively. Figure 132.131 is an example of a single frame

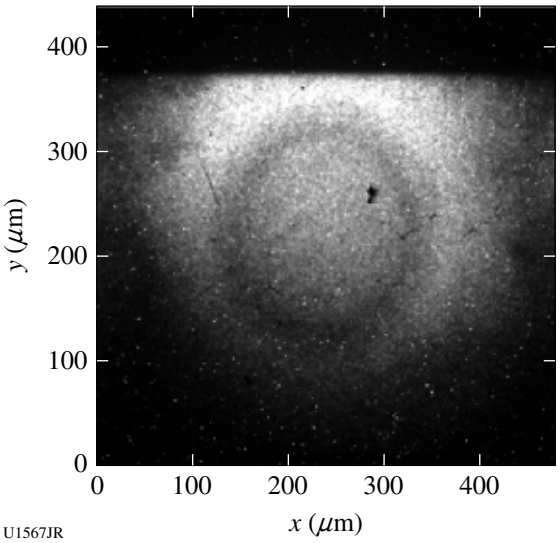

Figure 132.131
Gated 2-D radiograph from a shock propagating through a solid sphere, demonstrating a key capability needed for high-pressure equation-of-state measurements.

from a radiograph image from which the density profile can be inferred.

Equation of State for Foams Using OMEGA EP

Principal Investigator: J. Hawreliak

The equation of state (EOS) of porous materials is of great interest in high-energy-density (HED) science because it allows conventional shock techniques to achieve different thermodynamic end states than the principal Hugoniot. Figure 132.132 is an example of the pressure–density space of shock-compressed quartz for a range of different initial densities. For the low-density foam materials, where the final density is below the ambient density of the base material, the pressure is dominated by the thermal pressure caused by compressing the voids in the material. Many carbon-based foams are opaque, unlike transparent foams where the shock front becomes reflective at high pressures and velocity can be measured directly. The opaque materials require an x-ray technique to view the shock. We are developing an *in-situ* radiograph technique to make Hugoniot EOS measurements of shock-compressed opaque low-density foams. We had success using a chlorinated plastic (PVC) area backlighter for 50-mg/cm^3 carbon resorcinol foam (CRF).

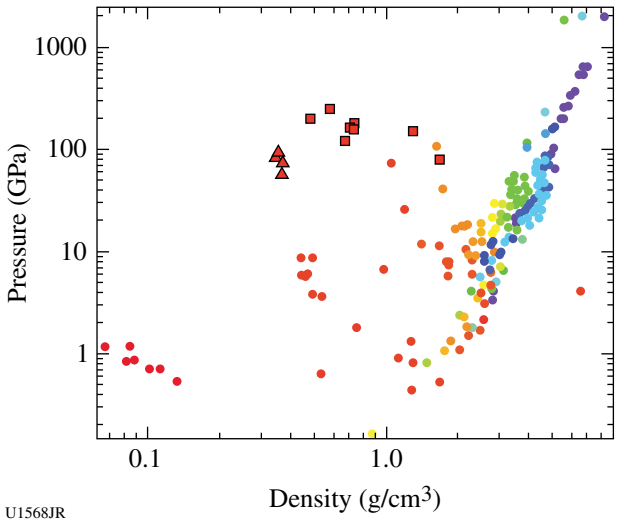

Figure 132.132
Pressure-density space of shock-compressed quartz foams.

Advanced X-Ray Diffraction Techniques

Principal Investigator: J. Hawreliak

Since the discovery of x rays by Rontgen over a century ago, x-ray diagnostic techniques have been used to examine the macroscopic structure of samples through radiography, the atomic structure of materials through x-ray diffraction (XRD), and electronic structure of atoms through x-ray spectroscopy. X-ray diffraction has been one of the most widely used techniques to determine a material's atomic structure. It has recently been applied to dynamic experiments where a shock or ramped pressure wave is applied to a material and then x rays are flashed in a pump–probe experiment to examine the atomic structure as the pressure wave propagates. An effort is currently underway to achieve ultrahigh pressure on laser systems using dynamic compression; in concert with this effort is the development of new advanced XRD techniques that will enable one to structurally probe the material at high pressure. This campaign was the first implementation of a technique that uses a Soller slit-like array of grids to provide limited line of sight of the detector. Figure 132.133 shows the effective geometric shielding the Soller slits provide and a sample image of the x-ray source, which is limited to a small portion of the image plate. This is part of an ongoing development project.

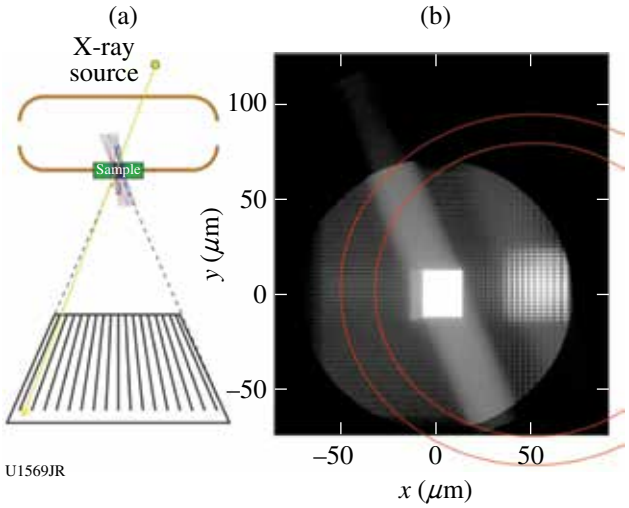

Figure 132.133
Initial data from the new Soller slit diffraction diagnostic.

2. Radiation Transport

Heated Wall

Principal Investigator: K. Baker

The heated-wall campaign measured radiation transport in a geometry that enabled the heat wave to propagate as if there were no wall loss. This was accomplished by placing a thin CRF annulus around a low-density, 30-mg/cm^3, SiO_2 cylindrical foam. One end of the SiO_2 foam and the outer surface of the CRF annulus were heated by the radiation environment inside a hohlraum driven by 15 OMEGA beams. The thickness of the CRF annulus was chosen such that the time-dependent position

as a function of Z of the supersonic heat wave propagating down the SiO_2 cylindrical foam would match the time and Z position of the subsonic heat wave traveling radially inward through the CRF annulus and reaching the SiO_2 foam from the side. In this manner the front of the supersonic heat wave traveling along the z axis of the SiO_2 foam did not see a significant radial disparity in radiation temperature and consequently propagated as if it were being driven in a 1-D geometry.

The heated-wall campaign used the SXI/SSC-A (an imaging x-ray streak camera) diagnostic to measure the uniformity and breakout time of the supersonic heat wave from the rear of the SiO_2 foam. The diagnostic measured breakout times consistent with simulations, including a delayed breakout of the heat wave as the density increased in the SiO_2 foam. Two control experiments were performed: one with a gold disk covering the front of the SiO_2 foam to block radiation from entering the SiO_2 foam along the z axis; and a second in which the CRF tube was replaced with gold to prevent radiation from entering the SiO_2 foam from the radial direction. The shot with a cylindrical block showed no evidence of a heat wave reaching the end of the SiO_2 foam; the shots with a gold annulus to block radial transport of the hohlraum x rays into the SiO_2 foam showed a delayed signal that was significantly weaker and significantly shorter temporal emission as compared to the two heated-wall shots.

Crystal Window

Principal Investigator: B. Maddox

The CrystalWindow-12A campaign was designed to test fused silica as a VISAR window up to pressures exceeding 50 Mbar (5 TPa). Quartz had been shown to be an excellent high-pressure VISAR window at ultrahigh pressure. Although quartz blanks at low shock pressures, the shock wave in the quartz becomes reflective at higher shock pressures and can be used to measure the shock velocity transmitting into the quartz crystal. Fused silica is a noncrystalline form of silicon dioxide (SiO_2), the crystalline form being quartz. Due to the amorphous nature of fused silica, it can be polished readily making it an ideal window material for state-of-the-art experiments on the NIF that require nonplanar VISAR witness windows. The CrystalWindow-12A campaign used the 15 H7 Cones 2 and 3 beams to drive a scale-one halfraum to 190 eV. To collect the VISAR signal, the aluminum-coated VISAR samples were attached to the open end of the halfraum and mounted on a 2.65-mm-diam gold washer with a 0.4-mm central aperture. A 2-mm-diam, 2-mm-long gold tube was also mounted on the VISAR side of the target to shield the VISAR optics from any scattered light from the drive laser. Figure 132.134(a) depicts a photo of the completed target. Two thicknesses of aluminum were tested (50 μm and 70 μm) to study any blanking caused by preheating in the 50-μm-thick Al samples. Additionally, two samples were fitted with reference quartz windows for comparison. Figure 132.134(b) shows VISAR traces for 70-μm Al/quartz and 70-μm Al/fused-silica window targets. The decaying velocity seen here represents the ultrahigh-pressure shock wave traveling through the quartz and fused silica. The data obtained in this campaign confirmed that fused silica works well as a VISAR window at a peak shock pressure of

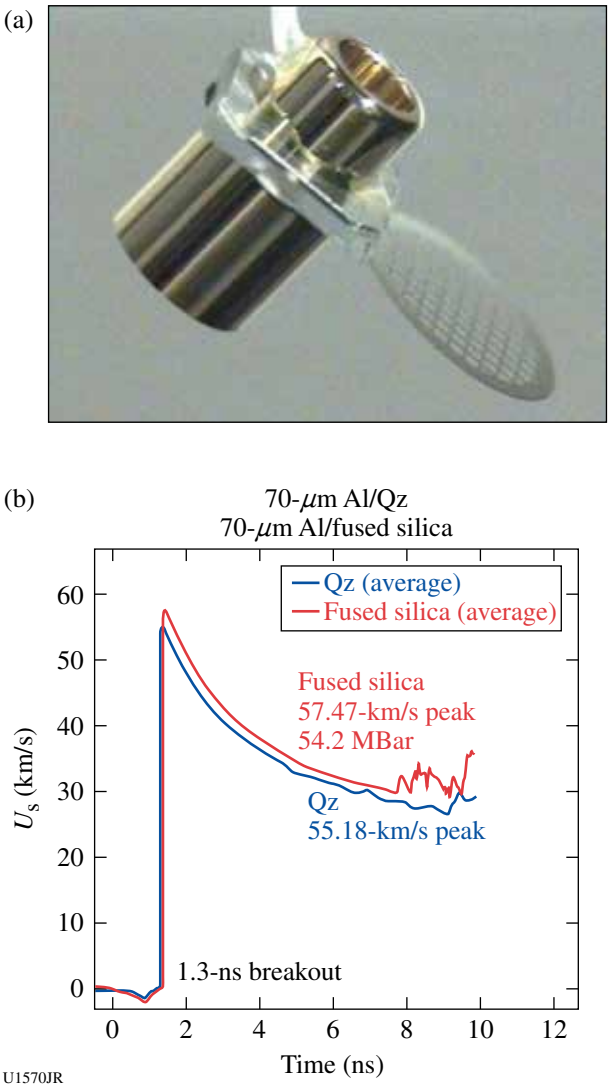

Figure 132.134
(a) CrystalWindow-12A target used to verify fused silica as a VISAR window and shock witness material to >50 Mbar. (b) VISAR data confirming that fused silica works well as a VISAR window at a peak pressure of 54.2 Mbar. The velocity versus time trace represents the shock wave traveling through the fused-silica and quartz (Q_2) windows.

54.2 Mbar with little to no blanking using a 70-μm Al ablator. Some blanking was seen in the 50-μm aluminum ablator targets, likely related to x-ray preheat.

3. High-Temperature Plasma Opacity

High-Temperature Plasma Opacity Experiments on OMEGA and OMEGA EP

Principal Investigator: R. F. Heeter
Co-investigators: A. Graf, G. V. Brown, C. Mauche, and R. E. Marrs

LLNL's high-energy-density (HED) opacity research on OMEGA in FY12 had three main directions: First, the MBOP-12 campaign followed up on physics questions from the very successful 2009–2011 Ti opacity shots, where the observed Ti continuum opacity and one to three line opacity regions did not match code expectations. New data obtained with a modified hohlraum design indicated that up to that 50% higher sample temperature was achieved.

The second campaign, NLTE-Dynamics-12, continued previous work on the non-LTE x-ray emission properties of hot high-Z plasmas as found in hohlraums at the laser-driven "hot spots." Uranium was chosen as the sample material because of its use on ignition and other shots on the NIF and also the paucity of experimental data. Shots performed in FY12 extended earlier work on uranium emission to 2× lower intensity (material temperature) and the data are now being compared with simulations.

The third research direction was the EPOp-12 series, which substantially upgraded the novel short-pulse "absorption-emission" opacity platform developed on OMEGA EP in FY10–FY11. The new platform uses a sample driven with up to 200 J via 100-ps FWHM Gaussian UV laser pulses using two of the "long-pulse" beams on OMEGA EP. The two short-pulse beams deliver up to 1500 J in 10 ps to a pair of continuum x-ray backlighters that probe the plasma after some delay. Figure 132.135 shows the first face-on transmission spectrum obtained from this new platform using a silicon sample and a probe beam delayed about 300 ps. Multiple L-shell charge states are observed in absorption. Self-emission from helium- and hydrogen-like silicon (produced prior to the backlighter probe but recorded on the time-integrated detector) is also observed. The presence of the Be-like and Li-like ions implies that this new platform achieves temperatures similar to those observed with the single-backlighter platform and titanium samples in FY11.

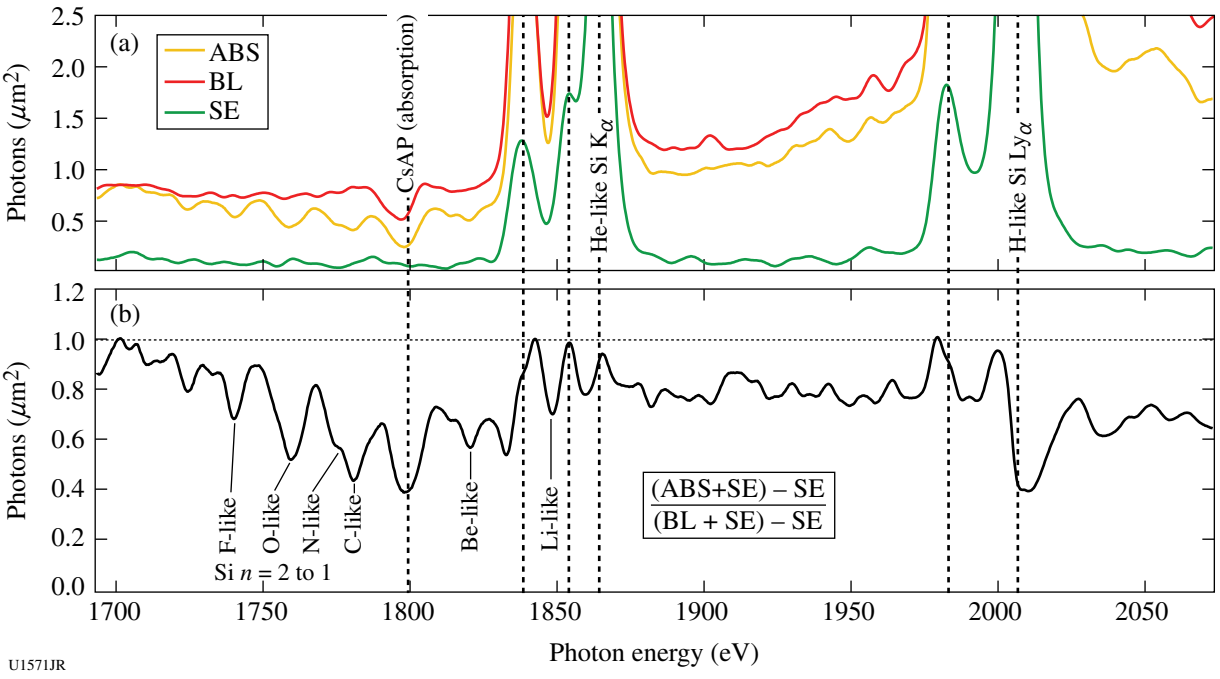

Figure 132.135
Initial silicon opacity spectra from OMEGA EP. (a) Backlighter, sample absorption, and sample self-emission spectra recorded on Biomax film; (b) sample transmission.

4. Burn Physics

Non-LTE Transport and Nuclear Lifetimes
Principal Investigator: A. Kritcher

Plasma coupling to nuclei in high-energy-density plasmas, or *nuclear–plasma* physics, is a cutting-edge field that traverses the areas of nuclear physics, plasma physics, and atomic physics. Nuclear–plasma interactions occur in hot dense plasmas such as inertial confinement fusion (ICF) environments and astrophysical bodies. The effect of high-energy-density–plasma (HEDP) environments on astrophysical nucleosynthesis—the formation of heavy elements from pre-existing nucleons in astrophysical plasmas—is expected to play a significant role.[48] Nuclei in stellar plasmas reach a thermal population of low-lying excited nuclear states from photoexcitation, free electrons in the plasma (NEEC),[49–52] excitation from atomic transitions (NEET),[53–55] and inelastic electron scattering in the dense plasma. In these experiments at the Omega Laser Facility we investigate the NEEC process in underdense plasmas by illuminating mini hot hohlraums (400 or 600 μm in diameter) with ~15 kJ of laser light.

The goal of these first experiments was to identify the plasma conditions of hot Tm hohlraums with spectral line emission analysis and optical Thomson scattering, measure the energy and time-resolved atomic emission background, investigate this experimental platform to study nuclear lifetime shortening in hot plasmas, and determine the possibility of investigating nuclear–plasma interactions on OMEGA. In these first experiments we have collected high-quality data and are in the process of analyzing the results. Future campaigns will continue to measure plasma conditions of hot hohlraums and investigate nuclear–plasma interactions in HEDP plasma environments. We will also field additional isotopes in this configuration.

5. Hydrodynamics

Short-Pulse, UV Backlighting Development for the NIF
Principal Investigator: V. A. Smalyuk

High-energy-density complex hydrodynamics experiments on the NIF require short-pulse backlighting capability. Experiments on OMEGA EP tested the short-pulse, UV beam backlighting concept for the NIF. Four OMEGA EP beams were focused onto 10-μm-thick Ag wires, mounted on 300 × 300-μm-sq, 10-μm-thick polyimide foils to mimic the illumination conditions of one quad on the NIF. The total laser energy was ~400 J with an ~100-ps Gaussian pulse shape, a peak laser intensity of ~3×10^{16} W/cm^2, and a mispointing of <50-μm rms. Three beams were co-timed while the fourth beam was advanced up to 300 ps from the co-timed beams to maximize the x-ray backlighter signal. Results were compared with ~1.2-kJ short-pulse (~100-ps) IR beam backlighting with the same Ag-wire targets, driven at an intensity of ~1×10^{17} W/cm^2. Figure 132.136 shows a measured image of the target, created with Ag-wire backlighting on an image plate using a high-energy radiography imager for EP (HERIE) diagnostic located 50 cm from target chamber center on OMEGA EP. The configuration consists of a Au grid to determine magnification, a 100-μm-thick Au plate to determine resolution, and seven Cu steps with 18-μm thickness between adjacent steps to determine contrast and sensitivity. Areas inside and outside the Au plate were also used to measure noise. Figure 132.137 shows the change in the intensity across the Cu step wedge. The 300-ps advance produced the brightest signal, while a 150-ps advance produced nominally the same results as all four beams co-timed. The ~20-μm spatial resolution was similar to IR-beam experiments, while the signal was ~100× lower. The short-pulse UV backlighting might be feasible for complex hydrodynamics experiments on the NIF if hohlraum and backlighter x-ray backgrounds do not exceed ~10 PSL (photostimulated luminescence) on the image plate at 50 cm from the NIF target chamber center.

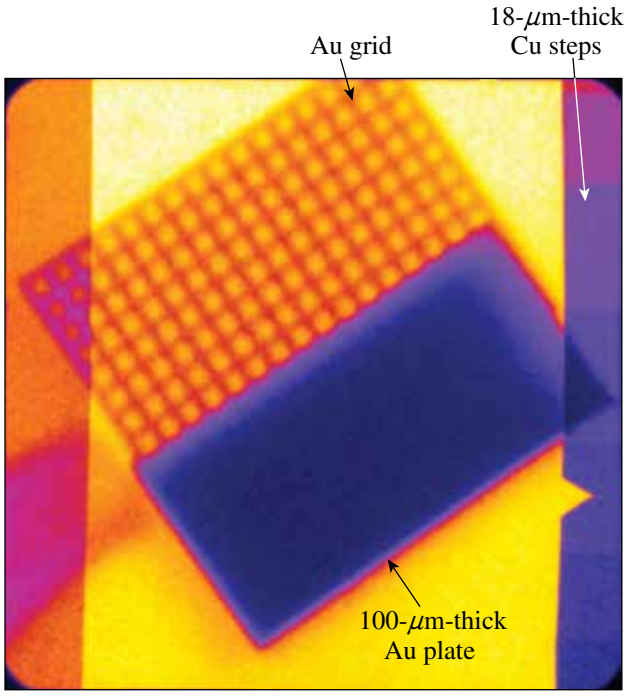

Figure 132.136
X-ray radiograph of the target consisting of an Au grid, a 100-μm-thick Au plate, and seven 17-μm-thick Cu steps.

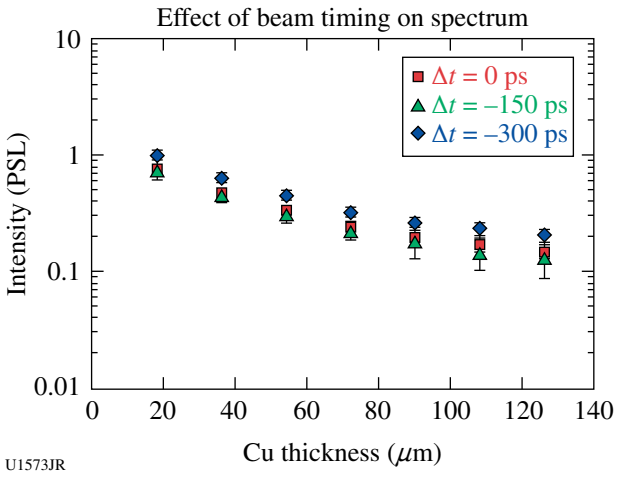

Figure 132.137
Intensity across the step wedge shows relative differences in backlighter emission. A 300-ps advance in beam timing shows a small increase in signal. Uncertainties illustrate shot-to-shot variation.

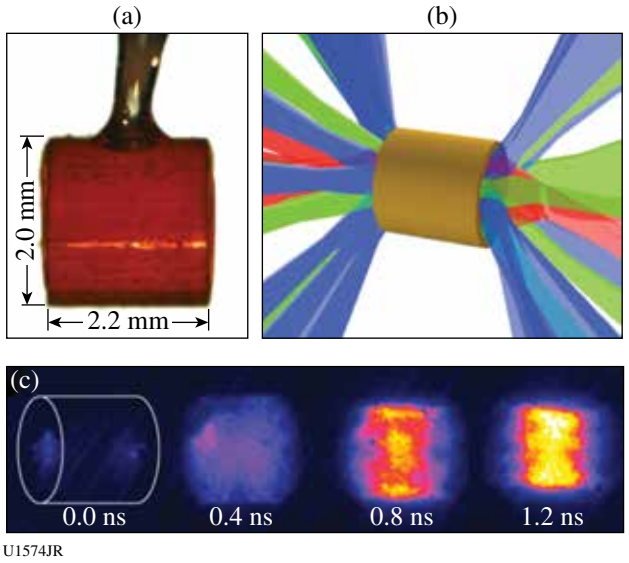

Figure 132.138
(a) Photograph of a cylindrical aerogel target held inside a thin plastic tube. (b) Irradiation structure from 40 OMEGA beams. (c) Example of x-ray emission images at different times relative to the beginning of the interaction.

6. X-Ray Source Development and Application

X-Ray Source Development with Nanostructured Materials

Principal Investigator: R. Patterson

Progress in the fabrication of new metallic aerogels for x-ray generation[94] led to a campaign for optimizing titanium x-ray sources, as illustrated in Fig. 132.138. Experiments were conducted in FY12 by the X-Ray Source Development team in collaboration with the Defense Threat Reduction Agency and researchers from Commissariat à l'Énergie Atomique (CEA). In the FY12 shots, when irradiated by 40 OMEGA beams, Ti-doped aerogels (4 mg/cm^3, 4 at. % of Ti) made by a wet-chemistry process yielded only a 0.7% laser-to-x-ray conversion efficiency (CE) in the x-ray band between 4.6 and 5 keV, which is significantly lower than the previous record of 3% CE (Ref. 95). However, in this campaign novel aerogels were measured to provide a 5.5% CE in the same energy range. These new targets were made by coating SiO_2 aerogel templates with TiO_2. They are of similar ultralow density (4 mg/cm^3) but reach a higher Ti concentration (22 at. %).

Current analysis is focused on precise understanding of the x-ray spectra, which will bring interesting new insights to our understanding of the heating of these targets. Analysis will also cover the heating dynamics[96,97] and yield optimization of these targets using hydrodynamic simulations. The objective is to design future targets by optimizing the Ti concentration and aerogel pore size, which are now controllable.

Solar Cell Electrostatic Discharge

Principal Investigator: R. Patterson

During FY12, the X-Ray Source Development team, in collaboration with the Naval Research Laboratory and the Defense Threat Reduction Agency, conducted a series of experiments to examine the effects of x-ray loading on solar cells. Our tests were broken into two parts: We first evaluated the ability of the Omega facility to produce a laboratory environment suitable for conducting electrostatic discharge experiments on solar cells; then we subsequently conducted the first tests of active solar cell arrays. For each of these experiments, Fe- or Ge-based targets positioned at the center of the target chamber were irradiated with ~20 kJ in a 1-ns square pulse. The XRSA Langmuir Probe Diagnostic (XLPD) or a modification including active solar cells was positioned a few tens of cm from the target.

Building on initial tests in the previous year, we deployed XLPD configured as an array of eight cylindrical Langmuir probes [Fig. 132.139(a)] on 29 February 2012 to observe the arrival of the source plasma. Time-of-flight measurements resulted in an observed velocity of ~16±2 cm/μs for the leading edge of the source plasma.[98] Based on these measurements, we concluded that the OMEGA target chamber is suitable for conducting electrostatic discharge experiments on solar cells, provided that the cells are positioned sufficiently far from the target.

On 12 September 2012 we did indeed place an array of two solar cells along with four standard XLPD probes [Fig. 132.139(b)] a minimum of 40 cm from target chamber center to examine the response of these cells to the x-ray and plasma environment produced from Ge-aerogel targets. Figure 132.140 shows the prompt x-ray response of the probes as well as the solar cells. In addition, the Langmuir probes show signals consistent with sheath formation in the first 200 ns, followed by the arrival of charged particles from the target. While our analysis of the solar cell data is ongoing, the data are consistent with an electrostatic discharge, perhaps caused by current flowing to ground through the dense plasma formed from the ablation of the XLPD cassette itself. In future experiments, we will insulate the solar cells from the chassis in order to test the potential arc formation between cells.

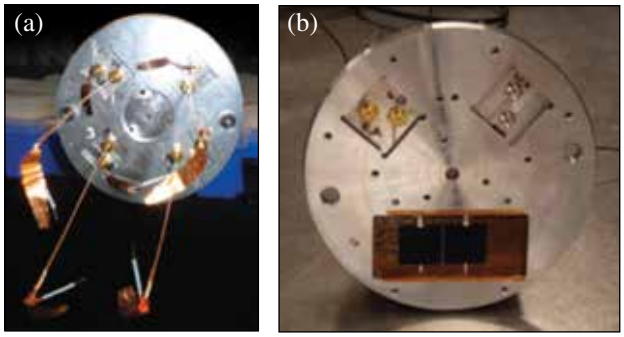

U1575JR

Figure 132.139
(a) An XLPD cassette with four pairs of Langmuir probes. Each pair is composed of one 2.5-cm and one 20-cm probe. (b) Modification of XLPD to include an active solar cell array. Two 2 × 2-cm Ge triple-junction solar cells are biased up to 100 V and can be fielded with up to two pairs of standard XLPD Langmuir probes.

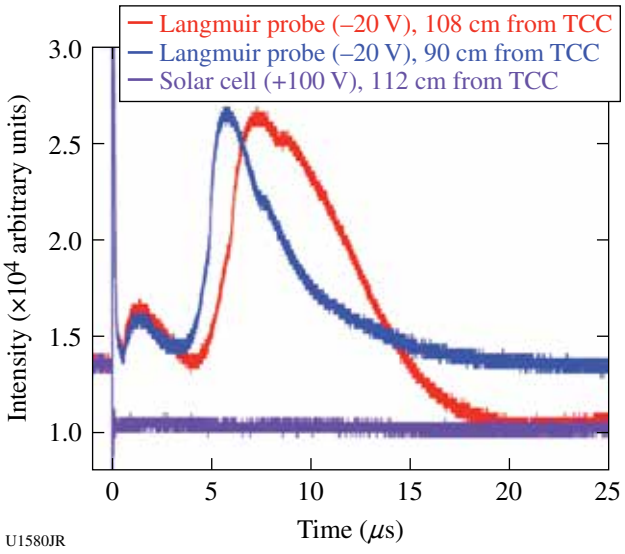

U1580JR

Figure 132.140
Initial results from the solar cell discharge experiments. Signals from two ion-collecting probes are shown in addition to the signal recorded from a solar cell biased at 100 V.

ACKNOWLEDGMENT

This work was performed under the auspices of the U.S. Department of Energy by Lawrence Livermore National Laboratory under Contract DE-AC52-07NA27344.

FY12 LANL Experimental Campaigns—Overview

In FY12, Los Alamos National Laboratory (LANL) executed 244 total shots on OMEGA. LANL experiments contributed to the National Ignition campaign (NIC) in the following ways:

- Measured the x-ray ablative Richtmyer–Meshkov growth of isolated defects on plastic ablators
- Studied branching ratios in DT fusion plasmas
- Continued neutron imaging and radchem scintillator development for the NIF

High-energy-density (HED) campaigns included

- Study of shear in a counter-propagating flow geometry and reshock-driven turbulent mixing
- Backlit defect implosion experiments to study the effect of trench defect and polar drive
- Measurement of the effect of capsule asymmetries on neutron yield and ion temperature
- Imaging x-ray Thomson-scattering platform development for dense plasmas and warm dense matter equation of state (EOS)
- Measurement of a supersonic radiation wave and foam aerogel EOS

CHaRM

The CH ablative Richtmyer–Meshkov (CHaRM) campaign had two shot days in FY12. The goal of these experiments was to measure the oscillation frequency of small perturbations on CH ablators driven by the x-ray–ablation Richtmyer–Meshkov effect. With this knowledge we would have a better understanding of how isolated defects behave during the first shock transit stage of a NIF ignition attempt, which could then provide methods for minimizing perturbations at the onset of Rayleigh–Taylor.

Our experiments used 15 beams inside large Au half-hohlraums, which were staggered in time to produce a 7.5-ns radiation drive with a radiation temperature of 70 eV (see Fig. 132.141). Targets with 2-D arrays of 5-μm-tall, 17-μm FWHM Gaussian bumps were attached over the opposite laser entrance hole with the defects facing inside the halfraum. During the experiment the bump arrays were backlit with Y and Ta backlighters (~2.2-keV emission) and imaged at 37× magnification into an x-ray framing camera.

Radiation–hydrodynamics simulations running with EOS tables for CH predict that these small bumps decay for our experimental conditions as shown in Fig. 132.142 (green curve). The trend in our data supports this prediction even though the data lie somewhat above the simulation curve, which we think is due to either systematic errors in the data analysis or errors in the models. Nevertheless, this decay in amplitude occurs at a rate that is much slower than under direct-drive conditions measured at Naval Research Laboratory (NRL). This has to do with the differences in absorption, transport, and ablation mechanisms between x-ray and laser drives. Under our conditions only very narrow bumps (<20 μm) exhibited this decay while wider bumps (>30 μm, FY11 data) only saturated.

Shear

In FY12 the Shear campaign focused on developing a counter-propagating flow platform for studying shear-driven turbulent mixing. These experiments use Be tubes containing

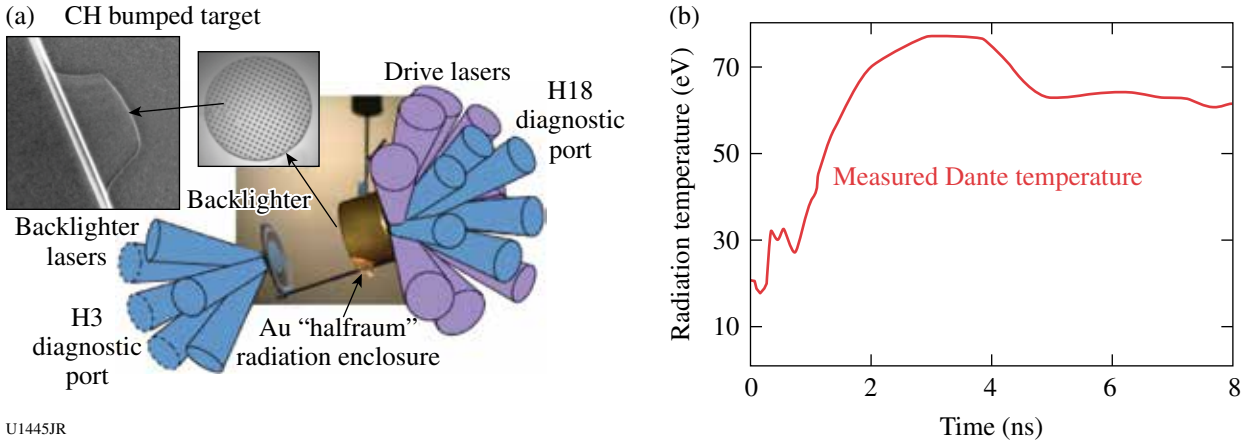

Figure 132.141
(a) Schematic of the CHaRM platform where a Au halfraum is heated to 70 eV, driving an ablation front into an array of isolated Gaussian bump defects. (b) Bumps are radiographed along the axis of the halfraum.

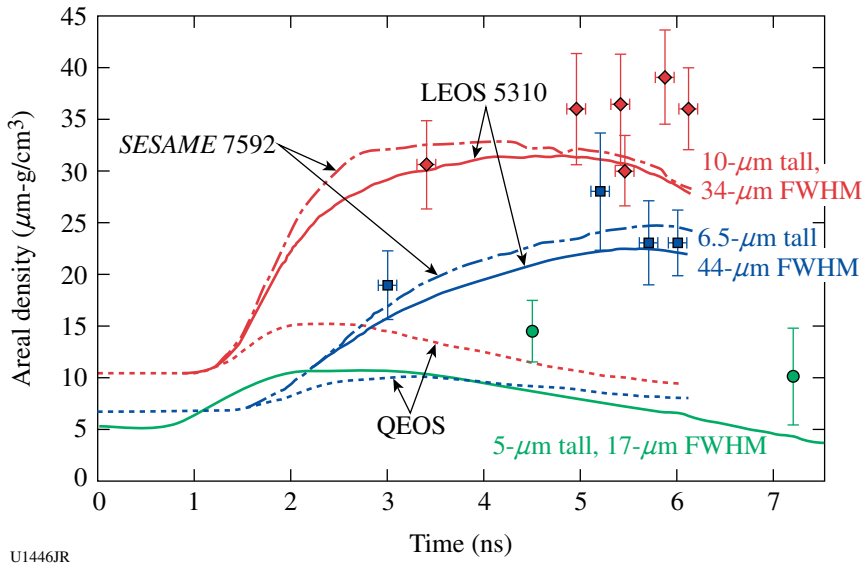

Figure 132.142
Summary of long drive duration data showing the saturation of bumps with >30-μm width and ablative RM decay for those with widths <20 μm.

low-density CH foam semi-cylinders separated by Al tracer layers. The counter-propagating flow is created by inserting Au "plugs" in front of each foam semi-cylinder at opposite ends to hold back the shock in each foam at one end (see Fig. 132.143). With the plugs in place, the Be tube ends are irradiated with 10^{15}-W/cm^2 laser intensity to initiate the counter-propagating flow. When the shocks cross, they establish a shear layer in the Al, which then grows due to turbulent mixing.

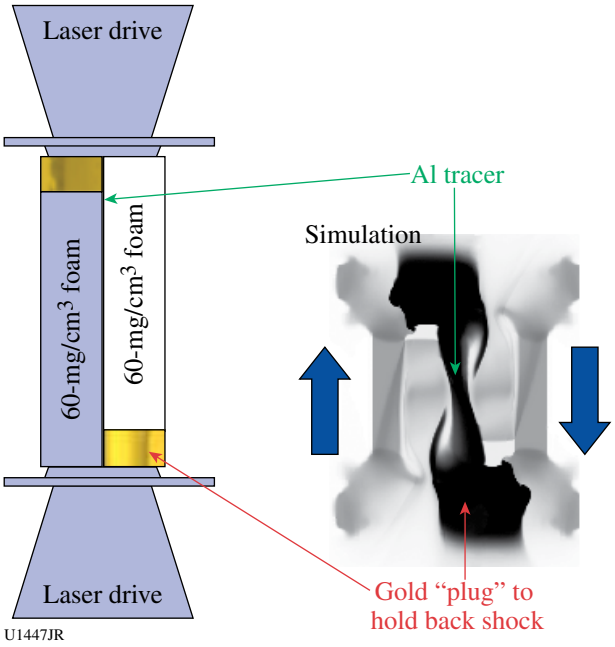

Figure 132.143
Geometry for a counter-flowing shear platform. Simulations with the Besnard–Harlow–Rauenzahn (BHR) mix model are also shown.

Over the course of the year, we improved the target design by extending the length of the Al tracer so that shocks from one end could not penetrate into the adjacent foam. This created a longer-duration, cleaner shear flow for studying the turbulence. We used x-ray radiography along two orthogonal lines of sight (edge-on and plan view of the tracer layer) to image the evolving turbulent structure at >20× magnification. In the edge-on view (see Fig. 132.144) the growing mix layer was imaged at times from 6 to 16 ns and in relatively good agreement with the LANL Besnard–Harlow–Rauenzahn (BHR) turbulent mix model. The same data times were used (on the same shot) for the plan view radiography, which appears to show a transition to turbulence around the 10-ns point where 3-D structures begin to form out of the initially homogeneous flow.

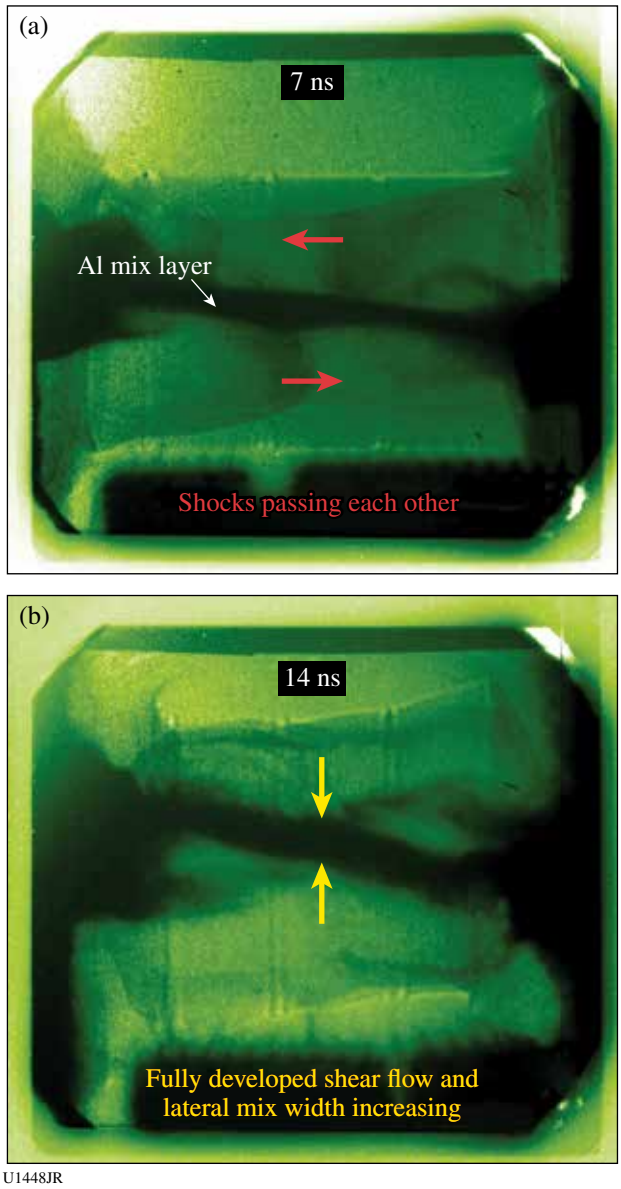

Figure 132.144
Radiographs at two different times showing development of counter-flowing shear and mixing.

ABEX

In laser-driven implosions, of importance to inertial confinement fusion and stockpile stewardship, the cold shell is known to mix into imploding nuclear fuel. Yet there are no direct observations of just where, and at what rate, shell material migrates into the fuel. In June 2012 experiments at the Omega Laser Facility, LANL's ABEX (asymmetric burn experiment) campaign, in collaboration with Prof. Roberto Mancini's University of Nevada, Reno group, has made advances toward providing time-resolved images of shell mix into fuel. Emission from titanium dopant in the shell is used to make quasi-

monochromatic images. Temperature, and ultimately a crude estimate of chord-integrated titanium, has been extracted (see Fig. 132.145). Three such separate views, each at multiple times, were obtained during each shot.

A capsule with pre-imposed perturbations (Fig. 132.146) showed images similar to those obtained with perfect spheres—but to just what depth the Ti has penetrated remains ambiguous. The team is now focused on advanced analysis and refinement of the target design to address the longstanding absence of mix images in laser-driven implosions.

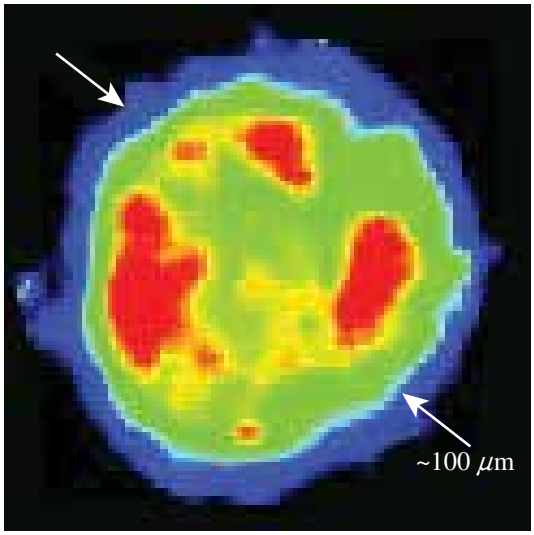

U1449JR

Figure 132.145
Ti originally in the shell has mixed into the fuel (typical false-color map is used, i.e., red corresponds to an increased signal).

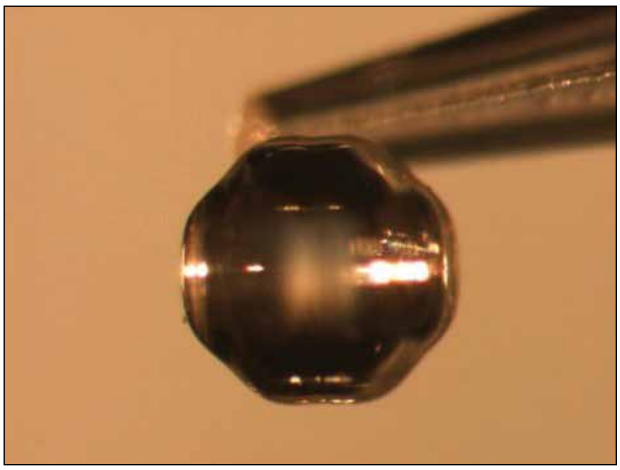

U1450JR

Figure 132.146
Photograph of a machined PAMS mandrel with ±10-mm-amplitude perturbation. The axis of symmetry is horizontal in this photograph.

RadChem

On 6 August 2012, the LANL Prompt Radchem Development team successfully tested new assay system designs on the OMEGA laser. Prompt radiochemical signatures generated in high-energy-density experiments provide insight into a variety of physical phenomena including late-time hydrodynamic performance of the implosion as well as particle stopping within the plasma. These signatures are created through charged- and neutral-particle nuclear interactions within the imploded capsule materials. Often the resulting radioactive products undergo beta decay with end-point kinetic energies approaching 14 MeV and half-lives as short as 20 ms. The short half-lives necessitate deploying an assay system within the target chamber that will withstand the harsh, prompt radiation environment but will readily assay the high end-point energy beta decays that immediately follow. Furthermore, the detector must have minimal sensitivity to the flux generated by background sources.

During the August campaign, the LANL-based team fielded a new four-element scintillator telescope to measure beta decay from various elements with different end-point energies ranging from 3 MeV up to 14 MeV and half-lives from 20 ms to several minutes. Figure 132.147 illustrates the strategy employed by the detector. The red curves represent the electron spectrum expected from decays of ^{16}N and ^{9,10}B. The colored vertical lines approximately represent the threshold sensitivity of the individual elements within the telescope detector, e.g., the first element will register hits from electrons above ~1 MeV, the second above ~2 MeV, etc. By requiring a coincidence between the elements of the telescope detector, not only is the background flux outside the solid angle of the detector acceptance reduced, but a threshold cut is placed on the electrons depositing energy within the telescope.

To test these concepts, the detector was fielded in the OMEGA target chamber during a set of high-yield implosions of DT-filled glass and plastic capsules. Activation targets, including a polytetrafluoroethylene (Teflon) puck, were located in front of the telescope yielding the data shown in Fig. 132.148. Figure 132.148(a) shows the coincidence rate of the first two scintillator elements shortly after a shot. A fit to the distribution clearly shows half-life contributions from ^{16}N and ^{19}O decays, as expected from ^{19}F(n,α) ^{16}N, and ^{19}F(n,p)^{19}O reactions. Figure 132.148(b) shows the coincidence rate using the first three elements, thereby requiring a ~5-MeV threshold. This higher threshold eliminates the ^{19}O contribution and significantly

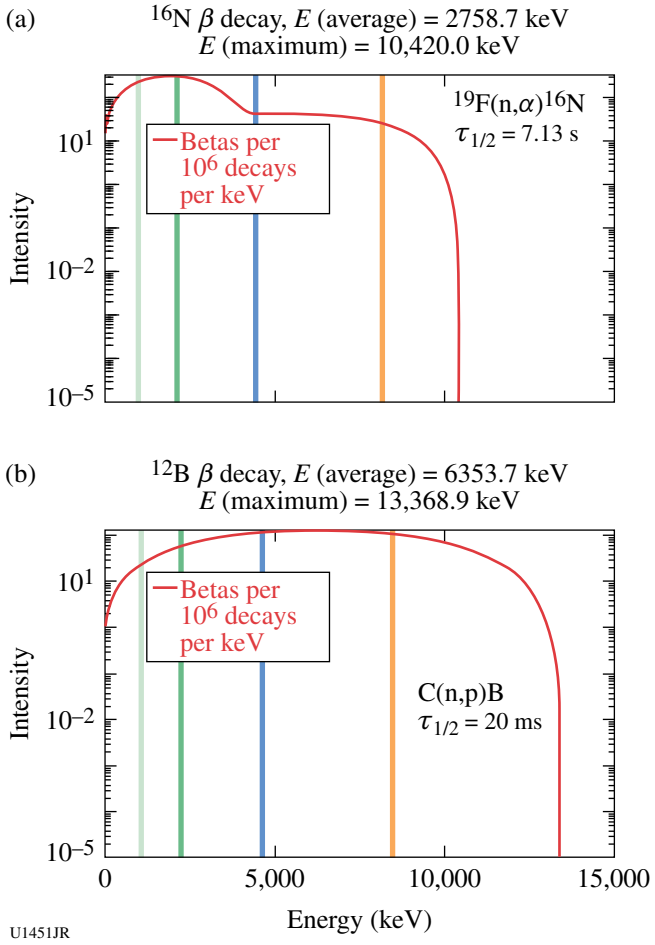

Figure 132.147
Beta-decay spectrum with approximate detector element thresholds. (a) ^{16}N beta spectrum and (b) ^{9,10}B beta spectrum.

reduces the ^{16}N to the lower-intensity, higher-energy decay. The fit shown in Fig. 132.148(b), using an exponential and no background, gives a half-life measurement of $\tau_{1/2}(^{16}\text{N})$ = 7.11±0.14 s, in excellent agreement with the published value of 7.13 s.

In future experiments planned at the Omega Facility, the telescope will be moved closer to the imploding capsule to test the robustness of the detector to prompt radiation, as well as to provide the opportunity for other activation measurements.

DPEOS

The purpose of the DPEOS project is to measure the EOS of material in the warm dense matter regime. To accomplish this, we are developing an experimental platform to do this at the Omega Facility. Our experimental platform uses the OMEGA laser to drive a very strong shock into an aluminum or graphite sample. The shock is then released into a 0.2-g/cm^3 aerogel foam that is used as a pressure standard. A shock-breakout measurement is used to determine the shock velocity and pressure in the foam. We have also developed an imaging x-ray Thomson spectrometer to measure Compton-scattered x rays from the released sample. This information can be used to determine the temperature and density of the released material, providing the necessary measurements to determine the EOS.

Our experimental plan for FY12 was to test and measure the shock and release conditions produced in the aluminum sample, get our new imaging x-ray Thomson spectrometer (IXTS) approved, test its operation, and obtain the first x-ray scattering measurements of WDM aluminum and/or carbon.

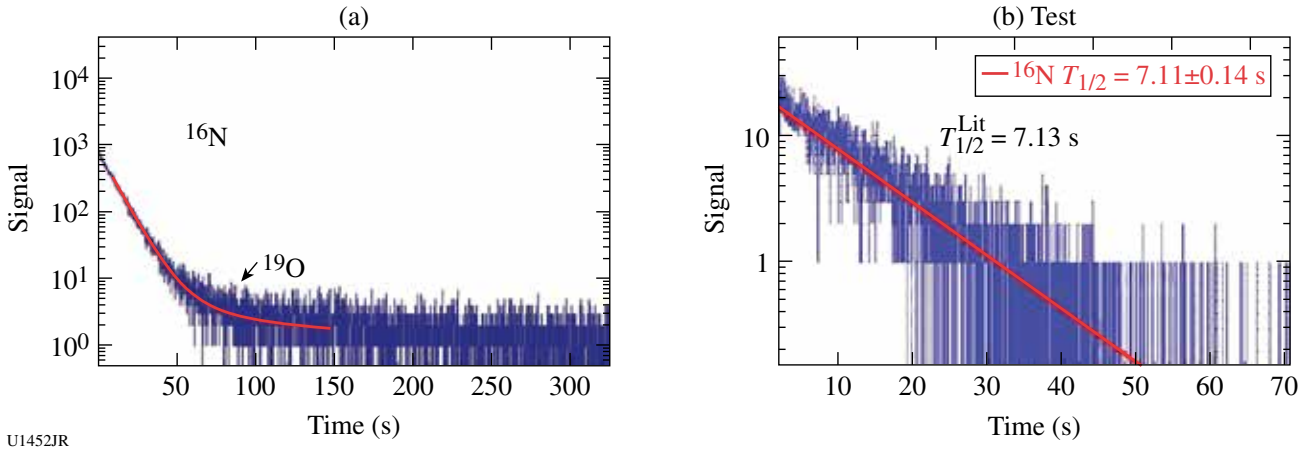

Figure 132.148
Prompt decay data from a high-yield OMEGA implosion. (a) Two-element coincidence rate and (b) three-element coincidence rate.

We were successful in reaching these goals. We completed a total of 24 shots in two days on OMEGA. On the first day, we successfully fielded the IXTS for the first time and obtained scattering data. However, our signals were contaminated by background x-ray signals from our x-ray backlighter. Our shielding and target design were improved for the second shot day in August, and we obtained our first detailed x-ray scattering measurements from warm dense matter carbon. These measurements enabled us to determine the temperature of the shock and released carbon. In addition, we verified the shock conditions for both carbon and aluminum, which were consistent with our previous measurements. An example of the IXTS data we obtained is shown in Fig. 132.149. This figure contains the analyzed x-ray scattering signal along with a series of fits to the data. Two shot days are planned for FY13 in which we will perfect our target design to obtain better signal to noise for this data and in addition will carry out x-ray radiography measurements to pin down the density of the material. This will provide a complete EOS measurement for these warm dense matter conditions and be used to test EOS models in this regime.

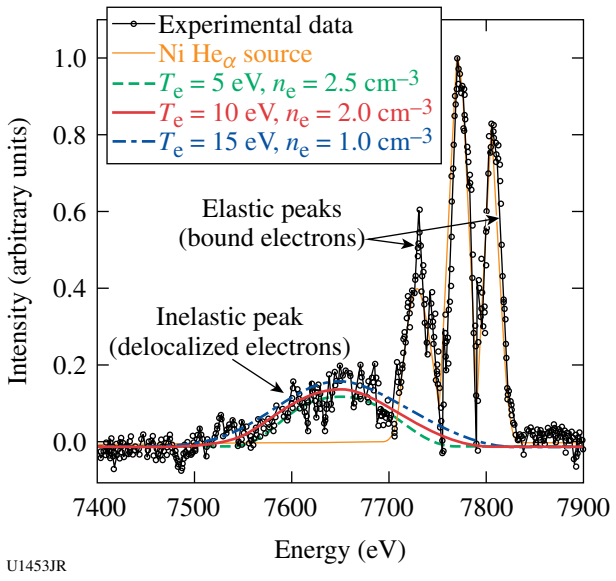

Figure 132.149
X-ray Thomson-scattering measurements from shock and a released warm dense matter graphite target. The elastic peaks correspond to scattering from bound electrons while the inelastic peak is due to scattering from free electrons. The measurements indicate a temperature of ~10 eV and density near 2 g/cm^{-3}.

NIF-5

The purpose of the NIF-5 project is to test both diagnostics and physics ideas that are important for facilitating our understanding of important radiation flow experiments being carried out on the NIF. In the past, this project has focused significantly on diagnostic development and testing and experimental platform development. This fiscal year we changed the focus of the project to address an important physics issue for these experiments, namely the EOS of the foams used in these experiments. Foams sometimes exhibit significantly different material behavior than normal materials, both in their response to shocks and in their relatively high specific heats at moderate energy density.

To address these concerns, we carried out two days of experiments and a total of 28 shots on OMEGA in FY12. These experiments built on the platform development of other shock physics experiments on OMEGA, including target geometries and diagnostics. This immediately enabled us to be relatively successful. Our specific purpose for these experiments was to measure the temperature of shocked aerogel foam in the few-Mbar range. The foam would have an initial density of 0.2 g/cm^{-3}, which has the advantage that the principal Hugoniot for this foam is well known, requiring only a measurement of the shock velocity to determine the state. We were very successful obtaining both good shock-velocity measurements and streaked optical pyrometer (SOP) measurements for a wide range of pressures. A brief analysis of the shock velocity and SOP data is given in Fig. 132.150. We found that the temperature dependence on the shock velocity was weak for a wide range of shock velocities, indicating a very high specific heat and also indicating the

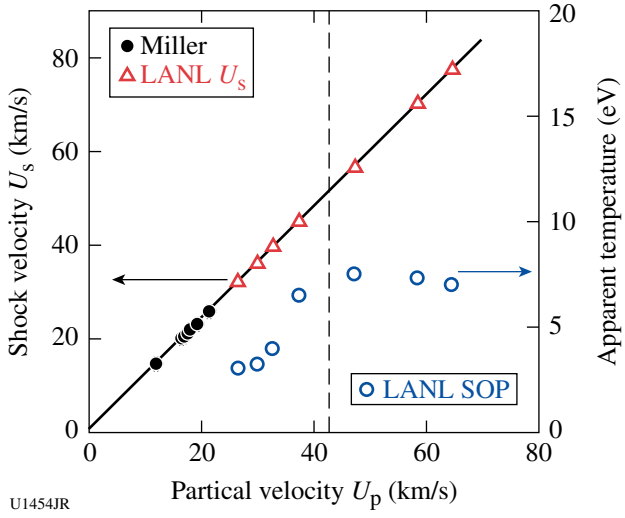

Figure 132.150
Temperature and shock-velocity measurements for 0.2-g/cm^{-3} aerogel foam targets. The straight line fit is based on Hugoniot measurements for this foam and the vertical dashed line corresponds to a pressure of ~4.4 Mbar.

important energy density range where ionization and dissociation occur. We also see a saturation of the SOP temperature at higher shock pressures. We believe either a limitation of the diagnostic or more likely radiative heating at the shock front is confusing the measurement. Since the two shot days were quite close together, few modifications were made to the target design, so this effect could not really be further investigated. We expect to learn more about this effect through a series of double-shock experiments to be carried out in FY13.

DTRat

On 9 August 2012, LANL's ICF Gamma Ray Physics team conducted ongoing DT Ratio Campaign experiments on OMEGA. Y. Kim and H. Herrmann led the collaborative effort including participation from LLNL, AWE, MIT, Colorado School of Mines, Cornell, and LLE. The capsules consisted of D^3He, $^3He^3He$, and DT fills for the primary purpose of characterizing the D^3He γ-ray spectrum. D^3He γ-ray measurements have been used by Kim *et al.*[99] as a cross-calibration for the recently published DT gamma-to-neutron branching ratio (BR) inference under the assumption that ^5He from DT and mirror nucleus ^5Li from D^3He generate virtually identical γ-ray spectra. This shot day was intended to test this assumption.

Figure 132.151 shows preliminary data taken by the gas Cherenkov detector (GCD) during a Cherenkov threshold scan indicating that, as expected, the primary peak from D–^{3}He fusion gammas decreases with an increasing energy threshold. More-quantitative analysis is awaiting the results of CR-39–based proton-yield measurements. One interesting feature, however, is what appears to be a secondary peak (~0.2 ns) that is not reduced as readily by thresholding, implying that it is from photons of higher energy than the 16.6 MeV D–^{3}He fusion gammas. The peak remains when the capsules contain no D (i.e., ^{3}He–^{3}He implosions). Since there is no expectation of a fusion gamma from the unbound and therefore extremely short-lived ^{6}Be, the current speculation is that this peak is the result of extremely high energy laser–plasma instability (LPI) x rays (>20 MeV) coming from the two-plasmon instability. This mechanism is known to be amplified for thin-walled glass capsules in which fusion bang time occurs before the end of the laser pulse. Over the past two years we have observed that this secondary peak becomes more pronounced with capsule thinness. It is now clear that this secondary peak must be accounted for when measuring the D–^{3}He gamma yield and cross-calibrating D–T γ/n BR to D–^{3}He γ/p BR. Doing so will result in making the cross-calibrated BR value more consistent with the previously determined absolute BR value published in Y. H. Kim *et al.*[100] This discovery may also lead to greater insight into LPI mechanisms leading to ultrahot electrons having deleterious effects on ignition.

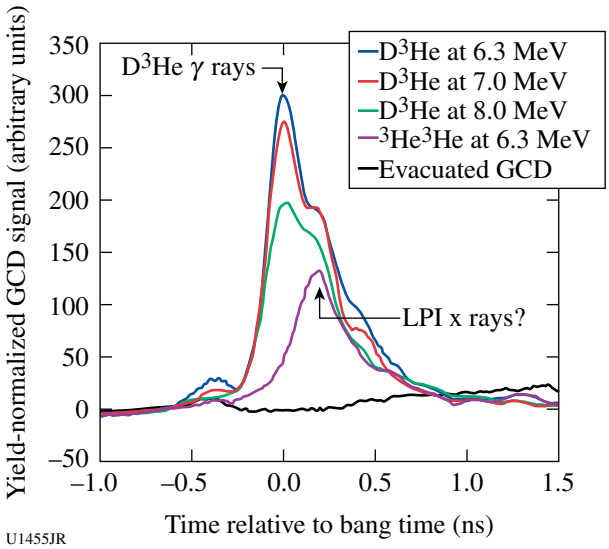

Figure 132.151
Data from the GCD showing fusion gamma decreasing with an increasing energy threshold.

DIME

The DIME campaign had two shot days in 2012 on OMEGA. On the first of the shot day, we used symmetric 60-beam illumination with ~800-μm-spot phase-plate smoothing for 1 ns to drive spherical implosions. The objective was to measure the mix depth of an embedded Ti layer (1% by atom) in the spherical capsule wall. The variable was the separation of the 2-μm impurity layer from the inner wall of the 435-μm-radius capsule for the ten targets. The embedded depth was 0.0, 1.4, 3.0, or 4.8 μm. The 19-μm wall thickness was sufficient to prevent burnthrough by the laser drive. Therefore, we collected data for the 4π mix. A first look at normalized data is shown in Fig. 132.152.

Neutron yield data were provided by V. Yu. Glebov (LLE). B. Yaakobi (LLE) facilitated the spectral analysis of the Ti K_α absorption feature and Ti line emission from the x-ray spectrographic data. One calculates the ρR of Ti from the transmission T of the continuum at 4.5 keV: $\rho R = -\ln T/\sigma$, where σ is the x-ray attenuation coefficient (cm^2/gm) of cold Ti. The line emission of Ti, heated by mix with the hot deuterium fill gas, peaks at zero depth and damps quickly with burial depth, thereby corroborating this picture of mix. The curved lines are to "guide the eye." The anticorrelation between yield and the Ti spectral data, which indicates a mix depth of ~1.5 μm, is consistent with expectations. A similar campaign, identical in

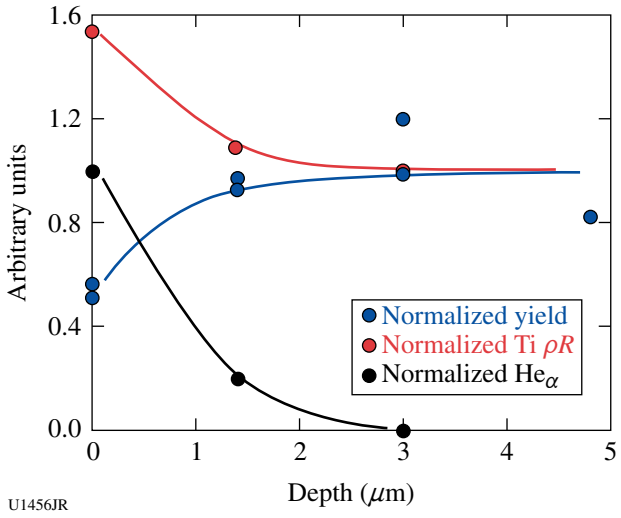

Figure 132.152
Correlation of mix parameters for the 60-beam drive.

every respect for targets, was executed for polar direct drive (PDD) later in the year. The objective for this campaign was to assess how PDD altered the mix depth and the spatial variations inherent with PDD. Steps in the inner CH wall layer were smaller. Data analysis is pending.

Colliding Shock

The LANL Colliding Shock Campaign had nearly 30 shots on OMEGA in November 2011 and March and July 2012. Radiographs of the colliding shocks were obtained on two cameras looking on orthogonal axes and at 2-ns delays with respect to each other. Excellent quality images were obtained, and a series of three are shown in Fig. 132.153 from 6, 12, and 18 ns. The experimental target shown in the top of Fig. 132.153 consists of a Be tube filled with foam and a 20-μm Ti foil tracer on one side. The target is driven from both ends (with a slight delay to the beam opposed to the foil). At 6 ns the foil is just beginning to be driven into the foam; at 12 ns the foil has propagated into the foam and is just meeting the oncoming shock; and at 18 ns it has been recompressed and stalled by the counter-propagating shock passing through it. The Be tube and shocks are visible in the radiographs as faint outlines perturbed by the propagating shock at the walls and in the foam. At 18 ns the tube is almost completely unrecognizable. The information from the turbulent mixing of the Ti layer in the reshocked area is contained in the width of the Ti layer. This width can be compared to our BHR-2 mix model in hydrodynamic simulations to understand how turbulence can affect the mixing of materials at material boundaries.

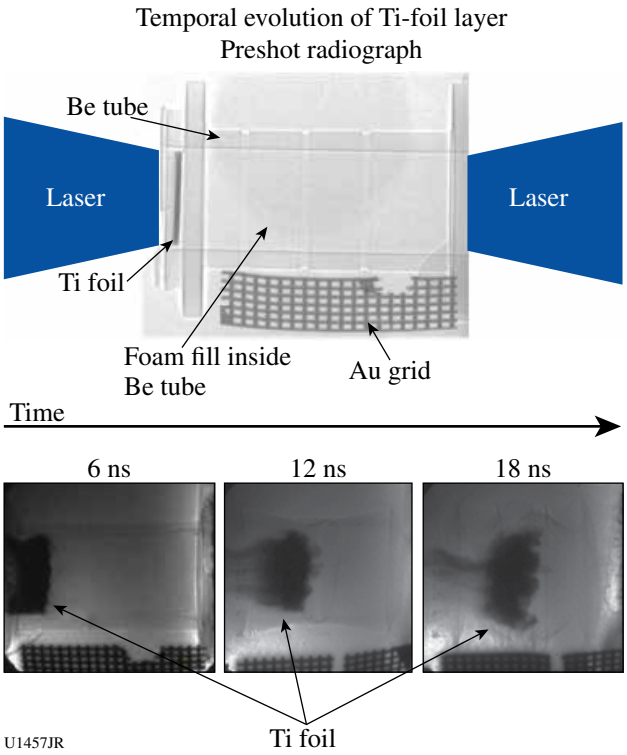

Figure 132.153
The temporal evolution of a 20-μm Ti tracer foil inside a Be shock tube filled with foam. The laser pushes a shock into the tube from both ends, with a resultant recompression and stall of the shocked layer.

FY12 CEA Experiments at the Omega Laser Facility

CEA Vulnerability Diagnostics on OMEGA

Vulnerability is a key point for plasma diagnostic design in megajoule-class lasers: hardened diagnostics must preserve their nominal performances for neutron yields up at least to 10^{17}. Since the DT shots at the Omega Laser Facility reproduce the perturbing source expected during the first 100 ns on megajoule-class laser facilities like Laser Mégajoule (LMJ) or the National Ignition Facility (NIF), this facility can be used to study the survivability of diagnostic elements such as optical relays or optical analyzers.

A standard imaging system, consisting of a fiber bundle, a light amplifier, and a cooled charge-coupled–device (CCD) camera, has been exposed to high neutron yield shots 5 m from target chamber center (TCC) (see Fig. 132.154). The level of nuclear background generated at the Omega Laser Facility leads to visible effects on the recording device that can be quantified thanks to masks positioned between the various optical interfaces. As a result (Fig. 132.155), the increasing background level of the recording device has been clearly

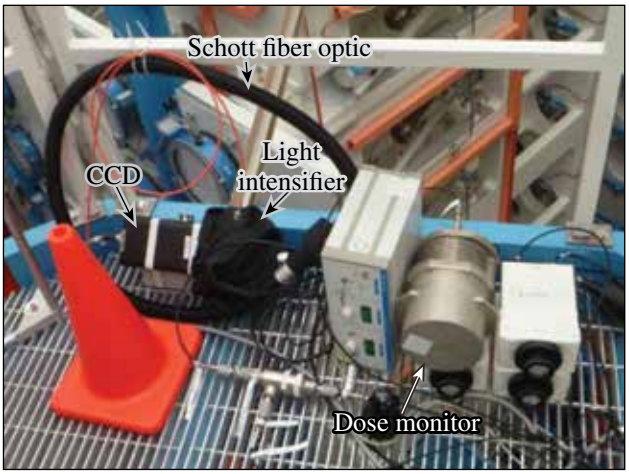

U1530JR

Figure 132.154
Experimental setup.

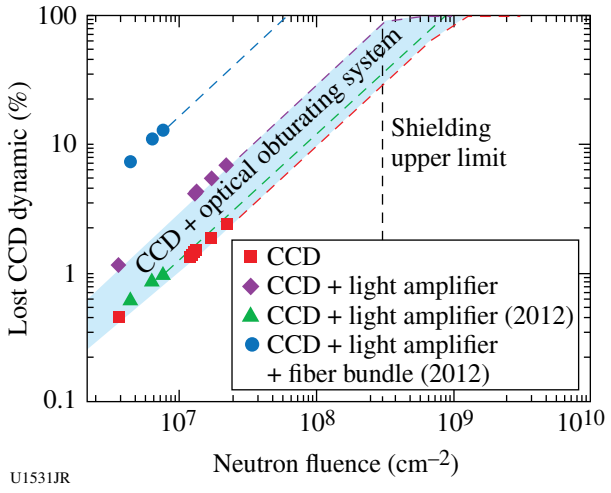

U1531JR

Figure 132.155
Parasitic signal intensity converted into the CCD dynamic range reduction.

observed: the dynamic range reduction appears to be directly proportional to the neutron fluence. The extreme sensitivity of the fiber bundle has been checked and extrapolation to NIF or LMJ radiative constraints leads us to expect a complete failure of the diagnostic. As a conclusion, such an optical relay must be avoided in a hardened diagnostic architecture.

A new mitigation technique to improve the radiation tolerance of a CMOS image sensor used in plasma diagnostics has been tested. It consists of resetting the charges generated by the incoming particles and then shortly after start to record a second image of a decaying scintillator, free of neutron impacted pixels. Such a scheme, based on the use of a custom global reset (GR) functionality designed by the Institut Supérieur de l'Aéraunotique et de l'Espace (ISAE), University of Toulouse is illustrated in the timing diagrams in Fig. 132.156.

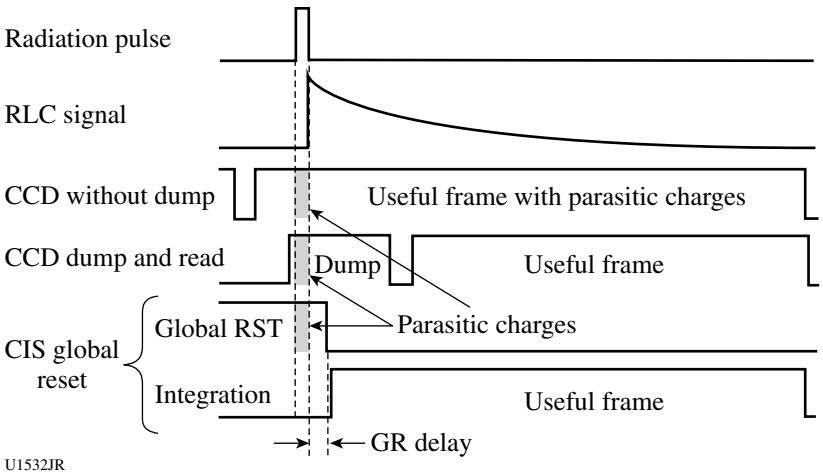

U1532JR

Figure 132.156
Timing diagrams illustrating the standard CCD readout operation, the dump and read technique, and the proposed CIS global reset technique.

A dedicated radiation-hardened test bench has been developed to simulate a plasma diagnostic and has been exposed to neutron yields produced by OMEGA DT shots.[101] The useful signal is generated by a pulsed UV light-emitting diode (LED) synchronized with bang time to excite a long decay-time scintillator. A test pattern has been placed after the radiation-to-light convertor (RLC) to validate that the sensor properly acquires the useful signal. As a first result, the GR reset mode significantly reduces the transient perturbation (parasitic white pixels) without degradation of the image quality (Fig. 132.157). Nevertheless, there is still a small number of remaining disturbed pixels in the image taken with the GR mode. Monte Carlo simulations show that some delayed high-energy particles impinge the sensor after the GR dump phase and create these perturbations during the image acquisition.

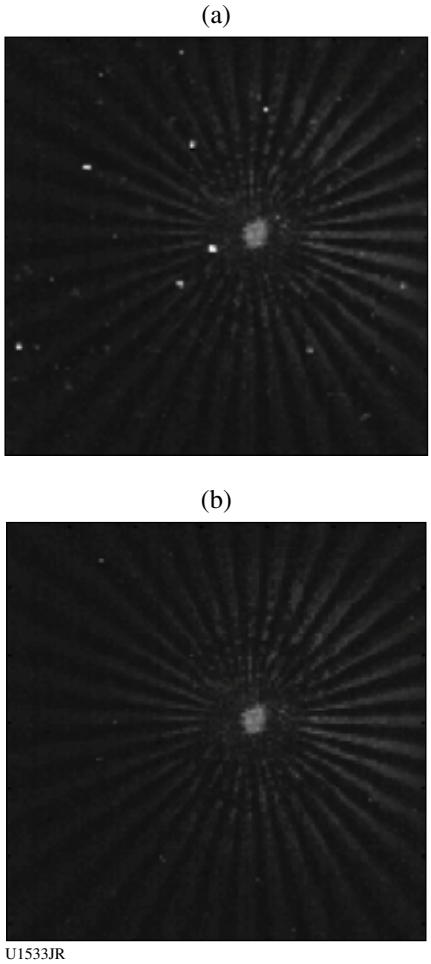

Figure 132.157
RLC and test pattern image captured during a laser shot. (a) Image acquired with the standard timing diagram (no GR) and (b) image acquired with the GR fast dump phase.

High-Resolution Imaging at LLE for CEA Shots

An extended high-resolution x-ray imager (EHRXI) was successfully implemented on OMEGA in May 2012 for the CEA "preheat" campaign. This diagnostic consists of an x-ray microscope and a charge-injection–device (CID) camera. The microscope is a two toroidal mirror pseudo-Wolter microscope. EHRXI is the extended version of an already existing diagnostic, the high-resolution x-ray imager (HRXI). We have replaced its mirrors with similar ones yet coated with a non-periodic multilayer coating that extends their reflectivity up to 12 keV at a grazing angle of 0.6°. The overall layout of the EHRXI is shown in Fig. 132.158.

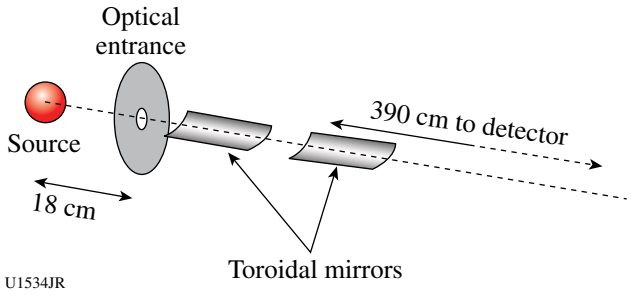

Figure 132.158
Schematic showing the layout of the EHRXI diagnostic.

The design of the microscope allows it to obtain a resolution of 4 μm in a 1-mm-diam field of view. This resolution was measured on a low-energy Riber x-ray generator at CEA.[102]

The goal of the experiment led at LLE was to observe the preheating of a metallic sample on a cavity laser entrance hole (LEH) using radiography while the cavity is being shot. The purpose of the EHRXI was to get a precise image of the Ti backlighting x-ray source. The EHRXI was aimed at the center of the backlighting source, with an angle of 56° regarding the back normal vector of that source. It was placed 30 cm from the backlighter. The microscope entrance was filtered with 75 μm of vanadium to get the spectrum presented Fig. 132.159. The CID camera was placed in a dedicated holder at the back of a ten-inch manipulator (TIM-1) as shown Fig. 132.160.

The target used for the experiment is presented in Fig. 132.161(a). The radiography target is the black disk in the foreground. Figure 132.161(b) shows an image of a shot recorded by the EHRXI. The expected x-ray source size was 200×300 μm and the measured size is 230×300 μm. The results are, therefore, in good agreement with the expectations.

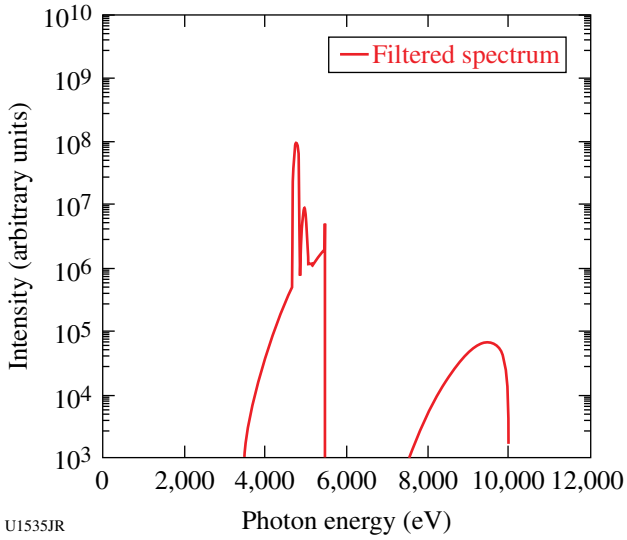

Figure 132.159
Emission spectrum filtered with 75 μm of vanadium.

Figure 132.160
Photo of the EHRXI in TIM-1; the CID camera holder sits at the back of the TIM.

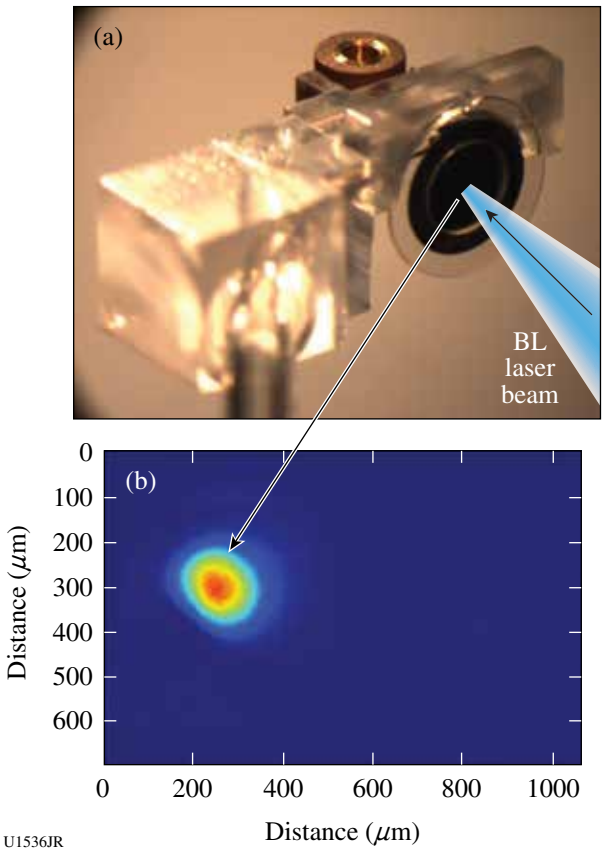

Figure 132.161
(a) Target photo taken on the EHRXI line-of sight. (b) An EHRXI image of the backlighting source of the preheat campaign.

The image is post-treated to remove the charge injection device (CID) noise and the anamorphosis caused by the angle of the line of sight. In conclusion, the EHRXI implementation on OMEGA was a success and it proved to be a versatile, easy-to-use diagnostic.

X-Ray Crystal Spectrometers (XCCS)

Two x-ray crystal spectrometers in the TIM have been built by CEA. The first one is the XCCS-CID (Fig. 132.162). It is time integrated. It features three channels with an imaging slit (magnification 3), a blast shield, filters, a cylindrical crystal, and detection is performed by a CID detector. The distance of the CID to target chamber center (TCC) is 1055 mm. The second one is XCCS-FC (Fig. 132.163). It features four channels with an imaging slit (magnification 3), filters, a cylindrical crystal, and detection is performed by a framing camera (FC). Two adjacent channels share the same 20-mm-width crystal. The distance of the framing camera to TCC is 701 mm. Both spectrometers can accommodate crystals on spacers and shims with a fixed angle ranging from 7.5° to 35° inside a large box.

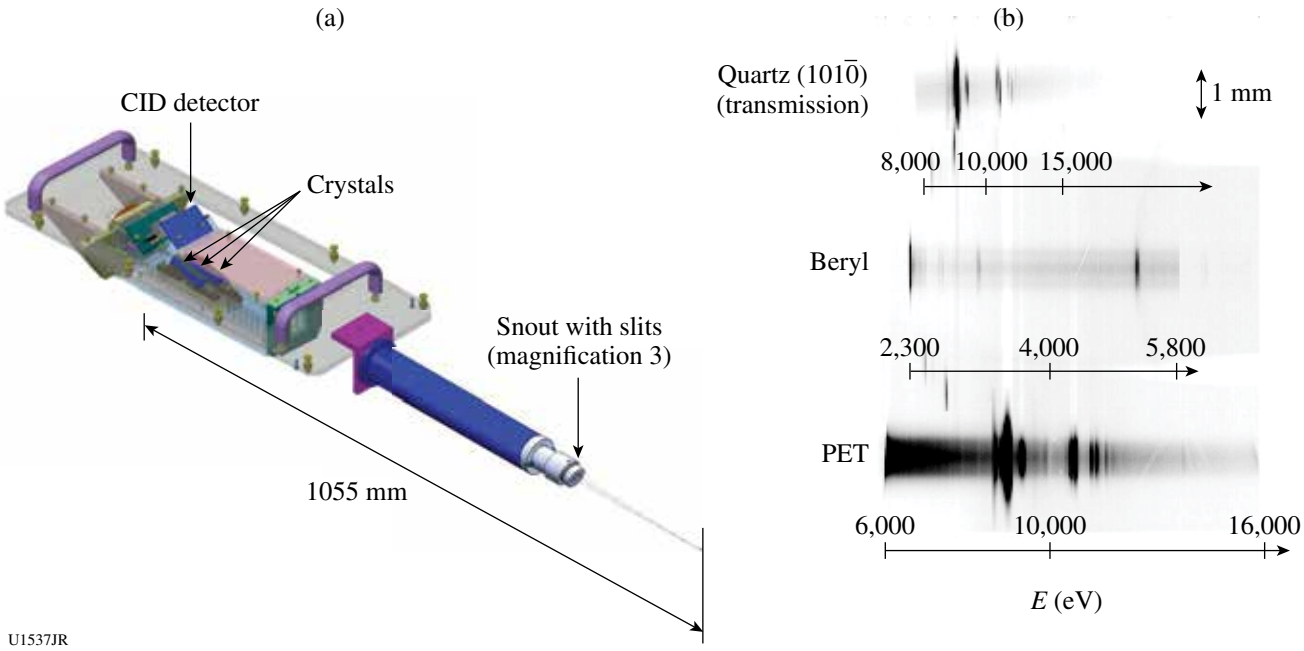

Figure 132.162
(a) Schematic of the XCCS-CID; (b) Zn spectrum recorded on shot 62653.

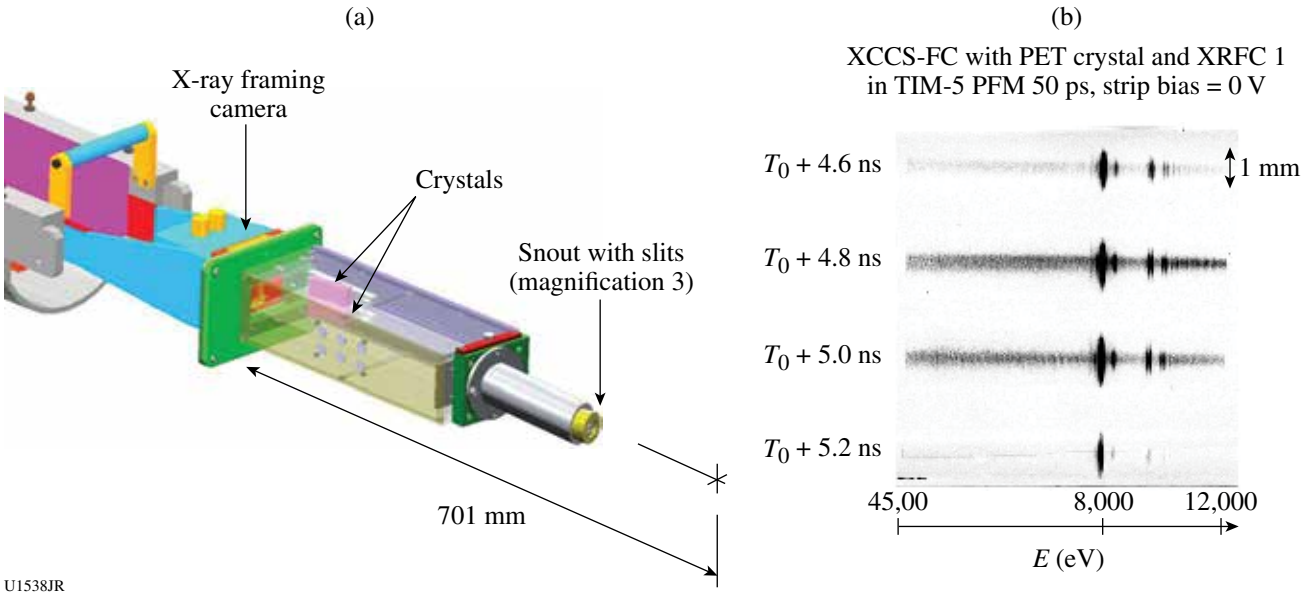

Figure 132.163
(a) Schematic of the XCCS-FC; (b) Ni spectrum obtained on shot 67454.

With the available crystals, configurations covering 1.5 to 15 keV can be achieved.

CEA Rugby Implosions and Convergent Ablation Experiments on OMEGA

CEA is pursuing indirect-drive–implosion experiments on OMEGA using rugby-shaped hohlraums in preparation for early implosion on the Laser Mégajoule (LMJ). It has been previously demonstrated that an increased x-ray drive (+18% in flux) was achieved with a vacuum rugby-shaped hohlraum in comparison with a cylinder.[103] These results were confirmed and even enhanced in the case of gas-filled hohlraums.The question of the precise wall shape of the rugby hohlraum has been addressed recently[104] and it was demonstrated that elliptically shaped hohlraums [see Fig. 132.164(a)] are more efficient than spherically shaped hohlraums. There is less wall hydrodynamic motion and less absorption for the LMJ inner cone, providing a better control of time-dependent symmetry swings. The goal of one experiment was, therefore, to characterize energetics and capsule implosion in elliptical hohlraums compared to rugby- and cylinder-shaped hohlraums during last year's shots.

The round core image acquired on an implosion performed in a gas-filled elliptical hohlraum confirms our capability to control the symmetry in this new hohlraum geometry [see Fig. 132.164(b)].

The increased x-ray drive in rugby measured with Dante was confirmed by enhanced nuclear performances and more ablated mass.[103] It is nevertheless important to perform convergent ablation measurements[105] to assess the implosion velocity—a key metric for ignition performance. ConA experiments with gas-filled rugby hohlraums were, therefore, shot for the first time. The schematic of the experimental configuration is shown in Fig. 132.165(a). A time-resolved 1-D streaked radiography is

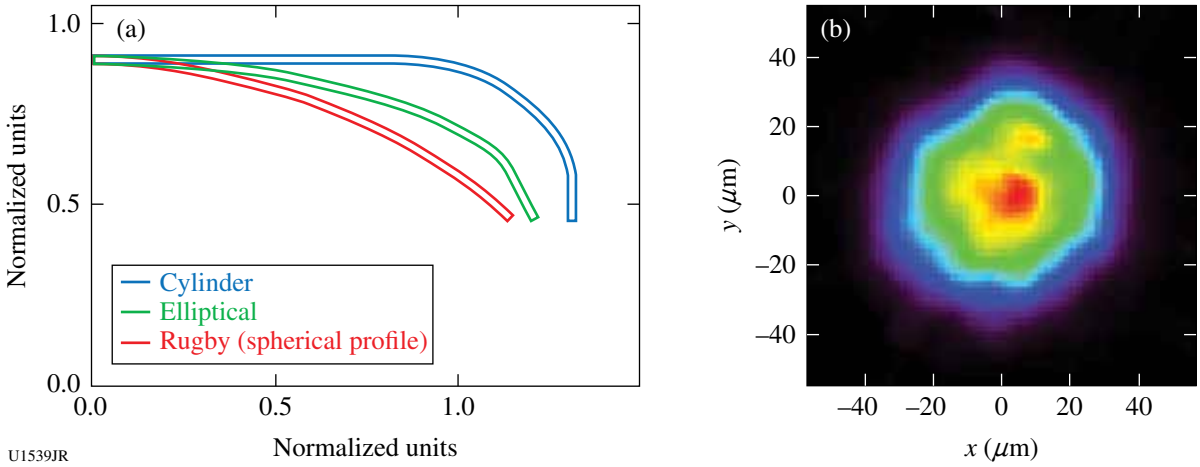

Figure 132.164
(a) Shaped-hohlraum profiles and (b) an x-ray core image for a D_2 implosion performed in an elliptically shaped hohlraum.

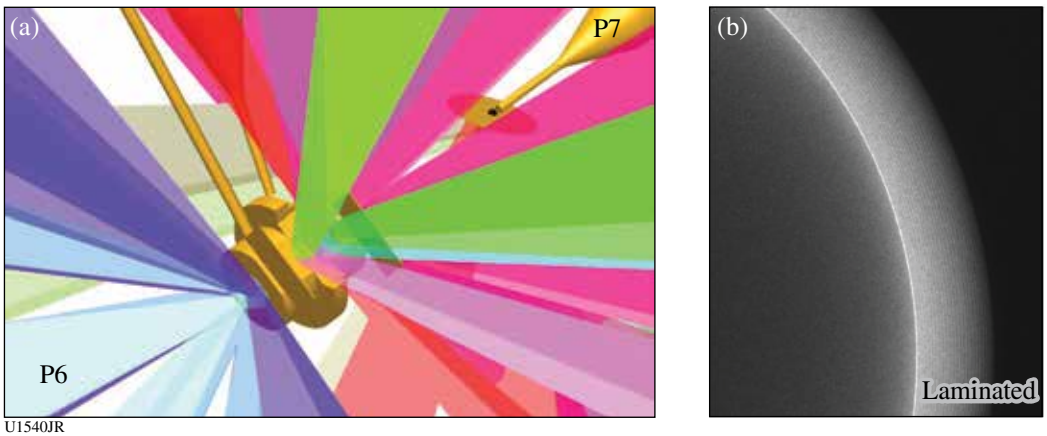

Figure 132.165
(a) Experimental configuration along P6/P7. The streaked implosion radiography is performed toward H14, perpendicular to the hohlraum axis. (b) A typical laminated capsule.

acquired with SSC A in the direction perpendicular to the hohlraum axis, whereas a 2-D time-resolved radiography is acquired at the same time along the hohlraum axis on an x-ray framing camera. These experiments were also aimed at comparing the implosion performance of a uniformly doped and laminated ablator.[106] A laminated ablator consists of thin alternate layers of undoped and germanium-doped CH. Figure 132.165(b) presents a pre-shot radiography of a laminated capsule, on which the thin layers of doped and undoped material are clearly visible. It has been experimentally demonstrated in planar geometry that laminated ablators could mitigate Rayleigh–Taylor growth at the ablation front.[107]

A typical backlight implosion is shown on Fig. 132.166(a). The limb of the shell is well defined and its position could be extracted from the radiography. Preliminary data comparing uniformly doped and laminated capsule trajectory do not indicate discrepancies for the implosion. This corroborates the trajectory measurements already acquired for planar samples.[107]

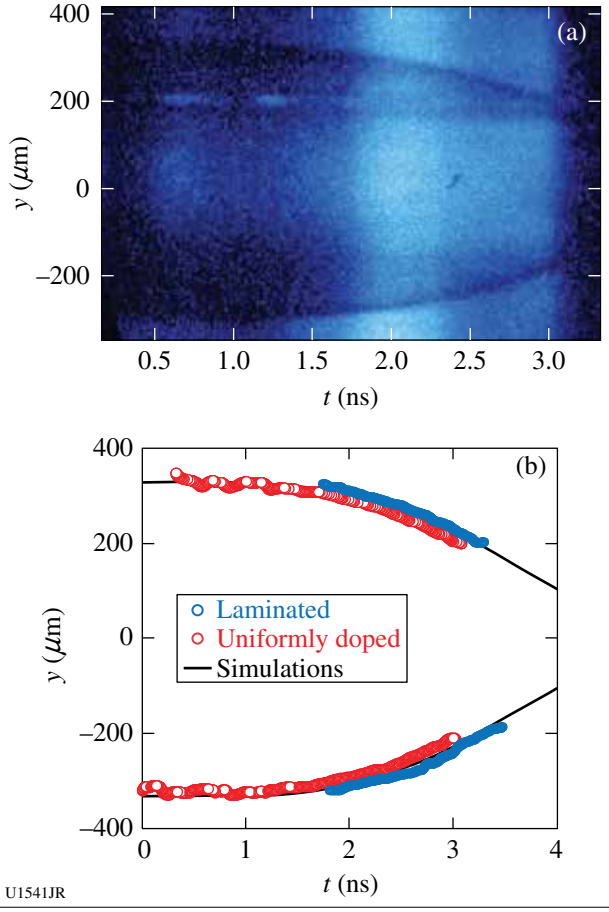

Figure 132.166
(a) Typical streaked radiography acquired on a gas-filled rugby implosion. (b) Comparison of capsule trajectory for laminated and uniformly doped ablators.

FY12 AWE OMEGA EP and OMEGA Experimental Programs

ShkLaue-12A

Principal Investigator: A. J. Comley (AWE)

In the ShkLaue-12A campaign, we made a first attempt to diagnose ramp-compressed, single-crystal tantalum [100] using our established broadband x-ray ("white light") Laue diffraction platform. This platform utilizes an implosion capsule backlighter (980-μm outer diameter, with a 10-μm-thick CH wall) driven by 30 beams [each beam contained 500 J in a 1-ns square pulse and SG4 distributed phase plate (DPP)] to generate a smoothly varying and broadband spectrum of x rays from a "point" source. VISAR (velocity interferometer system for any reflector) is also employed simultaneously with the x-ray diffraction technique.

The target design is shown in Fig. 132.167. Three beams were employed (each ~200 J in a 3.7-ns square pulse and SG8 DPP) to produce a shock in the BrCH reservoir. Upon shock breakout, the reservoir material crosses the gap and stagnates near the sample (which is protected from direct heating by a CH heat shield), such that a smoothly increasing ramp-compression drive is produced, with a peak pressure of ~100 GPa. X-ray diffraction and VISAR data were obtained successfully (Fig. 132.168). Analysis of the diffraction patterns, in which we see a clear signature from the driven tantalum sample, is currently undergoing detailed analysis in conjunction with information obtained from VISAR.

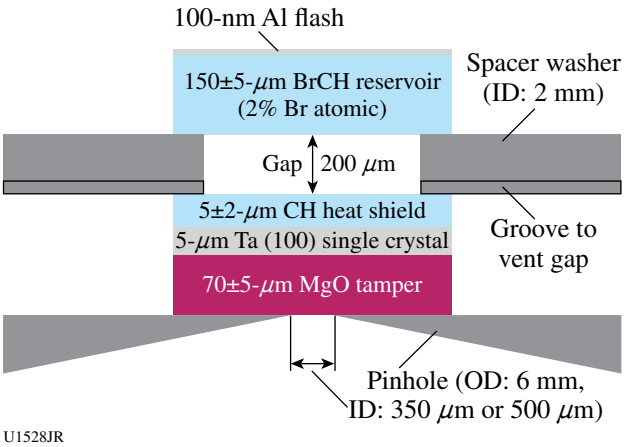

Figure 132.167
ShkLaue-12A ramp-compression target design.

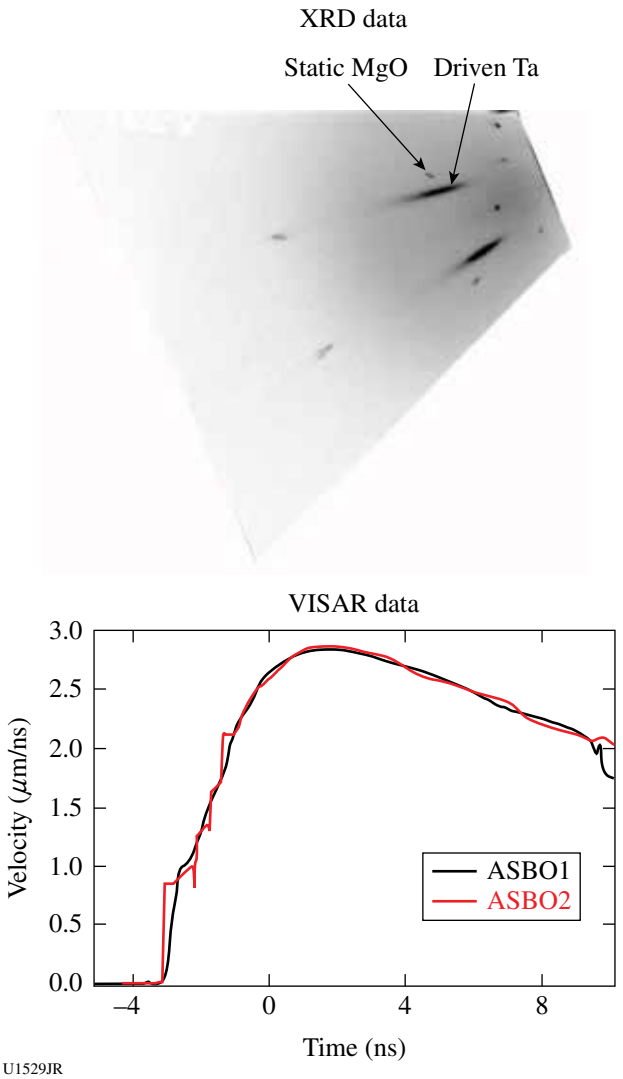

Figure 132.168
(a) The x-ray diffraction (XRD) pattern contains characteristic spots, each of which can be attributed to either the tantalum or MgO layers in the target package and to specific crystallographic lattice planes. (b) VISAR records the compression history of the sample.

REFERENCES

1. T. S. Duffy, R. J. Hemley, and H. Mao, Phys. Rev. Lett. **74**, 1371 (1995).

2. A. R. Organov, M. J. Gillian, and G. D. Price, J. Phys. Chem. **118**, 10,174 (2003).

3. T. Nagayama, R. C. Mancini, R. Florido, R. Tommasini, J. A. Koch, J. A. Delettrez, S. P. Regan, and V. A. Smalyuk, J. Appl. Phys. **109**, 093303 (2011).

4. T. Nagayama, R. C. Mancini, R. Florido, D. Mayes, R. Tommasini, J. A. Koch, J. A. Delettrez, S. P. Regan, and V. A. Smalyuk, Phys. Plasmas **19**, 082705 (2012).

5. D. T. Casey, J. A. Frenje, M. Gatu Johnson, M. J.-E. Manuel, N. Sinenian, A. B. Zylstra, F. H. Séguin, C. K. Li, R. D. Petrasso, V. Yu. Glebov, P. B. Radha, D. D. Meyerhofer, T. C. Sangster, D. P. McNabb, P. A. Amendt, R. N. Boyd, S. P. Hatchett, S. Quaglioni, J. R. Rygg, I. J. Thompson, A. D. Bacher, H. W. Herrmann, and Y. H. Kim, Phys. Rev. Lett. **109**, 025003 (2012).

6. N. Sinenian, G. Fiksel, J. A. Frenje, C. G. Freeman, M. J.-E. Manuel, D. T. Casey, P. M. Nilson, C. Stoeckl, W. Theobald, D. D. Meyerhofer, and R. D. Petrasso, Phys. Plasmas **19**, 093118 (2012).

7. M. J.-E. Manuel, C. K. Li, F. H. Séguin, J. A. Frenje, D. T. Casey, R. D. Petrasso, S. X. Hu, R. Betti, J. D. Hager, D. D. Meyerhofer, and V. Smalyuk, Phys. Plasmas **19**, 082710 (2012).

8. N. Sinenian, A. B. Zylstra, M. J. E. Manuel, H. G. Rinderknecht, J. A. Frenje, F. H. Seguin, C. K. Li, R. D. Petrasso, V. Goncharov, J. Delettrez, I. V. Igumenshchev, D. H. Froula, C. Stoeckl, T. C. Sangster, D. D. Meyerhofer, J. A. Cobble, and D. G. Hicks, Appl. Phys. Lett. **101**, 114102 (2012).

9. M. J.-E. Manuel *et al.*, Appl. Phys. Lett. **100**, 203505 (2012).

10. M. J.-E. Manuel, C. K. Li, F. H. Séguin, J. Frenje, D. T. Casey, R. D. Petrasso, S. X. Hu, R. Betti, J. D. Hager, D. D. Meyerhofer, and V. A. Smalyuk, Phys. Rev. Lett. **108**, 255006 (2012).

11. D. T. Casey, J. A. Frenje, M. Gatu Johnson, M. J.-E. Manuel, H. G. Rinderknecht, N. Sinenian, F. H. Séguin, C. K. Li, R. D. Petrasso, P. B. Radha, J. A. Delettrez, V. Yu. Glebov, D. D. Meyerhofer, T. C. Sangster, D. P. McNabb, P. A. Amendt, R. N. Boyd, J. R. Rygg, H. W. Herrmann, Y. H. Kim, and A. D. Bacher, Phys. Rev. Lett. **108**, 075002 (2012).

12. C. K. Li, F. H. Séguin, J. A. Frenje, M. J. Rosenberg, H. G. Rinderknecht, A. B. Zylstra, R. D. Petrasso, P. A. Amendt, O. L. Landen, A. J. Mackinnon, R. P. J. Town, S. C. Wilks, R. Betti, D. D. Meyerhofer, J. M. Soures, J. Hund, J. D. Kilkenny, and A. Nikroo, Phys. Rev. Lett. **108**, 025001 (2012).

13. F. H. Séguin, C. K. Li, M. J.-E. Manuel, H. G. Rinderknecht, N. Sinenian, J. A. Frenje, J. R. Rygg, D. G. Hicks, R. D. Petrasso, J. Delettrez, R. Betti, F. J. Marshall, and V. A. Smalyuk, Phys. Plasmas **19**, 012701 (2012).

14. N. Sinenian *et al.*, "A Multithreaded Modular Software Toolkit for Control of Complex Experiments," to be published in Computing in Science and Engineering.

15. D. T. Casey, J. A. Frenje, M. Gatu Johnson, F. H. Séguin, C. K. Li, R. D. Petrasso, V. Yu. Glebov, J. Katz, J. P. Knauer, D. D. Meyerhofer, T. C. Sangster, R. M. Bionta, D. L. Bleuel, T. Döppner, S. Glenzer, E. Hartouni, S. P. Hatchett, S. Le Pape, T. Ma, A. MacKinnon, M. A. Mckernan, M. Moran, E. Moses, H.-S. Park, J. Ralph, B. A. Remington, V. Smalyuk, C. B. Yeamans, J. Kline, G. Kyrala, G. A. Chandler, R. J. Leeper, C. L. Ruiz, G. W. Cooper, A. J. Nelson, K. Fletcher, J. Kilkenny, M. Farrell, D. Jasion, and R. Paguio, Rev. Sci. Instrum. **83**, 10D912 (2010).

16. F. H. Séguin, N. Sinenian, M. Rosenberg, A. Zylstra, M. J. E. Manuel, H. Sio, C. Waugh, H. G. Rinderknecht, M. Gatu Johnson, J. Frenje, C. K. Li, R. Petrasso, T. C. Sangster, and S. Roberts, Rev. Sci. Instrum. **83**, 10D908 (2012).

17. M. J.-E. Manuel *et al.*, Rev. Sci. Instrum. **83**, 063506 (2012).

18. N. Sinenian *et al.*, Rev. Sci. Instrum. **83**, 043502 (2012).

19. A. Zylstra, C. K. Li, H. G. Rinderknecht, F. H. Séguin, R. D. Petrasso, C. Stoeckl, D. D. Meyerhofer, P. Nilson, T. C. Sangster, S. Le Pape, A. Mackinnon, and P. Patel, Rev. Sci. Instrum. **83**, 013511 (2012).

20. A. B. Zylstra *et al.*, Nucl. Instrum. Methods Phys. Res. A **681**, 84 (2012).

21. M. Hohenberger, P.-Y. Chang, G. Fiksel, J. P. Knauer, R. Betti, F. J. Marshall, D. D. Meyerhofer, F. H. Séguin, and R. D. Petrasso, Phys. Plasmas **19**, 056306 (2012).

22. N. Sinenian *et al.*, Rev. Sci. Instrum. **82**, 103303 (2011).

23. T. R. Boehly, D. L. Brown, R. S. Craxton, R. L. Keck, J. P. Knauer, J. H. Kelly, T. J. Kessler, S. A. Kumpan, S. J. Loucks, S. A. Letzring, F. J. Marshall, R. L. McCrory, S. F. B. Morse, W. Seka, J. M. Soures, and C. P. Verdon, Opt. Commun. **133**, 495 (1997).

24. L. J. Waxer, D. N. Maywar, J. H. Kelly, T. J. Kessler, B. E. Kruschwitz, S. J. Loucks, R. L. McCrory, D. D. Meyerhofer, S. F. B. Morse, C. Stoeckl, and J. D. Zuegel, Opt. Photonics News **16**, 30 (2005).

25. C. K. Li, F. H. Séguin, J. A. Frenje, J. R. Rygg, R. D. Petrasso, R. P. J. Town, P. A. Amendt, S. P. Hatchett, O. L. Landen, A. J. Mackinnon, P. K. Patel, V. Smalyuk, J. P. Knauer, T. C. Sangster, and C. Stoeckl, Rev. Sci. Instrum. **77**, 10E725 (2006).

26. N. L. Kugland, D. D. Ryutov, P. Y. Chang, R. P. Drake, G. Fiksel, D. H. Froula, S. H. Glenzer, G. Gregori, M. Grosskopf, M. Koenig, Y. Kuramitsu, C. Kuranz, M. C. Levy, E. Liang, J. Meinecke, F. Miniati, T. Morita, A. Pelka, C. Plechaty, R. Presura, A. Ravasio, B. A. Remington, B. Reville, J. S. Ross, Y. Sakawa, A. Spitkovsky, H. Takabe, and H. S. Park, Nat. Phys. **8**, 809 (2012).

27. J. S. Ross, S. H. Glenzer, P. Amendt, R. Berger, L. Divol, N. L. Kugland, O. L. Landen, C. Plechaty, B. Remington, D. Ryutov, W. Rozmus, D. H. Froula, G. Fiksel, C. Sorce, Y. Kuramitsu, T. Morita, Y. Sakawa, H. Takabe, R. P. Drake, M. Grosskopf, C. Kuranz, G. Gregori, J. Meinecke, C. D. Murphy, M. Koenig, A. Pelka, A. Ravasio, T. Vinci, E. Liang, R. Presura, A. Spitkovsky, F. Miniati, and H.-S. Park, Phys. Plasmas **19**, 056501 (2012).

28. H.-S. Park, D. D. Ryutov, J. S. Ross, N. L. Kugland, S. H. Glenzer, C. Plechaty, S. M. Pollaine, B. A. Remington, A. Spitkovsky, L. Gargate, G. Gregori, A. Bell, C. Murphy, Y. Sakawa, Y. Kuramitsu, T. Morita, H. Takabe, D. H. Froula, G. Fiksel, F. Miniati, M. Koenig, A. Ravasio, A. Pelka, E. Liang, N. Woolsey, C. C. Kuranz, R. P. Drake, and M. J. Grosskopf, High Energy Density Phys. **8**, 38 (2012).

29. A. Spitkovsky, presented at the Colloquium at Northwestern University, Evanston, IL, February 2012.

30. A. Spitkovsky, presented at the 9th International Conference on High Energy Density Laboratory Astrophysics, Tallahassee, FL, 30 April–4 May 2012.

31. A. Spitkovsky, presented at the Twenty-Second International Conference on Numerical Simulations of Plasmas (ICNSP 2011), Long Branch, NJ, 7–9 September 2011.

32. A. Spitkovsky, presented at the Center for Magnetic Self-Organization (CMSO) General Meeting, Durham, NH, 17–20 October 2011.

33. J. Ross, Bull. Am. Phys. Soc. **56**, 282 (2011).

34. M. Grosskopf *et al.*, presented at High Energy Density Laboratory Astrophysics, Tallahassee, FL, 30 April–4 May 2012.

35. L. Willingale, P. M. Nilson, A. G. R. Thomas, J. Cobble, R. S. Craxton, A. Maksimchuk, P. A. Norreys, T. C. Sangster, R. H. H. Scott, C. Stoeckl, C. Zulick, and K. Krushelnick, Phys. Rev. Lett. **106**, 105002 (2011).

36. S. P. D. Mangles *et al.*, Phys. Rev. Lett. **94**, 245001 (2005).

37. N. Naseri, S. G. Bochkarev, and W. Rozmus, Phys. Plasmas **17**, 033107 (2010).

38. S. Fritzler *et al.*, Phys. Rev. Lett. **89**, 165004 (2002).

39. G. H. Miller and T. J. Ahrens, Rev. Mod. Phys. **63**, 919 (1991), Eq. (127).

40. H. Chen, S. C. Wilks, D. D. Meyerhofer, J. Bonlie, C. D. Chen, S. N. Chen, C. Courtois, L. Elberson, G. Gregori, W. Kruer, O. Landoas, J. Mithen, J. Myatt, C. D. Murphy, P. Nilson, D. Price, M. Schneider, R. Shepherd, C. Stoeckl, M. Tabak, R. Tommasini, and P. Beiersdorfer, Phys. Rev. Lett. **105**, 015003 (2010).

41. H. Chen, D. D. Meyerhofer, S. C. Wilks, R. Cauble, F. Dollar, K. Falk, G. Gregori, A. Hazi, E. I. Moses, C. D. Murphy, J. Myatt, J. Park, J. Seely, R. Shepherd, A. Spitkovsky, C. Stoeckl, C. I. Szabo, R. Tommasini, C. Zulick, and P. Beirsdorfer, High Energy Density Phys. **7**, 225 (2011).

42. O. A. Hurricane, High Energy Density Phys. **4**, 97 (2008).

43. E. C. Harding *et al.*, Phys. Rev. Lett. **103**, 045005 (2009).

44. O. A. Hurricane *et al.*, Phys. Plasmas **16**, 056305 (2009).

45. V. A. Smalyuk *et al.*, Phys. Plasmas **19**, 092702 (2012).

46. K. S. Raman *et al.*, Phys. Plasmas **19**, 092112 (2012).

47. O. A. Hurricane *et al.*, Phys. Rev. Lett. **109**, 155004 (2012).

48. Z. Y. Bao *et al.*, At. Data Nucl. Data Tables **76**, 70 (2000).

49. N. Cue, J.-C. Poizat, and J. Remillieux, Europhys. Lett. **8**, 19 (1989).

50. A. Pálffy *et al.*, Phys. Lett. B **661**, 330 (2008).

51. A. Pálffy, W. Scheid, and Z. Harman, Phys. Rev. A **73**, 012715 (2006).

52. M. R. Harston and J. F. Chemin, Phys. Rev. C **59**, 2462 (1999).

53. M. Morita and K. Otozai, Hyperfine Interact. **2**, 418 (1976).

54. S. Kishimoto *et al.*, Nucl. Phys. A **748**, 3 (2005).

55. M. R. Harston and J. J. Carroll, Laser Phys. **14**, 1452 (2004).

56. N. L. Kugland, presented at the 9th International Conference on High Energy Density Laboratory Astrophysics, Tallahassee, FL, 30 April–4 May 2012.

57. H.-S. Park, N. L. Kugland, J. S. Ross, B. A. Remington, C. Plechaty, D. D. Ryutov, A. Spitkovsky, G. Gregori, A. Bell, J. Meinecke, C. Murphy, Y. Sakawa, Y. Kuramitsu, H. Takabe, D. H. Froula, G. Fiksel, F. Miniati, M. Koenig, A. Ravasio, E. Liang, N. Woolsey, R. P. Drake, C. Kuranz, M. Grosskopf, and R. Presura, presented at the 9th International Conference on High Energy Density Laboratory Astrophysics, Tallahassee, FL, 30 April–4 May 2012.

58. D. D. Ryutov *et al.*, presented at the 9th International Conference on High Energy Density Laboratory Astrophysics, Tallahassee, FL, 30 April–4 May 2012.

59. J. S. Ross *et al.*, Rev. Sci. Instrum. **83**, 10E323 (2012).

60. N. L. Kugland *et al.*, Rev. Sci. Instrum. **83**, 101301 (2012).

61. D. D. Ryutov *et al.*, Plasma Phys. Control. Fusion **54**, 105021 (2012).

62. D. D. Ryutov *et al.*, Phys. Plasmas **19**, 074501 (2012).

63. D. D. Ryutov *et al.*, Phys. Plasmas **18**, 104504 (2011).

64. N. L. Kugland *et al.*, "Visualizing Electromagnetic Fields in Laser-Produced Counter-Streaming Plasma Experiments for Collisionless Shock Laboratory Astrophysics," to be submitted to Physics of Plasmas.

65. M. J. Grosskopf, R. P. Drake, C. C. Kuranz, E. M. Rutter, J. S. Ross, N. L. Kugland, S. Pollaine, B. A. Remington, D. D. Ryutov, A. Spitkovsky, L. Gargate, G. Gregori, A. Bell, C. D. Murphy, J. Meinecke, B. Reville, Y. Sakawa, Y. Kuramitsu, H. Takabe, D. H. Froula, G. Fiksel, F. Miniati, M. Koenig, A. Ravasio, E. Liang, N. Woolsey, and H.-S. Park, "Simulation of Laser-Driven, Ablated Flows in Collisionless Shock Experiments on OMEGA and the NIF," submitted to High Energy Density Physics.

66. S. P. Regan, K. Falk, G. Gregori, P. B. Radha, S. X. Hu, T. R. Boehly, B. J. B. Crowley, S. H. Glenzer, O. L. Landen, D. O. Gericke, T. Doeppner, D. D. Meyerhofer, C. D. Murphy, T. C. Sangster, and J. Vorberger, "Inelastic X-Ray Scattering from Shocked Liquid Deuterium," to be published in Physical Review Letters; *LLE Review Quarterly Report* **131**, 143, Laboratory for Laser Energetics, University of Rochester, Rochester, NY, LLE Document No. DOE/NA/28302-1064 (2012); *LLE Review Quarterly Report* **130**, 72, Laboratory for Laser Energetics, University of Rochester, Rochester, NY, LLE Document No. DOE/NA/28302-1058 (2012).

67. G. Gregori *et al.*, High Energy Density Phys. **3**, 99 (2007).

68. E. García Saiz *et al.*, Nat. Phys. **4**, 940 (2008).

69. G. Kresse and J. Furthmüller, Phys. Rev. B **54**, 11169 (1996).

70. J. Vorberger *et al.*, Phys. Rev. B **75**, 024206 (2007).

71. W. Theobald, A. A. Solodov, C. Stoeckl, K. S. Anderson, R. Betti, T. R. Boehly, R. S. Craxton, J. A. Delettrez, C. Dorrer, J. A. Frenje, V. Yu. Glebov, H. Habara, K. A. Tanaka, J. P. Knauer, R. Lauck, F. J. Marshall, K. L. Marshall, D. D. Meyerhofer, P. M. Nilson, P. K. Patel, H. Chen, T. C. Sangster, W. Seka, N. Sinenian, T. Ma, F. N. Beg, E. Giraldez, and R. B. Stephens, Phys. Plasmas **18**, 056305 (2011).

72. P. B. Radha, T. J. B. Collins, J. A. Delettrez, Y. Elbaz, R. Epstein, V. Yu. Glebov, V. N. Goncharov, R. L. Keck, J. P. Knauer, J. A. Marozas, F. J. Marshall, R. L. McCrory, P. W. McKenty, D. D. Meyerhofer, S. P. Regan, T. C. Sangster, W. Seka, D. Shvarts, S. Skupsky, Y. Srebro, and C. Stoeckl, Phys. Plasmas **12**, 056307 (2005).

73. J. A. King, K. Akli, B. Zhang, R. R. Freeman, M. H. Key, C. D. Chen, S. P. Hatchett, J. A. Koch, A. J. MacKinnon, P. K. Patel, R. Snavely, R. P. J. Town, M. Borghesi, L. Romagnani, M. Zepf, T. Cowan, H. Habara, R. Kodama, Y. Toyama, S. Karsch, K. Lancaster, C. Murphy, P. Norreys, R. Stephens, and C. Stoeckl, Appl. Phys. Lett. **86**, 191501 (2005).

74. C. Stoeckl, J. A. Delettrez, R. Epstein, G. Fiksel, D. Guy, M. Hohenberger, R. K. Jungquist, C. Mileham, P. M. Nilson, T. C. Sangster, M. J. Shoup III, and W. Theobald, Rev. Sci. Instrum. **83**, 10E501 (2012).

75. H.-S. Park *et al.*, Phys. Rev. Lett. **104**, 135504 (2010).

76. J. F. Barnes *et al.*, J. Appl. Phys. **45**, 727 (1974).

77. H.-S. Park *et al.*, Phys. Plasmas **17**, 056314 (2010).

78. H.-S. Park *et al.*, AIP Conf. Proc. **1426**, 1371 (2012).

79. N. R. Barton *et al.*, J. Appl. Phys. **109**, 073501 (2011).

80. B. Remington *et al.*, AIP Conf. Proc. **1426**, 1375 (2012).

81. J. L. Belof *et al.*, AIP Conf. Proc. **1426**, 1521 (2012).

82. J. Edwards *et al.*, Phys. Rev. Lett. **92**, 075002 (2004).

83. H.-S. Park, D. M. Chambers, H.-K. Chung, R. J. Clarke, R. Eagleton, E. Giraldez, T. Goldsack, R. Heathcote, N. Izumi, M. H. Key, J. A. King, J. A. Koch, O. L. Landen, A. Nikroo, P. K. Patel, D. F. Price, B. A. Remington, H. F. Robey, R. A. Snavely, D. A. Steinman, R. B. Stephens, C. Stoeckl, M. Storm, M. Tabak, W. Theobald, R. P. J. Town, J. E. Wickersham, and B. B. Zhang, Phys. Plasmas **13**, 056309 (2006).

84. L. Burakovsky *et al.*, Phys. Rev. Lett. **104**, 255702 (2010).

85. A. Dewaele, P. Loubeyre, and M. Mezouar, Phys. Rev. B **70**, 094112 (2004).

86. D. G. Hicks, T. R. Boehly, P. M. Celliers, J. H. Eggert, S. J. Moon, D. D. Meyerhofer, and G. W. Collins, Phys. Rev. B **79**, 014112 (2009); M. D. Knudson *et al.*, Phys. Rev. B **69**, 144209 (2004).

87. S. Root *et al.*, Phys. Rev. Lett. **105**, 085501 (2010).

88. C. E. Ragan III *et al.*, Los Alamos National Laboratory, Los Alamos, NM, LA-UR-83-2081 (1983).

89. Y. Ping, D. G. Hicks, B. Yaakobi, F. Coppari, D. E. Fratanduono, S. Hamel, J. H. Eggert, J. R. Rygg, R. F. Smith, T. R. Boehly, and G. W. Collins, "EXAFS Study of Iron Ramp-Compressed up to 560 GPa," submitted to Physical Review Letters.

90. A. Salamat *et al.*, Phys. Rev. B **84**, 140104 (2011).

91. R. Briggs *et al.*, J. Phys.: Conf. Ser. **377**, 012035 (2012).

92. B. Schwager *et al.*, J. Chem. Phys. **133**, 084501 (2010); S. T. Weir *et al.*, J. Appl. Phys. **111**, 123529 (2012).

93. S. Desgreniers, Y. K. Vohra, and A. L. Ruoff, Phys. Rev. B **39**, 10359 (1989).

94. F. Pérez *et al.*, Phys. Plasmas **19**, 083101 (2012).

95. K. B. Fournier *et al.*, Phys. Rev. Lett. **92**, 165005 (2004).

96. C. Constantin *et al.*, Phys. Plasmas **12**, 063104 (2005).

97. M. Tanabe *et al.*, High Energy Density Phys. **6**, 89 (2010).

98. J. R. Patterson *et al.*, Rev. Sci. Instrum. **83**, 10D725 (2012).

99. Y. Kim, J. M. Mack, H. W. Herrmann, C. S. Young, G. M. Hale, S. Caldwell, N. M. Hoffman, S. C. Evans, T. J. Sedillo, A. McEvoy, J. Langenbrunner, H. H. Hsu, M. A. Huff, S. Batha, C. J. Horsfield, M. S. Rubery, W. J. Garbett, W. Stoeffl, E. Grafil, L. Bernstein, J. A. Church, D. B. Sayre, M. J. Rosenberg, C. Waugh, H. G. Rinderknecht, M. Gatu Johnson, A. B. Zylstra, J. A. Frenje, D. T. Casey, R. D. Petrasso, E. K. Miller, V. Yu Glebov, C. Stoeckl, and T. C. Sangster, Phys. Plasmas **19**, 056313 (2012).

100. Y. Kim, J. M. Mack, H. W. Herrmann, C. S. Young, G. M. Hale, S. Caldwell, N. M. Hoffman, S. C. Evans, T. J. Sedillo, A. McEvoy, J. Langenbrunner, H. H. Hsu, M. A. Huff, S. Batha, C. J. Horsfield, M. S. Rubery, W. J. Garbett, W. Stoeffl, E. Grafil, L. Bernstein, J. A. Church, D. B. Sayre, M. J. Rosenberg, C. Waugh, H. G. Rinderknecht, M. Gatu Johnson, A. B. Zylstra, J. A. Frenje, D. T. Casey, R. D. Petrasso, E. K. Miller, V. Yu Glebov, C. Stoeckl, and T. C. Sangster, Phys. Rev. C **85**, 061601 (2012).

101. V. Goiffon *et al.*, Electron. Lett. **48**, 1338 (2012).

102. D. Dennetiere, P. Audebert, R. Bahr, S. Bole, J. L. Bourgade, B. Brannon, F. Girard, G. Pien, and Ph. Troussel, in *Target Diagnostics Physics and Engineering for Inertial Confinement Fusion*, edited by P. Bell and P. Grim (SPIE, Bellingham, WA, 2012), Vol. 8505, p. 85050G.

103. F. Philippe, A. Casner, T. Caillaud, O. Landoas, M. C. Monteil, S. Liberatore, H. S. Park, P. Amendt, H. Robey, C. Sorce, C. K. Li, F. Seguin, M. Rosenberg, R. Petrasso, V. Glebov, and C. Stoeckl, Phys. Rev. Lett. **104**, 035004 (2010).

104. S. Laffite and P. Loiseau, Phys. Plasmas **17**, 102704 (2010).

105. D. G. Hicks, B. K. Spears, D. G. Braun, R. E. Olson, C. M. Sorce, P. M. Celliers, G. W. Collins, and O. L. Landen, Phys. Plasmas **17**, 102703 (2010).

106. L. Masse, Phys. Rev. Lett. **98**, 245001 (2007).

107. L. Masse *et al.*, Phys. Rev. E **83**, 055401(R) (2011).

Publications and Conference Presentations

Publications

J. Bromage, C. Dorrer, M. Millecchia, J. Bunkenburg, R. Jungquist, and J. D. Zuegel, "A Front End for Ultra-Intense OPCPA," in *Light at Extreme Intensities 2011, AIP Conf. Proc. 1462*, edited by K. Osvay, P. Dombi, J. A. Fulop, and K. Varju (American Institute of Physics, New York, 2012), pp. 74–77.

D. T. Casey, J. A. Frenje, M. Gatu Johnson, M. J.-E. Manuel, N. Sinenian, A. B. Zylstra, F. H. Séguin, C. K. Li, R. D. Petrasso, V. Yu Glebov, P. B. Radha, D. D. Meyerhofer, T. C. Sangster, D. P. McNabb, P. A. Amendt, R. N. Boyd, S. P. Hatchett, S. Quaglioni, J. R. Rygg, I. J. Thompson, A. D. Bacher, H. W. Herrmann, and Y. H. Kim, "Measurements of the T(t,2n)^{4}He Neutron Spectrum at Low Reactant Energies from Inertial Confinement Implosions," Phys. Rev. Lett. **109**, 025003 (2012).

M. Chini, B. Zhao, H. Wang, Y. Cheng, S. X. Hu, and Z. Chang, "Subcycle ac Stark Shift of Helium Excited States Probed with Isolated Attosecond Pulses," Phys. Rev. Lett. **109**, 073601 (2012).

J. M. N. Djiokap, S. X. Hu, W.-C. Jiang, L.-Y. Peng, and A. F. Starace, "Enhanced Asymmetry in Few-Cycle Attosecond Pulse Ionization of He in the Vicinity of Autoionizing Resonances," New J. Phys. **14**, 095010 (2012).

W. R. Donaldson, C. Zhao, L. Ji, R. G. Roides, K. Miller, and B. Beeman, "A Single-Shot, Multiwavelength Electro-Optic Data-Acquisition System for ICF Applications," Rev. Sci. Instrum. **83**, 10D726 (2012).

D. H. Edgell, D. K. Bradley, E. J. Bond, S. Burns, D. A. Callahan, J. Celeste, M. J. Eckart, V. Yu. Glebov, D. S. Hey, G. Lacaille, J. D. Kilkenny, J. Kimbrough, A. J. Mackinnon, J. Magoon, J. Parker, T. C. Sangster, M. J. Shoup III, C. Stoeckl, T. Thomas, and A. MacPhee, "South Pole Bang-Time Diagnostic on the National Ignition Facility," Rev. Sci. Instrum. **83**, 10E119 (2012).

G. Fiksel, F. J. Marshall, C. Mileham, and C. Stoeckl, "Note: Spatial Resolution of Fuji BAS-TR and BAS-SR Imaging Plates," Rev. Sci. Instrum. **83**, 086103 (2012).

C. J. Forrest, V. Yu. Glebov, V. N. Goncharov, A. Pruyne, J. P. Knauer, P. B. Radha, M. Romanofsky, T. C. Sangster, M. J. Shoup III, C. Stoeckl, D. T. Casey, M. Gatu-Johnson, and S. Gardner, "High-Resolution Spectroscopy Used to Measure ICF Neutron Spectra on OMEGA," Rev. Sci. Instrum. **83**, 10D919 (2012).

D. H. Froula, R. Boni, M. Bedzyk, R. Brown, R. S. Craxton, T. Duffy, F. Ehrne, S. Ivancic, R. Jungquist, N. Kugland, J. Puth, R. G. Roides, M. C. Rushford, W. Seka, M. J. Shoup III, W. Theobald, and D. Weiner, "Optical Diagnostic Suite (Schlieren, Interferometry, and Grid-Image Refractometry) on OMEGA EP Using a 10-ps, 263-nm Probe Beam," Rev. Sci. Instrum. **83**, 10E523 (2012).

L. Gao, P. M. Nilson, I. V. Igumenshchev, S. X. Hu, J. R. Davies, C. Stoeckl, M. G. Haines, D. H. Froula, R. Betti, and D. D. Meyerhofer, "Magnetic-Field Generation by Rayleigh–Taylor Instability in Laser-Driven Planar Plastic Targets," Phys. Rev. Lett. **109**, 115001 (2012).

V. Yu. Glebov, C. Forrest, J. P. Knauer, A. Pruyne, M. Romanofsky, T. C. Sangster, M. J. Shoup III, C. Stoeckl, J. A. Caggiano, M. L. Carman, T. J. Clancy, R. Hatarik, J.McNaney, and N. P. Zautseva, "Testing a New NIF Neutron Time-of-Flight Detector with a Bibenzyl Scintillator on OMEGA," Rev. Sci. Instrum. **83**, 10D309 (2012).

R. Q. Gram, A. She, R. S. Craxton, and D. R. Harding, "Thermal Conductivity of Solid Deuterium by the 3ω Method," J. Appl. Phys. **112**, 033504 (2012).

J. D. Hager, V. A. Smalyuk, S. X. Hu, J. P. Knauer, D. D. Meyerhofer, and T. C. Sangster, "Study of Rayleigh–Taylor

Growth in Directly Driven Cryogenic Deuterium Targets," Phys. Plasmas **19**, 072707 (2012).

S. X. Hu, V. N. Goncharov, and S. Skupsky, "Burning Plasmas with Ultrashort Soft-X-Ray Flashing," Phys. Plasmas **19**, 072703 (2012).

J. Katz, R. Boni, M. J. Shoup III, R. Follett, and D. H. Froula, "A Reflective Optical Transport System for Ultraviolet Thomson Scattering from Electron Plasma Waves on OMEGA," Rev. Sci. Instrum. **83**, 10E349 (2012).

B. E. Kruschwitz, S.-W. Bahk, J. Bromage, M. D. Moore, and D. Irwin, "Accurate Target-Plane Focal-Spot Characterization in High-Energy Laser Systems Using Phase Retrieval," Opt. Express **20**, 20,874 (2012).

T. Y.-H. Lee, Q. Wang, J. U. Wallace, and S. H. Chen, "Temporal Stability of Blue Phosphorescent Organic Light-Emitting Diodes Affected by Thermal Annealing of Emitting Layers," J. Mater. Chem. **22**, 23,175 (2012).

F. J. Marshall, "Compact Kirkpatrick–Baez Microscope Mirrors for Imaging Laser–Plasma X-Ray Emission," Rev. Sci. Instrum. **83**, 10E518 (2012).

D. T. Michel, C. Sorce, R. Epstein, N. Whiting, I. V. Igumenshchev, R. Jungquist, and D. H. Froula, "Shell-Trajectory Measurements from Direct-Drive Experiments," Rev. Sci. Instrum. **83**, 10E530 (2012).

M. Mikulics, J. Zhang, J. Serafini, R. Adam, D. Grützmacher, and R. Sobolewski, "Subpicosecond Electron-Hole Recombination Time and Terahertz-Bandwidth Photoresponse in Freestanding GaAs Epitaxial Mesoscopic Structures," Appl. Phys. Lett. **101**, 031111 (2012).

M. Millecchia, S. P. Regan, R. E. Bahr, M. Romanofsky, and C. Sorce, "Streaked X-Ray Spectrometer Having a Discrete Selection of Bragg Geometries for Omega," Rev. Sci. Instrum. **83**, 10E107 (2012).

J. B. Oliver, P. Kupinski, A. L. Rigatti, A. W. Schmid, J. C. Lambropoulos, S. Papernov, A. Kozlov, S. Smith, and R. D. Hand, "Stress Compensation in Hafnia/Silica Optical Coatings by Inclusion of Alumina Layers," Opt. Express **20**, 16,596 (2012).

P. B. Radha, J. A. Marozas, F. J. Marshall, A. Shvydky, T. J. B. Collins, V. N. Goncharov, R. L. McCrory, P. W. McKenty, D. D. Meyerhofer, T. C. Sangster, and S. Skupsky, "OMEGA Polar-Drive Target Designs," Phys. Plasmas **19**, 082704 (2012).

S. P. Regan, R. Epstein, B. A. Hammel, L. J. Suter, J. Ralph, H. Scott, M. A. Barrios, D. K. Bradley, D. A. Callahan, G. W. Collins, S. N. Dixit, M. J. Edwards, D. R. Farley, S. H. Glenzer, I. E. Golovkin, S. W. Haan, A. Hamza, D. G. Hicks, N. Izumi, J. D. Kilkenny, J. L. Kline, G. A. Kyrala, O. L. Landen, T. Ma, J. J. MacFarlane, A. J. MacKinnon, R. C. Mancini, F. J. Marshall, R. L. McCrory, N. B. Meezan, D. D. Meyerhofer, A. Nikroo, K. J. Peterson, T. C. Sangster, P. Springer, and R. P. J. Town, "Diagnosing Implosions at the National Ignition Facility with X-Ray Spectroscopy," in *The 17th International Conference on Atomic Processes in Plasmas (ICAPiP), AIP Conf. Proc. 1438*, edited by K. Aggarwal, and F. Shearer (American Institute of Physics, New York, 2012), pp. 49–54.

H. G. Rinderknecht, M. Gatu Johnson, A. B. Zylstra, N. Sinenian, M. J. Rosenberg, J. A. Frenje, C. J. Waugh, C. K. Li, F. H. Séguin, R. D. Petrasso, J. R. Rygg, J. R. Kimbrough, A. MacPhee, G. W. Collins, D. Hicks, A. Mackinnon, P. Bell, R. Bionta, T. Clancy, R. Zacharias, T. Döppner, H. S. Park, S. LePape, O. Landen, N. Meezan, E. I. Moses, V. U. Glebov, C. Stoeckl, T. C. Sangster, R. Olson, J. Kline, and J. Kilkenny, "A Novel Particle Time of Flight Diagnostic for Measurements of Shock- and Compression-Bang Times in D^3He and DT Implosions at the NIF," Rev. Sci. Instrum. **83**, 10D902 (2012).

J. E. Schoenly, W. Seka, J. D. B. Featherstone, and P. Rechmann, "Near-UV Laser Treatment of Extrinsic Dental Enamel Stains," Lasers Surg. Med. **44**, 339 (2012).

C. Stoeckl, J. A. Delettrez, R. Epstein, G. Fiksel, D. Guy, M. Hohenberger, R. K. Jungquist, C. Mileham, P. M. Nilson, T. C. Sangster, M. J. Shoup III, and W. Theobald, "Soft X-Ray Backlighting of Direct-Drive Implosions Using a Spherical Crystal Imager on OMEGA," Rev. Sci. Instrum. **83**, 10E501 (2012).

Forthcoming Publications

N. L. Kugland, D. D. Ryutov, P.-Y. Chang, R. P. Drake, G. Fiksel, D. H. Froula, S. H. Glenzer, G. Gregori, M. Grosskopf, M. Koenig, Y. Kuramitsu, C. Kuranz, M. C. Levy, E. Liang, J. Meinecke, F. Miniati, T. Morita, A. Pelka, C. Plechaty, R. Presura, A. Ravasio, B. A. Remington, B. Reville, J. S. Ross, Y. Sakawa, A. Spitkovsky, H. Takabe, and H.-S. Park, "Self-Organized Electromagnetic Field Structures in Laser-Produced Counter-Streaming Plasmas," to be published in Nature Physics.

T. Y.-H. Lee, Q. Wang, L. Zeng, J. J. Ou, J. U. Wallace, L. J. Rothberg, and S. H. Chen, "Charge Transport Through Vacuum-Sublimed Glassy Films of *s*-Triazine- and Carbazole-Based Bipolar and Unipolar Compounds," to be published in Chemistry of Materials.

K. Mehrotra, H. P. Howard, S. D. Jacobs, and J. C. Lambropoulos, "Mechanical Characterization of 'Blister' Defects on Optical Oxide Multilayers Using Nanoindentation," to be published in the Materials Research Society Proceedings.

K. Mehrotra, H. P. Howard, S. D. Jacobs, and J. C. Lambropoulos, "Nanoindentation Probing of High-Aspect-Ratio Pillar Structures on Optical Multilayer Dielectric Diffraction Gratings," to be published in the Material Research Society Proceedings.

D. T. Michel, A. V. Maximov, B. Yaakobi, S. X. Hu, J. F. Myatt, A. A. Solodov, R. W. Short, and D. H. Froula, "Experimental Validation of the Two-Plasmon-Decay Common-Wave Process," to be published in Physical Review Letters.

S. Papernov, "Defect-Induced Damage," to be published in Laser-Induced Damage in Optical Materials.

S. P. Regan, K. Falk, G. Gregori, P. B. Radha, S. X. Hu, T. R. Boehly, B. J. B. Crowley, S. H. Glenzer, O. L. Landen, D. O. Gericke, T. Doeppner, D. D. Meyerhofer, C. D. Murphy, T. C. Sangster, and J. Vorberger, "Inelastic X-Ray Scattering from Shocked Liquid Deuterium," to be published in Physical Review Letters.

W. Theobald, R. Nora, M. Lafon, A. Casner, X. Ribeyre, K. S. Anderson, R. Betti, J. A. Delettrez, J. A. Frenje, V. Yu. Glebov, O. V. Gotchev, M. Hohenberger, S. X. Hu, F. J. Marshall, D. D. Meyerhofer, T. C. Sangster, G. Schurtz, W. Seka, V. A. Smalyuk, C Stoeckl, and B. Yaakobi, "Spherical Shock-Ignition Experiments with the 40 + 20-Beam Configuration on OMEGA," to be published in Physics of Plasmas.

H. X. Vu, D. F. DuBois, J. F. Myatt, and D. A. Russell, "Suprathermal Electron Production and Heat Flux Scaling with Laser Fluence from the Two-Plasmon-Decay Instability," to be published in Physics of Plasmas.

H. X. Vu, D. A. Russell, D. F. DuBois, and J. F. Myatt, "Hot-Electron Generation by Cavitating Langmuir Turbulence in the Nonlinear Stage of the Two-Plasmon-Decay Instability," to be published in Physics of Plasmas.

Conference Presentations

The following presentations were made at the European Physical Society 2012 Conference, Stockholm, Sweden, 2–6 July 2012:

D. H. Froula, D. T. Michel, R. S. Craxton, D. H. Edgell, R. Follett, V. Yu. Glebov, V. N. Goncharov, S. X. Hu, I. V. Igumenshchev, F. J. Marshall, J. F. Myatt, P. B. Radha, T. C. Sangster, W. Seka, R. W. Short, A. A. Solodov, C. Stoeckl, and B. Yaakobi, "Direct-Drive Laser–Plasma Interaction Experiments."

M. LaFon, X. Ribeyre, G. Schurtz, A. Casner, W. Theobald, R. Nora, M. Hohenberger, K. S. Anderson, R. Betti, C. Stoeckl, and D. D. Meyerhofer, "Hydrodynamic Modeling for Shock-Ignition Implosions and Simulations for Experiments on OMEGA."

The following presentations were made at the Optics and Photonics 2012, San Diego, CA, 12–16 August 2012:

B. Beeman, A. G. MacPhee, J. R. Kimbrough, G. A. Lacaille, M. A. Barrios, J. Emig, J. R. Hunter, E. K. Miller, and W. R. Donaldson, "Mach-Zehnder Modulator Performance Using the Comet Laser Facility and Implications for Use on NIF."

K. L. Marshall, C. Dorrer, M. Vargas, A. Gnolek, M. Statt, and S.-H. Chen, "Photoaligned Liquid Crystal Devices for High-Peak-Power Laser Applications."

C. Mileham, C. Stoeckl, W. Theobald, G. Fiksel, D. Guy, R. K. Jungquist, P. M. Nilson, T. C. Sangster, and M. J. Shoup III, "Crystal Imager Development at the Laboratory for Laser Energetics."

K. L. Marshall, A. Schulz, J. Lee, M. Rutan, E. Jones, G. Mitchell, C. Smith, and A. L. Rigatti, "Chemically Modified Organosilane Optical Coatings and Their Applications in High-Peak-Power Lasers," presented at the 244th American Chemical Society Fall 2012 National Meeting, Philadelphia, PA, 19–23 August 2012.

The following presentations were made at the International Committee on Ultra-High Intensity Lasers, Mamaia, Romania, 16–21 September 2012:

S.-W. Bahk, I. A. Begishev, and J. D. Zuegel, "An Anamorphically Imaged, Programmable Beam-Shaping System for High-Power Lasers."

J. Bromage, J. B. Oliver, C. Dorrer, and J. D. Zuegel, "Optical Coatings for Ultra-Intense OPCPA Systems."

C. Dorrer, "Characterization of Highly Dispersive Components Using Direct Instantaneous Frequency Measurements."

C. Dorrer, K. L. Marshall, S. H. Horn, M. Vargas, M. Statt, C. Caggiano, S. K.-H. Wei, J. B. Oliver, P. Leung, K. Wegman, J. Boulé, and Z. Zhao, "High-Damage-Threshold Beam Shaping Using Optically Patterned Liquid Crystal Devices."

H. P. Howard, A. F. Aiello, J. G. Dressler, N. R. Edwards, T. J. Kessler, A. A. Kozlov, S. LaDelia, J. B. Oliver, S. Papernov, A. L. Rigatti, A. W. Schmid, C. C. Smith, B. N. Taylor, and S. D. Jacobs, "An Improved Cleaning Method to Enhance the Damage Threshold of MLD Gratings."

J. Qiao, P. A. Jaanimagi, R. Boni, J. Bromage, and E. Hill, "Uniform Illumination and Space-Charge–Broadening Calibration for Accurate Short-Pulse Measurement Using a High-Speed Streak Camera."

J. Qiao, A. Kalb, Z. De Santis, and J. Papa, "Design and Analysis of a Meter-Scale Deformable Multilayer-Dielectric-Grating–Based Compressor for Kilojoule, Petawatt Laser Systems."

J. D. Zuegel, I. A. Begishev, J. Bromage, S.-W. Bahk, C. Dorrer, R. B. Brannon, and D. D. Meyerhofer, "Design and Status of an Energy Upgrade to the Multi-Terawatt Laser at the University of Rochester's Laboratory for Laser Energetics."

S. Papernov, E. Shin, T. Murray, A. W. Schmid, and J. B. Oliver, "355-nm Absorption in HfO_2 and SiO_2 Monolayers with Embedded Hf Nanoclusters Studied Using Photothermal Heterodyne Imaging," presented at Laser Damage, Boulder, CO, 23–26 September 2012.


1850
MELIORA
UNIVERSITY of
ROCHESTER